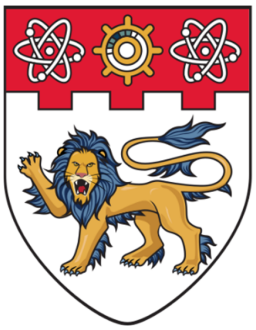

NANYANG TECHNOLOGICAL UNIVERSITY

SINGAPORE

STRUCTURAL INTEGRITY ASSESSMENT OF RAIL STEEL FAILURE MODES AND MECHANISM

LIU YANG

SCHOOL OF MECHANICAL AND AEROSPACE ENGINEERING

2021

STRUCTURAL INTEGRITY ASSESSMENT OF RAIL STEEL FAILURE MODES AND MECHANISM

LIU YANG

SCHOOL OF MECHANICAL AND AEROSPACE ENGINEERING

A thesis submitted to the Nanyang Technological University
in partial fulfilment of the requirement for the degree of
Doctor of Philosophy

2021

Statement of Originality

I hereby certify that the work embodied in this thesis is the result of original research, is free of plagiarised materials, and has not been submitted for a higher degree to any other University or Institution.

03 Jan 2021

Date

Liu Yang

Supervisor Declaration Statement

I have reviewed the content and presentation style of this thesis and declare it is free of plagiarism and of sufficient grammatical clarity to be examined. To the best of my knowledge, the research and writing are those of the candidate except as acknowledged in the Author Attribution Statement. I confirm that the investigations were conducted in accord with the ethics policies and integrity standards of Nanyang Technological University and that the research data are presented honestly and without prejudice.

18 Dec 2020

.....

Date

.....

John Pang Hock Lye

Authorship Attribution Statement

This thesis contains material from 3 paper(s) published in the following peer-reviewed journal(s) / from papers accepted at conferences in which I am listed as an author.

a) Chapter 3 and Section 6.2 are published as Y. Liu, K. S. Tsang, E. Z. Tan, N. A. Subramaniam, J. H. L. Pang, "Investigation on material characteristics and fatigue crack behavior of thermite welded rail joint", *Construction and Building Materials*, Volume 276, 2021, 122249, ISSN 0950-0618.

b) Chapter 4 and Section 6.4 is published Y. Liu, K. S. Tsang, N. A. Subramaniam, J. H. L. Pang, "Structural fatigue investigation of thermite welded rail joints considering weld-induced residual stress and stress relaxation by cyclic load", *Engineering Structures*, Volume 235, 2021, 112033, ISSN 0141-0296.

c) Chapter 5 and Section 6.3 is published as Y. Liu, K. S. Tsang, H. J. Hoh, X. Shi, and J. H. L. Pang, "Structural fatigue investigation of transverse surface crack growth in rail steels and thermite welds subjected to in-plane and out-of-plane loading," *Engineering Structures*, vol. 204, p. 110076, 2020.

The contributions of the co-authors are as follows:

- Prof John Pang Hock Lye provided the initial project direction and edited the drafts for all three manuscripts.
- For all 3 papers, I prepared the manuscript drafts. Manuscript a) was reviewed by Mr. Tsang, Mr. Tan, Mr. Subramaniam, while manuscript b) was reviewed by Mr. Tsang, Mr. Subramaniam and manuscript c) reviewed by Mr. Tsang, Dr. Shi and Dr Hoh.
- I co-designed the study with Prof John Pang Hock Lye and performed all the laboratory work at the School of Mechanical and Aerospace Engineering.
- All microscopy, including sample preparation, was conducted by me in the Materials Laboratory 1.
- Dr Hoh assisted in the Abaqus FE simulation by providing direction and guidance in the modelling in manuscript c). I designed and investigate the FE simulation in other manuscript.
- I collect and analyze the testing data.

03 Jan 2021 ....

Date Liu Yang

Acknowledgement

Foremost, I would like to express my sincere gratitude to my advisor Professor John Pang Hock Lye for his guidance and encouragement throughout my PhD study and related research work. Besides my supervisor, I would like to thank my thesis advisory committee: Professor Raju Ramanujan and Professor Fan Zheng David for their insightful comments and help to improve and widen my research.

I am also grateful to the following university staff: Dr. Hoh Hsin Jen, Dr. Shi Xiaopeng, and Dr. Tan Kok Ee from the SMRT-NTU Smart Urban Rail Corporate Laboratory, for their expertise and assistance during my research journey. I am also deeply thankful to these PhD students: Mr. Tsang Kin Shun, Mr. Nellian Alagu Subramaniam, Mr. Eddie Tan Zhi'En, Mr. Wang Jinglong, and Mr. Liu Zhufeng for their useful discussions.

Last but not the least, I also owe my thanks to my dearest family members for their continuous love and spiritually understanding during my life, especially during the four-year study to pursue a career in academia.

Table of Contents

List of Figures

List of Tables

Abstract

Rail steels are susceptible to fatigue failures resulting in rail breaks that can lead to unplanned downtime and safety concerns in railway operations. The main concern of the structural integrity in the rail track system is rail breaks resulting from fatigue failures of continuously welded rail structures, particularly, the thermite welded rail joints.

The objective of this research is to study the fatigue structural integrity behaviour and fracture mechanics properties of the thermite welded rail joints. The thermite welded rail joint, particularly the weld-toe region, is susceptible to fatigue crack formation. This is because of reasons as a) the geometry irregularities of the weldment at the weld toe region, b) the local weakness of metallurgical properties across the welded joint, and c) the presence of high tensile residual stress arising from the welding process. These three reasons interact with each other, affect the fatigue mode at the weld toes and deteriorate the fatigue endurance of the thermite welded rail joints.

In this research, a range of techniques and procedures were adopted to develop a framework for structural integrity assessment in three main areas of interest. Firstly, the fatigue behaviour of the welded joint with respect to the weldment geometry profile variation was studied using Fracture Mechanics. The stress intensity factor solutions were determined through finite element analysis and presented by the geometry factor, Y and weld magnification factor, M_k. Secondly, the mechanical and fatigue properties, and the size and distribution of weld defects were characterized. Transverse weld-toe surface cracks at the fusion line of the welded joint are found to be caused by the high density of weld defects and the mismatch of strength and fatigue properties between the thermite weld metal and unaffected rail steel. Lastly, a three-dimensional finite element model including the sequentially coupled thermal-mechanical simulation and cyclic plasticity constitutive simulation was developed to investigate the

welding process-induced tensile residual stress and the redistribution of the residual stresses due to cyclic bend fatigue loading, respectively. The numerical results of the finite element model were compared with experimental residual stress measurement data.

A structural integrity assessment methodology of the thermite welded rail joint with the analytical discussion of the underlying fatigue failure mechanism and the quantitative evaluation of fatigue propagation life was developed. The factors on the risk of fatigue failures at a given stress level, such as the variation in geometry profile, material discontinuities, and tensile residual stresses from the welding process, were also discussed. The structural integrity is established by providing a reliable Fracture mechanics-based fatigue model to predict the fatigue propagation life of the weld-toe transverse surface cracks at specific locations under the given sets of loading conditions.

Chapter 1 Introduction

Rails are produced in specific lengths and joined to each other to form a continuous rail track structure. Increasing demand for more frequent and reliable urban rail transportation leads to higher expectations for the structural integrity of the railway track system. The rail steel and its welded joints play a key role in the railway track system since failures of rail steel and joints can lead to unplanned system downtime and even rail breaks affecting the safe operation of the system and safety of passengers [1-6]. Despite improvements in rail steel maintenance and non-destructive inspections [7], structural fatigue research to assess the integrity of continuously welded railway steel structures is still a necessity in understanding rail break failures.

The service performance of the thermite welds can be considered in terms of the integrity of the welded joint and its ability to maintain the service without fatigue damage or fracture. Structural integrity analysis has proved to be a powerful tool for analysing the failure risk of welded rail joints and assessing the fatigue endurance. The assessment of structural integrity is required to take account of the material properties and behaviour under certain load conditions, the tensile residual stress resulting from the welding process with respect to the potential failure modes by fracture or fatigue. The main aim of this research is to examine the fatigue behaviour of the thermite welded rail joints under certain loading conditions with the occurrence of weld defects and residual stress field. The discussion of the underlying fatigue failure mechanism and the determination of the factors on the risk of fatigue failures at a given stress level are also presented.

1.1 Background on failures of welded rails

Most railway tracks are laid parallel on sleepers to provide a continuous and level surface for the movement of rolling stocks. The rails are manufactured at standardized length and transported to sites for assembly. The rails are then laid in the track and welded together to make it continuous. Four different welding methods have been developed, namely, thermite welding, flash-butt

welding, gas-pressure welding, and enclosed-arc welding [8]. The most common types of rail welding are thermite welding and flash-butt welding. Flash butt welding is often used for the installation of new railway tracks while thermite welding is used for maintenance operations of rail steel such as rail repair and replacement.

Thermite welding, also known as aluminothermic weld, is a fusion welding process that takes place in the sand mould between two rail ends. The welded joints were created by a chemical thermite reaction between aluminium and iron oxide with a large amount of energy being released. However, due to the inherent limitations of the welding process, as well as the operator dependency, the thermite welded joints suffer from variable quality in finished welds and are therefore susceptible to fatigue failures under service conditions. One typical fatigue failure mode is identified as the transverse break of welded joint initiating from the surface stress concentration sites of the weld toe region and propagating inwards in the transverse plane [9].

The thermite welded rail joint, particularly the weld-toe region or the interface between the fusion zone and heat affected zone, is susceptible to fatigue crack formation. The rail welds represent a discontinuity of the welded rail track due to the variation in geometry profile and material property variations compared with unaffected parent rail. These variations are of great significance to increase the risk of weld fatigue failures. In addition, the thermite welding process introduces high tensile residual stresses in the vicinity of the welded joint. The role of residual stresses on the fatigue crack growth must be analyzed and understood to have accurate and reliable predictive models for structural integrity assessment. The assessment of structural integrity is required to take account of the effects of geometrical features, the change of material characterizations across the welded joint, and the presence of flaws or defects and residual stress filed or other circumstance with respect to the potential failure modes by fracture or fatigue.

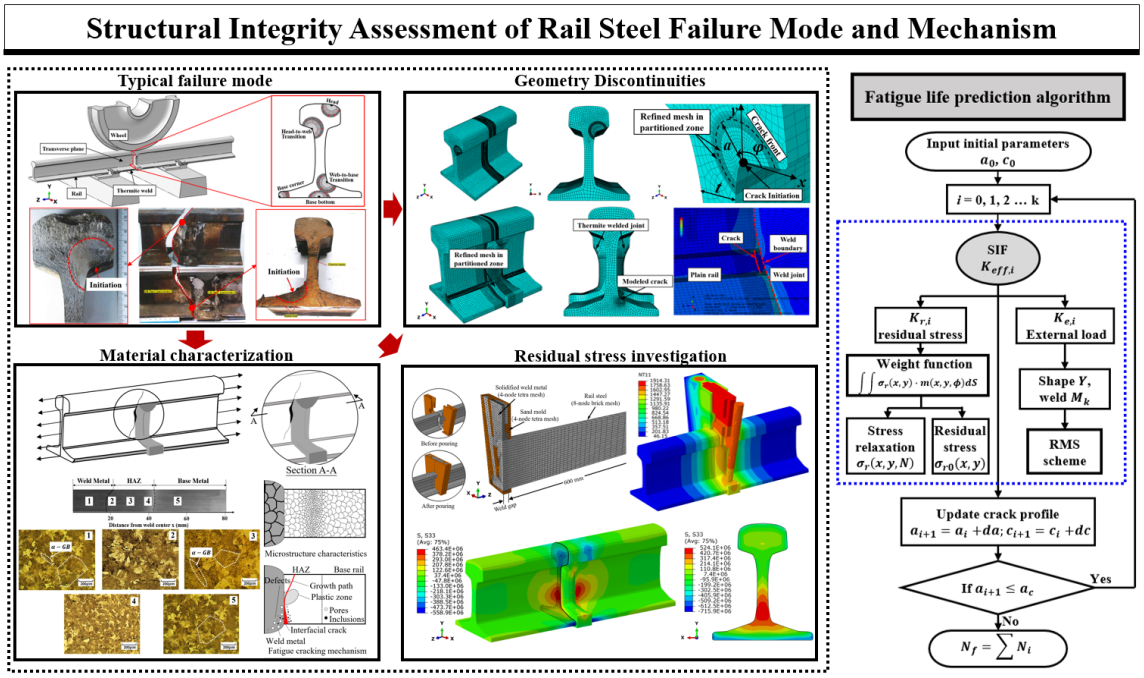

Figure 1-1: Research roadmap for structural integrity assessment of thermite welded rail

As shown in Figure 1-1, the structural integrity of the thermite welded rail joint is established by the study of the geometry discontinuities of weldment, the detailed characterization of the material properties across the welded joints, and the investigation of the welding induced residual stress field and relaxation behaviour under cyclic loading condition. The fatigue propagation life of the transverse weld-toe cracks under typical service load and welding induced residual stress were investigated by using fracture mechanics methodology. The stress intensity factor (SIF) is used as the crack propagation driving force parameter. The SIF solutions of these factors were determined through finite element analysis and presented by the geometry factor Y and weld magnification factor M_k. An algorithm was developed to calculate the fatigue propagation life using MATLAB code. The critical factors affecting the accuracy of fatigue life prediction, includes the stress level of typical loading types, the size of weld defects which treated as initial crack size, and the residual stress distribution and relaxation during the cyclic loading process, were discussed.

1.2 Objectives

The objectives of the research work include the following:

1. To characterize the material properties and performances for both parent rail and thermite weldment using the laboratory testing techniques. This involves: (a) Chemical composition analysis; (b) Mechanical properties determination, such as strength, fracture toughness and fatigue propagation rate; (c) Microstructure and hardness measurement and their variation across the welded joints; (d) Weld defects (pores and inclusions) investigation and the inherent correlation to the fatigue cracking resistance once treated as initial cracks.

2. To evaluate the residual stress and relaxation of the thermite welded rail joints and their effects on the fatigue behaviors. This involves: (a) To study the temperature/residual stress field via a sequentially coupled thermal-mechanical FE model and X-ray diffraction experimental measurement; (b) To investigate the residual stress variation resulting from different welding process parameters; (c) To evaluate the residual stress relaxation under external cyclic load from a cyclic plasticity constitutive model; (d) To analyze the effect of residual stress and stress relaxation on the fatigue performances.

3. To examine the fatigue behaviour of the thermite welded joint with respect to the weldment geometry profile variation. This involves: (a) To apply Fracture Mechanics for fracture analysis with crack propagation driving force parameter of stress intensity factor (SIF); (b) To develop a numerical model to investigate the stress state at the crack front of transverse surface cracks located at certain locations; (c) To derive the stress intensity factor (SIF) solutions of the conventional geometry factor Y and weld magnification factor M_k from finite element model analysis; (d) To investigate the crack size increment and shape change during the fatigue propagation process.

4. To develop a fracture mechanics methodology to quantitatively assess the fatigue propagation life of the thermite welded joints under typical fatigue loading conditions. This includes: (a) To develop an algorithm using MATLAB code for the calculation of the fatigue propagation life based on the SIF solutions; (b) To discuss the factors affecting the accuracy of fatigue life prediction, includes the stress level of typical loading types, the size of weld defects which treated as initial crack size, and the residual stress distribution and relaxation during the cyclic loading process.

1.3 Scope

The framework of the structural integrity assessment of the thermite welded rail steel is shown in Figure 1-2. Based on the framework, the technical basis for the structural integrity assessment of the thermite welded rail joint relates to the structural features as the material characteristics, thermite welding process and the fatigue cracking behaviour regarding the affecting factors.

Different materials have different fatigue cracking mechanisms and therefore the assessment of structural integrity involves an understanding of the material properties and behaviour under typical fatigue loading conditions. The experimental work of this research began with the characterization of the rail and thermite weld materials including chemical composition analysis, mechanical properties determination (fracture toughness and fatigue crack growth rate), microstructure and hardness measurement. Besides, the weld defects distributed across the welded joints were investigated and their effects on the fatigue cracking behaviour with respect to structural integrity were discussed.

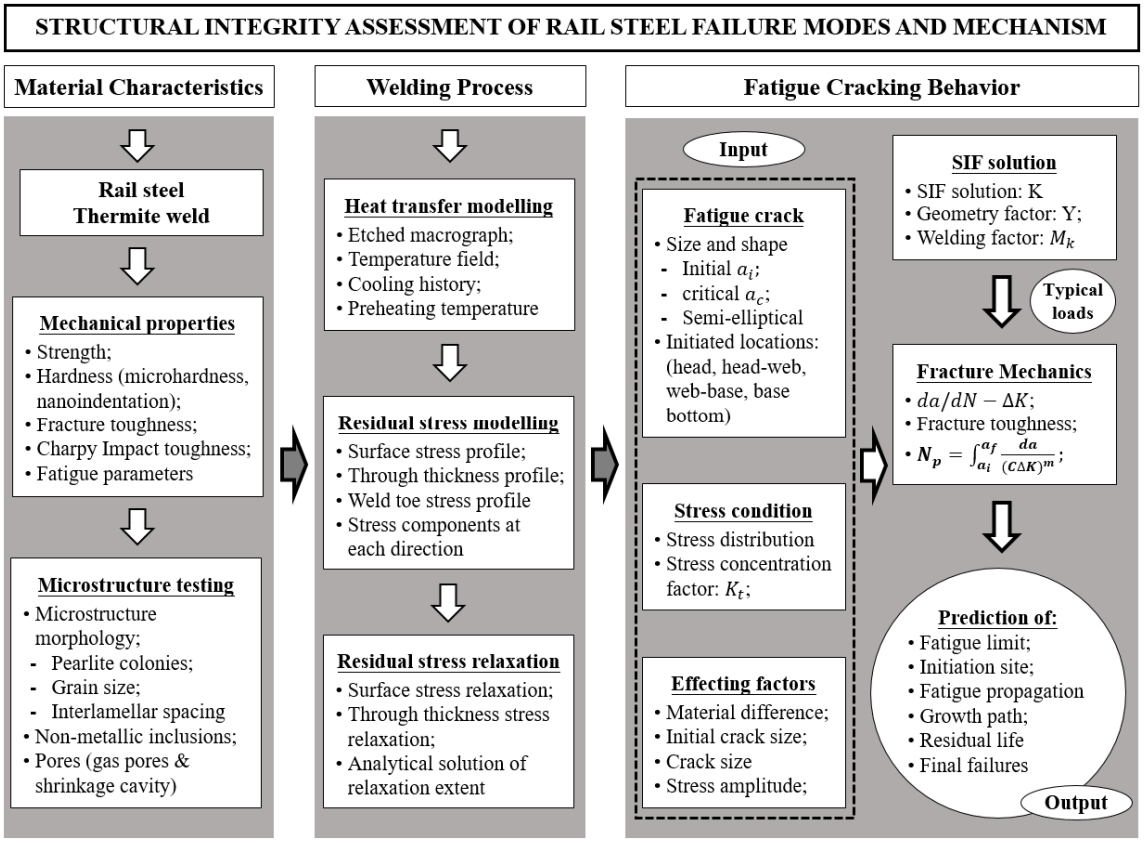

Figure 1-2: Framework for structural integrity assessment of thermite welded rail

The accuracy of the structural integrity assessment is also subject to considerations of the structural stress state, particularly, the residual stress field in the vicinity of the welded joint resulting from the thermite welding process. The role of residual stresses on the fatigue crack growth must be analyzed and understood to have an accurate and reliable predictive model for structural integrity assessment. The residual stress field at the thermite welded rail joint was simulated using a sequentially coupled thermal-mechanical simulation and compared with experimental measurements by X-ray diffraction method. A cyclic plasticity constitutive model was employed to investigate the redistribution of the residual stresses due to cyclic bend fatigue loading.

With the material properties and resistance to fatigue cracking, as well as the residual stress state prior to the crack growth obtained from both the experimental and numerical studies, the

quantitative investigation of the fatigue cracking tolerance capability of the thermite welded joint is possible by using MATLAB coded algorithm. Fracture Mechanics concept is applied to perform the fracture and fatigue analysis with crack propagation driving force parameter of stress intensity factor (SIF) under typical fatigue loadings. SIF solutions of the conventional geometry factor, Y, and weld magnification factor, M_k, were obtained from the finite element model analysis. The fatigue propagation life calculation was conducted by integrating the crack growth rate of the structures from the start to the finish crack lengths under the typical realistic service load types. The structural fatigue research to assess the integrity of the thermite welded rail joints taking account of the weld discontinuities and residual stresses from the welding process was examined.

1.4 Novelty and contribution

The main contribution of this research work is to develop a novel methodology for structural integrity assessment of thermite welded rail taking account of the weld discontinuities and residual stresses from the welding process. One significant challenge of this research lies on the very limited knowledge of the transverse weld toe surface cracks from the published information. In this context, the author tried to advance the understanding of the structural and fatigue performance of the complex thermite welded joints from laboratory testing and FEM simulations. A novel thermomechanical modelling is also implemented to investigate the residual stress field of the welded joint and the relaxation response to the cyclic load. Based on the collected data and knowledge, the author analyzed the corresponding fatigue cracking mechanism and proposed an appropriate fracture mechanics-based fatigue analysis approach. The quantitative assessment of fatigue life of the welded joint with an acceptable level of confidence is achieved. The development of the fatigue life estimation framework has important implications for solving the encountered engineering problems regarding the rail weld fatigue failures. The author believe that the designated solution and the insight gained from this dissertation will shed new light on the rail failure maintenance and the potential solutions of weld quality improvements.

1.5 Outline of the thesis

This thesis is partitioned into seven chapters. While the current chapter (Chapter 1) is a general introduction to the study, Chapter 2 deals with a review of the existing literature relevant to rail welded joint and the fatigue crack failure investigation. It begins with a brief look at the rail materials, profiles, and grades, before an introduction to the thermite welding process and the resulted material inhomogeneity across the welded joint, such as microstructure, hardness, weld defects and mechanical properties. A detailed review of the common fatigue failure modes occurring in the welded rail joints and the underlying failure mechanism was performed. In addition, the residual stress field resulting from the welding process and the influence on the fatigue cracking are highlighted. Chapter 3 presents the material characterization of microstructure, HAZ width, weld defects and hardness distribution across the welded joint. The discussion of the fatigue cracking mechanism at the weld toe region was provided based on the material characterization studies. Chapter 4 provides both experimental work and FE modelling of the residual stress field resulting from the thermite welding process. The laboratory X-ray diffraction technique was used to measure the surface residual stress components in different directions. A thermomechanical coupling model, integrated with the plasticity cyclic model, was developed to investigate the three-dimensional residual stress field and stress relaxation under external cyclic load. Chapter 5 elaborates more on stress intensify factor solutions of semi-elliptic cracks at different locations of thermite welded joint. The model will be used to generate the rail shape factor (Y) and welding magnification factor (Mk) for calculation of stress intensity factor. Besides, the experimental investigation of parent rail steel (R260 and R350HT) and thermite weld metal includes mechanical testing to evaluate the yield strength, impact energy, critical fracture toughness, and constants for fatigue propagation evaluation to understand the fracture and fatigue properties is presented. Consequently, Chapter 6 presents a fatigue propagation life prediction algorithm using MATLAB based on the research conclusions from previous chapters. The

affecting factors including material defect size, type and amplitude of loading condition, and residual stress resulting from the welding process are also investigated. Chapter 7 will provide the overall conclusion of this research as well as recommendations for future works.

Chapter 2 Literature Review

In this chapter, the technical studies for structural integrity assessment of the thermite welded rail joints were reviewed. The literature review on the thermite welding process and the physics involved during the welding process were performed. The material properties of the thermite welded rail joints and variation compared with unaffected parent rails were documented. A detailed review of the common fatigue failure modes occurring in the welded rail joints and the underlying failure mechanism was also performed. In addition, the residual stress field resulting from the welding process and the influence on the fatigue cracking were also highlighted.

2.1 Thermite welding of rail steels

Thermite welding, also known as aluminothermic weld, is a liquid state chemical welding process. The formation of such a joint takes place in a molten state. The result of the fusion between two pieces of metal to form a thermite weld joint is created by the products of a chemical reaction that arise due to the difference of free energy between aluminium and iron oxide. The application of thermite welding is especially prevalent in the field of rail track welding due to the advantages that arise from its process. The chemical reactions associated with the thermite weld process are highly exothermic. Hence, they release a great amount of heat. This heat is then channelled to the two pieces of metal to be joint permanently together through the product of the chemical reaction. The reactions used by the rail industry involves mainly aluminium powder and iron oxide powder. The two powders form a mixture to be poured into a crucible. The mixture is then ignited invoking the equations below [10]:

$$\begin{gathered} Fe_2O_3 + 2Al \rightarrow 2Fe + Al_2O_3 + Heat\ (181.5kcal) \\ 3Fe_3O_4 + 8Al \rightarrow 9Fe + 4Al_2O_3 + Heat\ (719.3kcal) \end{gathered} \tag{2-1}$$

The second equation creates a temperature of 2000 degrees Celsius after factoring heat losses due to the non-reacting alloy additions as well as radiation losses from the crucible. This temperature is well above the melting temperature of R350HT steel, which is at 1510 degrees Celsius. Upon the completion of the reaction, due to the difference in densities of the by-products, the aluminum oxide will rise to the top of the crucible leaving only molten iron at the bottom of the crucible. The molten iron is then poured into a mould containing the ends of two R350HT steel rail tracks to be fused together while the aluminum oxide is removed as slag. The molten iron enters the mould at a temperature higher than the melting point of R350HT steel, causing the ends of the rail track to melt partially to form a permanent bond, weld, upon the cooling of the molten iron and R350HT steel mixture. The presence of the mould is to provide the proper contour of the weld to fit the required shape that is required. The schematic of the above-mentioned steps is reflected in Figure 2-1.

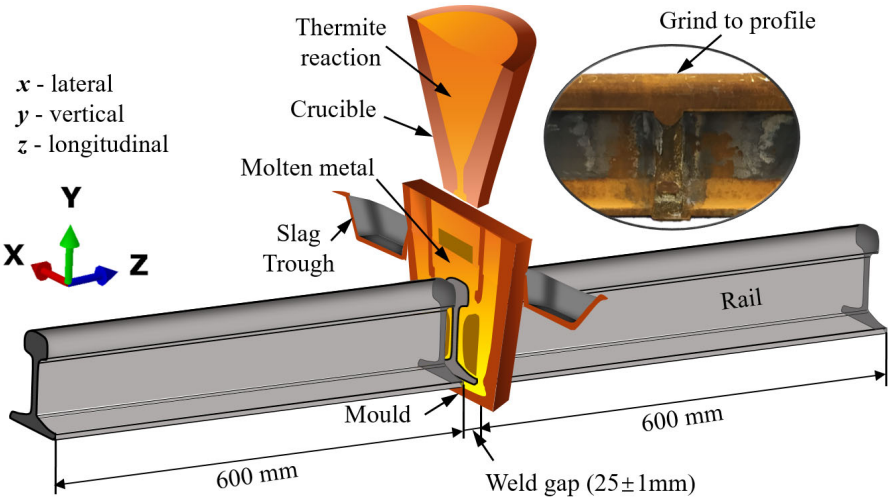

Figure 2-1: Schematic of thermite welding process

The welding of rail tracks through the means of thermite weld has several advantages. Thermite weld can be performed onsite at the location of the track after they have been laid in position. The equipment used in thermite welding is of a low cost and the speed at which a thermite weld can be complete is generally fast [11]. Hence, thermite welding is often the method of welding two

rail tracks together on site for rail replacement maintenance. Despite the advantages of simple process and relatively low cost with high mechanical strength and excellent wear and corrosion resistance, the thermite welding process can result in poor weld quality and lower fatigue life resistance compared to other processes. The fusion process may introduce the slag inclusion or pores which may cause weak points at weld toes for fatigue failures to occur [12].

2.2 Material properties of thermite welded rail joint

2.2.1 Macrographic characteristics

The macrographic examination of a tested specimen is conducted by visual observation under low microscope magnification. M. Jezzini-Aouad et al. [13] conducted a detailed metallurgical study of a thermite welded rail joint with the standard thermite welding process carried out in the laboratory. The welded joint was sectioned, polished, and etched before metallurgical observation to reveal the microstructure and the extend of heat affected zone. The observed macrography of thermite weld is as shown in Figure 2-2 and a typical pattern has been found. A 'vase' shape of section macrography was found where the thick portion is located at the web region and the thin portion located at the head and foot regions. This can be explained that less melting of the adjacent rail metal is involved for the thicker cross-section of rail profile.

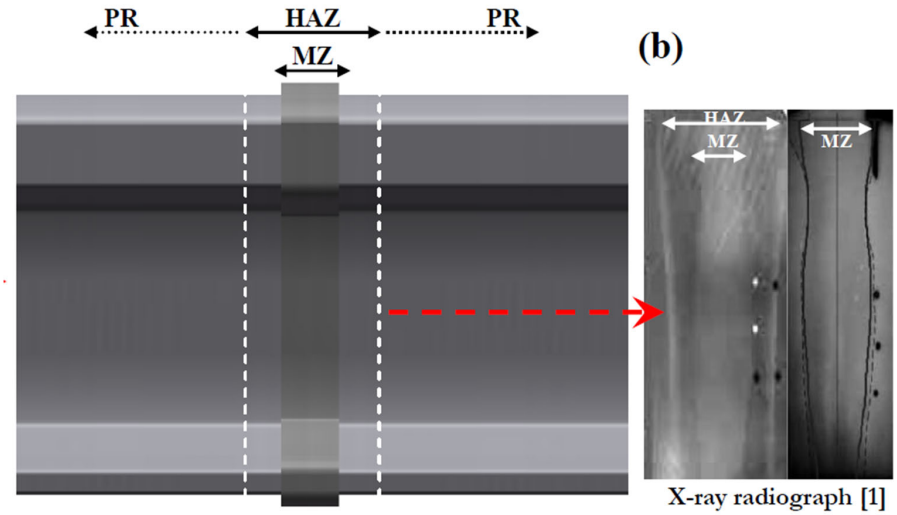

Figure 2-2: Microscopy of Thermite Weld and HAZ [13]

Ilić et al. [14] have studied further the discontinuities of the thermite welded joint in terms of the structural and mechanical characteristics. The macrostructure of the as-welded thermite welded joint in the longitudinal direction of the rail web was investigated. It revealed three symmetrical zones of a welded joint with a welding gap of 20 mm: the fusion zone, heat affected zone and the unaffected parent metal. It concluded that the width of the fusion zone is normally 40~50 mm and the visible heat affected zone is 15~25 mm as presented in Figure 2-3.

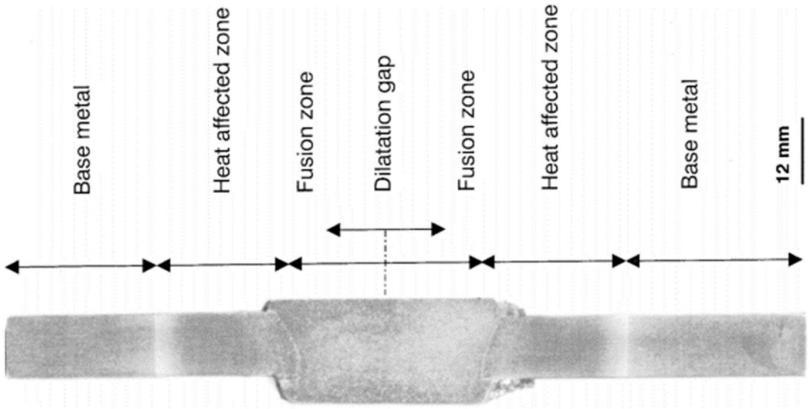

Figure 2-3: Detailed width of Thermite Weld and HAZ [14]

The in-depth discussion of the heat affected zone was conducted by Redkin et al. [15]. Besides the three distinguished zones mentioned by Ilić et al. [14], a nonvisible transition zone was observed between the heat affected zone and parent metal with the aid of the computer image analysis system. This zone with a width of around 20 mm is characterized by the obvious hardness decreasing and the hardness reaches lowest at approximately the center of this zone as shown in Figure 2-4.

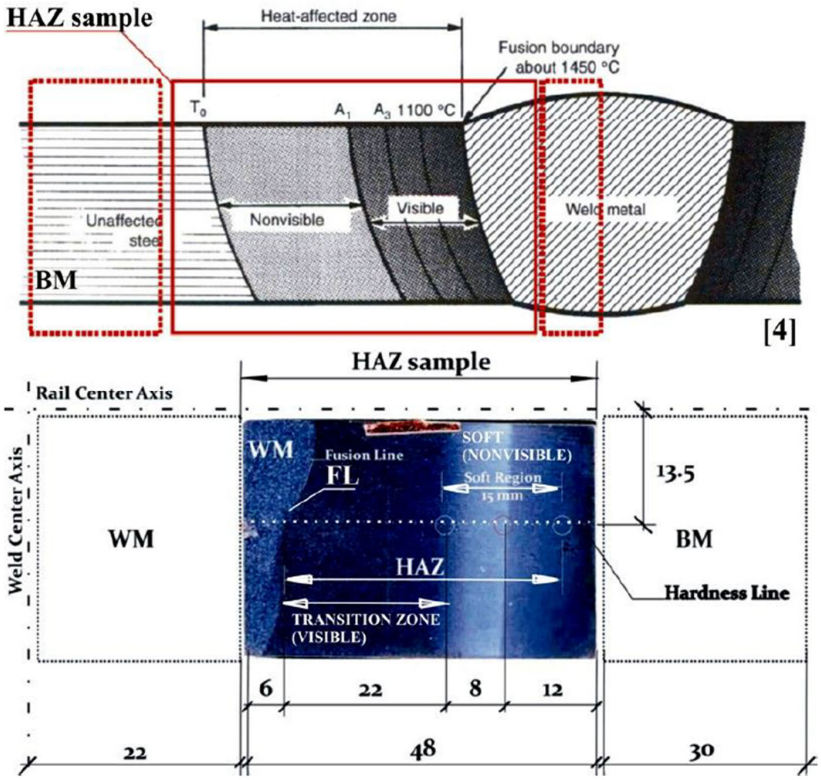

Figure 2-4: Critical Zones near Thermite Weld [15]

2.2.2 Material properties

The material characteristics across the thermite weldment joining rail steels and its effect on the fatigue cracking are generally recognized. The heat affected zone adjacent to thermite weld represents a change in many material characteristics, including hardness, microstructure, and strength, which is easy for fatigue cracks to initiate and propagate [16]. These material changes will be reviewed from different aspects as followed.

Chemical Composition:

Most rails applied around the world network are manufactured from low-alloy, carbon-manganese steels with medium to eutectoid carbon level. Two rail steel grades non-alloy (C-Mn) R260 and Non-alloy (C-Mn) heat treated R350HT which shall conform to the requirements of BS EN13674-1-2017 [17] are widely applied. R260 rails are used in straight tracks and curves of large radii (≥500m) in the mainline, and tracks that are less critical. R350HT rails are hardened in the

manufacturing process for use in locations that are exposed to adverse operating conditions especially in curves of smaller radii (<500m). The chemical composition and mechanical properties of parent rail steels are summarized in Table 1 below.

Table 1: Chemical composition/mechanical properties of rail steels

Steel grade (Parent material for weld metal)	Chemical composition % by mass								
	C	Si	Mn	P max.	S max.	Cr	Al max.	V max.	N max.
R260	0.60/ 0.82	0.13/ 0.60	0.65/ 1.25	0.030	0.030	0.15 max.	0.004	0.030	0.010
R350HT	0.70/ 0.82	0.13/ 0.60	0.65/ 1.25	0.025	0.030	0.15 max.	0.004	0.030	0.010
Thermite weld (R260)	0.40/ 0.75	0.00/ 1.75	0.50/ 1.40	0.035	0.035	0.20	0.02/ 0.60	0.25	0.02
Thermite weld (R350HT)	0.50/ 1.0	0.00/ 1.75	0.50/ 1.40	0.035	0.035	0.80	0.02/ 0.60	0.65	0.02
Steel grade	Mechanical properties								
	Tensile strength R_m min. (MPa)			Elongation after fracture A min. (%)			Hardness of the running surface center line (HBW)		
R260	880			10			260/300		
R350HT	1175			9			350/390		

The application of welded joints requires it to be hard with high wear resistance, and has a close match to the parent rail material, which is achieved mainly by chemical composition [18]. The material of the weld metal is normally with similar chemical composition to the parent rail steel with minor differences. A typically used material of weldment is high carbon steel with carbon (C) composition up to a maximum of 0.82 % which makes the steel hard and strong. Besides, another dominant composition is manganese (Mn) and its content is up to a maximum of 1.7 % and normally is around 1 % in rail steel and welded joints. Manganese will increase the hardness and strength of steel to a less extend than carbon. The chemical components of the weld metal are

dependent on the welded parent rail material and the composition shall comply with the limiting value listed in the EN standard [19]. The required limits for thermite weld metal when the parent rail steel is R260, R350HT are shown respectively in Table 1.

Microstructural Characteristics:

The material structure of rail steel is greatly dependent upon alloy composition and time-temperature history. Currently, most rail steels have a carbon content that varies from 0.5 to 0.8 wt%. Based on the iron-carbon phase diagram from Figure 2-5 (a), the rail steel is in the austenite phase with a face-centred cubic crystal structure when the temperature is between A_3 and up to around 1300 ℃. The crystal structure changes to body-centred cubic when it slowly cools to the temperature below A_1 (eutectoid temperature). The face-centred cubic crystal structure has a higher carbon solubility than the body-centred cubic structure.

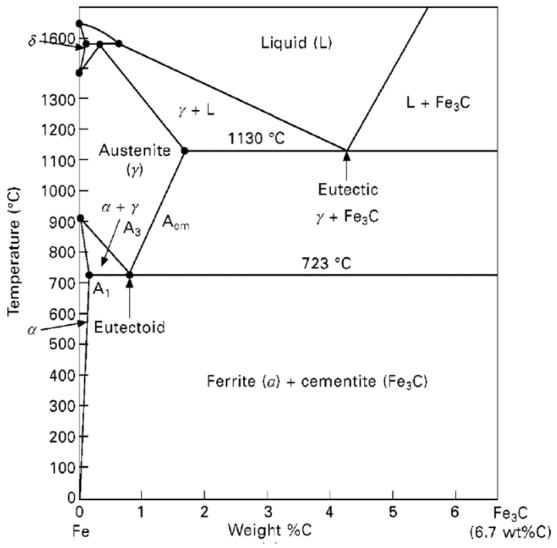

(a) complete diagram

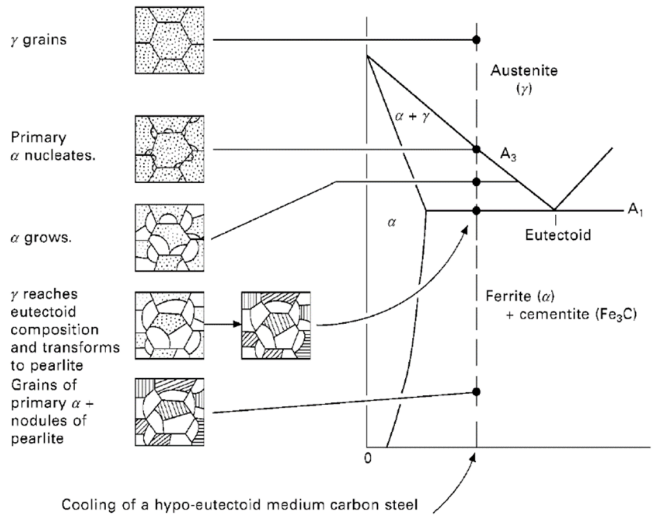

(b) schematic illustration of microstructure development

Figure 2-5: Iron-carbon phase diagram [1]

The carbon comes out of solution by a diffusional process during the normal air-cooling and therefore iron-carbide (Fe_3C) and eutectoid ferrite are separated in the form of lamellar structure as shown in Figure 2-5 (b). The 'pearl-like' structure, also termed as 'pearlite' forms with a lamella structure of carbide and ferrite. The degrees of pro-eutectoid (PE) ferrite at the prior austenite (PA) boundaries varies with the carbon content, and higher carbon content results in a lower percentage of PE ferrite. The microstructure of R260 (Figure 2-6) and R350HT shall be a pearlitic structure with a low percentage or even without any PE ferrite since the carbon content is close to the eutectoid point. no martensite, bainite or grain boundary cementite.

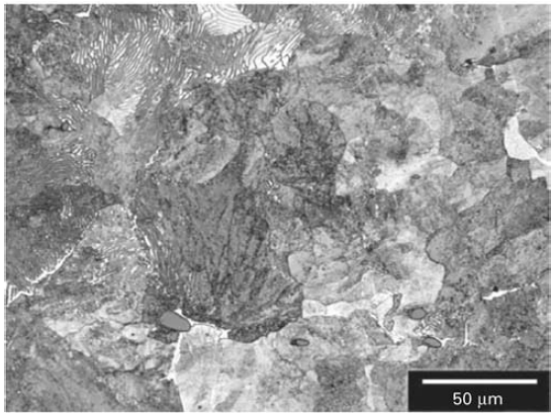

(a) optical image (ferrite light and carbide dark)

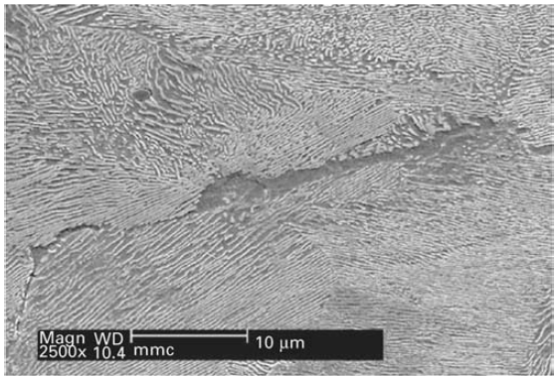

(b) electron microscope image (ferrite dark and carbide light)

Figure 2-6: Microstructure of rail material R260 showing PE ferrite and pearlite [1]

Similarly, the carbon composition of thermite weld metal is normally within 0.7% ~ 0.8%, which corresponds to a full pearlite structure under the microscope. The pearlite structure comprises a mixture of ferrite and iron carbide named cementite. The ferrite is soft while the cementite is hard and with lower fracture toughness, which can achieve both good strength and toughness. Some typical microstructure images were observed by optical microscope and scanning electron microscope (SEM) are showed in Figure 2-7 & 2-8. The microstructural images from SEM observations shows some prior austenite grain boundaries and they appear to be decorated by pro-eutectoid cementite. The grain size is relatively coarse in thermite weld due to the expected high temperature during the welding process.

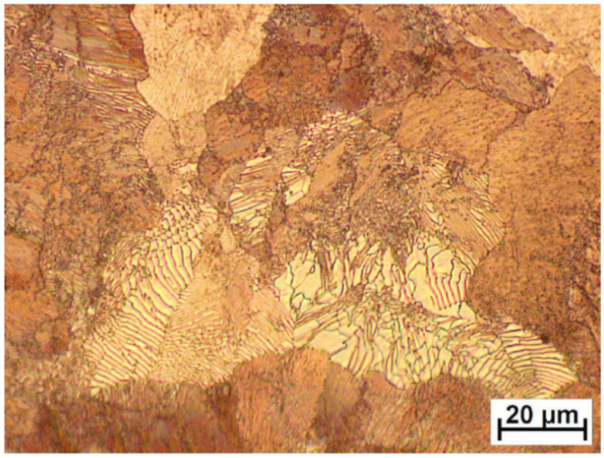

Figure 2-7: Optical Image of Thermite Weld [20]

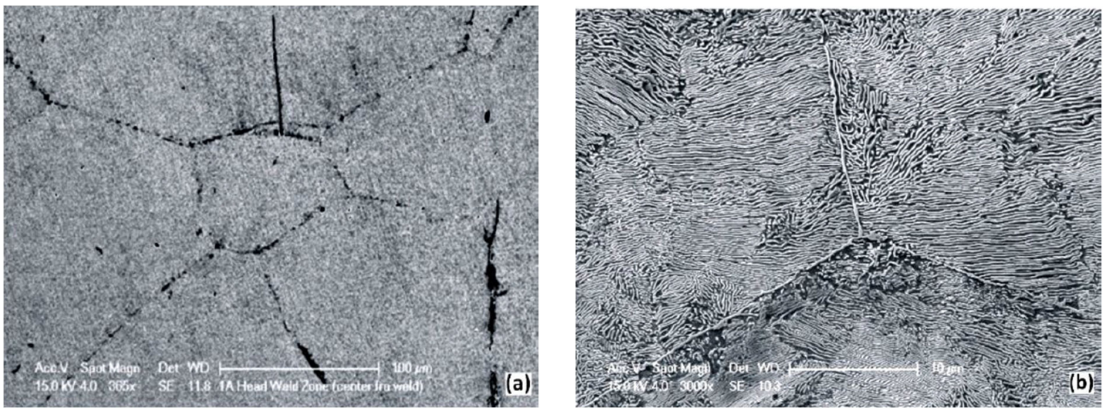

Figure 2-8: SEM images of thermite weld [15]

Hardness Distribution:

Hardness is one of the most important properties of metal when conducting metallurgical studies [21]. It represents the resistance of a metal to deformation or penetration and the study of hardness can also reveal several other mechanical properties including strength and brittleness. Furthermore, the longitudinal hardness distribution across the welded joint represents the material discontinuities or changes of the parent metal resulting from the welding process.

An example of the longitudinal hardness distribution across the thermite welded rail joint is from Saita et al. [8] and the result is presented in Figure 2-9. For this specific case, the chemical composition of the parent rail material and thermite weld metal is almost the same. As seen from the figure, the hardness of the thermite weld metal is around HV300 while the parent material hardness is around HV390. However, a distinguished heat affected zone of which the hardness firstly increases to as high as HV360 and decreases to a similar level of weld metal was observed. This rapid change of hardness results in material discontinuities and further lead to fatigue cracking initiation for welded structures. Saita et al. [8] have also proposed an approach of reheating with accelerated cooling to obtain the same hardness level of thermite weld as the parent rail and the resulted hardness distribution is also shown in Figure 2-9.

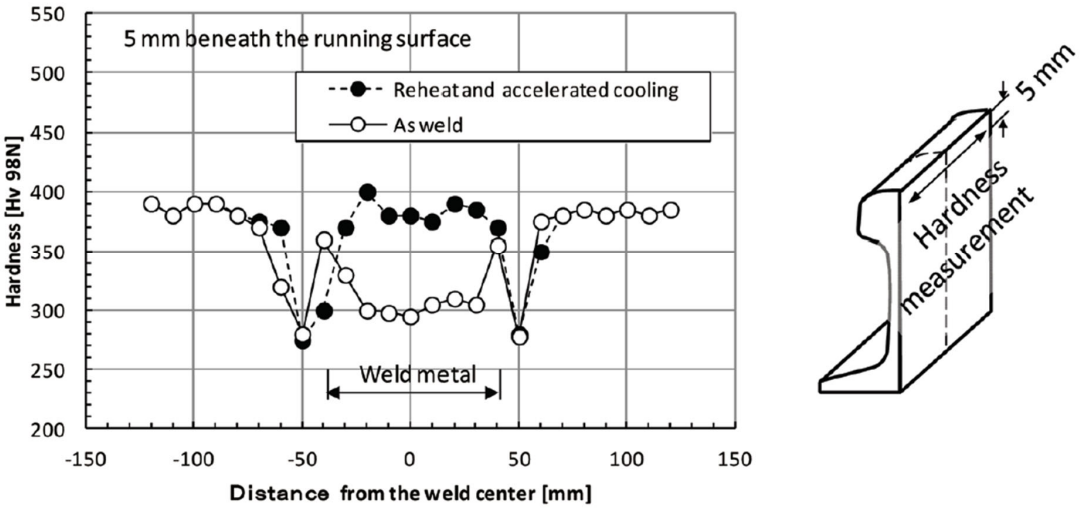

Figure 2-9: Longitudinal hardness distribution of thermite weld [8]

Strength and fracture properties:

The strength and fracture properties of the welded metal is highly dependent on the chemical composition and the welding process parameters [11]. Myers et al. [22] have characterized the thermite welds made either between "standard controlled-cooked" (SCC) rails or between "high silicon" (HiSi) rails with welding process from two thermite suppliers (type A and B). The tensile test was conducted for specimen cut out from the middle weld zone as shown in Figure 2-10.

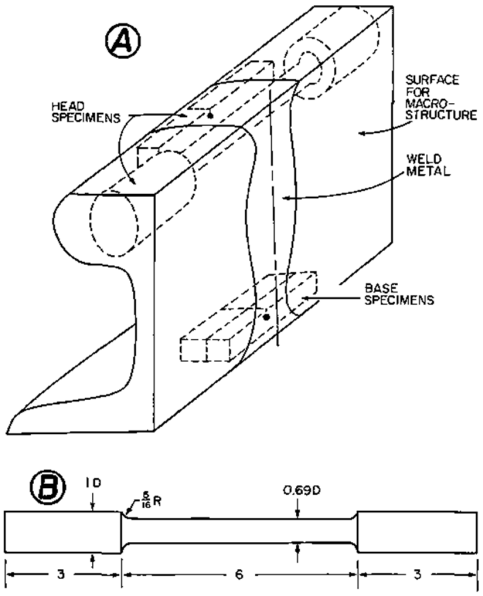

Figure 2-10: Test plan for mechanical tests of thermite weld metal

The evaluation of mechanical properties was performed for thermite welds under condition combinations with different preheating temperature and welding gap as shown in Table 2. The tensile result of each condition is presented in terms of ultimate tensile strength, elongation and area reduction as shown in Table 3. It is concluded that the strength of the weld metal is lower at equivalent hardness compared with parent rail material. The weld metal, no matter from which process, exhibit limited ductility or even no measurable ductility in terms of area reduction.

Table 2: Condition of thermite weld and rail [22]

Weld No. and type	Rail No. and type	Preheat time, min	Gap, in. (cm)	Thermal data
1-A	2-SCC	0	⅝ (1.6)	Yes
2-A	2-SCC	0	1 (2.5)	No
3-A	2-SCC	0	1½ (3.8)	Yes
4-A	1-HiSi	5	⅝ (1.6)	No
5-A	1-HiSi	5	1 (2.5)	Yes
6-A	1-HiSi	5	1½ (3.8)	No
7-A	1-HiSi	9	1½ (3.8)	Yes
8-A	1-HiSi	9	1 (2.5)	No
9-A	1-HiSi	9	⅝ (1.6)	Yes
1X-B	3-SCC	0	½ (1.3)	Yes
2X-B	4-SCC	0	½ (1.3)	Yes
3X-B	5-HiSi	0	½ (1.3)	No
4X-B	6-SCC	0	⅝ (1.6)	Yes
5X-B	7-SCC	0	½ (1.3)	Yes

Table 3: Tensile properties of weld metal and rail [22]

Material	Ultimate tensile strength, ksi	Ultimate tensile strength, MPa	Elongation,[a] %	Reduction in area, %
Type A:				
Rail 1[b]	143.0	985.8	13.0	13.6
Rail 2[b]	131.5	906.5	12.0	13.3
Weld 1	116.3	801.8	2.5	N.D.[c]
Weld 2	106.4	733.5	2.5	N.D.
Weld 3	115.0	792.8	1.0	N.D.
Weld 4	115.5	796.2	1.0	N.D.
Weld 5	112.3	774.2	1.0	N.D.
Weld 6	112.7	776.9	1.0	N.D.
Weld 7	115.9	799.0	1.0	N.D.
Weld 8	110.4	761.1	1.0	N.D.
Weld 9	108.3	746.6	1.0	N.D.
Type B:				
Weld 1x	115.3	792.8	2.7	1.8
Weld 2x	121.0	834.1	2.3	3.5
Weld 3x	121.8	839.6	2.2	2.6
Weld 4x[d]	123.0	847.9	3.5	2.9
Weld 5x	128.7	887.2	5.6	2.9

[a]Based on 5 in. (127 mm) gage length.
[b]Yield strengths are 91.6 ksi (631.5 MPa) and 84.0 ksi (579.4 MPa) for rails 1 and 2, respectively.
[c]N.D. – not detected.
[d]Did not break in center.

Fracture toughness and fatigue crack growth rate:

Fatigue crack growth rate (FCGR) and fracture toughness (K_C) properties play a significant role in damage tolerance capacity studies. The pre-cracking was performed for the tested specimen at a low enough stress intensity to minimize the plastic zone ahead of the crack before the test. The requirements for the specimen dimension, test procedure and results analysis of these two test are established in the standard of ASTM E399 [23] and ASTM E647 [24] respectively. The most recent work about the mode I fracture toughness (K_{IC}) tests and FCGR tests were done by Motameni and Eraslan [25]. The specimen for tests was cut from parent rail material in L-T direction with a metal grade of both R260 and R350HT. The specimen dimension and test results are shown in Figure 2-11 and Table 4 & 5. Most of the previous K_{IC} tests and FCGR tests are conducted on the parent metal. The results show that the fracture toughness of R350HT is higher than the R260 rail material. The fatigue crack growth resistance of both materials at the head location is higher than the web and foot locations.

However, most of the current studies are mainly focus on the parent rail material and testing related to the thermite weld metal is seldom reported due to relatively high cost and the limitation of dimension for specimen extraction.

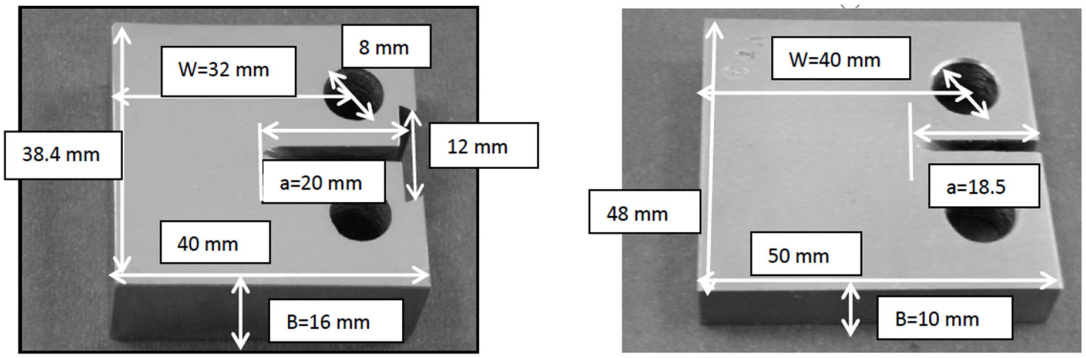

Figure 2-11: Specimen dimension of K_{IC} tests and FCGR tests [25]

Table 4: KIC test results for parent rail material of R260 and R350HT [25]

Fracture toughness R260 results

Specimen No	Fracture Toughness K_Q $Mpa\sqrt{m}$	Plane –Strain Fracture Toughness K_{IC} $Mpa\sqrt{m}$
HEAD	34.1	34.1
WEB	44.1	---
FOOT	46.7	46.7

Fracture toughness R350 HT

Specimen No	Fracture Toughness K_Q $Mpa\sqrt{m}$	Plane –Strain Fracture Toughness K_{IC} $Mpa\sqrt{m}$
HEAD	42.2	42.2
WEB	68.1	---
FOOT	43.4	43.4

Table 5: FCGR test results for parent rail material of R260 and R350HT [25]

Specimen No	C	m	R^2
R350HT HEAD	$2.525X10^{-13}$	3.91	0.94
R350HT WEB	$1.004X10^{-12}$	3.62	0.97
R350HT FOOT	$5.034X10^{-14}$	4.62	0.91
R260 HEAD	$1.64X10^{-13}$	4.1	0.95
R260 WEB	$1.78X10^{-13}$	4.66	0.95
R260 FOOT	$6.42X10^{-13}$	3.91	0.97

Other Fatigue Test of Rail Weld:

A four-point fatigue test is required to evaluate the fatigue performance of rail weld according to the standard. Unlike the S-N data that is material property, the tested load-life data is dependent on the structure geometry and size. The criterion of the fatigue test is that the rail weld has an endurance of minimum 5×10^6 cycles under cyclic loading with a ratio min/max equal to 0.1 and a frequency of 10 Hz. Some other fatigue tests were then conducted by J.I. Verdeja [26] for thermite weld with rail grade of R260 and profile of UIC 60. Frederick et al. [27] studies the failures occurring in the thermite weld and concluded that the failures initiate from the web-to-base transition region and base bottom are due to the stress concentration resulting from insufficient heat input and oxides contamination. He then optimised the shape of mould and conducted a four-

point fatigue test to compare the results as below. It shows that the shape changing of mould will significantly improve the service cycles of thermite welding.

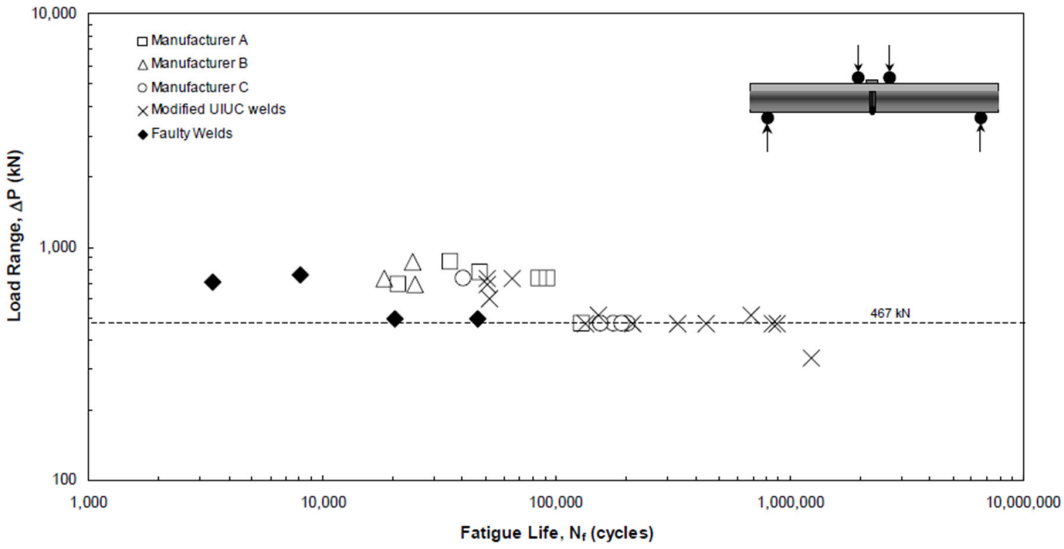

Figure 2-12: Results of four-point fatigue test [27]

2.3 Thermite welded joint fatigue failures and mechanism

2.3.1 Thermite welded joint failure mode

The continuously welded joints are the weak points of the rail [28-31]. The past studies showed that more than 60% of rail failures are resulted from welded joints failures [32] and among these welding failures thermite welding was the most frequent compared with other welding methods [33]. There is no clear classification and definition of the failure modes in continuously welded joints. Rail defects are classified by the plane of the crack surface as shown in Figure 2-13a and its specific location (head, head-to-web, web-to-foot, foot base or foot corner regions) as shown in Figure 2-13b [34].

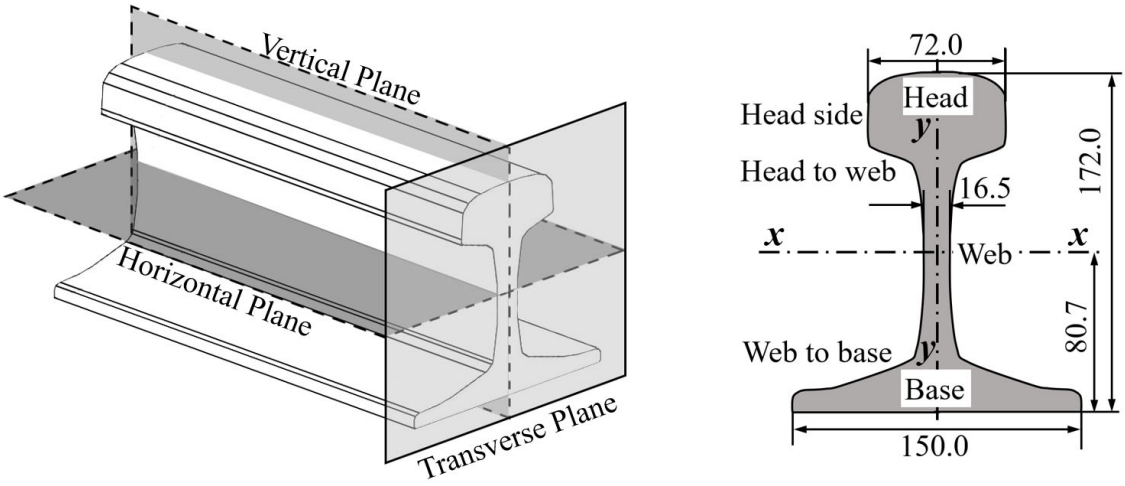

(a) definition of planes in rail (b) definition of regions for transverse rail

Figure 2-13: Illustration of terminology used in the simulation

Based on current researches, one of the most often occurred failures in thermite welded rail joint is the transverse failure or straight breaks. The transverse fatigue failures fail in the way as shown in Figure 2-14. The transverse failures or transverse cracks initiate from the stress concentration sites of the transverse plane and propagate in the vertical direction or direction with a small angel to the transverse plane [9]. The stress concentration sites include the edge of weld collar (centre of welding) or the interface between the welding and parent rail (Figure 2-14b), centreline shrinkage defects in the web to base region (Figure 2-14a) [35], and the base corner in the field side of the curved rail.

(a) failure occurring in middle of welding [36] (b) failure occurring in the weld-toe region

Figure 2-14: Transverse failure or straight break failure

The initiation and propagation of transverse failures are highly dependent on the loading condition, welding process, cooling environment, and post-heat treatment. Current studies only revealed the causes of the transverse failures occurring in the centreline of weldment (Figure 2-14a), which is due to the insufficient fusion resulting from improper preheating. Most of these failures are found to be associated with the shrinkage defects in the centreline of the weldment due to insufficient preheat. The past tests revealed that the thermite welded joints are prone to centreline shrinkage even the welding process strictly follows the standard procedure [32]. This type of failure is more likely to occur in the colder when the temperature is below the stress-free temperature. The rapid changes in the rail temperature during the cold weather results in a high level of longitudinal rail stresses. The presence of longitudinal tensile residual stress resulting from the welding process further increases the risk of such fatigue failures.

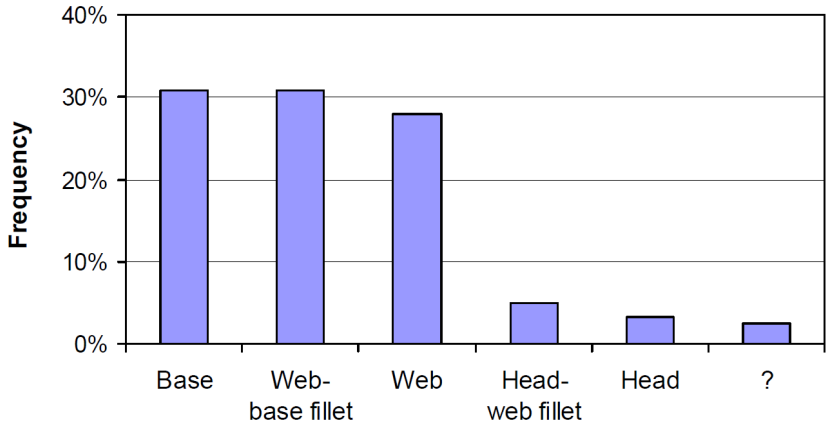

Figure 2-15: Histogram of failure locations caused by thermite weld [27]

The cause of failures initiating from the interface between the weld fusion zone and heat affected zone is still not very clear and deeper research about the initiation and development is not as well researched. The transverse failures often occur in a few specific locations, including head, head-to-web, web, web-to-base, base, or base corner (Figure 2-15 & 2-16b). These locations are critical positions that require special attention. Some images of these failures due to transverse cracks are shown in Figures 2-16c & 16d.

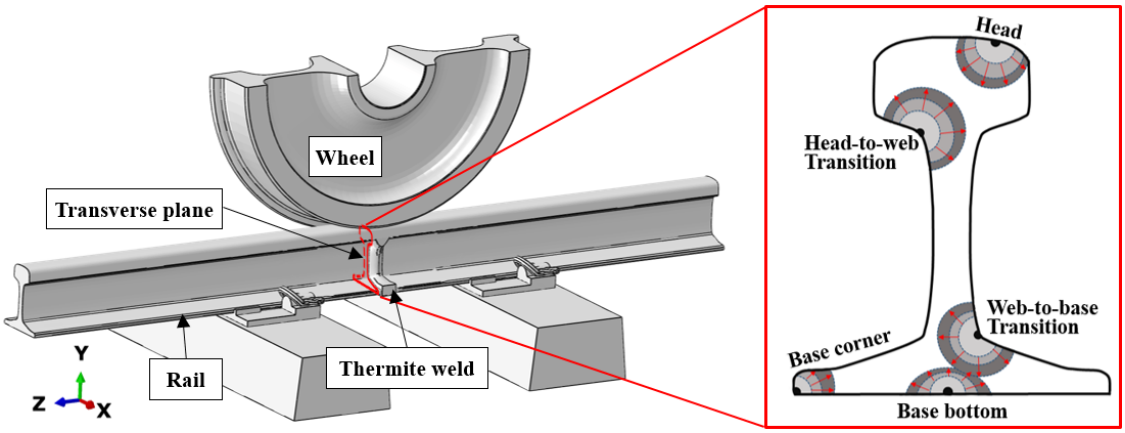

(a) illustration of rail transverse plane (b) crack regions definition

(c) crack in the head-to-web transition region (d) crack in the web-to-base transition region

Figure 2-16: Typical transverse weld-toe failures

2.3.2 Thermite welded joint failure mechanism

The thermite welded rail joint, particularly the weld-toe region or the interface between the fusion zone and heat affected zone, is susceptible to fatigue damage formation [37-39]. The assessment of structural integrity is required to take account of the effects of the unusual service loadings [9, 32, 40-43] including the residual stress state, and the presence of discontinuities [14, 30, 44-46] or other circumstance with respect to the potential failure modes by fracture or fatigue. The unusual service load, together with the residual stress arisen from the welding process plays a role in the structural deterioration of the welded joint. The presence of discontinuity is due to two main reasons. The first one is the geometry irregularity of the weldment, particularly at the weld toe region [31, 47], generates a stress concentration site at which the stress state resulting from the

wheel/rail contact dynamic load [1, 48-54] is amplified. The second reason is the locally varying metallurgical properties along the welded rail [55-60]. Thermite welding of high-strength rail can result in a heat affected one adjacent to the weld, leading to heterogeneities of material properties includes hardness, microstructural disturbance, and weld defects along the surface or subsurface. These affecting factors, interacting with each other, significantly affect the damage mechanisms and further increase the fatigue damage speed of the welded joint.

Service load of welded rail

Rails are subjected to a combination of local dynamic stresses resulting from wheel/rail contact and global bending stresses. In the continuously welded rails, tensile residual stresses from the welding process also play an important role in the deterioration of service behaviour.

The bulk stresses resulting from the loading above can be summarized in both the longitudinal plane and transverse plane. In the longitudinal plane, the vertical load from the train will cause the rail to bend vertically under the support of sleepers in two sides. The thermal stresses due to thermal expansion and contraction from continuous welding and environmental temperature changes are established as either tensile or compressive loading. The residual stress results from the manufacturing process of rail steel such as head hardening or straightening. Some localized residual stress will also be introduced during thermite welding. In the transverse plane, eccentric head loading between the train wheel and rail will cause a torsional load to the rail. Also, the lateral wheel load will lead to tensile stress in the rail web.

Rail track and welded joints are subjected to a harsh loading environment during service. From past researches, the rail experiences mainly three types of stresses during service life [61] as shown in Figure 2-17. Hence besides serving as a guide for the wheels, the rail must withstand the stresses listed and transmit the load to the ground through sleepers and ballasts.

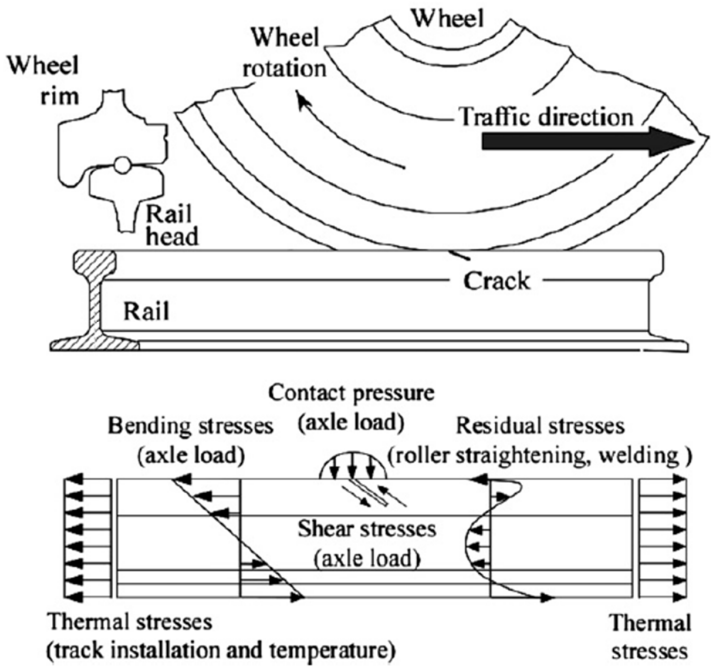

Figure 2-17: Loading condition acted on the rail in service [62]

The first loading comes from the interaction with the running vehicles which results in contact pressure due to contact, shear stress from sliding and bending force from the train weight. The simplest model to consider the bending force of the rail is to assume that the rail is sitting on a continuous elastic foundation with multiple wheels running on the railhead surface. Fletcher and Kapoor [63] developed a model to predict the bending of the rail and the accompanying longitudinal stress and lateral stress as shown in Figure 2-18. It shows that although the bending in the lateral direction is possible, the dominant bending load is in the longitudinal direction which makes it susceptible to mode I fatigue cracking.

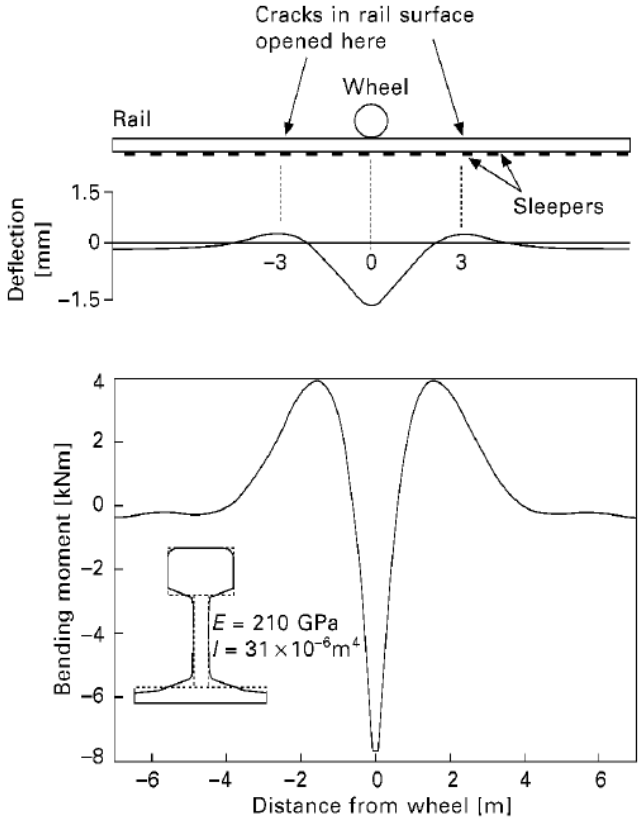

Figure 2-18: Schematic illustration of rail bending [1]

Secondly, rail steels contract at low temperatures and expands at high temperatures and the thermal stresses will be resulted from the welding process and extreme weather conditions. The longitudinal thermal stress is of great concern since the longitudinal expansion and contraction is restricted for the continuously welded rails. Longitudinal stress can be developed due to the temperature change of the weather condition. The resulting compressive and tensile longitudinal stresses must be both avoided as the former leads to rail buckling in hot weather and the latter open small cracks to become rail breaks.

The residual stress from the manufacturing in factory and onsite welded joints is also of great significance. The residual stress from the manufacture, particularly the “roller straightening” process, is locked into the rail. Typical residual stress distribution in the longitudinal direction [64] is present as shown in Figure 2-19.

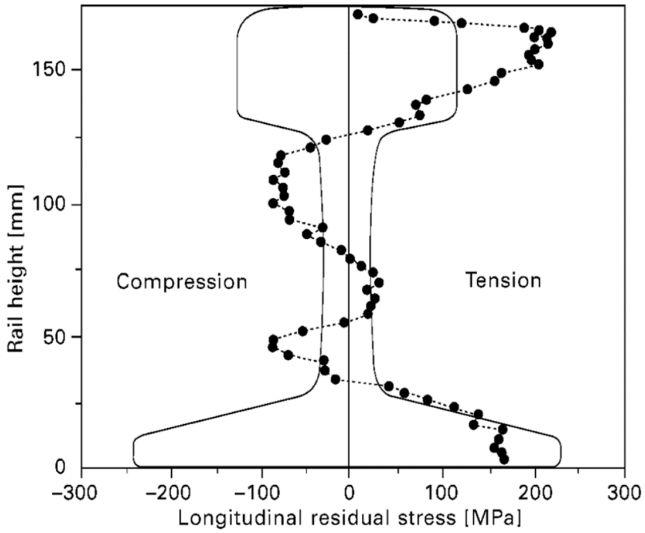

Figure 2-19: Typical longitudinal residual stress along the rail height from rail manufacturing process [64]

Residual stress from the welding process

Another source of residual stress is from the welding process. Thermite welded joints often suffer from non-uniform and highly localized temperature distribution associated with localized plastic deformation due to the non-linearity of material properties. It is well established that residual stresses play an important role in the structural behaviour of welded joints [65, 66], especially for their fatigue performance in the presence of cyclic loading [67, 68]. Various studies had been carried out to study the residual stress and its effect on the fatigue life of the thermite welded rail joints. Webster et al. [69] mapped the residual stress field generated by a standard gap thermite welding process using the neutron strain scanning method. A 400 mm longitudinal section of thermite welded rail, with the weldment located at the centreline, was extracted for residual stress measurement as shown in Figure 2-20.

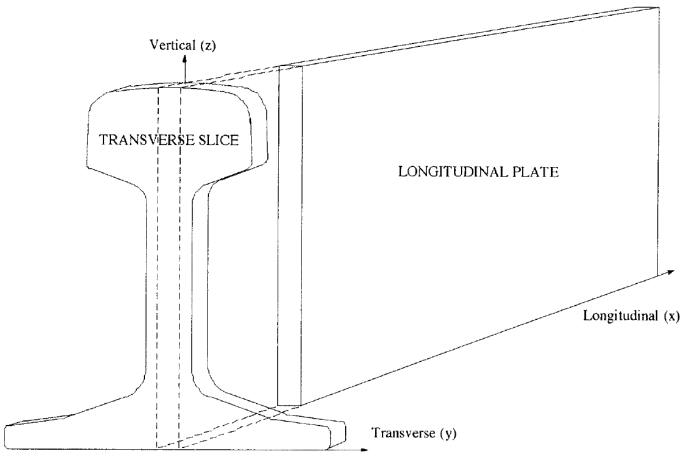

Figure 2-20: Longitudinal and transverse plate and slide sections used for residual stress of welded rail (x) at different vertical heights (z) [69]

The residual stress measured results of the longitudinal plate were shown in Figure 2-21. The symmetrical pattern is could be expected for the welded structure. It is shown that the transverse residual stress exhibits no particular pattern and the magnitude is relatively low compared with other stress components. However, a distinct zone with high tensile residual stress was observed located at the web location of the welded joint in the longitudinal and vertical directions.

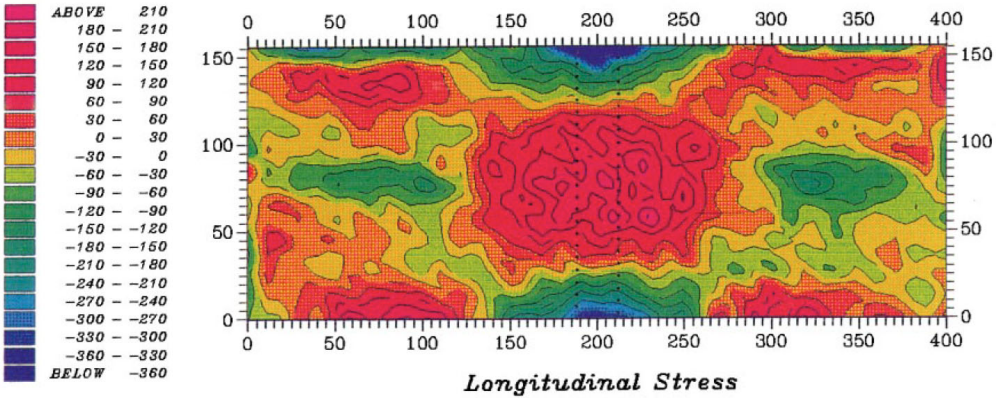

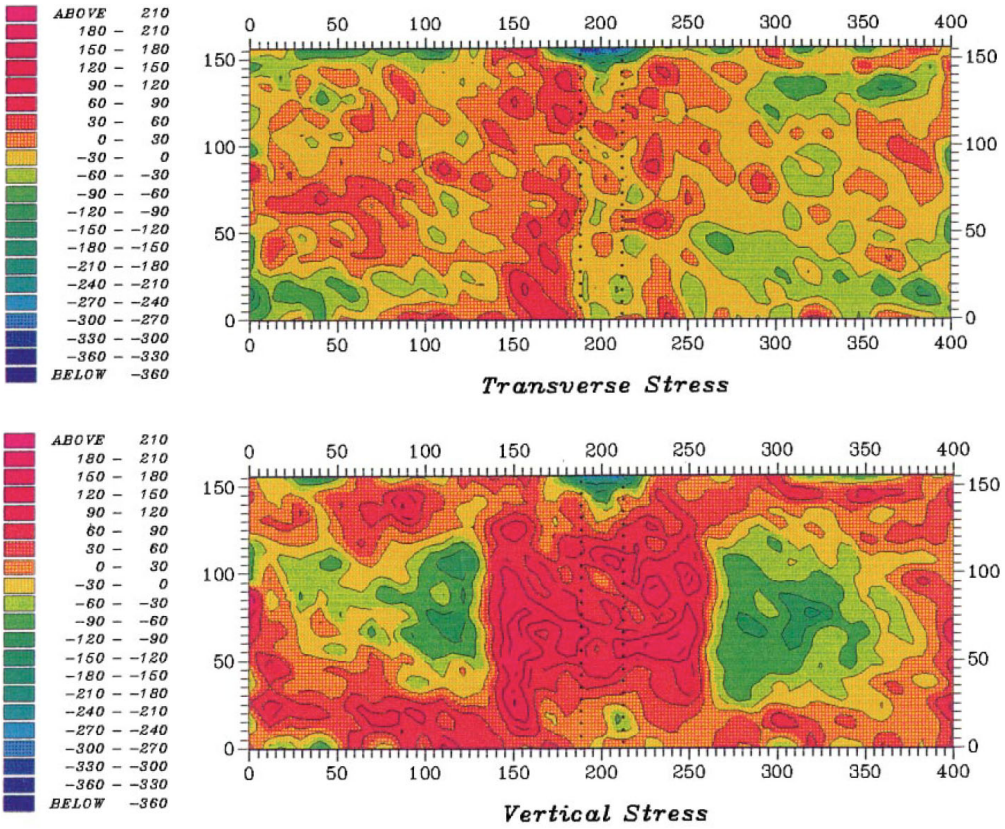

Figure 2-21: Residual stress measured results, in MPa for the welded plate sample

The results of the longitudinal residual stress at different rail heights are presented in Figure 2-22. The steep longitudinal change of residual stress was found near the weld toe region where the abrupt change of temperature occurs. It can also find that the tensile residual stress is always located in the web region along the rail height direction. Hence, the transverse surface cracks propagating from defects tend to present in the web region.

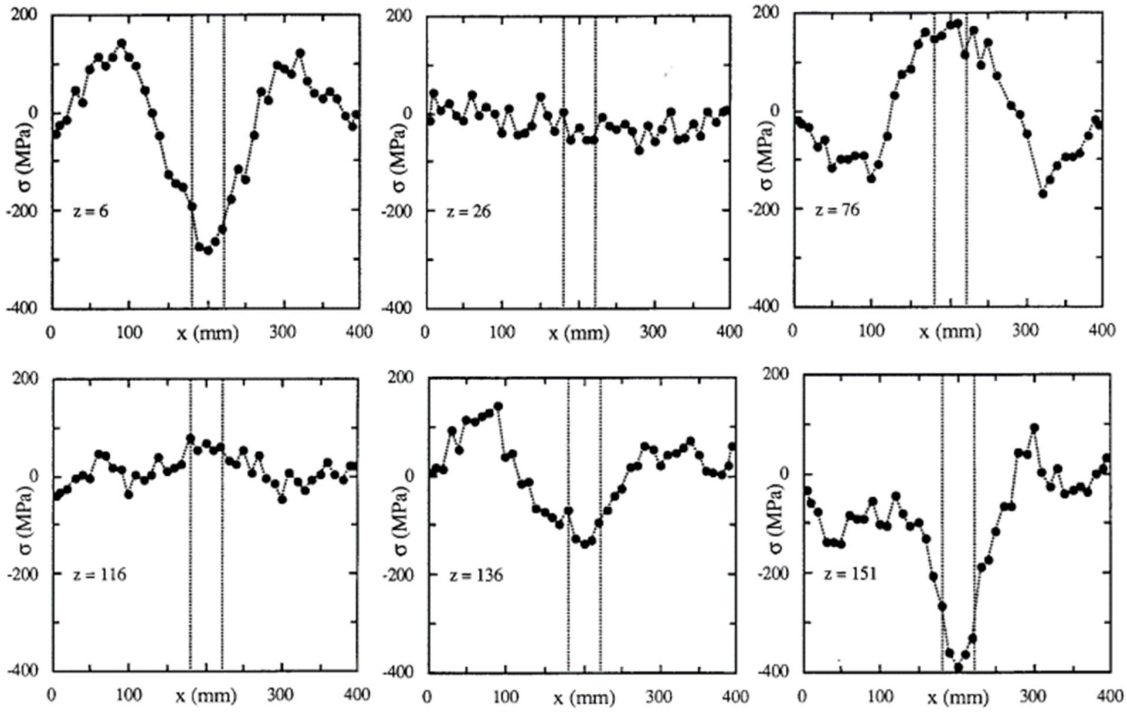

Figure 2-22: Longitudinal residual stress of welded rail (*x*) at different vertical heights (*z*) [69]

FE simulation is highly effective in predicting the residual stress field of the thermite welded joints [70]. The numerical investigation of the heat transfer phenomena from the thermite welding process was carried out by Chen et al. [71]. Using the proposed heat transfer model, the temperature history curve of the thermite welded rail joint can be compared with the measured results in the rail base using thermocouples as in Figure 2-23. An adequate agreement between experiment and simulation at most thermocouple locations has been achieved

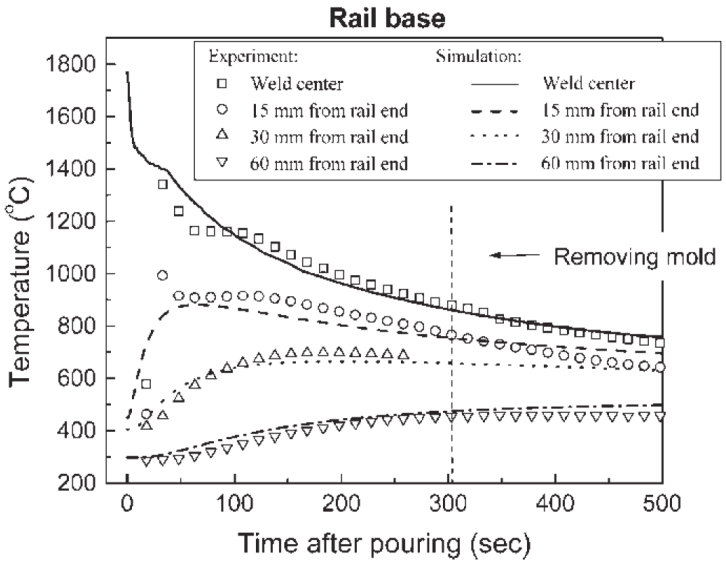

Figure 2-23: Comparison of temperature history at rail base between experiment and simulation

Based on the heat transferring results, Moarrefzadeh [72] has studied the effect of the parameter variation on the temperature field, as well as the optimization of the welding process. To reduce the computational effort, Manzke et al. [73] developed a reduced numerical model for the heat transferring in the commonly applied thermite welding process and a good result was achieved. 3D thermal elastic-plastic FE method is well recognized since it is able to deal with the complicated thermal and structural problems arising from the welding process [74]. Tawfik et.al. [75] investigated the residual stress field of the flash butt welded rail joint using FE method and compared with the experimental measurement. The residual stress distribution is presented in Figure 2-24. The measured principal stresses were plotted in terms of the rail height and the results shows that the peak tensile residual stress was found in the mid-web region within the fusion zone.

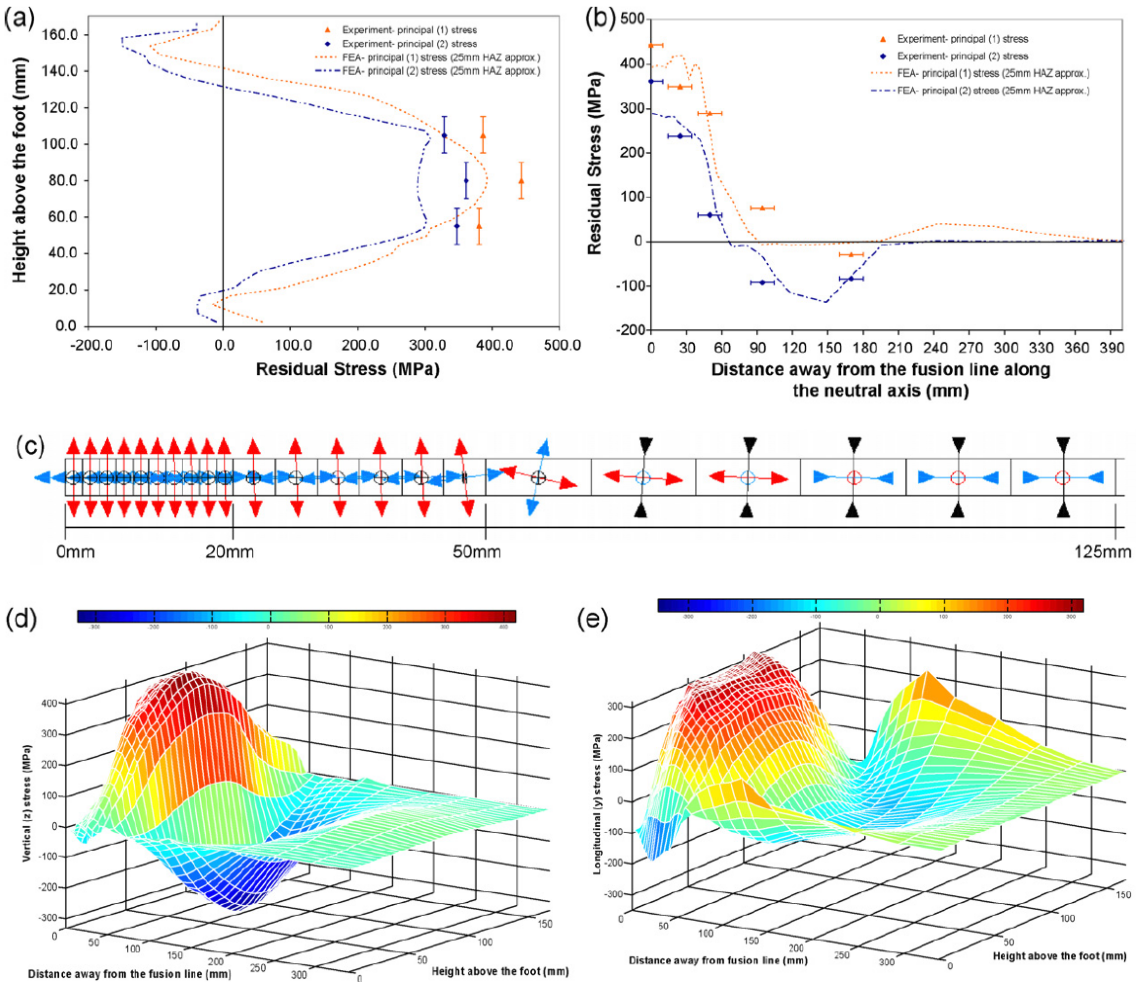

Figure 2-24: Comparison of temperature history at rail base between experiment and simulation

Skyttebol et al. [4] also investigated the residual stress of the cross section of flush butt welded rail and studied the effect of residual stresses on the fatigue crack growth using fracture mechanics. A more recent investigation was done by Tuchkova [76] and he has investigated the correlation between the heat transfer phenomena and the microstructure evolution during the thermite welding process.

However, residual stress will be partially relaxed under cyclic fatigue load [77] and it will reach a stabilized stage after a few fatigue cycles. Several empirical models have been proposed to evaluate the stabilized residual stress under cyclic load [78], but the accuracy become only acceptable recently with the wide application of finite element (FE) method. However, the finite

element method to investigate the residual stress relaxation behaviour under the cyclic fatigue load of the rail welded joint is seldom developed from the existing literature.

Thermite weld discontinuity

The geometric feature of the welded joint is characterized by the shape of the weld collar which is associated with the mould applied during the welding process. Before starting the process, two pieces of sand mould were applied on both sides to form a welding cavity and to seal the rail end gap. After that, the thermite powder in the sand crucible was ignited and the molten metal from the thermite reaction was poured into the mould. The mould was removed after the pouring and the thermite weld was dressed and grinded back to the connected rail profile.

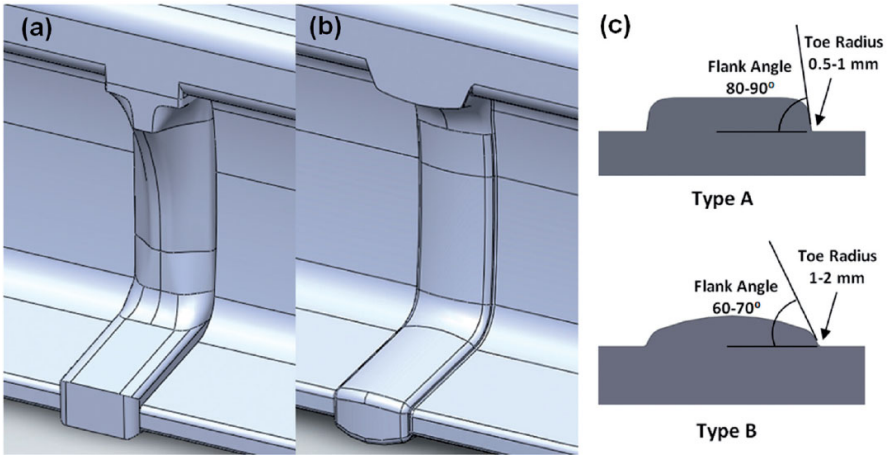

Figure 2-25: (a) Type A weld (b) Type B and (c) collar section from top of the rail foot [27]

Lawrence et al. [27] and Salehi et al. [35] have investigated the effect of the weld collar geometry on the fatigue initiation behaviour of the welded rail joints using the multi-axial fatigue criterion. Two types of weld geometry as shown in Figure 2-25 regarding the weld collar shape and the weld toe geometry were investigated in terms of the fatigue damage probability of the welded rails. The Dang Van multi-axial fatigue criterion [48, 49, 79] in conjunction with the finite element method were applied to investigate the stress distribution and fatigue behaviour of the thermite welded joints with two different types of geometrical features. It is found that the thermite welded joint

with type A geometry is prone to fatigue cracking of transverse failures at the head-to-web and web-to-base locations due to the high flank angle and small weld-toe radius as shown in Figure 2-26c. The type B geometry with a lower flank angle and larger toe radius relieves the stress severity and further reduces the risk of fatigue crack initiation. However, the correlation between the weld geometry and the fatigue crack propagation properties is not reported which needs further investigations.

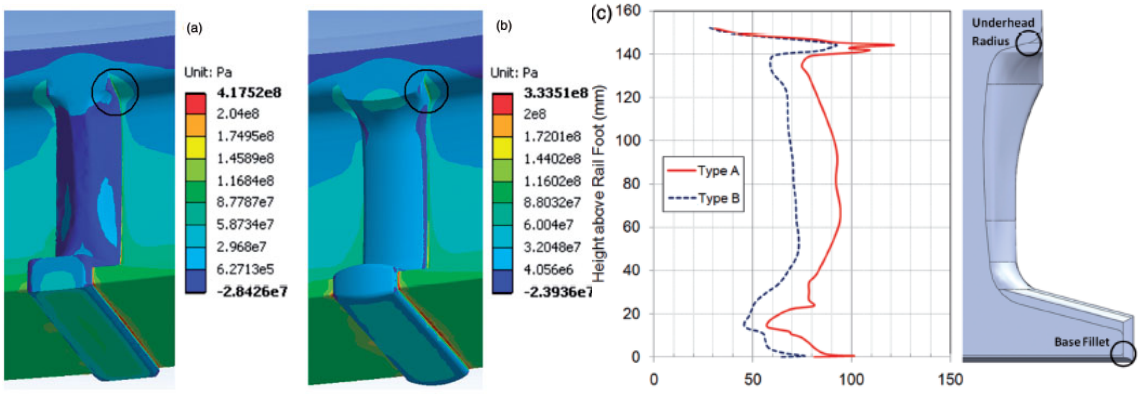

Figure 2-26: (a) Longitudinal stress contour for a Type A weld, and for (b) Type B weld and (c) Dang Van damage parameter at the collar edge [35]

Metallurgical properties variation across the welded joint

Various studies have been carried out to understand the mechanical and microstructural properties of rail steel to meet service requirements and these investigations are centred around the manufacturing process and in-service condition. Godefroid et al. [80] has investigated the microstructure and mechanical behaviour of rail steels from the manufacturing perspective and proved that the presence of Vanadium refined the microstructure. Debehets et al. [81] analysed the influence of microstructural orientation on the variation of the nanohardness in the pearlitic rail steel. Several other investigations focused on the roll contact fatigue cracking investigation and their correlation with the microstructure characterizations. Kumar et al. [82] studied the formation of etching layers during service loading which caused the initiation of microcracks leading to final failures. Kim et al. [83] evaluated the crack growth behaviour of shelling cracks

in the rail head transiting to transverse cracks in the rail steel. Bonniot et al. [5] obtained an intrinsic mixed mode crack growth kinetics for rail steel (R260) and it was validated by microstructural observations. More recent studies were performed to attempt to design and develop new materials with improved performance for application in rail tracks [84, 85].

The thermite reaction during the welding process is described as a long duration of high temperature in the fusion zone which reaches up to 1750~2050 °C followed by a large amount of heat release and subsequent cooling process. It causes localized changes of material characteristics across the welded joints, causing the assembled rails susceptible to fatigue failures [58]. The material characteristics across the thermite weldment joining rail steels and its effect on the fatigue cracking are generally recognized. The HAZ adjacent to thermite weld represents a change in many material characteristics, including hardness, microstructure, and strength, which is easy for fatigue cracks to initiate and propagate [16]. Sarikavak et al. [86] investigated the influence of welding on the microstructure properties and mechanical strength of flash butt welded steels. It is concluded that the differences in microstructure affect the strength and further fracture properties.

Hernandez et al. [87] have investigated the metallurgical changes taking place during the thermite welding process. A full mapping of the microstructure across the thermite welded rail joint with the comparison with the Vickers hardness distribution is presented in Figure 2-27. It shows that a fully pearlitic structure is observed for the thermite welded metal while the proeutectoid cementite on the grain boundary is found in the heat affected zone. Before a rapid transition from the heat affected zone to the unaffected parent rail material, the spheroidization of the cementite is found and therefore the ductility of this zone is increased.

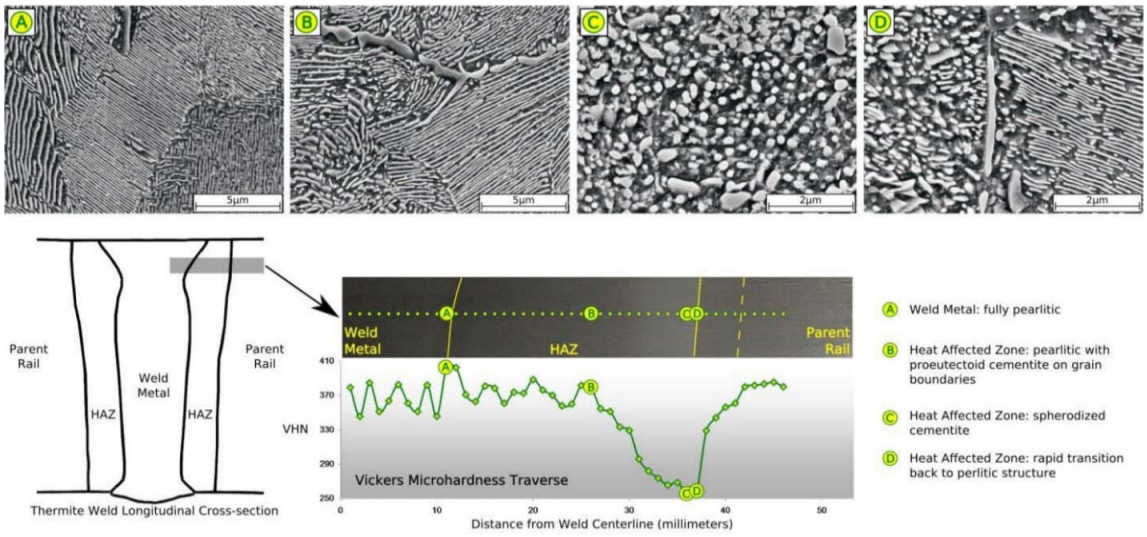

Figure 2-27: Microstructure across the thermite welded rail joint [87]

Meriç et al. [88] examined the mechanical properties of a thermite welded steel with a material type of S49 SAE/AISI 1050 and conducted microstructural studies to reveal the pro-eutectoid ferrite and pearlite. Magel et al. [52] concluded that the change of microstructure in the HAZ is the reason for the initiation of micro-crack in the railhead and the cracks propagation to macro fatigue crack that leads to final failure. Younise et al. [89] have found that the resistance to crack initiation and growth is greatly affected by the mechanical characteristics of the weldment, and the importance of the HAZ for fracture behaviour of welded joints was also emphasized. Jiang et al. [6] investigated the impact wear behaviour of rail weld joint under the dry condition and showed that the wear volume of the weld is less than of rail material. A lot of prediction models to predict the effect of weld-induced material inhomogeneity on the rail/weld contact were developed based on these researches. Sichani and Yann [90] introduced a model to predict the wear performance between rail and wheel due to the presence of geometrical difference from thermite weld. Fry et al. [44] built a model for fatigue defects nucleation from metallurgical discontinuities in thermite weld and showed that the shape and orientation of pores had a strong influence on fatigue defect formation.

2.4 Fracture mechanics crack growth methodology

The physical process of the fatigue cracking in the welded joint can be divided into three stages: the crack initiation, propagation and final fracture [91]. In the thermite welded rail joints, stress concentrations occur at the specific locations of the weld toe from which fatigue cracks may initiate [92]. After the cracks have been initiated, the fatigue crack growth or propagation controlled by the material resistance and environmental cyclic load conditions is followed until it reaches a final fracture. With the consideration of the geometrical features and material properties across the welded joint, the presence of weld defects in the heat affected zone can trigger the fatigue crack initiation and further affect the fatigue propagation. In addition to these impacts, the structural details and cyclic loading conditions have a significant influence on the fatigue performance regarding the crack propagation stage.

Three types of approaches are widely used for the fatigue analysis of structural components: stress –life ($S-N$) approach, strain-life approach ($\varepsilon-N$) and fracture mechanics crack growth approach (da/dN - ΔK). The stress-life approach is used to assess the fatigue strength of the welded structure in terms of life cycles at a certain elastic load level which is above the fatigue limit. The structural features including the weld type, geometry details and resulted local stress concentration effects are considered. When the stresses or strains exceed the elastic region of the material, the strain-life approach is applied for fatigue assessment. The strain-life approach takes account of both elastic and plastic deformation of the material under cyclic fatigue load. However, the presence of defects or flaws is not considered when using these two approaches. Material defects are quite common resulting from many manufacturing processes, particularly the welding process. Fatigue failures of welded joints generally start from surface weld defects at specific locations of the weld toe region and propagate inwards to the material in a direction perpendicular to the axis of main tensile loading.

2.4.1 Fracture-mechanics approach

The fracture mechanics approach has been frequently used to evaluate the severity of the crack geometry, operating conditions and material properties to predict fatigue life. The fracture mechanics approach allows the fatigue life assessment of the welded structure with the known presence of a crack [63, 93-95] and provides a more accurate fatigue damage tolerant design [5, 59, 83, 96].

The analysis of the fatigue life of the welded structure using fracture mechanics technique requires an accurate calculation of the stress intensity factor (SIF). The application of the SIF solution to investigate the fatigue crack propagation life is referred as "linear elastic fracture mechanics (LEFM)". The LEFM, which accounts for the remote stress magnitude and geometry details of the welded joints, calculates the stress state at a crack front in terms of SIFs during the propagation process. The SIF is derived as a function of the nominal stress the material is subjected to, its geometrical properties, and finally the size of its flaws.

$$K = \mathrm{Y}\sigma\sqrt{\pi \mathrm{a}} \tag{2-2}$$

while σ is the applied remote stress, a is the crack size and Y is the dimensionless factor depending on the structure geometry features and loading conditions. Follow the solution of SIF, the fatigue cracks usually propagate in the direction perpendicular to the main principle stress. This type of crack opening is defined as "mode I" and it is considered as the most relevant mode for the fatigue cracks. Other modes of crack opening are also presented in Figure 2-28.

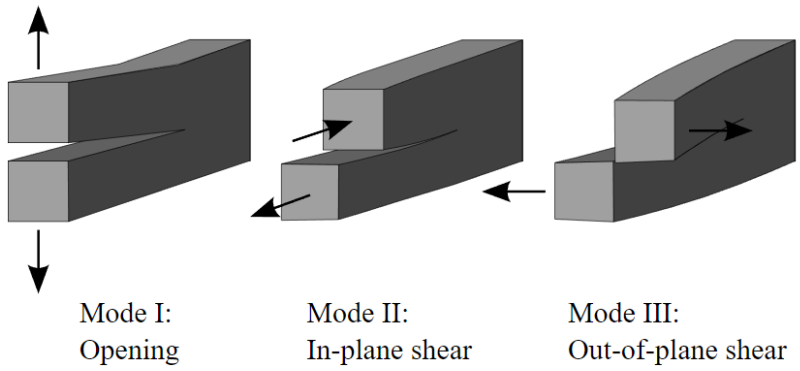

Figure 2-28: Modes of fracture [97]

For mode I crack, the stress intensity factor K_I of surface crack in finite plate under remote tension or bending could be expressed following Newman and Raju's empirical equation as below [98].

$$K_I = (S_F + HS_M)\sqrt{\pi\frac{a}{Q}}F\left(\frac{a}{t},\frac{a}{c},\frac{c}{b},\theta\right) \quad (2\text{-}3)$$

Where S_F and S_M are the resulted stress from the tension and bending load respectively. H is the correction factor of the bending load, Q is the shape factor, F is the boundary correction factor and it is a function of crack depth, crack length, plate thickness and width, and crack angle. t is the thickness of the plate. The illustration of all symbols used was shown as in Figure 2-29.

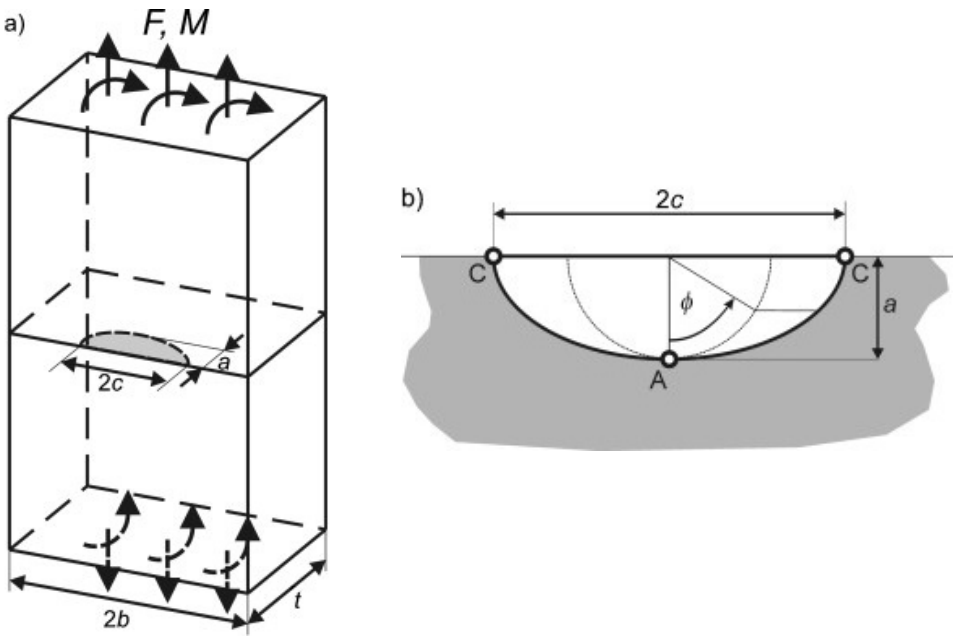

Figure 2-29: (a) Semi-elliptical surface crack in a finite width plate subject to tension or bending and (b) detailed schematic illustration of crack dimensions [98]

In the application of fatigue growth life prediction using fracture mechanics, the determination of the SIF, which accounts for the magnitude of cyclic stress, pre-existing crack size and weld joint details geometries are needed. As shown from Figure 2-30, the crack propagation rate is related to the variation of the corresponding SIF in the logarithmic scale. Three distinguished phases can be observed. The first phase refers to the non-propagating cracks, i.e. the crack won't propagate below the threshold region. For a given pre-existing crack, is used to determine whether the crack will propagate under the applied ΔK. The cracks are found to be initiated at the weld toe region with maximum stress concentration effect. The fatigue initial stage is assumed to be negligible and therefore the estimation of initial crack size, a_i, by using the microstructure characterization is also of great significance for the accuracy of fatigue life prediction. The second phase is considered as a stage when the initiated cracks are propagated in a linear pattern, which can be described using Paris's Law [7]:

$$da/dN = C\Delta K^m \tag{2-4}$$

where C & m are constants which are unique to every type of material, da/dN refers to the crack growth per unit cycle and ΔK refers to the stress intensity factor range. The fatigue failures will occur once the SIF at a crack front reaches the critical value of SIF, the fracture toughness. The linear-elastic fracture toughness is a material property that acts as a gauge for the maximum stress intensity factor a crack in the material can be exposed to.

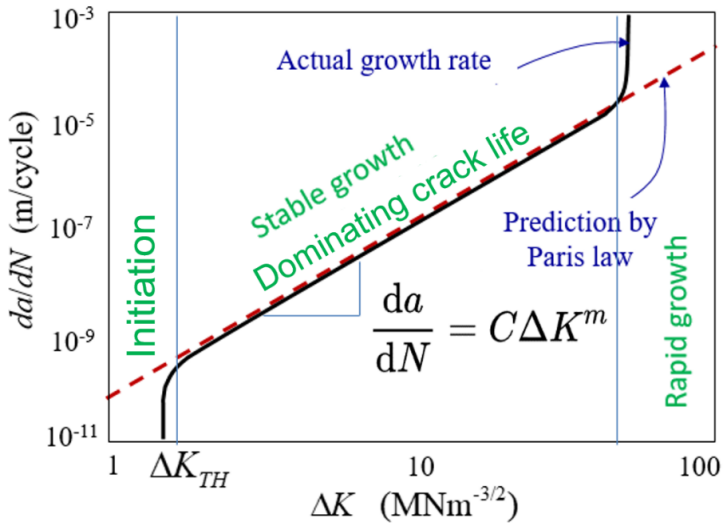

Figure 2-30: Schematic illustration of typical fatigue crack growth behaviour in metals [99]

2.4.2 Residual stress effects

For the welded joint subject to complicated loading conditions, the superposition law can be used to calculate the stress resulting from both applied load simultaneously [100]. Computas et al. [101] have proven that the SIF for different types of loading could be simply superposed along the entire crack front regardless of whether the loadings tend to open or close the cracks. This means that the SIF resulting from the combination of the tension stress and bending stress is given by the sum of SIF under each separate loading as below:

$$K_{Total} = K_{Tension} + K_{Bending} \tag{2-5}$$

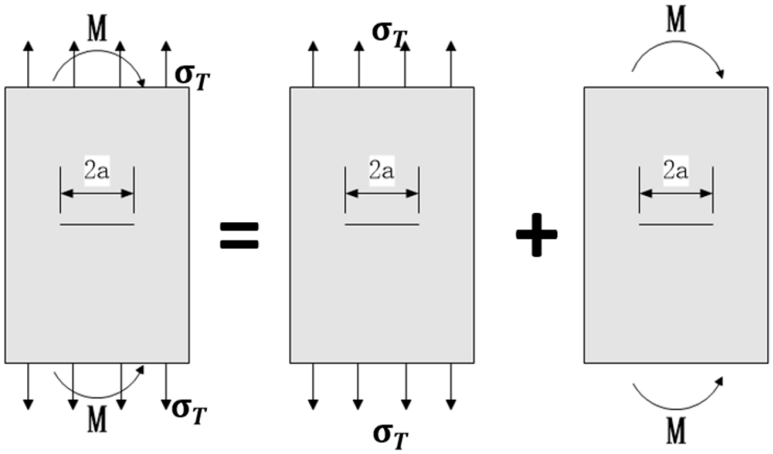

Figure 2-31: Schematic illustration of superposition law

The principle of superposition can also be applied to the calculation of total stress intensity factor (K_{tot}) subject to both the external fatigue cyclic load and residual stress based on the linear elastic fracture mechanics (LEFM) [102-104] The expression of total stress intensity factor range (ΔK_{eff}) and effective SIF ratio (R_{eff}) subject to both the external fatigue cyclic load and residual stress induced by the welding process can be calculated using the elastic superposition law as:

$$\Delta K_{eff} = (K_{app.max} + K_{res}) - (K_{app.min} + K_{res}) = \Delta K_{app} \tag{2-6}$$

$$R_{eff} = (K_{app.min} + K_{res})/(K_{app.max} + K_{res}) \tag{2-7}$$

where K_{app} and $K_{res}$are the stress intensity factor (SIF) associated with the external cyclic loading and welding residual stress, respectively. Therefore, it is found that the residual stress intensity factor term (K_{res}) is cancelled and the residual stress effect is not accounted. in Eqn. 2-6. However, in the linear elastic fracture mechanics framework, residual stress effect is accounted for by the "effective R ratio" term, R_{eff}, as shown in the Eqn. 2-7. Noted that R_{eff} represent the resulted crack tip stress ratio instead of the nominal applied stress ration R.

The effect of the stress ratio, R, is accounted in the Paris' Law using Walker [105] equation as:

$$\frac{da}{dN} = C\left[\Delta K_{app}(1-R)^{\gamma-1}\right]^m \tag{2-8}$$

where γ is a constant of material properties obtained from the testing result characterizing the effect of the stress ratio on the fatigue growth behaviour. Kim et al. [83] conducted the testing of mode-I fatigue crack propagation rate for rail steel at the stress ratio of 0.1, 0.3 and 0.5 and an empirical value of $\gamma = 0.82$ was derived. Normally the closing value of $\gamma = 1.0$ implies a weaker effect of stress ratio. This value can be used for fatigue life estimation when considering the effect of residual stress. By substituting the stress ratio R in Eqn. 2-8 with the "effective R ratio" R_{eff} from Eqn. 2-7, the Walker equation can be rewritten to

$$\frac{da}{dN} = C\left[\Delta K_{app}\left(\frac{\Delta K_{app}}{K_{app.max} + K_{res}}\right)^{\gamma-1}\right]^m \tag{2-9}$$

When applying this equation, the term of K_{res} is usually obtained by using weight function method [106, 107] as:

$$K_{res} = \int\int \sigma_{res}(x,y) \cdot m(x,y,\phi) dS \tag{2-10}$$

where σ_{res} is the residual stress distribution along the crack surface in the body without flaw and m is the point-load weight function at any point along the crack front and it is expressed as:

$$m(x,y,\phi) = \frac{\sqrt{2s}}{\pi^{1.5}\rho^2}\left[1 + M_K \cdot (1 - \frac{r(\phi)}{R(\phi)})\right] \tag{2-11}$$

where ρ is the distance between point load $P'$and an arbitrary point load P along the crack front as shown in Figure 2-32. s is the shortest distance between the point load and the crack front boundary. $r(\phi)$ and $R(\phi)$ are the distance as illustrated.

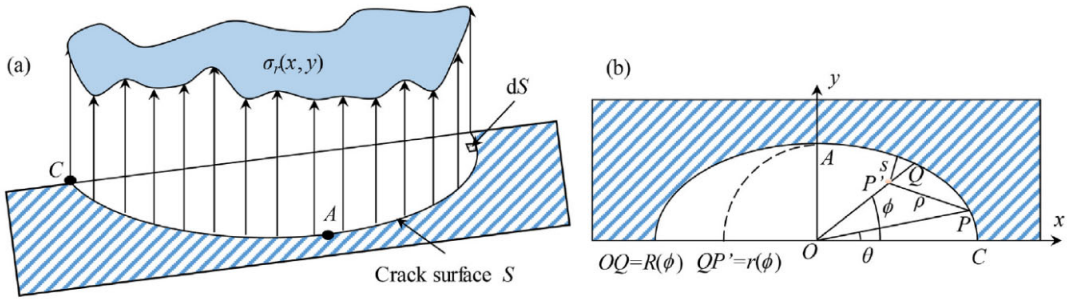

Figure 2-32: Schematic illustration of weight function [96]

The weight function method which is applied to consider the effect of residual stress on the fatigue behaviour only provides the qualitative assessment results without considering the crack closure phenomenon [108]. Crack closure, especially under the compressive residual stress field, also influences the fatigue life prediction of the welded structure. It occurs when the cracks remain closed or partially closed even when a tensile cyclic load is applied. The crack closure is depending on the sign of the K_r when calculating the ΔK_{eff} using the superposition law. Considering the tensile mode-I fracture condition, the crack will only propagate only when the $K_{eff} > 0$ and the

current weight function method simplified the effect of the compressive residual stresses by assuming the value as 0 for fatigue propagation prediction [109].

2.5 Concluding remarks

The performance of rail tracks depends greatly upon the integrity of structural fusion bonding between the parent rail steel and thermite weldment. The thermite welded rail joint, compared with the parent rail, is particularly susceptible to welding defects and fatigue damage formation. Studies have been conducted for the structural integrity of the thermite welded rail joint, but some limitations exist.

Firstly, the susceptibility of the thermite welded joint to fatigue damage formation of transverse weld toe surface cracks is not well researched, particularly with regards to the analysis of the transverse fatigue cracking behaviour at the web-to-head and web-to-base regions. Thermite welded rail joints are considered the track discontinuities of the running surface regarding their geometry irregularity and mechanical properties and therefore more attention was drawn on the fatigue damage formation of the rail head among the wheel/rail interface in the past studies [110]. The presence of the welded joints is treated as a geometrical irregularity leading to the variation of dynamic load and contact stress, acting as stress concentration site for rolling contact fatigue initiation.

However, the failure mode of transverse weld-toe surface fatigue cracks at the web-to-head and web-to-base regions is found to be a frequent concern [9, 32, 111] but the related integrity research is not well reported. This fatigue crack initiates from typical stress concentration sites of the weld toe region such as head-to-web and web-to-base locations and propagate inwards along the transverse plane of the joint, which makes it difficult to be detected by ultrasonic testing before a final fracture occurs. There is a high possibility that these transverse weld toe cracks will further result in a full rail transverse breakage involving derailment risks threatening the safety and

reliability of the rail track system. Special attention is required to investigate the fatigue cracking mechanism of such failures in order to maintain the structural integrity of the rail track system.

Secondly, the investigation of the transverse weld-toe fatigue failures remains a highly complex field and there is a need to develop a structural integrity assessment methodology that allows quantitative assessment of fatigue life of the welded joint with an appropriate level of confidence to provide the necessary level of reliability. A range of techniques and procedures is required to enable a framework for structural integrity assessment of thermite welded rail joints to be undertaken. The understanding of fatigue cracking mechanism is subject to investigations of the structural features such as the unusual cyclic loadings, the material characterization including the mechanical and fatigue properties across the weldment, and the presence of flaws or with respect to the potential failure modes by fracture or fatigue.

Regardless of the fatigue mechanism discussed above, the fatigue cracking behaviour of rail thermite welded joint in a residual stress field resulting from the welding process is undesirable. In addition, the residual stress will be partially relaxed under the external cyclic service load. The effect of the residual stress and stress relaxation on the fatigue crack growth in the welded rail joint is necessary to be analysed and understood in order to achieve a more accurate and reliable fatigue life prediction model for structural integrity assessment. The neglect of this issue will result in an over-conservative integrity prediction which leads to higher cost and safety margin of designed structures.

Arising from the literature review, it is noted that thermite welded joints are the weak link of continuous track and the failures occurring near the weld will cause transport downtime, costs of the replacement and even potential risk of derailment if are not treated properly. Compared with rail failures, defects occurring near weld are more difficult to be detected from inspection and thus have a high possibility to result in rail break or risk of derailment if not replaced immediately.

The fracture and fatigue characterization of transverse failures for rail and weld is an important area that needs further research. The fatigue damage tolerance of rail and welded joints is dependent on the loading environment, material properties, and manufacturing (welding) process. Calculation of crack growth rate of transverse weld cracks remains a highly complex field since currently there is no simple way to view a surface crack growing inwards and know how fast the crack grows. The fatigue failure pattern is not well characterized, and the failure cracking mechanism is not clearly understood. The research efforts corresponding to these areas are required to characterize the fracture and fatigue performance of thermite welded rail joints.

Chapter 3 Material Characterization

The assessment of structural integrity involves the study of material properties to understand the behaviour of the thermite welded rail joint under fatigue load conditions and furthermore the fatigue cracking mechanism. This material characterization in this chapter includes the chemical composition analysis, and microstructure and hardness measurement and their variation across the welded joints. Weld defects (pores and inclusions) investigation and the inherent correlation to the fatigue cracking resistance once treated as initial cracks are also performed.

3.1 Problem specification

The application of thermite welding is necessary during routine maintenance in replacing and joining rail steel tracks due to the advantages of its process [112]. It takes place in the sand molds between two rail ends and the joints were created by a chemical reaction between aluminum and iron oxide. The reaction is described as a long duration of high temperature in the fusion zone which reaches up to 1750~2050 °C followed by a large amount of heat release and subsequent cooling process. The welding process causes localized changes of material characteristics across the welded joints, causing the assembled rails susceptible to fatigue failures [58]. It is found that around 60~80% of rail weld failures occur at the heat affected zone (HAZ) [28, 29], especially at the fusion line [30, 31]. Based on the literature review of Chapter 2, the comprehensive material characterizations of thermite welded rail joints have not been clearly revealed. In this research, the microstructure and mechanical characteristics of the thermite welded joint are investigated and presented. The investigation will help to improve the understanding of material imperfections and their effects on the fatigue performance of the thermite welded joints.

3.2 Experiments set-ups

European R260 rails were welded together using standardized PLK thermite welding process. The thermite welding was performed in the workshop using two rails with length of 600 mm each. Rail

ends were cleaned and set up with a gap of 25mm ±1mm. The preheating was conducted for 6 mins using oxy-acetylene torch with the working pressure of 180 KPa/min for oxygen and 40 KPa/min for acetylene. When the preheating was completed, the thermite powder in the crucible was ignited and the molten metal from thermite reaction was poured into the mold. Both the mold and the crucible are made by sand. The mold was removed after 4 mins of pouring and the thermite weld was dressed using a weld chisel cutting set. The welded portion was then grinded precisely to the head profile of rail steel and cooled down to room temperature in air. Chemical composition of parent rail metal (R260) and thermite weld metal are given in Table 6. The tested specimens were extracted from three thermite welded specimen with welding process conducted by certified welding worder in the workshop in accordance with European standard BS EN 14730-1-2017 [19]. The base metal to be welded is with material of R260 rail steel from steel supplier of TATA Steel. The following investigations were then conducted in laboratory.

Table 6: Chemical composition of parent rail R260 and thermite weld material

Material	**Chemical Component (%)**				
	C	Si	Mn	P	S
Thermite Weld	0.76	0.87	0.93	0.032	0.013
Rail metal (R260)	0.74	0.30	1.0	0.021	0.014
	Cr	Mo	Ni	Al	Cu
Thermite Weld	0.356	0.005	0.057	0.053	0.062
Rail metal (R260)	1.11	0.01	0.03	0.01 (V)	-

The specimens for microstructure characterization and weld defects studies were machined from the longitudinal plane of the thermite welded joint with the depth of 3~5 mm from the rail head. The machined specimens were subsequently mounted and prepared for the grinding and polishing to 0.1 μm Ra surface roughness finish. The distribution and morphology of defects were examined using OLYMPUS LEXT OLS4100 3D laser microscope. The specimen was etched using 2% Nital solution and investigated using Scanning Electron Microscope with Energy Dispersive Spectroscopy (SEM/EDS). The weld defects and the ratio of area with defects to observed region

was measured and statistically analyzed using Image J. The 3D laser microscope was also used for fracture morphology characterization. The fractographical investigation of the fractured specimen from the service fatigue failures was also performed. All testing results are presented and compared with reported results if similar testing has been conducted from literature review [13-24, 26, 27].

3.3 Material characterization results

3.3.1 Characterization of HAZ positions

The cooling rate of the material during solidification process varies across the thermite welded joint and leads to locally different microstructures. In the case of thermite welding process, the typical thermal cycle of weld center is illustrated as Figure 3-1a and the welded rails experiences four steps during the thermal cycle: preheating, tapping, solidification and cooling process. The reported experimentally measurement [71] of peak temperature for a standardized thermite welding process (with welding gap as 25±1 mm and preheating time as 7 mins) is presented in Figure 3-1b. Consequently, a range of different microstructures in HAZ is resulted due to the different heat treatment experienced shown in Figure 3-1c.

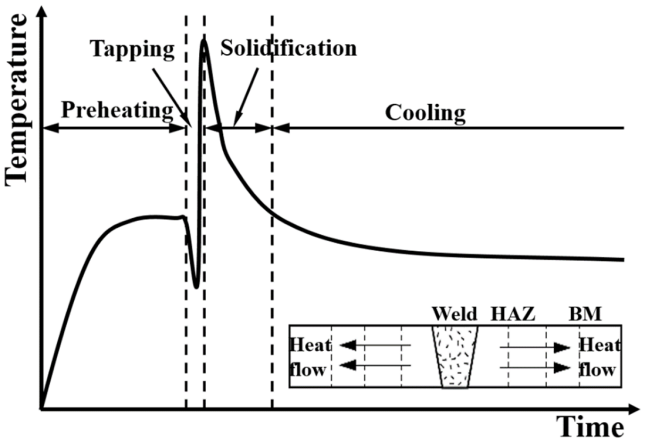

(a) Thermal condition

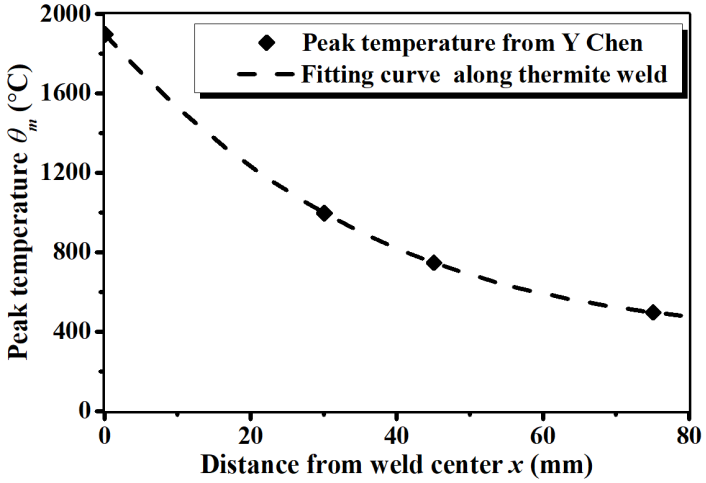

(b) peak temperature distribution

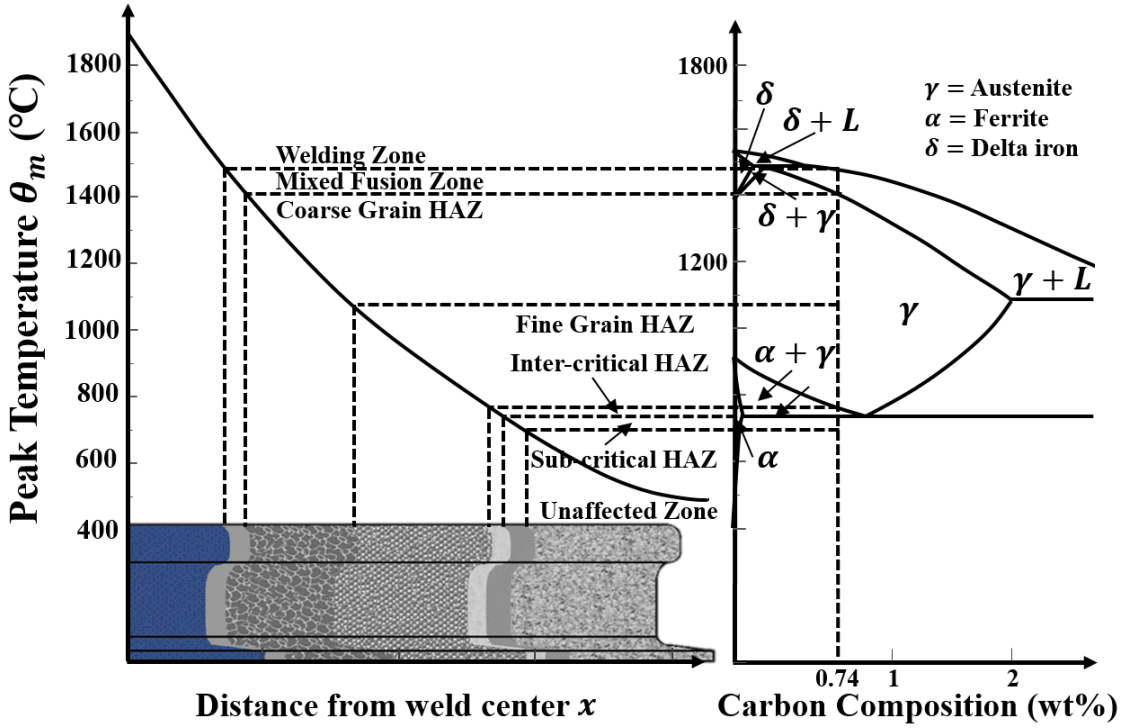

(c) schematic interpretation of heat affected zone

Figure 3-1: Diagrammatic of thermite welding process

An etched macrograph of the longitudinal section of the thermite weld specimen is shown as Figure 3-2a. The dimensions of the weld zone and HAZ were measured and listed in accordance with standard BS EN 14730-1-2017 [19]. The measurements show that the weld zone and HAZ have symmetrical features. The dark region toward the center illustrated by solid line is

representative of the weld fusion zone while the two dull colored columns at both sides (marked by dotted line) is representative of the HAZ. The width of weld region was measured to be approximately 32 mm in head-to-web transition region) and 96~100mm in rail head and bottom. The appearance and amount of microstructure in the different regions of HAZ is characterized by the chemical composition of the rail parent metal and weld metal, and the peak temperature experience during cooling process. The peak temperatures of each zone was calculated from chemical composition based on Vinokur's model [113]. The liquidus temperature was calculated as 1462 °C following formula below:

$$T_{Liq} = 1537 - 88 \cdot \mathrm{C} - 8 \cdot \mathrm{Si} - 5 \cdot \mathrm{Mn} - 30 \cdot \mathrm{P} - 25 \cdot \mathrm{S} - 1.5 \cdot \mathrm{Cr} - 4 \cdot \mathrm{Ni} \quad (3\text{-}1)$$

The solidus temperature was calculated as 1370 °C following similar formula based on Vinokur's model [113]. The upper and lower temperature thresholds at which austenite forms were calculated using the simplified model proposed by Trzaska [114] as 720 °C and 742 °C respectively. The relatively high A_{c1} is mainly due to the high composition of Chromium. The substrate temperature TS and subcritical annealing temperature SA are typically 1100 °C and 680 °C respectively.

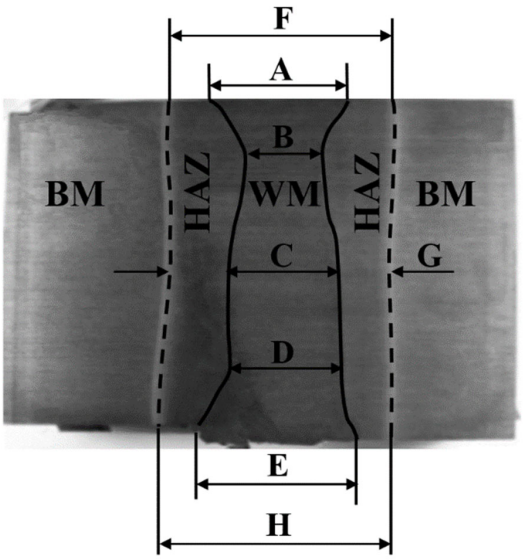

Dimension	Width (mm)
A	59.7
B	32.1
C	49.3
D	49.0
E	70.0
F	96.8
G	95.4
H	100.3

(a) Typical etched micrograph of a longitudinal surface of a thermite rail weld: weld metal (WM), heat affected zone (HAZ), parent metal (BM)

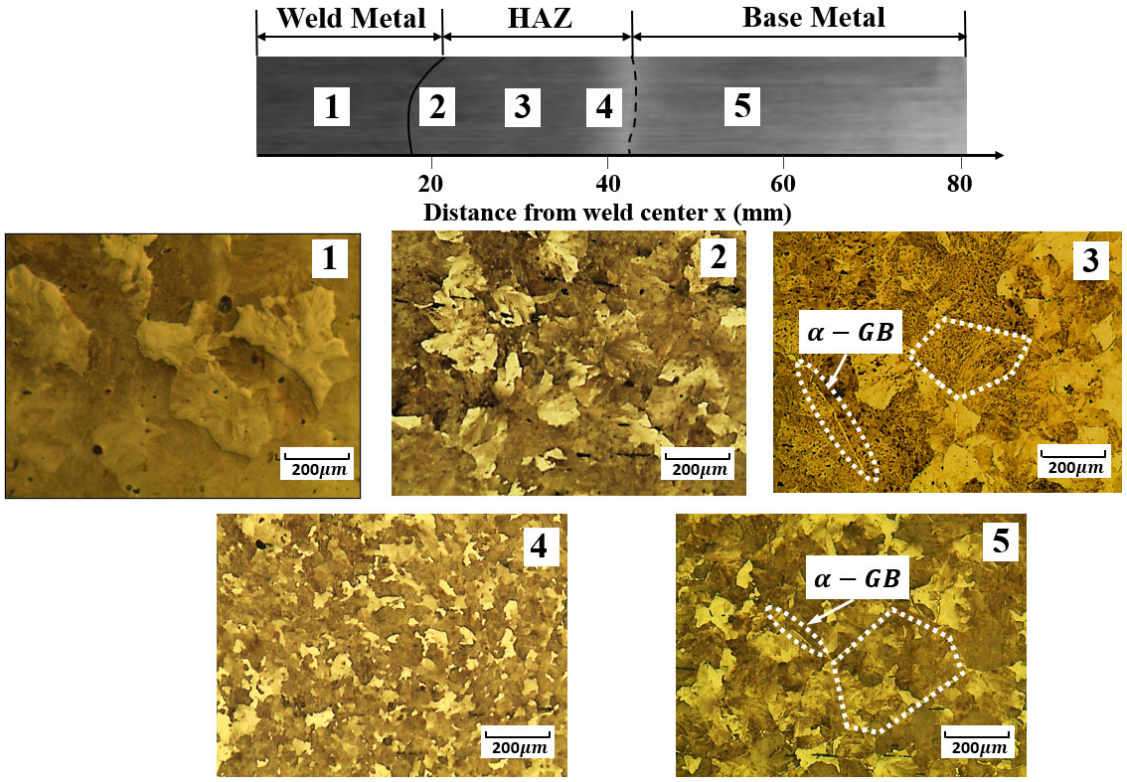

(b) Microstructure regions of thermite welded rail steels

Figure 3-2: Thermite weld features and HAZ regions

Six different microstructure regions were identified exclusively including the fusion zone and present in Figure 3-1c. The zonal situations of the heat affected zone and the width of each zone were estimated and compared with optical observation as show in Figure 3-2b. The weld fusion zone where the phase has transformed into austenite completed was estimated to be with a width of 38-42 mm. The austenitic grain enlargement occurs in this zone and large grain size was found. The fusion line next to weld is evidenced by the higher density of weld defects and mixture of different grain sizes. The heat affected zone (HAZ) was observed to have a width of approximately 24 mm in total and four subzones were presented. A microstructure with coarse grain size was found next to fusion line. Due to the recrystallization, grains grow dramatically and coarse structure forms due to the overheating for a long time. The inter-critical HAZ, followed by a

narrow sub-critical HAZ, was formed next to the fine grain area. Generally, the variations of microstructure at different HAZ zones, coupled with thermite weld material and unaffected parent rail metal, produce critical mismatch effects and it will further affect the mechanical and fatigue properties of the weldment.

3.3.2 Modification of microstructure and material properties

The complex thermomechanical phenomena that occur during the thermite welding process causes local differences of the material properties. Some undesirable or even detrimental effects are hard to be avoided in the specific affected regions. These modifications are discussed in this section.

Microhardness and nanoindentation

The microhardness value was obtained and converted to HBN in accordance with BS EN 14730-1-2017 [19]. The distribution results were plotted across the thermite weld joint as shown as Figure 3-3a. The hardness of thermite weld metal and fusion line is noticeably higher than parent rail due to the material overmatch. Two obvious variations of hardness were observed in the heat affect zone. The increase of hardness was found at the fine grain HAZ, which is associated with the finer grain size resulting from the recrystallization under steeper thermal gradient. The HAZ softening is also observed and it takes place in the outer side of HAZ, the intercritical HAZ. The results of nanoindentation were presented in Figure 3-3b and further characterizations by SEM and LSM were shown in Figure 3-3c. The values of Young's modulus and nanohardness become stable when the displacement increase to 100 – 200 nm, and the values are independent of the indentation depth into the surface. A Poisson's ratio of 0.3 was used for all the phases in this study. The result of indentation modulus shows a slight decreasing trend which is because of the microstructure morphology and further analysis was conducted in the next section.

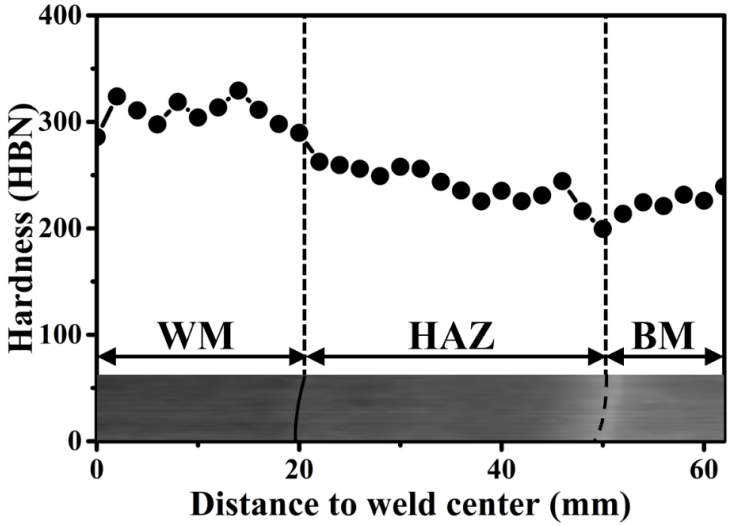

(a) Microhardness distribution

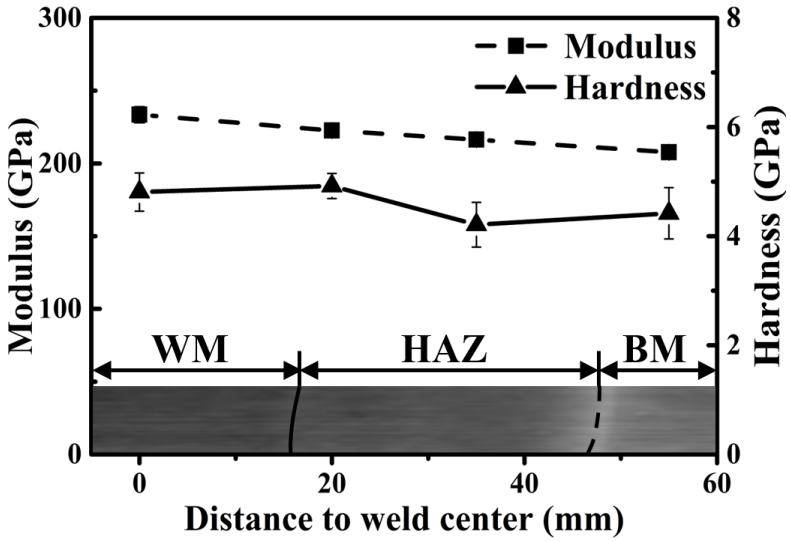

(b) Nanoindentation results

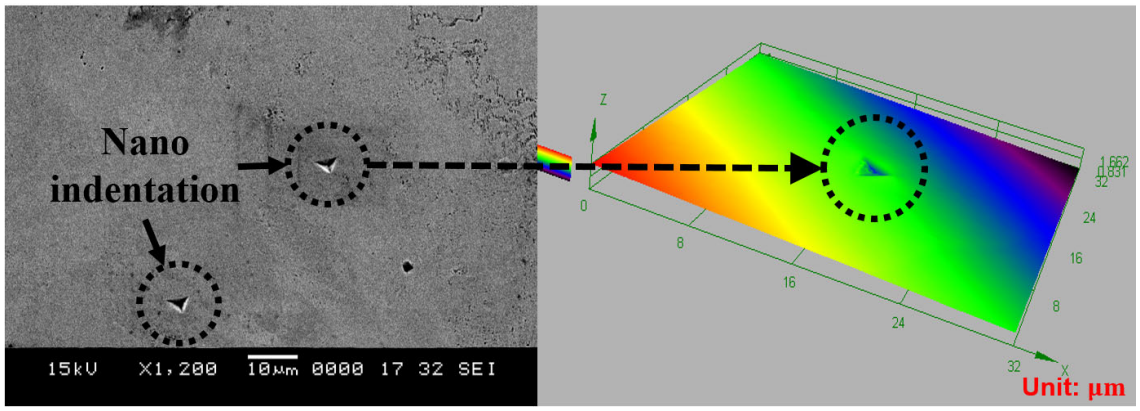

(c) nanoindentation marks

Figure 3-3: Results of microhardness and nanoindentation testing: weld metal (WM), heat affected zone (HAZ), parent metal (BM)

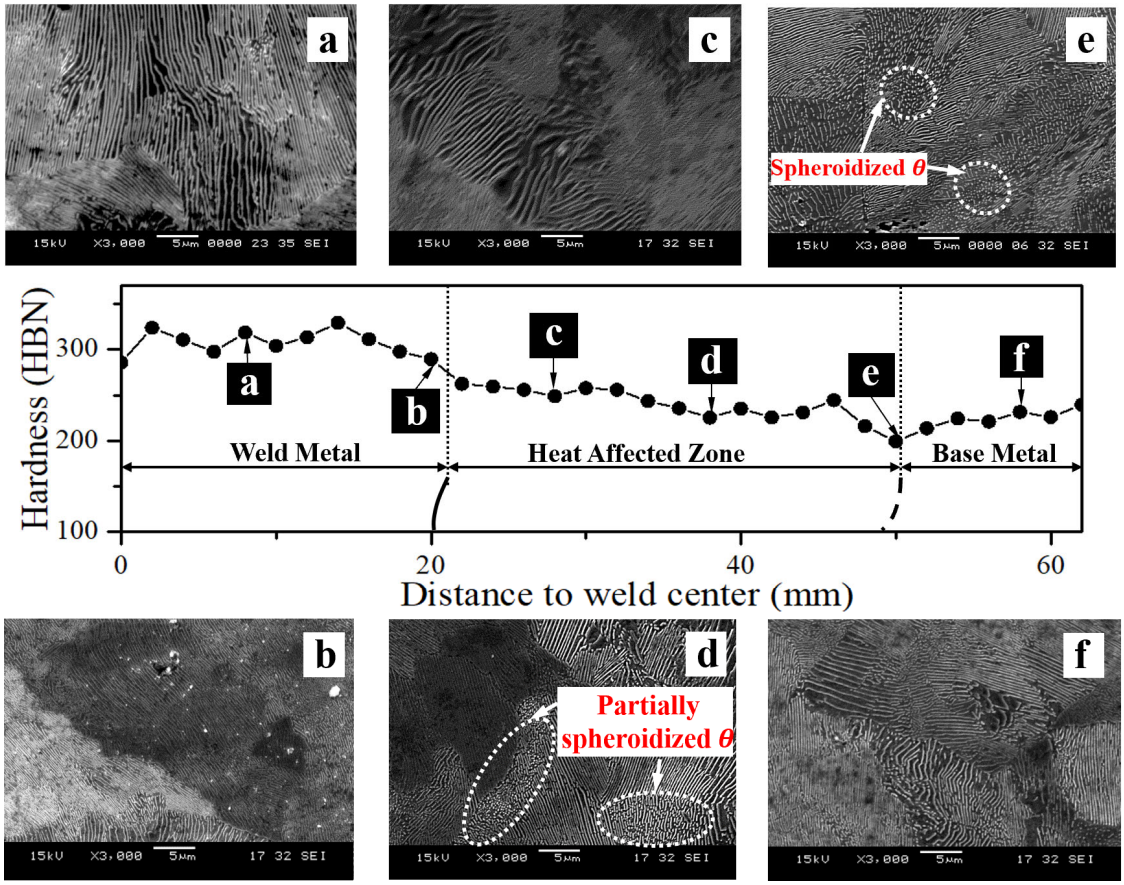

Figure 3-4: Microstructure vs. microhardness

The microstructural characterization using SEM was further studied and shown as in Figure 3-4. The microstructure of weld metal and rail steels were observed to be a pearlitic structure consisting multiple nodules. Each nodule is made up of multiple colonies with the same orientation of lamellar structure and the orientation varies with respect to the neighboring colonies. The two phases of cementite (black) and ferrite (white) form from eutectoid reaction when the austenite slowly cools down to the eutectoid temperature. Cementite generally has higher hardness and mechanical strength characteristics than ferrite. The mechanical properties of rail steel are significantly dependent on the composition and the arrangement of these two phases. The mechanism of hardening and softening can be explained from the microstructural characteristics

of these phases. The spheroidizing of the cementite lamellae was found to occur in the intercritical and sub-critical HAZ and it softens the material in this zone compared to unaffected parent rail metal. Figure 3-4d and 4e show that the cementite (θ) lamellae of perlite partially was converted into spherical cementite structures, resulting in hardness degradation and increase of ductility of the rail steel.

3.3.3 Weld defects

The investigation of weld defects is also necessary to understand the material characteristics of the various regions across the thermite welded joint. With the aid of LSM and SEM/EDS analysis techniques, the morphology, composition, and size distribution of these defects were measured. Image J was used for post-analysis.

Table 7: Percentage of defects in thermite weld and rail steel

Specimen	Weld center	Fusion line	Rail steel
Percentage of defects area (%)	1.22	0.54	0.35

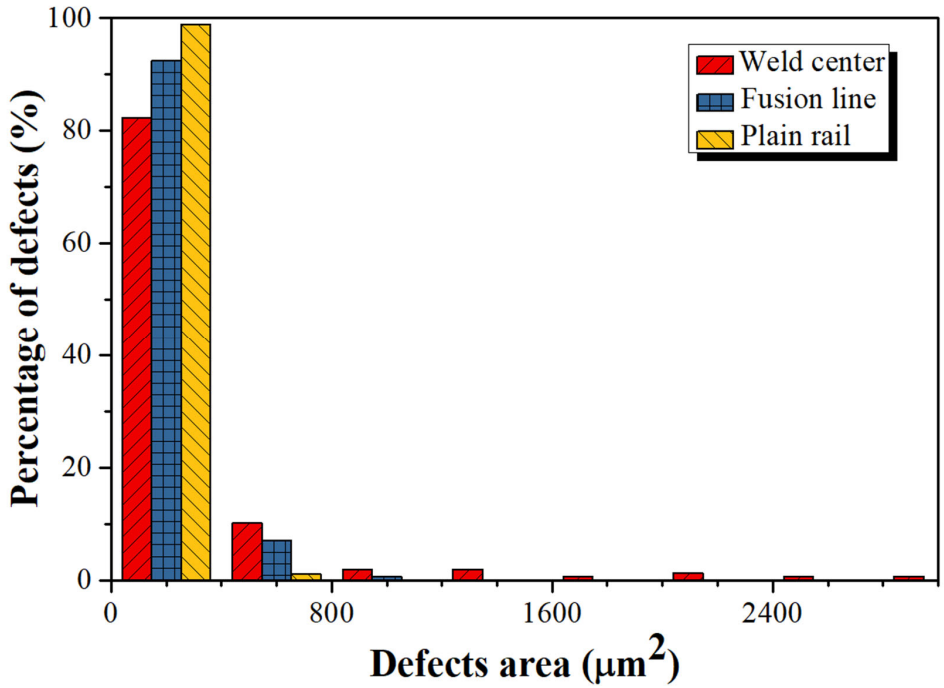

Figure 3-5: Distribution of defects and size

The defects detection was performed in weld center, fusion zone and parent rail steel respectively. For each specimen, at least 20 different locations were selected and averaged. The count and density distribution of general weld defects were consolidated as shown in Figure 3- 5 & 6 and Table11. From Figure 3-5, it was concluded that the percentage of defects with area not larger than 200 μm^2 is 98.82%, 92.40% and 82.28% for unaffected parent rail metal, fusion line and weld center, respectively. The detected defects for all three zones mostly concentrated within the Class I (0.0~20.0 μm) while the size of some defects in the weld center fell into Class II (21.0~40.0 μm) or even larger. The maximum defect size in weld center reaches up to around 60 μm. The percentage of defects area varies from 0.35 % to 1.22 % for each zone as shown in Table 7. The weld metal, together with the fusion line or mix fusion zone, exhibited a higher defect density and larger defect size compared to unaffected parent rail material. Such defects, either pores or inclusions, are critical sources for crack initiation and propagation and result a poor toughness of material.

1 - weld center

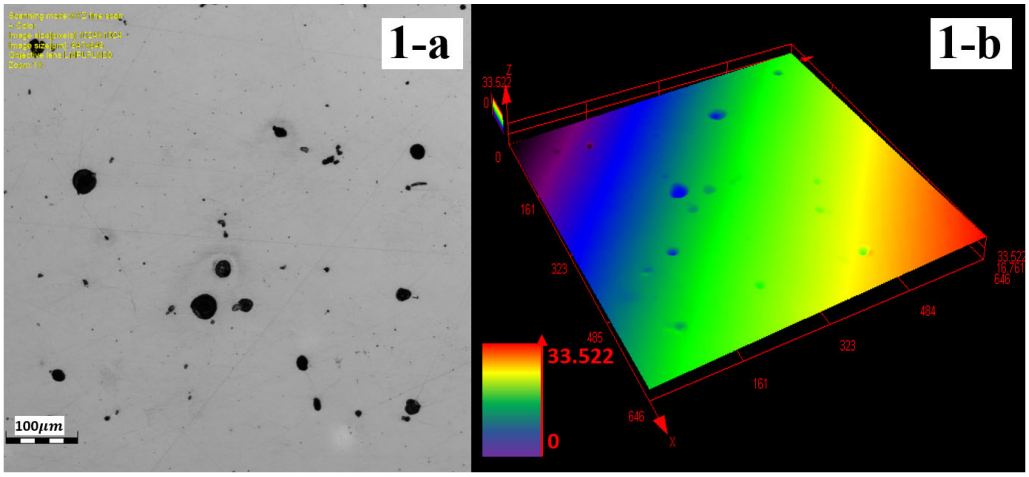

2 – Fusion line

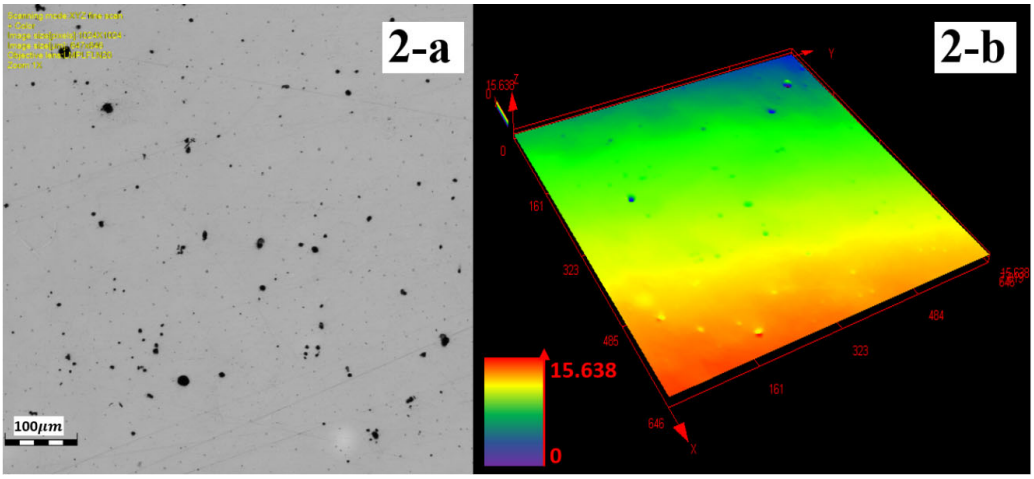

3 – Heat affected zone

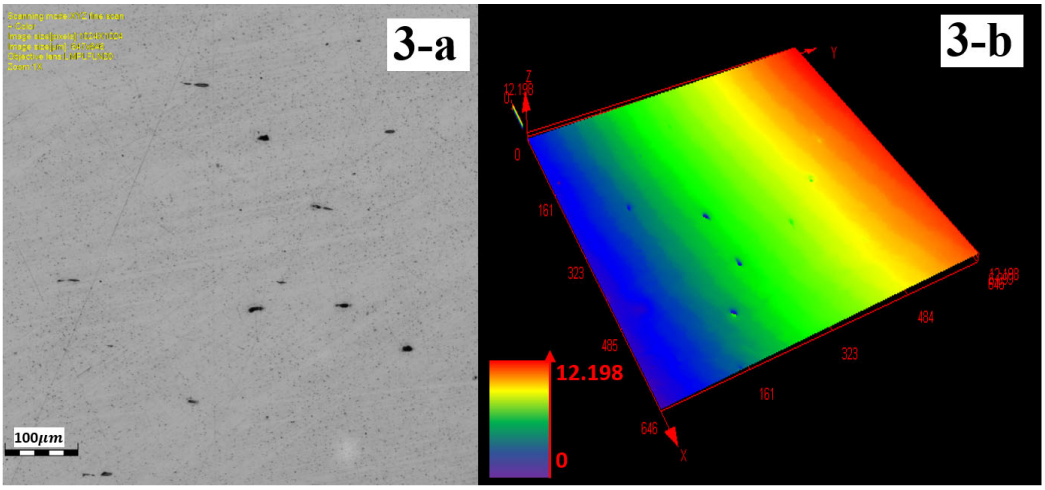

4 – Rail steel

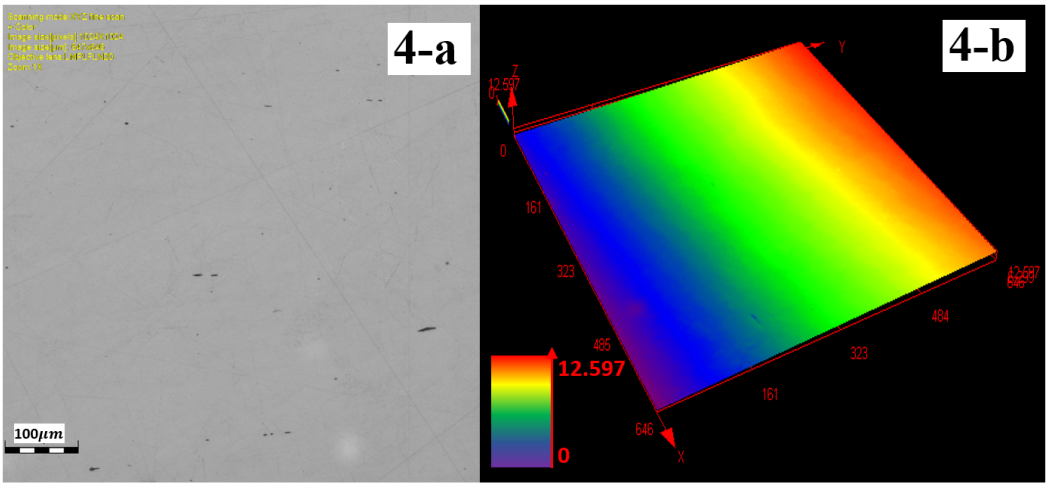

Figure 3-6: Defects measurement: a) 2-D view under optical microscope, b) 3-D view under laser scanning microscope

Two types of defects in the thermite weld and adjacent HAZ: pores (gas pores and solidification shrinkage cavities) and inclusions were observed in the subsurface area. The gas pores result from the gases entrapped in the solidifying molten metal during welding process. These gas pores are formed due to the moisture from the surrounding environment or welding material like thermite powder, mold. The shrinkage defects result from insufficient filling metal to compensate as the casting metal solidification process. Other impurities or dissolved gas induced closed shrinkage pores inside thermite welding. A 2-D microscopy images, as seen in Figure 3-6, was obtained from optical microscope to quantify the number of defects, while a 3-D image from the laser scanning microscope was used to analyze the morphology features. The 3-D profile obtained shows that those pores vary in depth from less than 1 µm up to tens µm. Those pores are not always as spherical as shown in 2-D view but from 3-D observation some are with quite sharp shape and deep depth while the cross section is still circular. Furthermore, shrinkage cavities are observed in the center of thermite weld metal as shown in Figure 3-7. The diameter and depth of shrinkage cavities in weld center easily reach up to 16~18 µm. The volumetric contraction during the solidification process is responsible for the formation of these shrinkage pores.

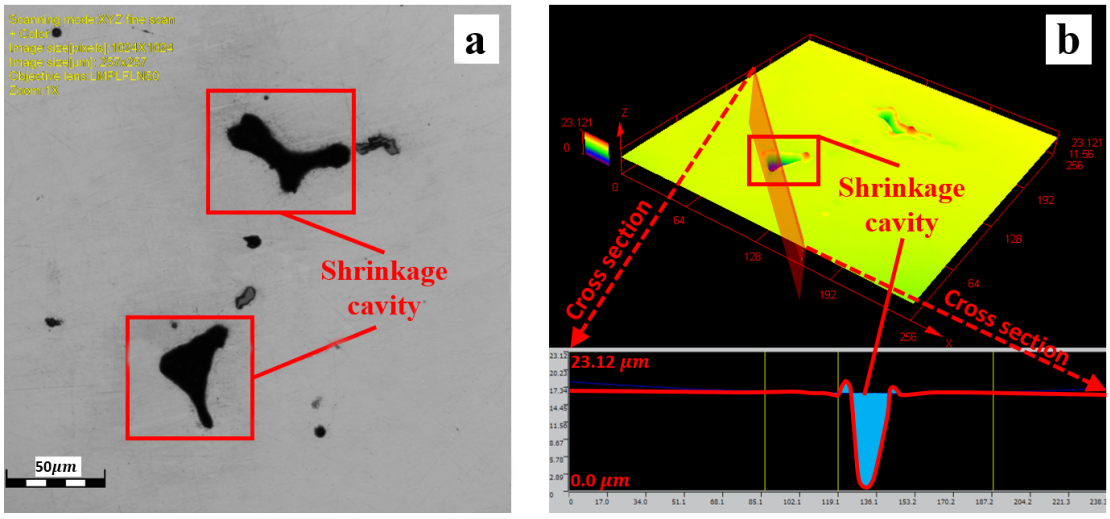

Figure 3-7: Shrinkage cavity in weld center a) 2-D view under optical microscope, b) 3-D view under laser scanning microscope

The formation of non-metallic inclusions is a major issue during service of thermite weld as they influence the structural properties significantly. The detailed investigation shows that non-metal inclusions exists mainly in the weld center and fusion line. The analysis of chemical composition analysis from the SEM/EDS system shows that Aluminum oxide (Al_2O_3) and Manganese sulfide (MnS) were identified as the dominant types of inclusions in the investigated samples as in Figure 3-8. After thermite reaction, the alumina Al_2O_3 typically forms on the top of the molten metal during the pouring process. As a result of insufficient preheating or incorrect weld gap during the preparation phase, the aluminum oxide inclusions form at the welding zone and the fusion line. The aluminum oxide particles are distributed at the thermite weld metal shown in Fig. 3-16b. This could be the important factor why the ductility of the weld metal and fusion line decrease dramatically. It should be noted that the distribution of the Al_2O_3 oxide particles deteriorate the plastic formation around the crack tips, which made a very high and complicated tri-axial state of stress.

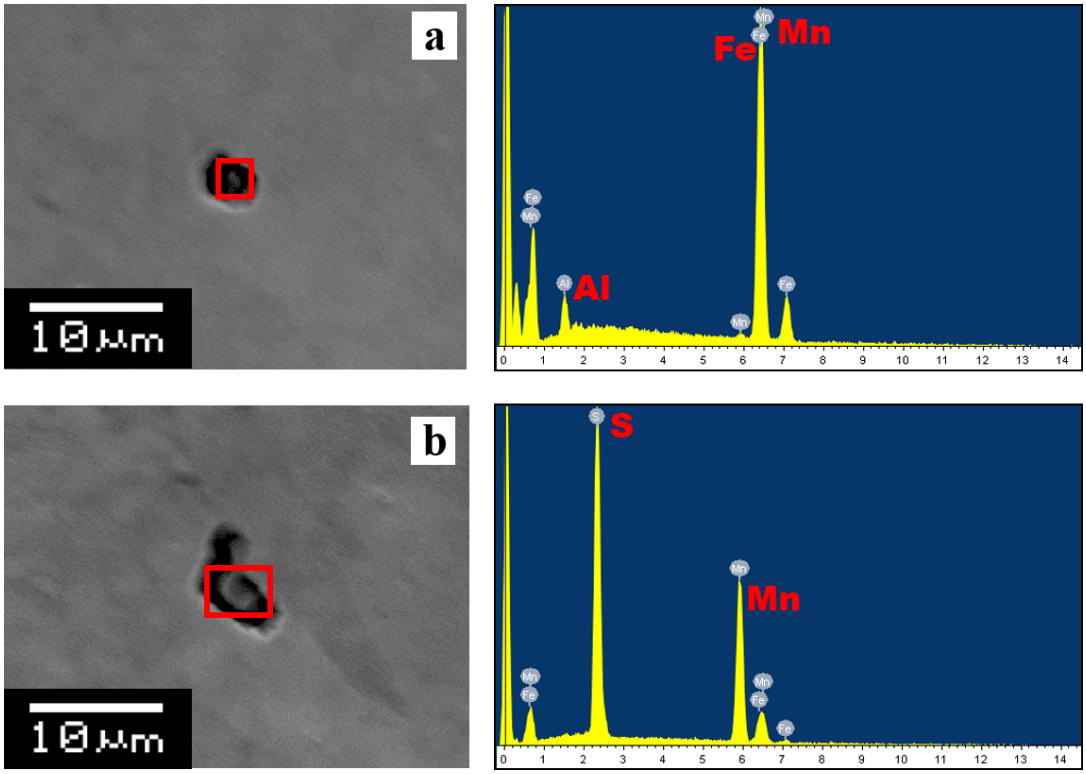

Figure 3-8: Weld defects: Inclusions: a) Aluminum oxide; b) MnS

3.4 Concluding remarks

In this chapter, the material characteristics across the thermite welded joints were investigated. The macrograph analysis of the thermite welded joints was performed and different affected zones resulting from the welding process were characterized. Coarse grains decorated with scatting welding defects were found at the embrittlement zone next to the fusion line due to the grain recrystallization. The grain was then observed to be reduced to be with finer size and further to normal size of unaffected parent rail material gradually. The microstructure of thermite weld metal and the parent rail material was observed to be pearlitic with a small amount of proeutectoid ferrite decorated in the grain boundary. No martensite was formed due to the slow continuous cooling. The hardness of thermite weld metal and fusion line is significantly higher than the parent rail. The highest hardness at the FGHAZ which is associated with the finer grain size resulting from the recrystallization under steeper thermal gradient and the soften zone in the intercritical zone is because of the spheroidization of cementite. Weld defects including pores (gas pores) and inclusions (Al_2O_3 and MnS) were found both in the weld metal and fusion line while solidification shrinkage cavities were found in the weld center, which act as potential crack initiation sites.

Chapter 4 Modeling of Thermite Welding Induced Residual Stresses

The accuracy of the structural integrity assessment is also subject to considerations of the structural stress state, particularly, the residual stress field in the vicinity of the welded joint resulting from the thermite welding process. In this chapter, thermite welding residual stresses were modelled using a sequentially coupled thermal-mechanical simulation and the calculated residual stress distributions were compared with portable XRD residual stress measurement results. A cyclic plasticity constitutive model was employed to investigate the redistribution of the residual stresses due to cyclic bend fatigue loading. Residual stress relaxation was observed in the direction of the applied load and significant relaxation was noted after the initial load cycle. An analytical model considering the initial residual stress, material properties, stress amplitude and the number of cycles was used to predict the stress relaxation.

4.1 Problem specification

Thermite welded joints often suffer from non-uniform and highly localized temperature distribution associated with localized plastic deformation due to the non-linearity of material properties. The resultant residual stresses, particularly the high tensile residual stresses near the weld toe region, can have adverse effects on the structural integrity of the connected running rails and potentially lead to fatigue cracking during the service life.

In this chapter, a novel investigation methodology including a coupled thermal-mechanical simulation and experimental measurement to investigate the residual stress and relaxation of the thermite welded rail joints is proposed. Firstly, the thermite welding residual stresses are modeled using a sequentially coupled thermal-mechanical simulation. The thermal model simulation is conducted to study the temperature history and the results are read into the structural model to study the residual stress distribution. This residual stress model is verified by measurements of thermite weld surface using a portable non-destructive X-ray diffraction method. A cyclic

plasticity constitutive model is then developed to study the residual stress relaxation by the cyclic fatigue bend load. The effect of welding process parameters on the residual stress development is also discussed.

4.2 Experimental measurement

Two 600mm R260 rails with profile of 60E2 [17] were welded together using the thermite welding process in the workshop. The material of parent metal and weldment is R260 carbon steel and the illustration of the process is shown in Figure 4-1. The residual stresses on the surface of the thermite welded joints were measured using non-destructive portable X-ray residual stress analyzer μ-X360s from Pulstec. Strains are obtained through measuring crystal structure information and stresses are calculated based on the "cos-alpha method". The residual stresses were measured at three different locations (head, web, and base corner) on the welded joint surface, as shown in Figure 4-2. The measurement of the head-to-web and web-to-base locations were not conducted due to the size limitation of the sensor unit and the geometry of the specimen. Noted that the XRD approach can be only used to measure the residual stress near the surface of the specimen, with sub millimeter range. However, the measured results using XRD method provide a good reference to validate the effectiveness of the finite element simulation in the next section.

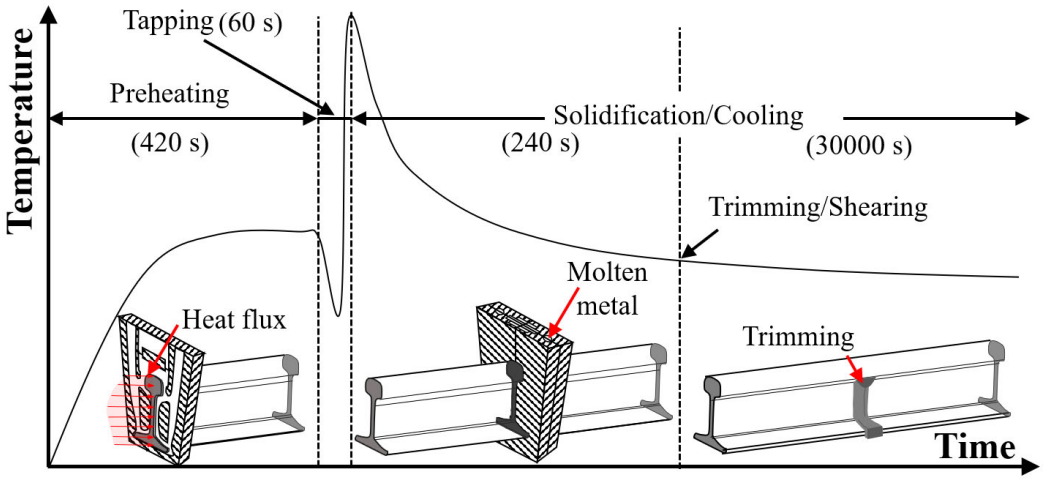

Figure 4-1: Thermal history of the thermite welding process

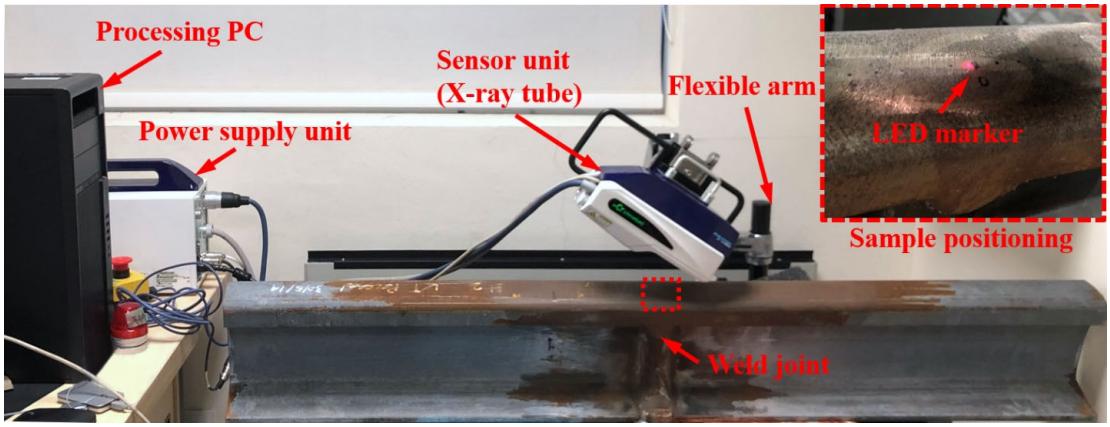

(a) portable X-ray residual stress analyzer set-up

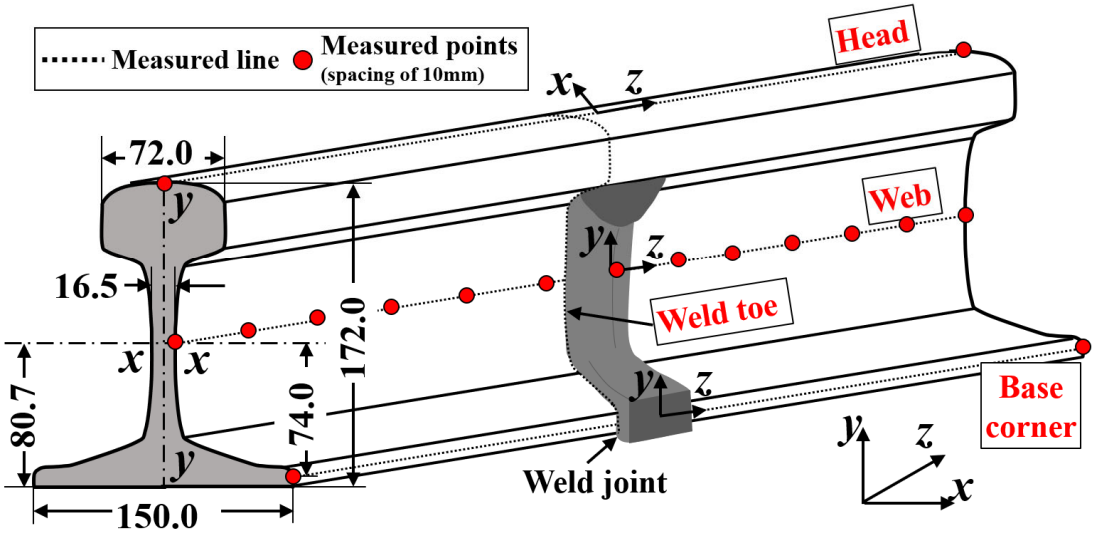

(b) residual stress measurement layout

Figure 4-2: Schematic illustration of residual stress measurement

4.3 Numerical Simulation

In this study, three main FE models were built following the sequence of thermal model, structural model, and plasticity constitutive model. The temperature field is obtained from the thermal model and it is read into the structural model to study the residual stress distribution. The calculated stress result from structural model is then imported into the cyclic constitutive model as initial stress state to investigate the residual stress relaxation. The schematic illustration of the numerical simulation process was present in Figure 4-3. Noted that the preheating phase is not explicitly included in the mechanical analysis due to its complexity of the of the boundary constraints and challenges when dealing with the pouring of liquid metal using the element death and rebirth technique. The temperature fields in the rail at the end of the preheating phase is carried cover to the pouring phase using the approach of element birth. Only temperature history after pouring was read into the residual stress analysis in the model and the effect of preheating temperature is considered implicitly by the resulted differences of temperature field. However, the current approach seems reasonable since the most significant effecting factors of residual stress, the volume change during phase transformation and the variations of mechanical properties, are taken into account in the current model. This can be also validated from the good agreement between the simulation results and the experimental measured.

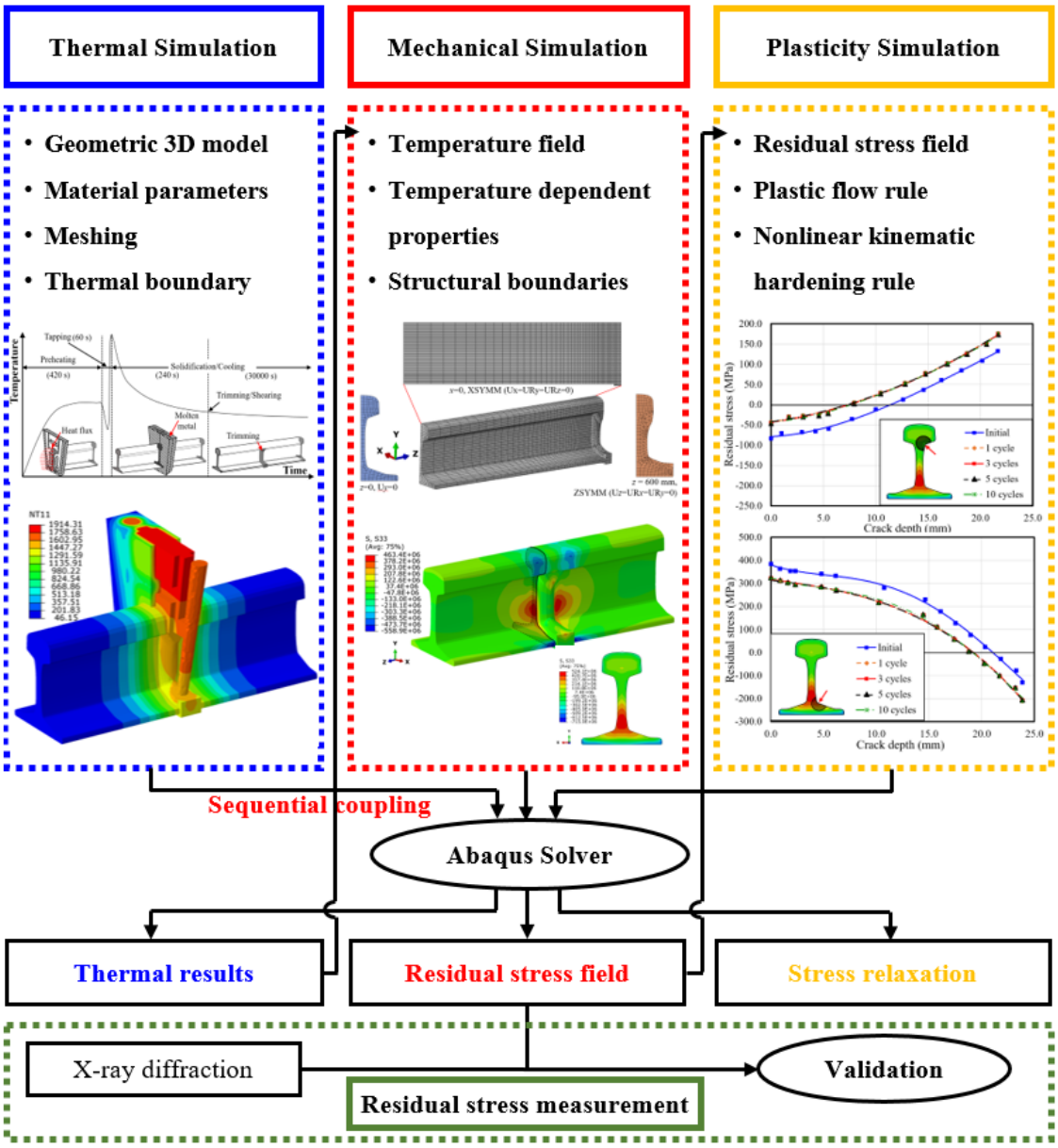

Figure 4-3: Schematic illustration of simulation process

Figure 4-4 shows the full geometry of the thermite welding system and the typically simplified quarter model due to the symmetry. The geometry of the welded joint was scanned from the laser scanner Handyscan 307. The numerical model is developed explicitly using Abaqus/CAE 2019 [115]. The total number of elements is 23864, with 12904 elements for rail (hexagon elements) and weld (tetrahedral element), and 10960 elements for the mold (tetrahedral element). The mesh

of the structural model and constitutive model is the same as the thermal model with weld and mold part deactivated.

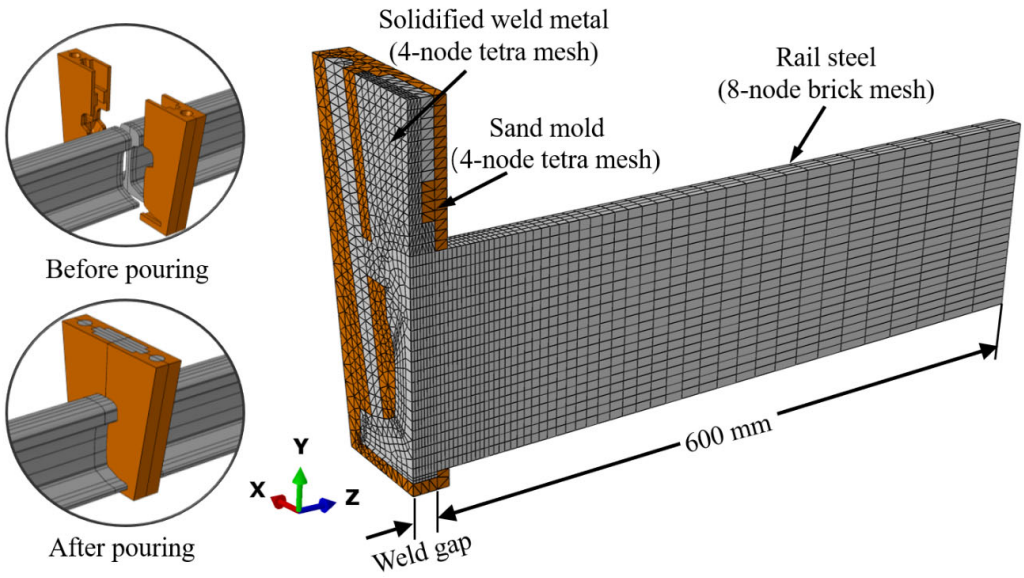

Figure 4-4: Geometry model and mesh for thermal analysis

4.3.1 Thermal simulation

The thermal model simulation was conducted to capture the accurate temperature history with steps and time period following the welding procedures as shown in Figure 4-1. To simplify the complexity of the thermal modelling, only heat conduction was considered and past research [71] proved that it has dominant effect on the temperature evolution. The thermal balance relation is expressed as

$$\rho \cdot C_p \frac{\partial T(x,y,z,t)}{\partial t} = k(T) \cdot \nabla^2 T(x,y,z,t) + \dot{Q}(x,y,z,t) \quad (4\text{-}1)$$

where ρ refers to the density, C_p is the specific heat, (x, y, z) are Cartesian coordinates, t is the time, k is the thermal conductivity, and $\dot{Q}$ is the heat generation rate. Other physical properties were reflected in the material properties, thermal loads and boundary conditions. Two different materials, the R260 carbon steel for the rail and thermite weld, and the sand for the mould were modelled and the temperature-dependent properties were obtained from previous studies [71]

(Figure 4-6). The latent heat resulting from phase transformation was included in terms of the specific heat versus temperature using enthalpy method.

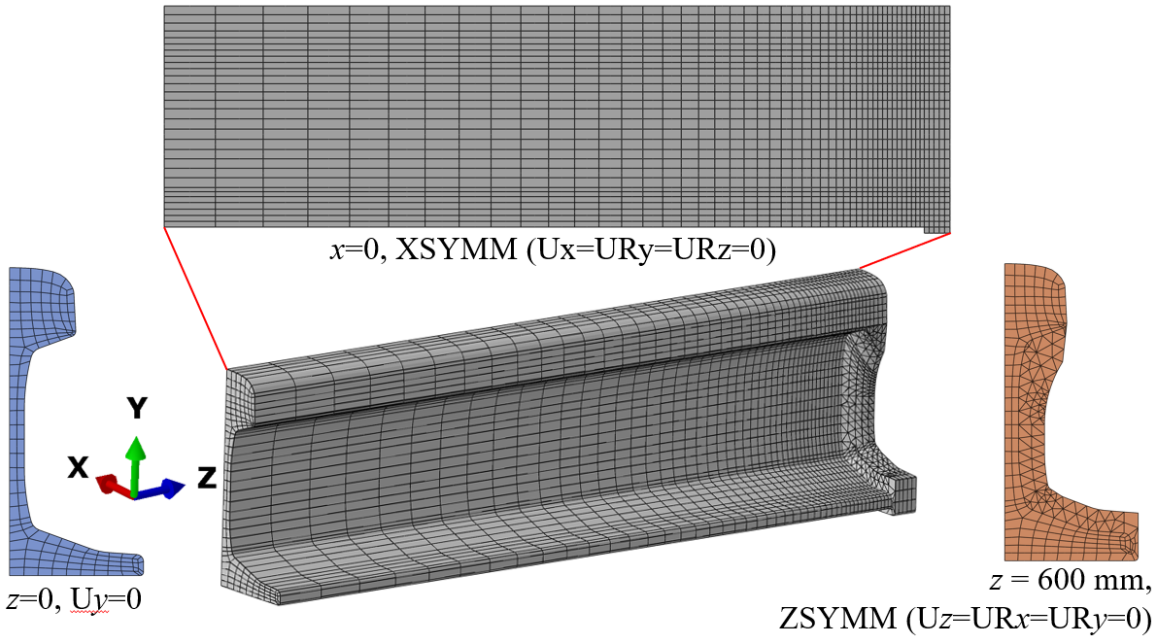

Figure 4-5: Model and boundary condition for residual stress and relaxation model

The thermal simulation was conducted as follows. In the first step of the preheating, a steady heat flux was applied to the free rail end transverse surface based on Y Chen's measurement [71]. Due to the symmetry of the rail profile, the heat flux profile was assumed to only varies in the height direction and applied as non-uniform mapping field input in Abaqus. The heat flux was subsequently deactivated during the second step of the tapping. The surface convective coefficients of 0.01 W/cm^3K and 0.002 W/cm^3K were applied on the inside and outside of sand mould, while a constant value of 0.001 W/cm^3K was used for rail and weld surface exposed to the surrounding air. The sink temperature was set to be 20 °C. Two significant phenomena were considered in the subsequent steps: pouring and trimming. The pouring of the molten metal was modelled instantaneously using element death and rebirth technique in Abaqus with a prescribed temperature of 2050 °C [71]. The mold was removed after 4 minutes and the excess thermite weld was dressed using a weld chisel cutting set. This is modelled by deactivating the extra weld metal

and defining a free convective surface in the previous contact surface. The remaining model of rail and weld was cooled down to the room temperature in the air.

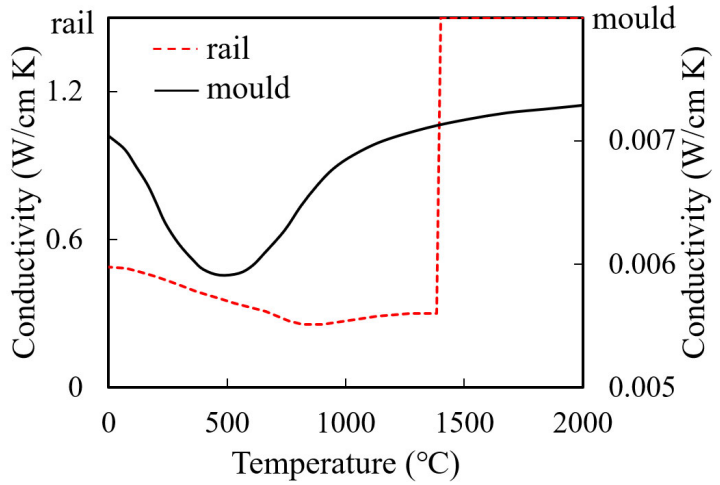

(a) material conductivity

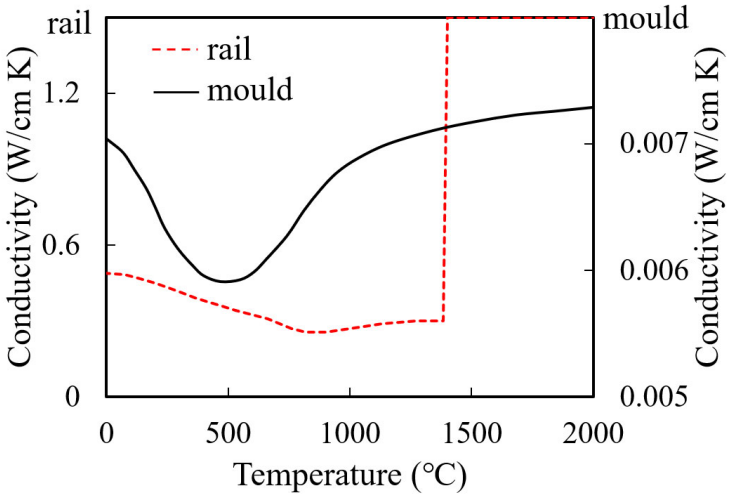

(b) special heat

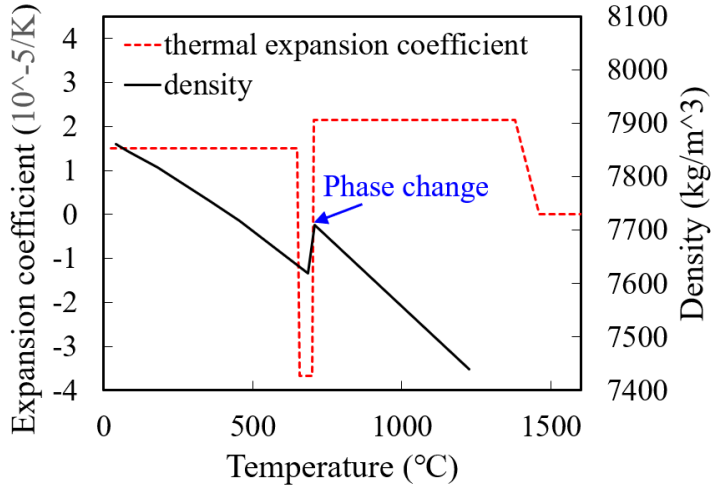

(c) rail density & expansion coefficient

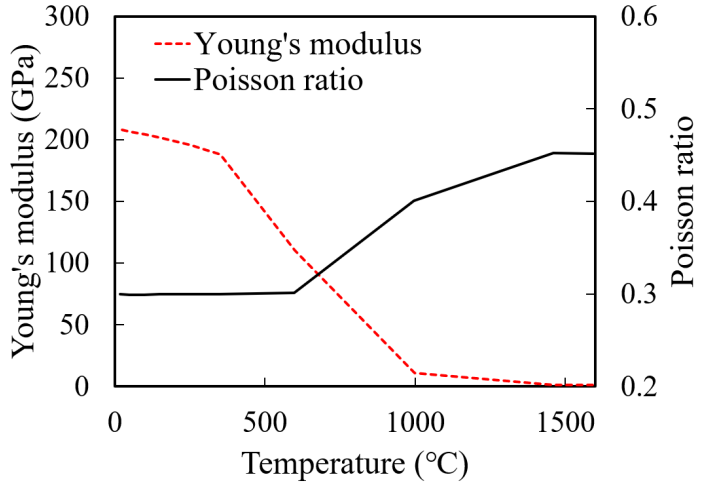

(d) rail elastic properties

Figure 4-6: Temperature dependent properties of rail steel and mould sand for simulation

4.3.2 Residual stress simulation

Next, the elastic-plastic structural analysis was performed to calculate the residual stress resulting from material yielding as the thermite welded rail is cooled down to room temperature. The output of time-dependent temperature distribution from the thermal model was sequentially read into the structural model as predefined field for stress analysis.

The strains of welded rails during the cooling process were decomposed into three components and characterized by the following equation:

$$\varepsilon_{total} = \varepsilon_e + \varepsilon_p + \varepsilon_{th} \tag{4-2}$$

where ε_e is refer to the elastic strain, ε_p is the plastic strain, and ε_{th} is the elastic thermal strain. The effect of the viscoplastic creep and strain induced by phase transformation is not significant and therefore were not considered to simply the calculation process. The mechanical properties of the R260 rail steel and thermite weldment were obtained from the author's previous research [29]. The time-dependent properties were obtained from Josefson's [116] work as shown in Figure 4-6. The plastic behaviour of the rail steel and weldment was estimated using linear kinematic hardening model [4]. The temperature-dependent stress-strain curves were scaled from the room temperature yield strength. The annealing temperature was set to be 700 °C to zero the equivalent plastic strain when the temperature is above that. The mold is not considered during the cooling process. The y-direction displacement of rail cross section at the free end was restricted to prevent rigid body motion as shown in Figure 4-5.

4.3.3 Cyclic plasticity constitutive model

The cyclic constitutive model taking into account the initial yield condition, the plastic flow rule and the nonlinear kinematic hardening rule was developed to investigate the residual stress relaxation under cyclic loading conditions. The residual stress field from the mechanical result was taken as the pre-stress condition in the present simulation. The model was built with details as below:

The Mises yield surfaces was used:

$$F = f(\sigma - \alpha) - \sigma^0 = \sqrt{\frac{3}{2}(S - \alpha^{dev}) : (S - \alpha^{dev})} - 0 \tag{4-3}$$

where $f(\sigma - \alpha)$ is the equivalent Mises stress in terms of backstress α. S is the deviatoric stress tensor and defined as $S = \sigma + PI$, where σ refers to the stress tensor and P and I refer to the equivalent pressure stress and identity tensor respectively. σ^0 is the radius of the yield surface

and α^{dev} refers the deviatoric part of the backstress tensor. The direction of plastic deformation increment after the yield point is described as:

$$\dot{\varepsilon}^{pl} = \dot{\bar{\varepsilon}}^{pl}\frac{\partial F}{\partial \sigma} \tag{4-4}$$

where $\dot{\varepsilon}^{pl}$ and $\dot{\bar{\varepsilon}}^{pl}$ describe the plastic flow rate and equivalent plastic strain rate respectively. The latter was obtained by:

$$\sigma^0 \dot{\bar{\varepsilon}}^{pl} = \sigma : \dot{\varepsilon}^{pl} \tag{4-5}$$

Two components of nonlinear kinematic hardening and isotropic hardening were considered to describe both the yield surface translation in stress space via the backstress α and the change of equivalent stress σ^0. The hardening laws are expressed as:

$$\dot{\alpha}_k = C_k\frac{1}{\sigma^0}(\sigma - \alpha)\dot{\bar{\varepsilon}}^{pl} - \gamma_k \alpha \dot{\varepsilon}^{pl} \tag{4-6}$$

where α is the overall backstress by calculating the summation of values in different level. k is the number of levels and 3 was selected in this study. C_k and γ_k are parameters with values shown in Table 8. The model reduces to an isotropic hardening model when C_k and γ_k equal to zero. The behaviour of isotropic hardening is defined as:

$$\sigma^0 = \sigma|_0 + Q_\infty(1 - e^{-b\bar{\varepsilon}^{-pl}}) \tag{4-7}$$

where $\sigma|_0$ refer to the equivalent stress defining the size of the yield surface at zero plastic strain. Q_∞defines the yield surface size and b refers to the change rate of the yield surface size as plastic straining develops.

Table 8: Cyclic plasticity constitutive model parameters

Cyclic mechanical load parameters						
Simulation	Applied deadweight (Tons)	Bending moment (kNm)	R ratio	Equivalent maximum stress σ_{max} (MPa)		
				Head	Head-to-web	Web-to-base
Vertical bending moment (compressive in rail head, tensile in rail base)						
1	-8	-24	0.1	-130.5	-67.4	80.1
2	-12	-36	0.1	-195.8	-101.1	120.2
3	-16	-48	0.1	-261.0	-134.8	160.2
Inverse bending moment (tensile in rail head, compressive in rail base)						
4	8	24	0.1	130.5	67.4	-80.1
5	12	36	0.1	195.8	101.1	-120.2
6	16	48	0.1	261.0	134.8	-160.2

Plasticity parameters of R260 rail steel [117]								
Material	C_1 (MPa)	γ_1	C_2 (MPa)	γ_2	C_3 (MPa)	γ_3	$\mathbf{Q}_\infty$ (MPa)	b
R260	24750	55	60000	600	200000	2000	-189	500

The uniaxial triangular cyclic load in the longitudinal direction was applied as bending moment at one end of rail while another end was constrained to avoid rigid movement. In order to evaluate the effect of the stress amplitude on the stress redistribution, three different levels of amplitude were used as 80 kN, 120 kN and 160 kN with load ratio R=0.1. The load of 80 kN (8 tons) is equivalent to the dead weight of a normal rapid transit train on the running rails. The magnification factors of 1.5 and 2.0 were studied considering the effect of dynamic loads in service. Orringer et al.[118] concluded that the rails, together with welded joints, are subjected to a wave-like deformation resulting from the dynamic rail/wheel contact. Hence both the rail head and base regions will experience the tension and compression stress from cyclic bend fatigue loading. In this study, both the vertical bending moment resulting in compressive stress in the rail head and tensile stress in the rail base, and the inverse bending moment resulting in tensile stress in the rail

head and compressive in the base were investigated to understand stress relaxation behaviors of different locations. The details of the applied loads and the equivalent stress states of each location are depicted as in Table 8.

4.4 Results and Discussion

4.4.1 Thermal results and temperature field

The shape of thermite welded metal and heat affected zone (HAZ) obtained from the thermal simulation are plotted in Figure 4-7. The figure shows that the size of the fusion zone where the temperature is above 1450 °C ranges from around 25.5 mm to 28.5 mm while the weld gap is 25±1mm. A comparison was made between the simulated result and the etched macrograph of the longitudinal section. Note that the predicted dimension is slightly smaller in the head and bottom region of thermite weld. This is because the actual trimming and grinding of extra weld is a continuous process while the "element deactivate" technique in Abaqus is a transient method. These delays were unavoidable in Abaqus but can be neglected due to its minor effect (with discrepancy of less than 5%) to the simulation results. It can be concluded that the temperature field was well reproduced by the finite element thermal simulation.

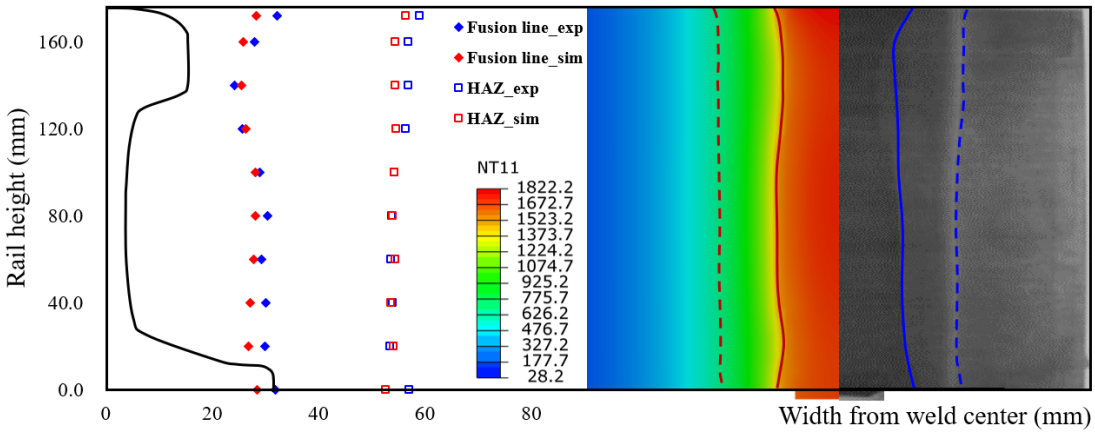

Figure 4-7: Comparison of etched macrograph with simulation

The simulated temperature fields after each step were depicted in Figure 4-8. For the convenience of discussion, only the simulation results with length of 500 mm (250 mm for each side) are

presented, although the discussion is applicable to the whole model. Figure 4-8a indicated that the maximum temperature of the rail end after preheating for 7 minutes is about 624 °C and it is more pronounced for the web and foot region. This can be explained by the relative low location of the preheating torches, as well as the narrow geometry of the rail web and foot resulting in ease of thermal transfer. The subsequent tapping process helps to expand the temperature more evenly to the cross section and the peak temperature decreased to around 412 °C (Figure 4-8b).

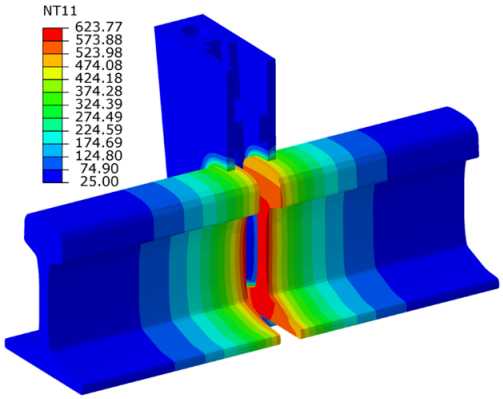

(a) at the end of preheating (7 mins)

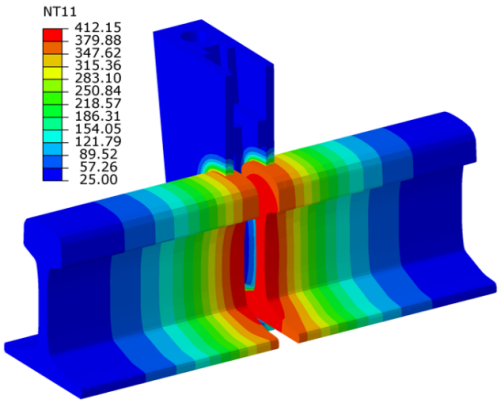

(b) at the end of tapping (1 min)

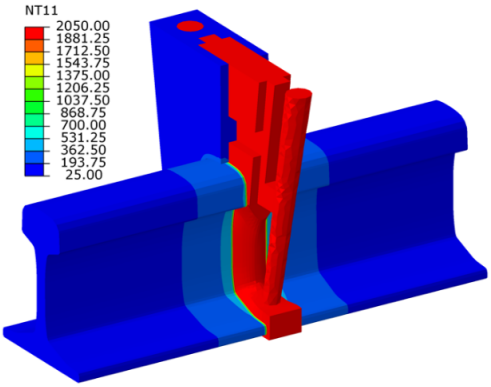

(c) pouring (transient)

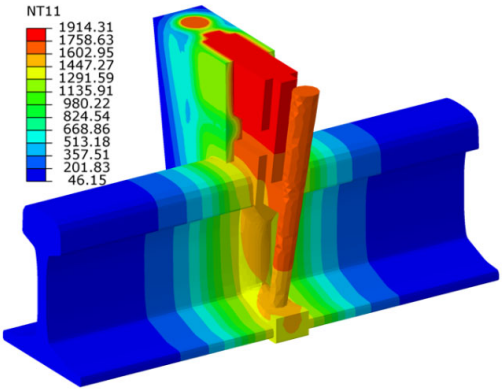

(d) cooling before trimming (4 mins)

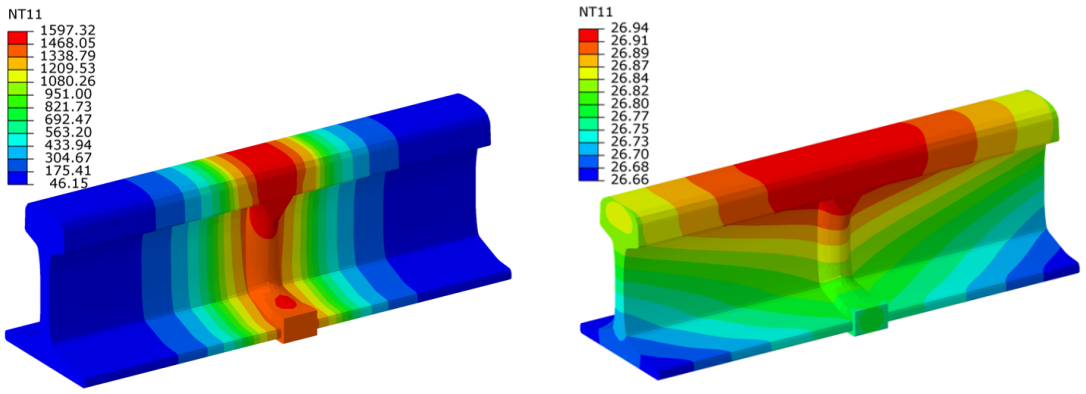

(e) trimming/shearing (transient) (f) cooling to room temperature

Figure 4-8: Nodal temperature (°C) of different stages of thermite welding process

The temperature of the poured metal was prescribed to be 2050 °C as shown in Figure 4-8c. The simultaneously spatial heat transfer to both sides of the welded rail steel was then started and the transferring is nearly uniform in the longitudinal direction. The filled metal solidified inside the attached mold for 4 minutes before the trimming process. After the trimming/tearing process, the peak temperature of about 1597 °C was observed at the location where the extra weld was trimmed. The temperature was then slowly cooled down to room temperature in air without any accelerating cooling method. The temperature history at different locations (head, web, and base corresponding to Figure 4-2) of the cross section were recorded and depicted as shown in Figure 4-9.

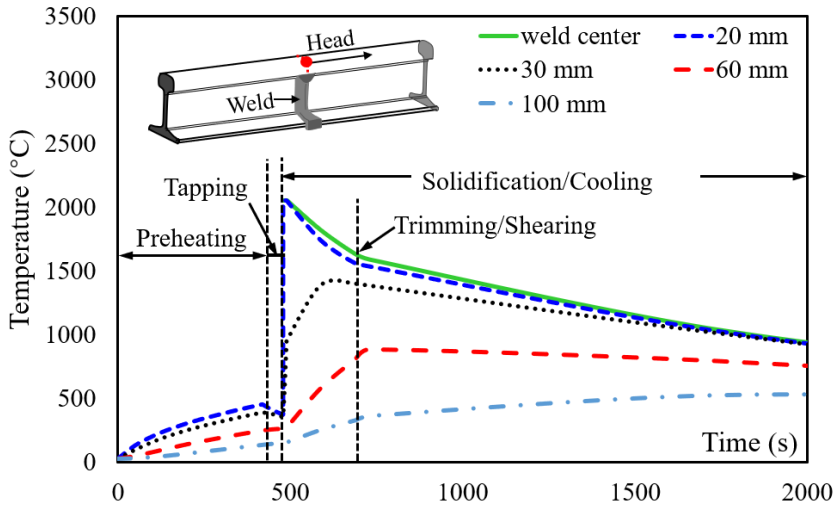

(a) temperature history at head location

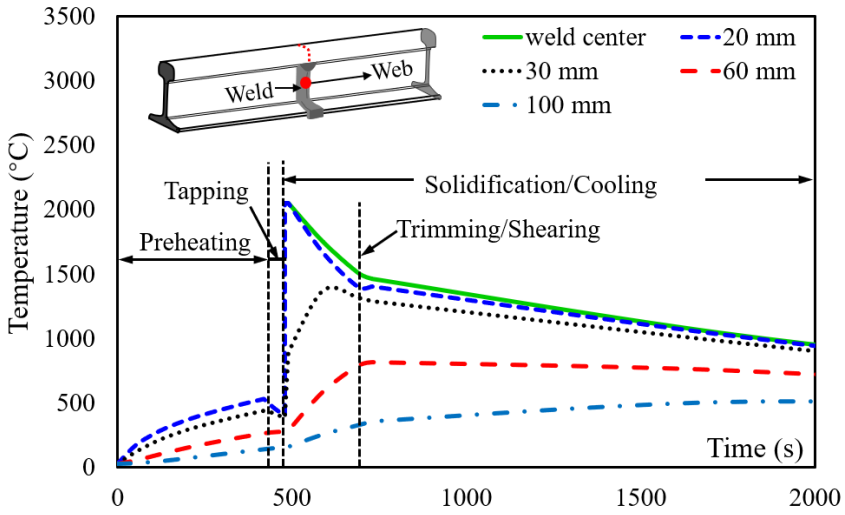

(b) temperature history at web location

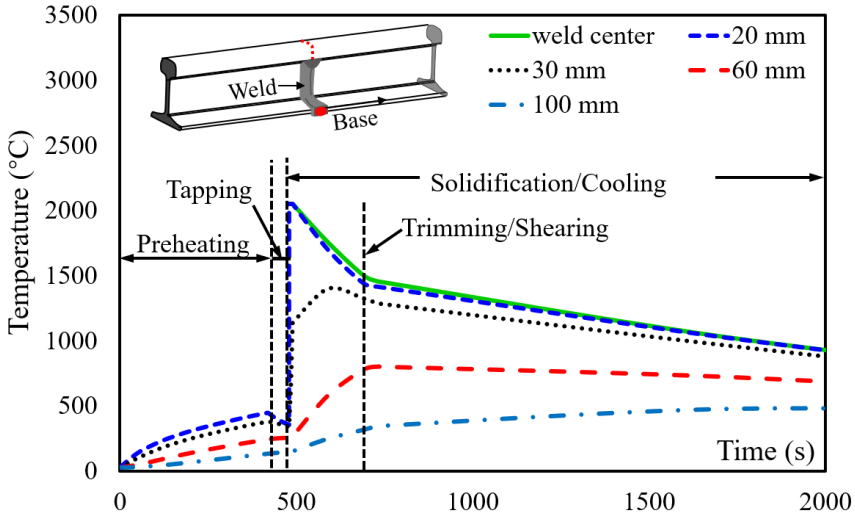

(c) temperature history at base location

Figure 4-9: Longitudinal temperature history at different location

4.4.2 3D residual stress distribution and parametric study

The 3Ddistributions of computed residual stress field were plotted as shown in Figure 4-10. The residual stresses in the transverse cracking plane at the weld toe region were also present and investigated. The residual stresses were observed to be substantially tensile in the weld toe region and becomes compressive towards the far end. The contours of different stress components in x-direction (lateral), y-direction (vertical) and z-direction (longitudinal) were illustrated in Figure 4-10a, 10b and 10c, respectively. The lateral residual stresses were relatively lower compared with

other directions. Maximum tensile stress was found at the web-to-base location of weld toe region while compressive stresses with insignificant magnitude were found at other locations. Unlike the lateral stress distribution, the tensile stress was observed to be maximum at the head-to-web and web locations of weld toe region. Large compressive stress was found in the head, head-side and web locations of weld center. For the longitudinal component (z-direction), the peak value of tensile residual stress is at web and web-to-base locations of weld toe region and high compressive stress zones were found both located at the head and base of the rail. For the transverse plane of weld toe region, similar patterns were observed for residual stresses in different directions. The substantial tensile stresses are concentrated in the rail head and web regions and the values reduces when it reaches towards the outer surface. This is can be explained by the thermal phenomena regarding the temperature and thermal gradient which result from the welding process. The high tensile stress occurring at the rail head and base regions, especially at the head-to-web and web-to-base locations, make it susceptible for fatigue cracking.

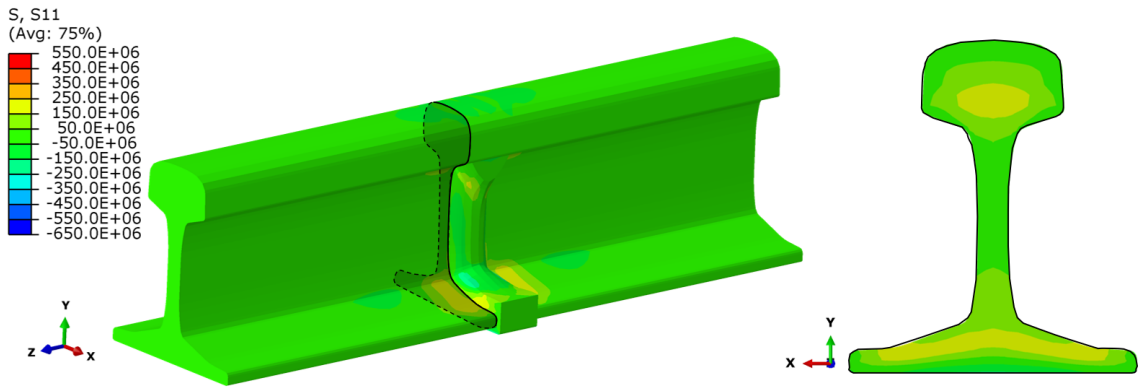

(a) stresses along transverse direction S11

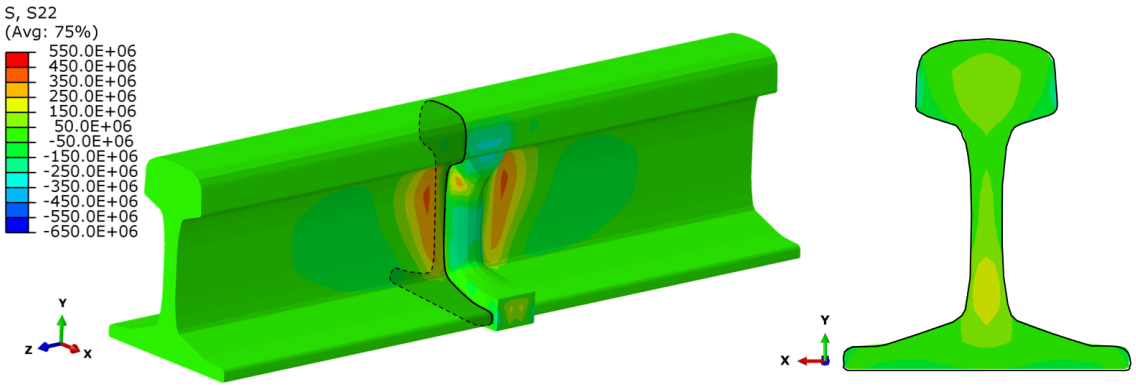

(b) stresses along vertical direction S22

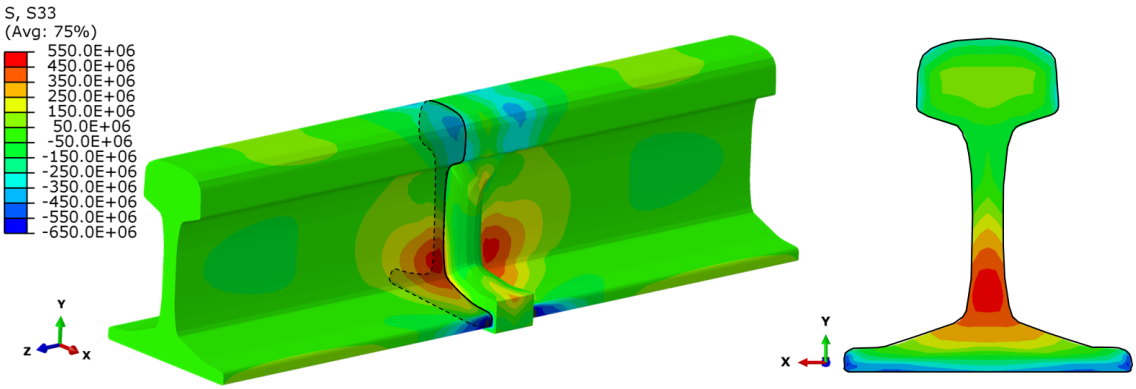

(c) stresses along longitudinal direction S33

Figure 4-10: Residual stresses from FE simulation

Figure 4-11 depicts the comparison of the simulation results and the experimental results, indicating that an accurate prediction of residual stresses using FE method was achieved. From the surface residual stresses of each location, the web region was concluded as more critical with higher tensile stresses. A distinct trend change can be found in the weld toe (near the fusion line), indicating a higher risk of fracture and failure resulting from inhomogeneity of stress field.

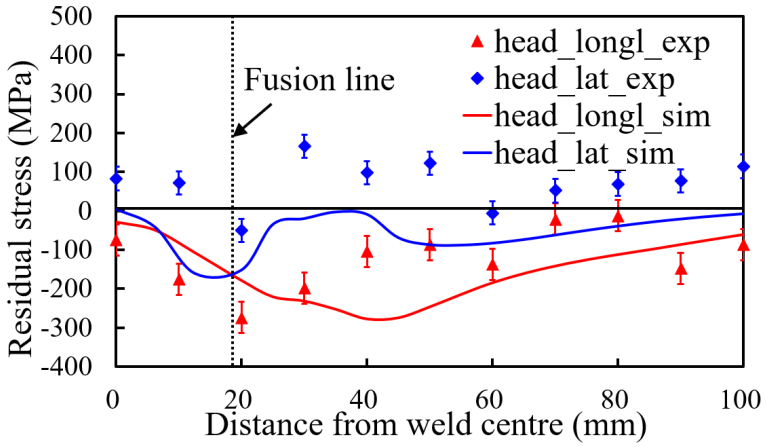

(a) residual stress of the head surface

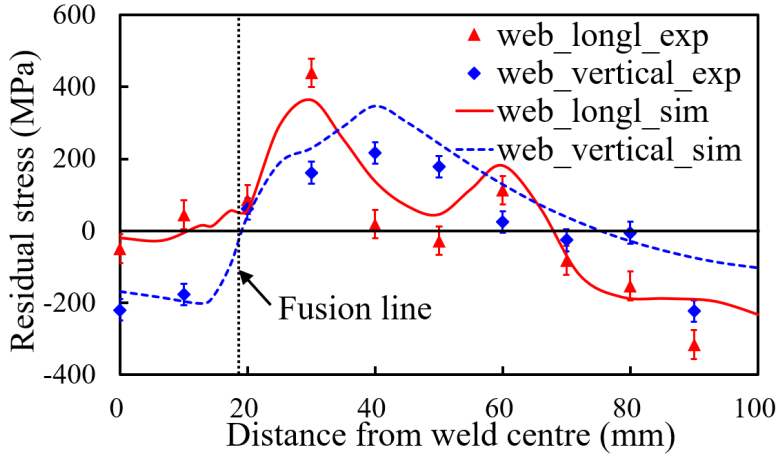

(b) residual stress of the web surface

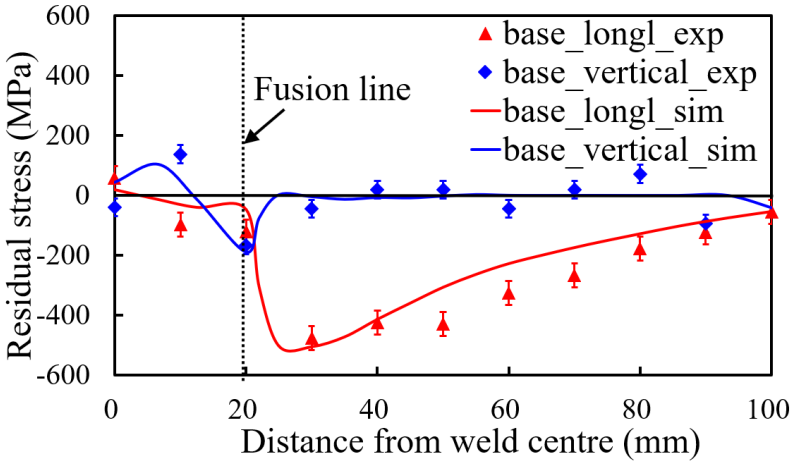

(c) residual stress of the base surface

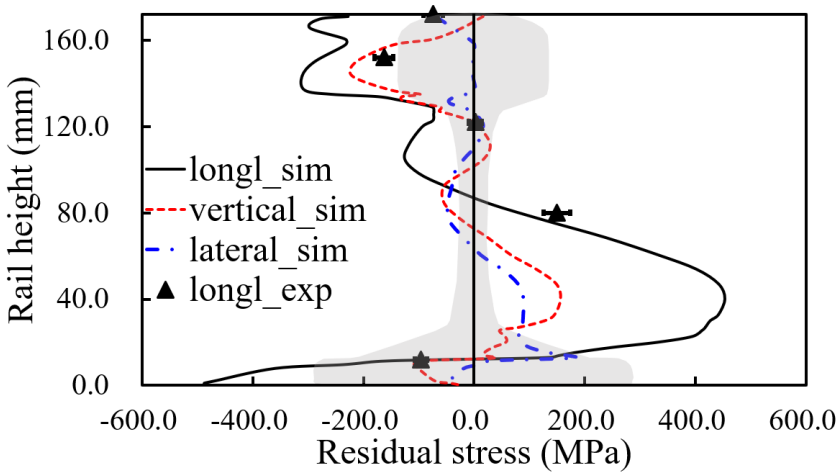

(d) residual stress of the weld toe surface

Figure 4-11: Comparison of the stress simulation results to experiment results

Some differences of the residual stresses in the rail head were observed from Figure 4-11a between the simulation and experimental result. This could be due to the simplification of shearing/grinding during the simulation process. The deactivation of extra weld metal elements simplified the grinding process which did not account for the induced temperature increase and corresponding thermal expansion. Hamdi et al. [119] determined that the residual stresses induced by grinding are affected by a lot of factors, such as the dressing techniques, grinding parameters, cooling conditions, and materials properties, and therefore the sophisticated investigation incorporating all affecting factors is not discussed in this study. Other causes such as the specific thermite welding process and the design of the mould used which resulting in a weld collar is also possible and detailed discussion is not included in this chapter.

The residual stresses of the weld toe regions versus rail height was shown in Figure 4-11d. Based on the presented results, clear patterns of distribution can be obtained for residual stresses in each direction. Generally, the maximum tensile stresses were observed to be concentrated in the weld region. In contrast, the stress decrease to maximum compressive at the two ends of rail height (head and base bottom region). This trend is more significant for residual stress in longitudinal direction compared with other two directions. For the head-to-web and web-to-base locations, a

small increment of stress was observed due to the profile change. The state of compressive residual stresses at both head and base regions are beneficial for structural performance.

Effect of preheating temperature on the residual stress

The final residual stresses are highly dependent on the temperature field resulting from the welding process. It seems necessary to investigate the effect of the preheating temperature on the residual stress formation. Five cases of preheating process were considered in the FE model: no preheating, preheat for 1 minute, 3 minutes, 5 minutes, and 7 minutes. The room temperature of 25 °C was applied to the model with the case of "no preheating". The final temperatures of rail head after preheating under each condition were observed to be around 25 °C (no preheat), 220 °C (1 minute), 415 °C (3 minutes), 545 °C (5 minutes), 650 °C (7 minutes), respectively. The corresponding temperature history of the head at the rail end was recorded and plotted as in Figure 4-12a.

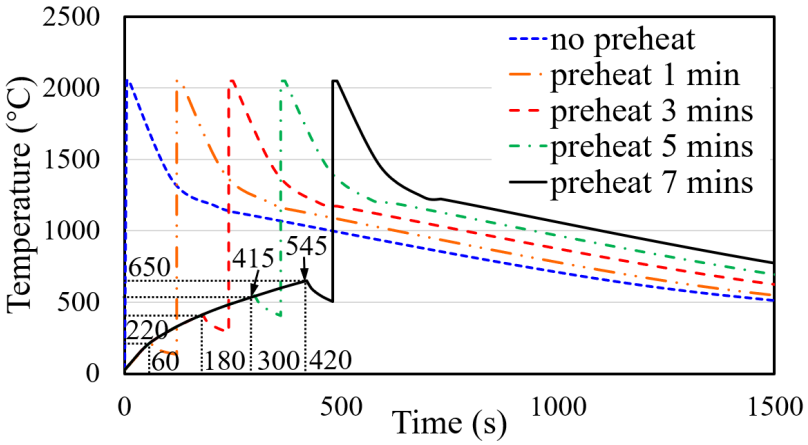

(a) temperature history

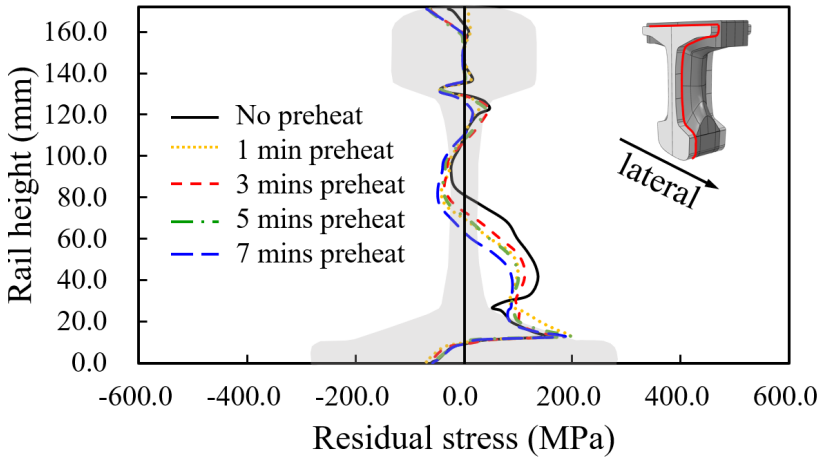

(b) residual stress in x-direction

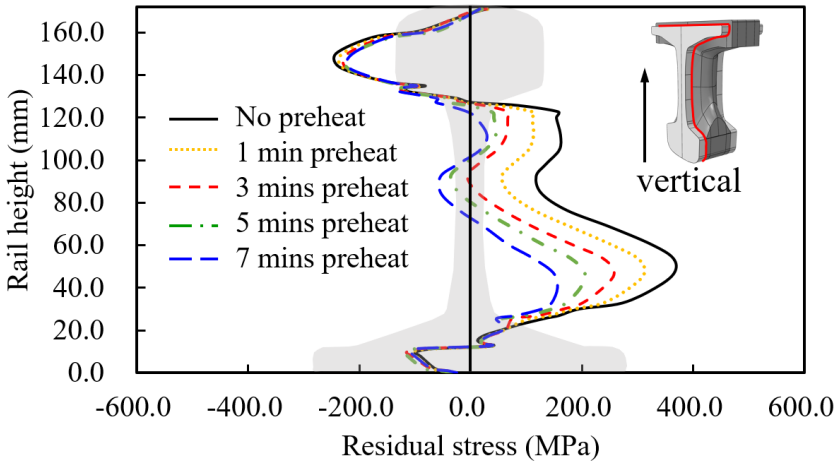

(c) residual stress in y-direction

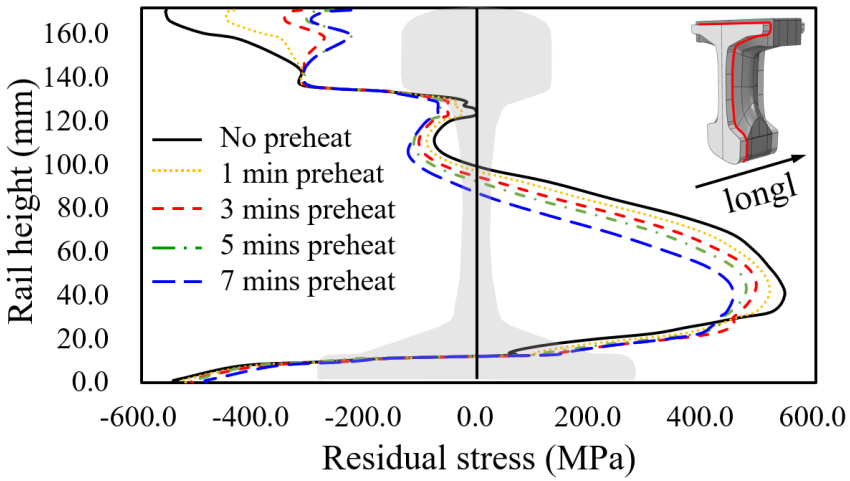

(d) residual stress in z-direction

Figure 4-12: Simulation results of each preheating case

Since the weld toe region is a critical zone with high residual stresses, special attention was paid to the investigation of the resulting residual stresses at this zone for different preheating conditions as present in Figure 4-12b ~ 12d. A significant difference between the residual stresses under different preheating condition can be observed. Generally, the higher the preheating temperature is, the lower residual stresses will be resulted. The local differences of stress distribution in each direction were also investigated. For lateral residual stress, the preheating mainly affects the tensile stress at the web region. The similar trend in the web was found to be applicable for both vertical and longitudinal stress components and the reduction is most significant in the vertical direction. No visible effect of the preheating temperature was observed for locations of rail head and base in the lateral and vertical direction. However, the highest compressive stress exists at the head location in the longitudinal direction and the magnitude was reduced by half when the preheating temperature reaches 650 °C. Generally, a higher preheating temperature with longer heating time will result in reduction of the absolute value of residual stress (both tensile and compressive) of weld toe regions.

4.4.3 Residual stress relaxation model by cyclic bending load

The surface and interior residual stress redistribution in the weld toe region at different locations was summarized and plotted in terms of number of cycles as shown in Figure 4-13 and 4-14 respectively. It shows that the simulation effectively predicts the reconstruction of the residual stress field. The residual stresses tend to release under the cyclic load, but the relaxation is limited to the initial cycle. The loads in the subsequent cycles are not able to change the stress distribution significantly. The surface relaxation behaviour varied in different directions. The lateral (Figure 4-13a) and vertical (Figure 4-13b) residual stress tend to remain at a constant level with minor initial drops while a pronounced redistribution of the residual stress field was observed within the first cycle in the longitudinal direction (Figure 4-13c). Similar trends have been found by other

researchers [120] showing that significant stress relaxation only occurs in the direction parallel to the applied external cyclic loading.

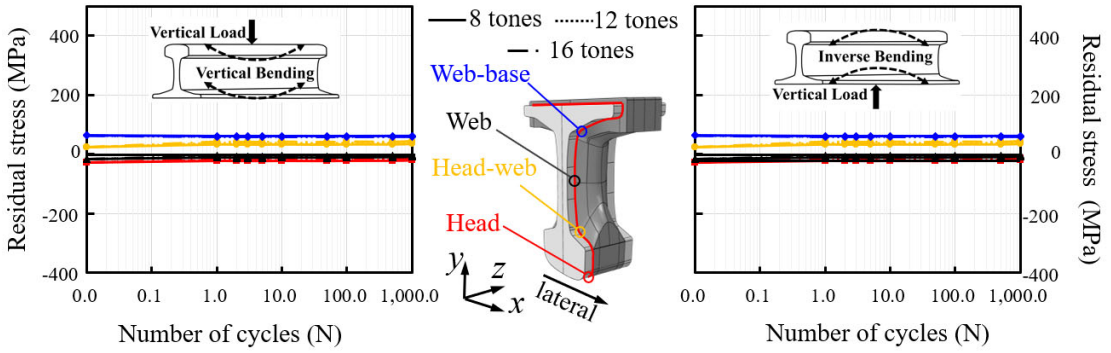

(a) stress relaxation in lateral direction

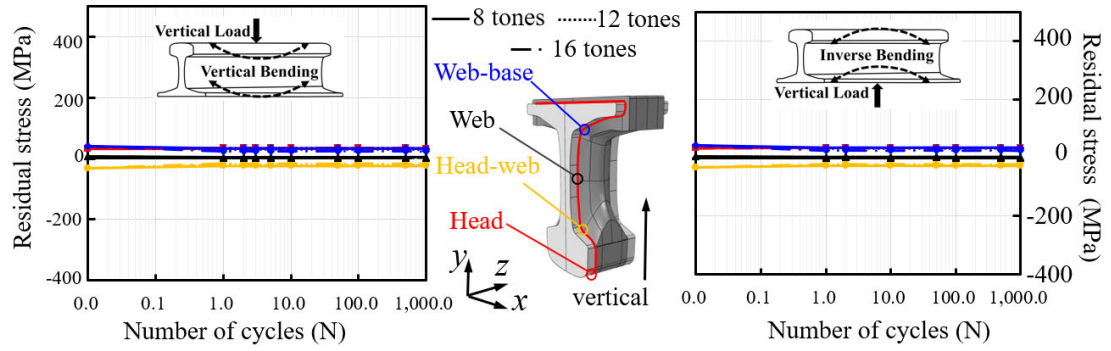

(b) stress relaxation in vertical direction

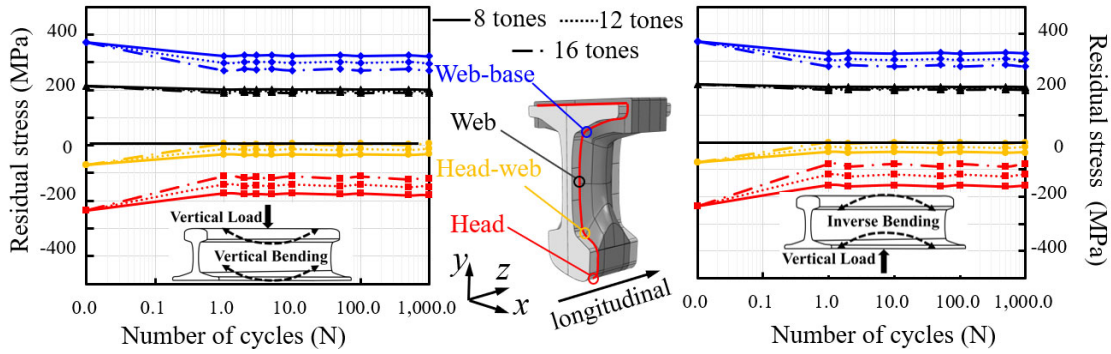

(c) stress relaxation in longitudinal direction

Figure 4-13: 3D residual stress relaxation at different locations of weld toe

It is also worth mentioning that the stress relaxation extent is highly dependent on the stress state at each location. Tensile stress is found at the web-to-base location while compressive stress at the head and head-to-web locations under the vertical bending load. This is in contrast to the stress

condition when the rail is under inverse bending. It is noticed that the relaxation is more obvious at locations under tensile cyclic load compared with compressive load. The difference becomes more observable with increasing applied load. Another finding is that even with the same stress state, the extent of residual stress relaxation is more dominant with higher stress amplitude. As a result, a significant plastic deformation occurs if the superposed stress exceeds the yield strength. The stress magnitude will be reduced due to the self-equilibrium of internal stresses. This magnitude will be further reduced once the cyclic load is unloaded. Similar phenomena occur in the next cycles and the stress becomes smaller even when the external applied load is kept constant.

Some mathematical models have been applied to investigate the extend of residual stress relaxation. Past research [120] shows that the relaxation extent is dependent on four factors: cyclic stress range, cycle numbers, loading type and material properties. In this section, the mathematical model proposed by Xie et al. [121] was adopted. The residual stress relaxation model is expressed as:

$$\sigma_r(x,y,N) = \sigma_{r0}(x,y) - \sigma_{r0}(x,y)(\alpha_1\left(\frac{\Delta\sigma_n}{\sigma_y}\right)^{\alpha_2} + \alpha_3)[\ln(N+1)]^{\alpha_4} \quad (4\text{-}8)$$

where σ_{r0} is the initial residual stress, $\Delta\sigma_n$ is the nominal amplitude of the applied cyclic load, σ_y is the yield stress, N is the number of cycles. α_1, α_2, α_3, α_4 are parameters and the values can be determined from either experimental measurement or FE simulation.

Table 9: Fitting parameters for residual stress relaxation model

Location	α_1	α_2	α_3	α_4	***R-square***
Normal cyclic bend moment					
Head	0.86	1.02	0.0025	0.16	0.91
Head-to-web	3.29	0.99	0.02	0.16	0.87
Web-to-base	-17.60	-0.0084	17.95	0.16	0.92
Inversed cyclic bend moment					
Head	1.37	0.75	-0.16	-0.0043	0.99
Head-to-web	6.98	0.13	-4.84	-0.025	0.93
Web-to-base	0.77	0.88	-0.029	-0.010	0.99

In this study, the simulation results of the longitudinal residual stress redistribution of weld toe (Figure 4-13c) was extracted to be calculate these four parameters. The results were shown as Table 9. The fitting is only performed for three typical locations (head, head-to-web, web-to-base) where most of the fatigue failures occur. The high value of R-square, close to 1.0, represents a good fit and therefore the mathematical model proposed is able to predict the residual stress relaxation accurately.

Figure 4-14 shows the longitudinal stress distribution and relaxation of the weld toe region along the depth direction after 1, 3, 5, 10 cycles of cyclic fatigue load (8 tons) by FE modelling. The residual stress increase from -85 MPa to 175MPa for head-to-web location and decrease from 380 MPa to -130 MPa, respectively, when reaching towards the interior from the surface. However, no steep gradient of residual stress variation was observed along the depth direction, especially near the subsurface. The effect of such residual stress variation on the fatigue life will be investigated in the next section. It also shows that the longitudinal residual stresses at the interior and surface are released with the same extent after the first cycle. In other words, the longitudinal deformation was concluded to be almost same at both the surface and interior of the weld toe region.

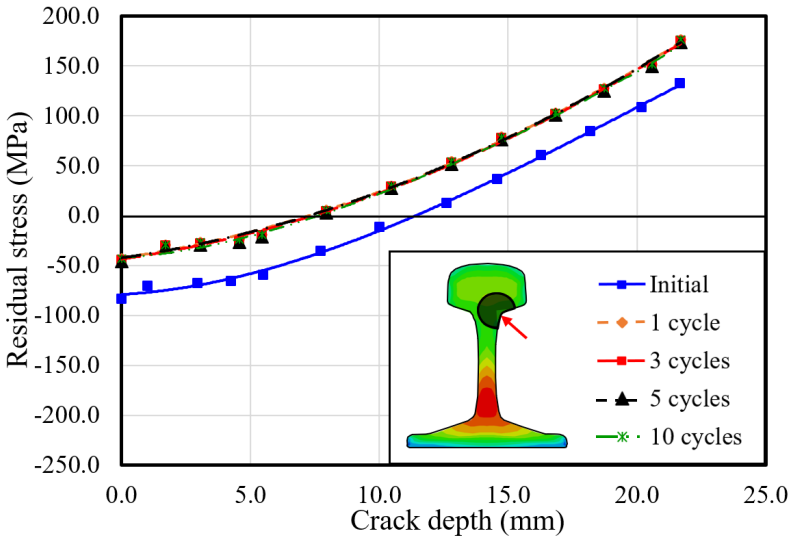

(a) longitudinal stress relaxation in the head-to-web location

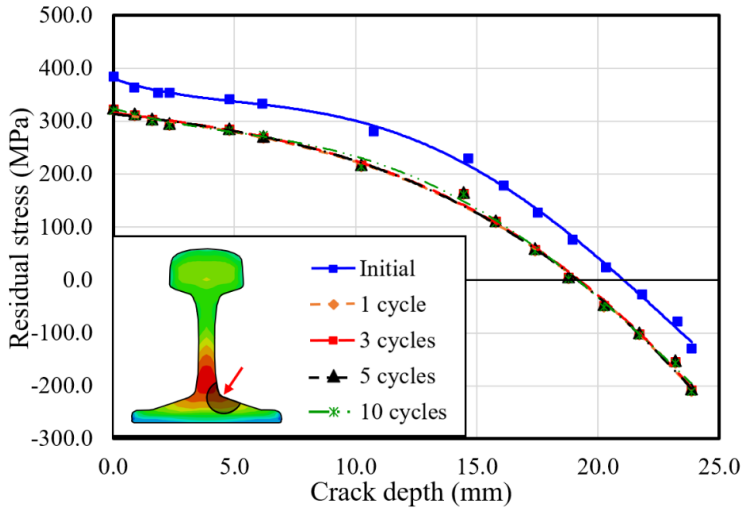

(b) longitudinal stress relaxation in the web-to-base location

Figure 4-14: Longitudinal weld-toe residual stress relaxation in the depth direction under cyclic load of 8 tons

4.5 Concluding remarks

This chapter provided a comprehensive evaluation of the residual stress arising from the thermite welding process and stress relaxation under cyclic fatigue bend load. Thermal elastoplastic and thermomechanical analysis were performed using FE techniques to evaluate the temperature evolution and residual stress field arising from the rail thermite welding process. The FE results were compared with experimental measurement and an accurate prediction has been achieved.

The effect of the welding process parameters such as preheating time on the residual stress field was also investigated. The 3D residual stress relaxation model was built taking into account the initial residual stress state and the cyclic hardening behaviors of the material. It shows that the stabilization of residual stress occurs after the first cycle. An analytical model was proposed to predict the stress relaxation and it revealed that the extent of residual stress relaxation is affected by the material properties, initial residual stress, applied stress amplitude, and the number of cycles. Further discussion about the influence of residual stress and its relaxation on the fatigue life of thermite welded joint is needed.

Chapter 5 Structural Fatigue Behaviour of Welded Joint

This work describes a methodology to investigate the structural fatigue crack growth behaviour of observed transverse surface cracks in rail steel and thermite weld subjected to in-plane and out-of-plane loading. Stress intensity factors (SIFs) solutions were derived from the finite element model analysis for transverse surface cracks located at five different crack initiation locations in the cross-section of rail steel and thermite weld. The SIFs were presented by the conventional geometry factor Y and weld magnification factor M_k solutions for rail steel and thermite weld. Results are further curve-fitted into a simple closed-form solution easily used for fatigue or fracture analysis. Fracture toughness and fatigue crack growth rate tests were conducted to determine the mechanical properties of thermite weld materials and are compared with reported data for rail steels (R260 and R350HT. The methodology can be used to study the fatigue crack propagation of a surface crack at the thermite welded rail joint using linear elastic fracture mechanics.

5.1 Problem specification

Rail steels are susceptible to fatigue failures resulting in rail breaks that can lead to unplanned downtime and safety concerns in railway operations [1-6]. Despite improvements in rail steel maintenance and non-destructive inspections [7], structural fatigue research to assess the integrity of continuously welded railway steel structures is still a necessity in understanding rail break failures. Fatigue crack growth assessments of cracks in rail steel and thermite weld structures require comprehensive stress intensity factor (SIF) solutions for surface crack geometries and fatigue crack growth rate test data for rail steel and thermite weld materials.

Rail defects are classified by the plane of the crack surface and its specific location at rail head, head-to-web, web-to-base, base bottom or corner regions [34]. In the cross-section, the cracks are observed to arise from different stress concentration sites and propagate in the transverse plane

leading to final fracture [9]. The majority of past railway service transverse rail failures occurred in the head-to-web (28%), web-to-base (30%) and base (include base corner, 30%) [27, 32] indicating that fatigue crack propagation analysis and life prediction of such failures are of great interest in the railway industry.

The fracture mechanics approach using stress intensity factors has been frequently used to evaluate the severity of the crack geometry, operating conditions and material properties to predict fatigue life, especially in the offshore and aerospace industries with codes such as BS7910 [122] and API 579 [123]. This approach could also be employed in the railway industry. Stress intensity factor related research have been conducted for rail rolling contact fatigue problems arising from squat defects [94] or subsurface defects [51]. Glinka et al. concluded that mixed fatigue-tensile crack growth in rails occurred when the stress intensity factor first exceeds fracture toughness [124]. The distributed dislocation technique has been used to model 2D propagation of internal vertical split head defects caused by contact loading [125]. Crack propagation of longitudinal flaws initiated from a weld under rolling contact has been studied by finite element method and testing approaches [49]. The effects of residual stress and thermal stresses on fatigue crack growth in flash-butt welding were studied [126]. However, stress intensity factor solutions that can be easily employed for fatigue crack propagation study in rails is still lacking.

The objective of this chapter is to develop a structural methodology to investigate the fatigue behaviour of rail steel and thermite weldment subjected to in-plane and out-of-plane loading conditions. In the application of fatigue growth life prediction using fracture mechanics, there are three sets of value to be determined: SIF, critical fracture toughness, and material constant C and m. The fatigue failures will occur once the SIF at a crack front reaches the critical value of SIF, the critical fracture toughness. In this Chapter, the solution of SIF, which accounts for the magnitude of cyclic stress, pre-existing crack size and weld joint details geometries, is determined from FE modelling. The SIF solutions for rail steel with UIC60E2 profile and thermite welded

joints subjected to in-plane and out-of-plane loading conditions are studied. The solutions are evaluated from FEM in terms of geometry factor Y and weld magnification factor M_k for cracks ranging from a surface crack (depth of 0.1 mm) to final fracture (depth of 25.0 mm). The material constants C and m of Paris' Law were obtained from experimental fracture and fatigue crack growth test data. The developed stress intensity factor solution, combined with the tested fracture and fatigue parameters, can be used for fatigue crack propagation life prediction in the next chapter.

5.2 SIF solutions of thermite welded rail joint

5.2.1 FEM for SIF solutions

The SIFs for different surface crack locations and sizes were derived from FEM of rail steel and thermite weld segments shown in Figure 5-1 and Figure 5-2. The resulting SIF solutions were presented as a geometric factor Y and weld magnification factors M_k. The geometric factor, Y, accounts for the effect of geometry to the SIF solution along the crack front while the weld magnification factor [127, 128], M_k, accounts for the weld's effect on the SIF solution in weld toe cracks [128].

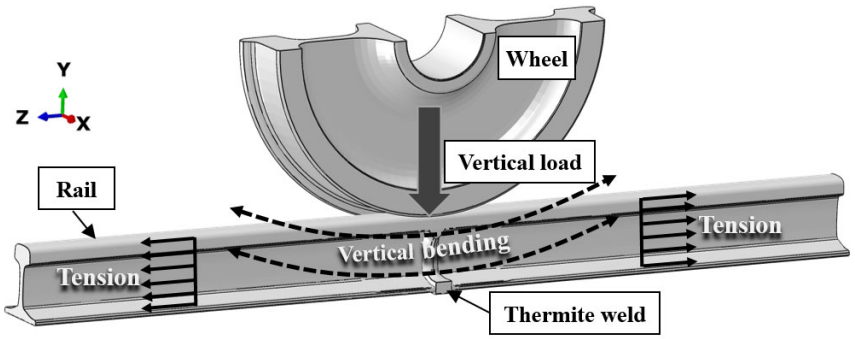

(a) In-plane loading condition

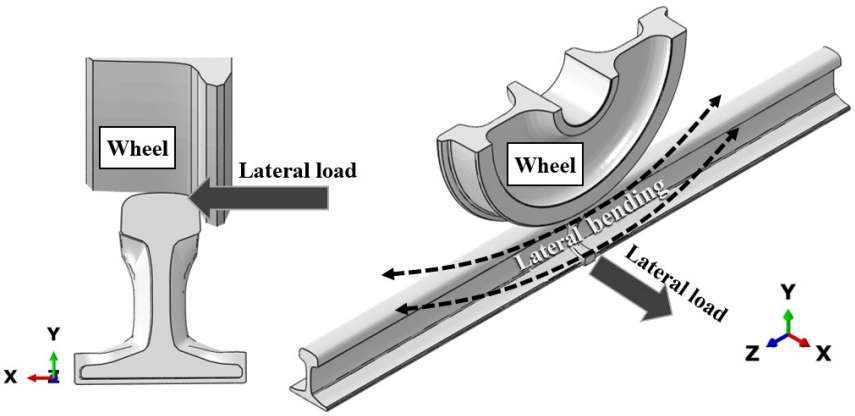

(b) Out-of-plane loading condition

Figure 5-1: Loading conditions used in FEM

In this study, in-plane and out-of-plane stresses were investigated to observe their contribution to fatigue propagation of transverse cracks in rail and thermite weld sections. The in-plane loading was modeled as vertical bending moment (Mx) and uniformly distributed tensile stress (Nz) as shown in Figure 5-1a while the out-of-plane loading was modeled as lateral bending (My) shown in Figure 5-1b. These loadings were simulated separately for cracks in different locations, where σx, σz, and σy represented the corresponding stress for each loading condition. Orringer et al.[118] noted that the rail and welded joints are subjected to a wave-like deformation due to the dynamic contact interaction between the wheel and rail. It was shown that both the rail head region and base region were subjected to cyclic in-plane tension and compression stress causing fatigue loading. In these models, a vertical bending was applied for the rail base cracks while a reverse bending was applied for the head cracks.

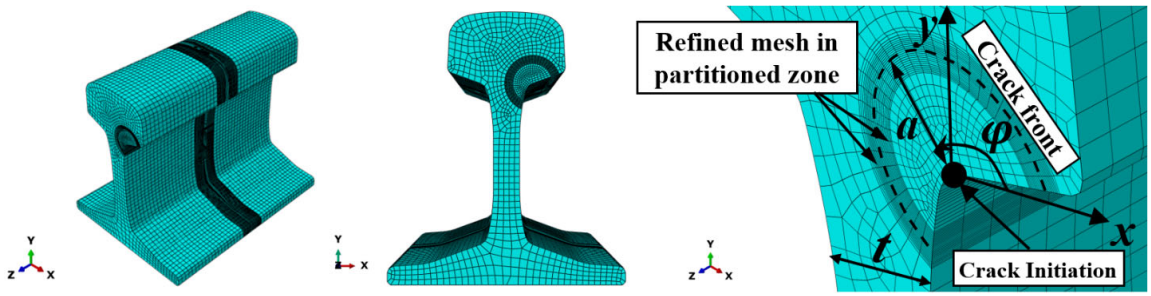

(a) head-to-web crack and mesh details

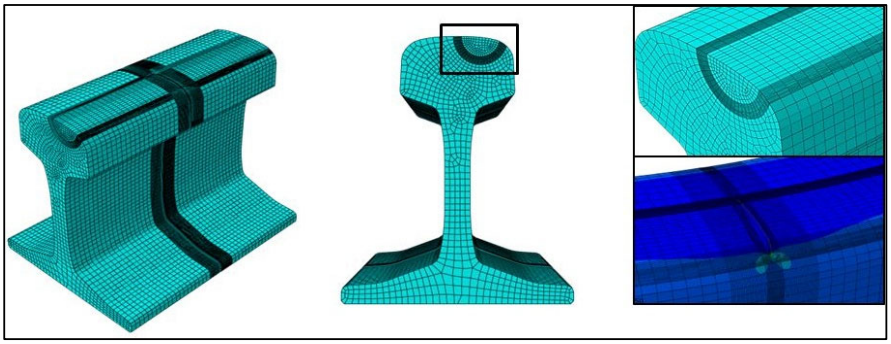

(b) head crack with offset of 15 mm

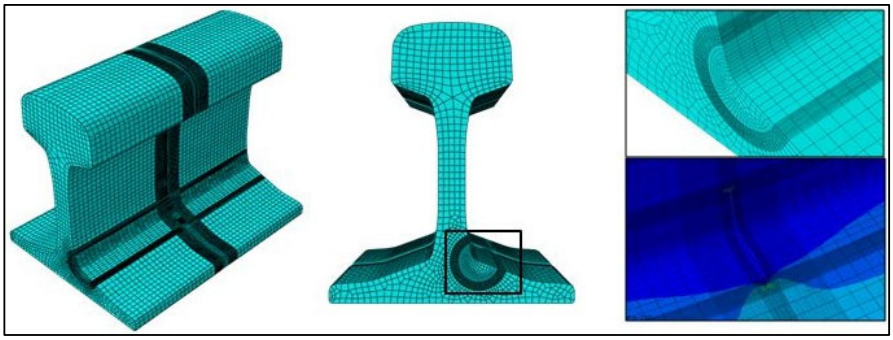

(c) web-to-base crack

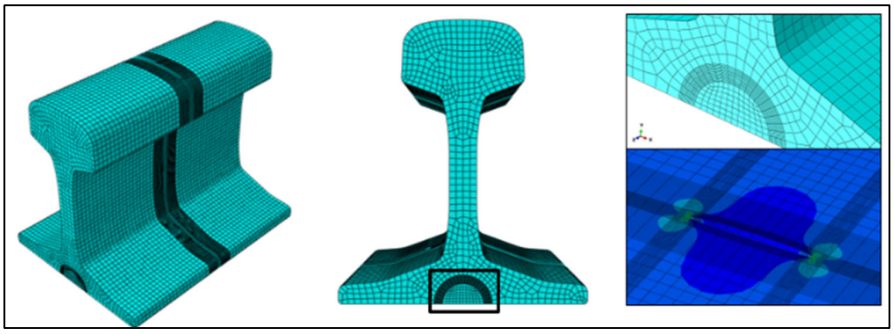

(d) base bottom crack

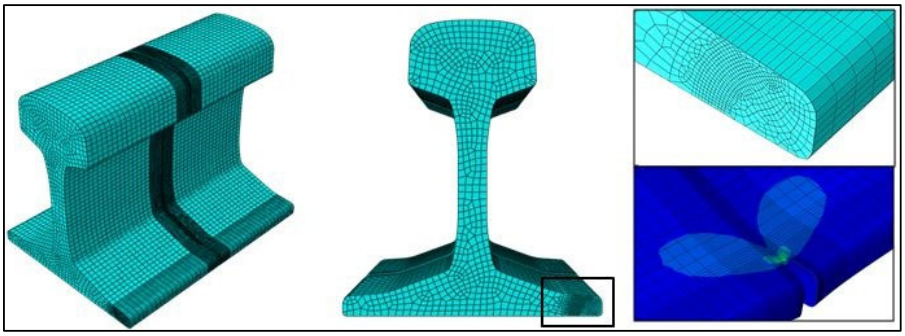

(e) base corner crack

Figure 5-2: FEMs for five different crack locations

A rail section with length of 200 mm was modeled using a Python script written to ease input file generation of parameters determined by crack position, crack geometry and load conditions. The global model and detailed mesh are shown in Figure 5-2. The loading was applied in the center point of one end with coupling constraint while the other end of rail was applied boundary conditions $U_x = U_y = U_z = UR_z = 0$ so as to prevent rigid body motion with coordinate system following Figure 5-2a. U_x, U_y and U_z refers to the displacement in x, y and z direction and UR_z is the rotation about the z-axis in accordance with the definition in ABAQUS software. The cracks were modeled starting from 0.1 mm, propagating to final fracture crack size. The final crack sizes were set to be 25 mm for cracks in the head (Figure 5-2b), base bottom (Figure 5-2d), base corner of field side (Figure 5-2e) and 20 mm for cracks in the head-to-web (Figure 5-2a), web-to-base (Figure 5-2c).

Meshing the finite element model required regions near the crack to be of finer mesh, while regions away from the crack were progressively coarser. The mesh partitions were designed to follow the crack front shape (concentric circles for this case) with finer mesh near the crack and progressively coarser when it goes far from crack front. Based on mesh sensitivity studies, 20 elements surrounding the crack were needed since at least 10 contours are requested for output in all directions. At least 40 elements along the crack front were required to obtain the distribution of SIF solutions. The sizes of these elements were adjusted accordingly to prevent any huge distortion in the elements. For transverse cracks at the head of the rail, the cracks did not always initiate at the center of the head, instead it deviated and started from the side. An offset distance of 15 mm from the centerline of the rail head as shown in Figure 5-2b was used in this study. The mode I SIFs were calculated using the contour integral from elements forming the ring contour around the crack front. A focused mesh of 20 elements surrounding the crack front was used to form the ring. Contour integral value of SIFs from the 4th to the 8th contours were averaged to obtain stable results.

The service loading condition considered will result in a combination of mode I crack opening and sliding due to shear stress (modes II and III) [62]. Since the propagation process of rail transverse cracks is mainly in the transverse plane normal to the loading direction, mode I failures has the most significant impact in the development of these transverse cracks and the mode I SIF can be simplified as

$$K_I = Y\sigma\sqrt{\pi a} = Y(\frac{a}{t}, \varphi)\sigma\sqrt{\pi a} \tag{5-1}$$

where σ is the applied remote stress, Y is the shape factor, a is the crack size and t is equal to width of rail web (16.5 mm). Following Newman and Raju's [98] classical empirical solutions, the shape factor Y was defined as a function of crack size, a and angle, φ. The angle φ starts from the x-axis following an anti-clockwise direction as shown in Figure 5-2a. Since the crack size is restricted by the shape of the transverse profile of rail and the web of rail is the narrowest part of the rail, the width of the web, t, was included with expression of a/t to normalize the crack size, a. To facilitate the analysis in the fitting process, the angle was normalized as:

$$\phi = (\varphi - \varphi_{\min})/(\varphi_{\max} - \varphi_{\min}) \tag{5-2}$$

To study the effect of the thermite weld segment on the SIF solution, a three-dimensional profile of a thermite welded joint from service was obtained using a portable laser scanner Handyscan 307 and the thermite weld geometry was built on top of the model for rail steel. Thermite weld models with a small semi-circular crack in the head-to-web region will be discussed in the section. Similar in-plane and out-of-plane loading, and boundary condition were used as in the rail steel models. Two different distances of the surface crack from the weld toe: 0.1 mm and 0.5 mm were modeled and calculated. The effect of weld to the SIF, M_k, is expressed as:

$$M_k = \frac{K_{(\text{welded rail})}}{K_{(\text{rail steel})}} \tag{5-3}$$

The SIF and M_k solutions will be discussed the next section.

5.2.2 SIF Solution

SIF Solution of Geometry Factor Y

Three loading types, vertical bending Mx, lateral bending My, and uniformly distributed tensile stress Nz, were applied in the FEM for cracks in each location. The geometry factor Y was then calculated using formula below:

$$Y = \frac{K_{(\mathrm{FEM})}}{\sigma\sqrt{\pi a}} \tag{5-4}$$

where $K_{(FEM)}$ refers to the SIF value calculated from FEM result.

The geometry factor Y of cracks at five different locations under three different loading conditions were plotted in terms of crack size and crack front angle in Figures 5-3~5-5. In these figures, different colors represented different crack sizes, ranging from 0.1 mm to 20 or 25 mm. Since the crack at the base bottom location is at the centerline of the rail, which is on the neutral axis of lateral bending in the transverse profile, σy resulting from lateral bending My is trivial and omitted.

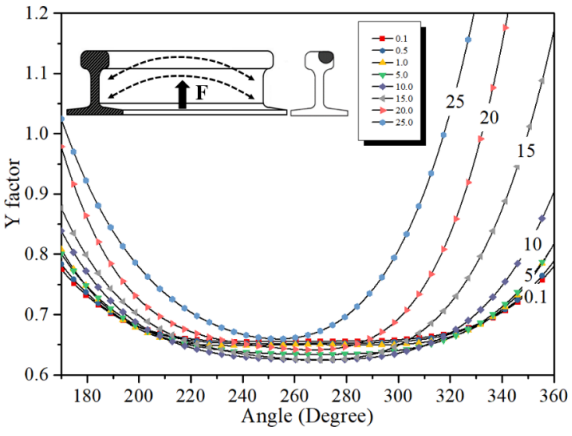

(a) head crack under vertical bending

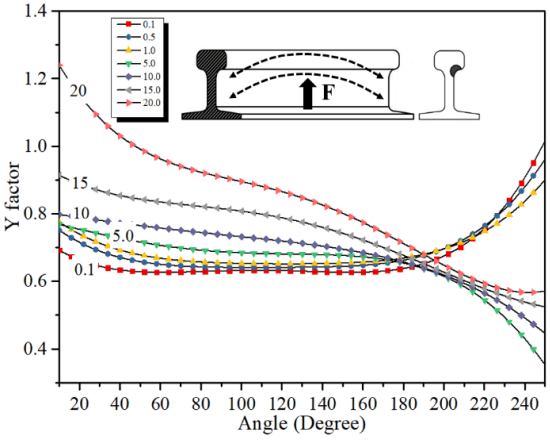

(b) head-to-web crack under vertical bending

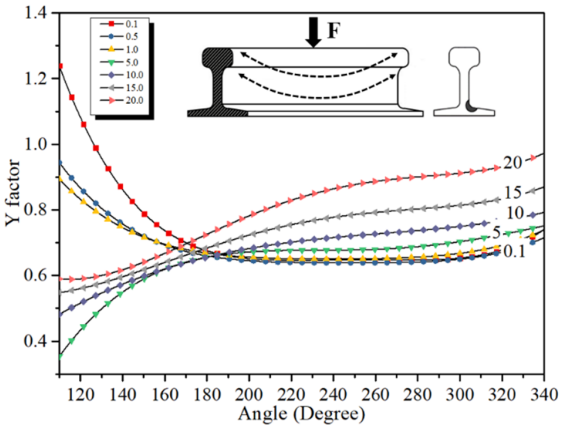

(c) web-to-base crack under vertical bending

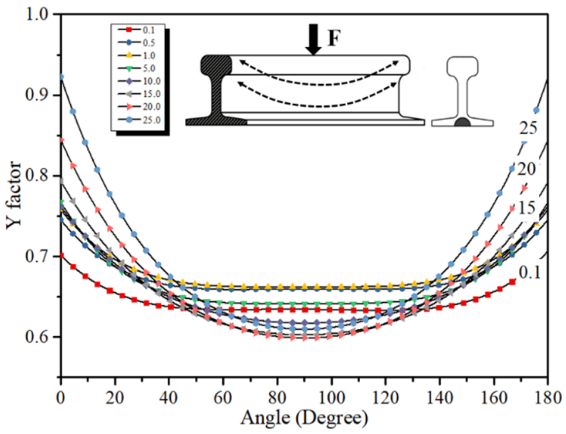

(d) base bottom crack under vertical bending

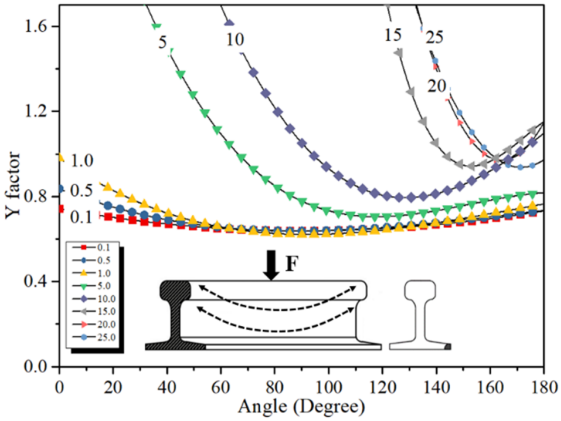

(e) base corner crack under vertical bending

Figure 5-3: Y factor for different locations under vertical bending Mx

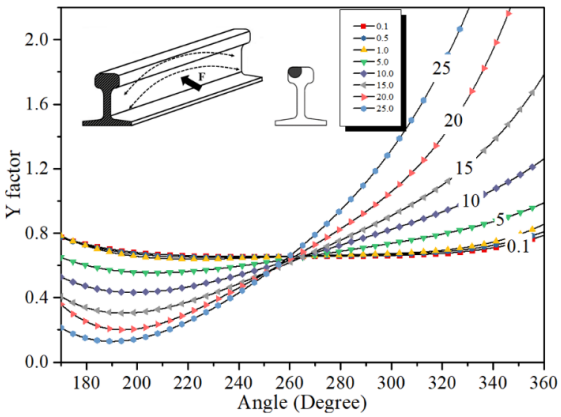

(a) head crack under lateral bending

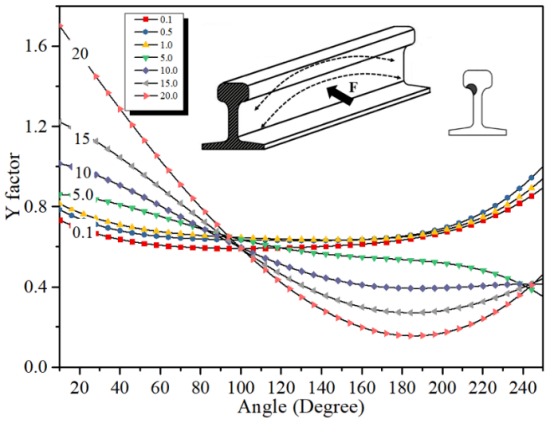

(b) head-to-web crack under lateral bending

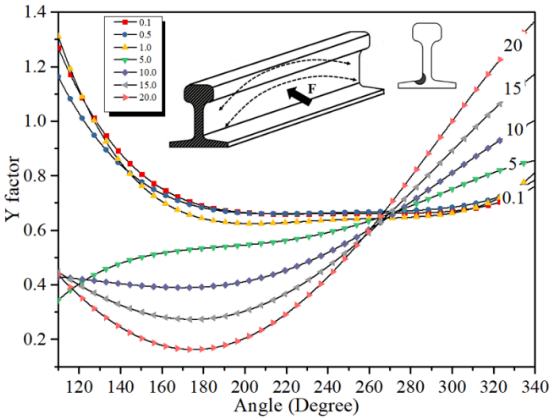

(c) web-to-base crack under lateral bending

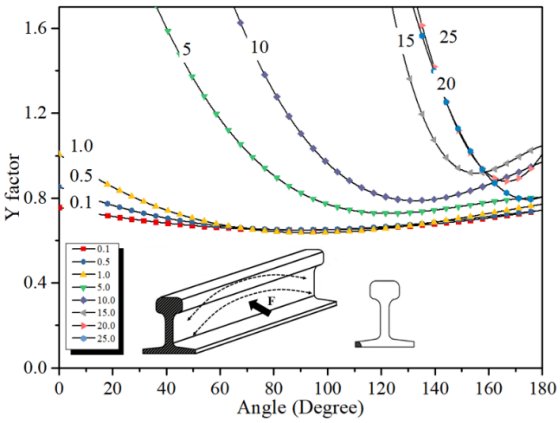

(d) base corner crack under lateral bending

Figure 5-4: Y factor of rail for different locations under lateral bending My

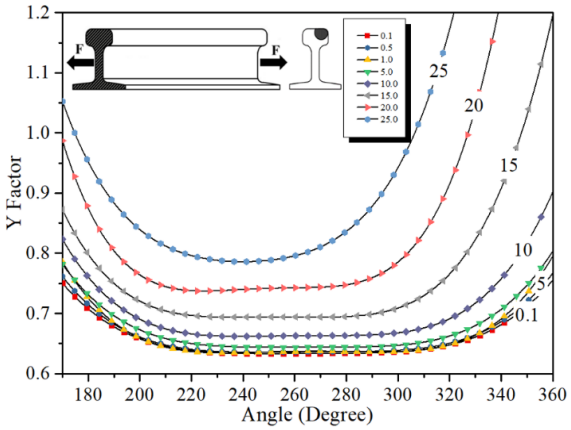

(a) head crack under tension

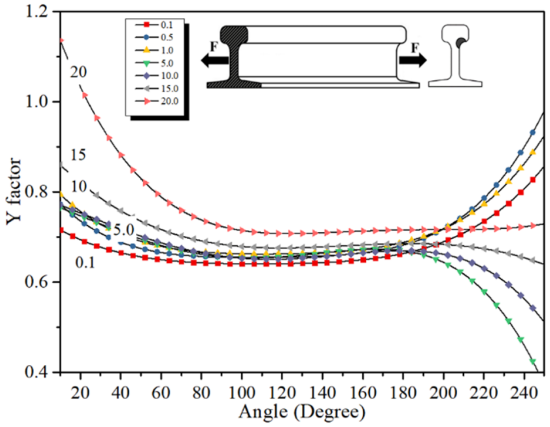

(b) head-to-web crack under tension

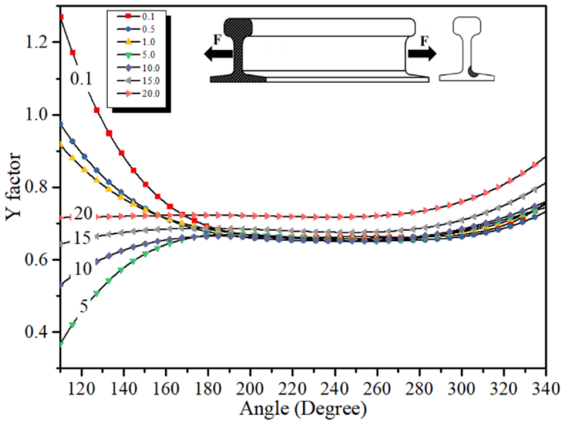

(c) web-to-base crack under tension

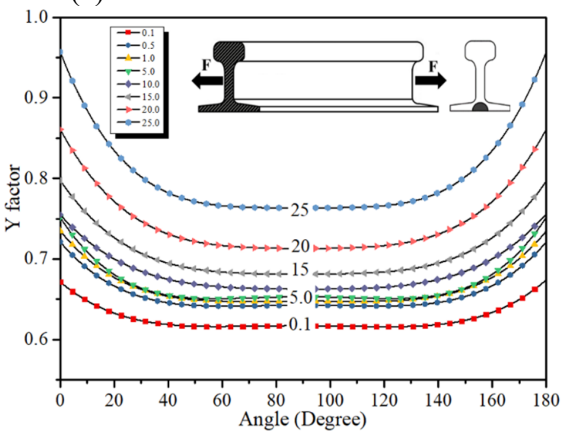

(d) base bottom crack under tension

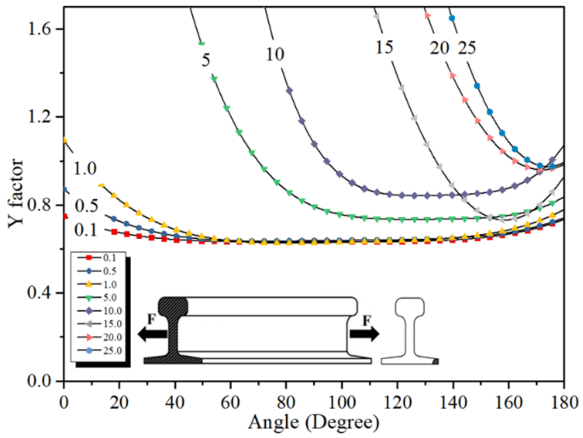

(e) base corner crack under tension

Figure 5-5: Y factor for different locations under uniformly distributed tensile stress N_z

The range in Y factor varies from 0.6 to 1.2 in most cases, but for cracks at head-to-web and base corner locations under lateral bending it extends up to 1.6 when the cracks size grows to 20 mm. At the surface, SIFs are observed to increase with crack size under in-plane and out-of-plane loads. At the rail head and base bottom, the SIFs are symmetric or near symmetric about the centerline under vertical bending and pure tension. For a crack at other locations under vertical bending and tension, the SIFs are asymmetric due to the crack placement which it does not pass through the centerline of the rail cross-section. This asymmetry was observed to be even more obvious for cracks subjected to lateral bending because of the asymmetric loading condition along the crack front regardless of the crack placement.

A nonlinear regression method was used to obtain suitable equations for the Y factor curves. It was accomplished using iterative algorithms to estimate parameters for the equations. An equation with the following form was proposed to fit these curves:

$$Y = \left[\mathrm{p}\left(\frac{a}{t}\right)^{\mathrm{n}}\right]\left\{1 + \left[0.1 + c_1\left(\frac{a}{t}\right)^2 + c_2\left(\frac{a}{t}\right)^3\right][1 - \sin(\phi + \theta)]^2\right\} \quad (5\text{-}5)$$

where $p\left(\frac{a}{t}\right)^n$ was applied to consider the local stress concentration raise by the geometric changes at the weld toe region, $\left[0.1 + c_1\left(\frac{a}{t}\right)^2 + c_2\left(\frac{a}{t}\right)^3\right]$ is the polynomial term to describe the trend of Y

in terms of crack size a; $[1-\sin(\phi+\theta)]^2$ is the trigonometric term to describe the trend of Y in terms of normalized crack angle ϕ.

Table 10: Y factor parameters from FEM analysis results

		Crack Location									
		Head Crack		Head to web crack		Web to base crack		Bottom crack		Base corner crack	
											
		a≤1mm	a>1mm	a≤1mm	a>1mm	a≤1mm	a>1mm	a≤1mm	a>1mm	a≤1mm	a>1mm
Vertical bending M_x	p	.627	.647	.694	.620	.643	.607	.702	.622	.623	.935
	n	-.010	.012	.022	.067	-.002	.080	.020	-.033	-.010	.185
	c_1	109.101	.383	-9.628	-.149	-40.028	-.112	62.854	.266	210.278	1.107
	c_2	-1419.576	-.096	198.206	.159	761.947	.111	-887.681	-.053	-2527.944	-.728
	θ	-.004	.118	-.051	-1.909	.075	2.240	.004	-	-.079	-.171
Lateral bending M_y	p	.636	.349	.693	.281	.610	.292	-	-	.641	.870
	n	-.008	-.402	.027	-.553	-.018	-.500	-	-	-.008	.101
	c_1	94.783	1.049	52.387	1.196	137.842	1.230	-	-	196.383	1.146
	c_2	-1167.520	-.336	-676.227	-.258	-1928.465	-.456	-	-	-2314.304	-.748
	θ	.119	1.341	-.169	-1.082	.137	1.184	-	-	-.100	-.322
Tension N_z	p	.622	.720	.697	.686	.646	.689	.692	.711	.618	.906
	n	-.005	.107	.017	.060	-.006	.074	.024	.085	-.007	.162
	c_1	102.740	.068	11.706	-.332	-18.361	-.240	44.328	-.094	195.961	.248
	c_2	-1348.908	.076	-106.053	.340	445.720	.201	-622.502	.121	-2320.040	-.124
	θ	-.002	.214	-.045	-.435	.054	.554	.002	-	-.082	-.477

The trend of geometry factors Y was observed to be different for crack size smaller and larger than 1 mm. This could be due to the surrounding geometry conditions on the stress field when the crack size increases to more than 1 mm. Therefore, curve fitting of Equation (5-5) to the geometry factors Y obtained from the FEM result was conducted and the value of each parameter is shown

in Table 10. The R^2, the coefficient of determination, is the statistical measure of how good the regression prediction approximate the input dataset. It ranges from 0 to 1 and a higher value indicates a better approximation. A value of R^2 of more than 0.9 of all curves fitted result was obtained, showing a good representation of the proposed equation fitted to FEM results.

Solution of Weld Magnification Factor M_k

The weld magnification factor M_k factor for transverse weld toe cracks located at head-to-web and web-to-base transition regions with crack depth from 0.1 mm to 10 mm is shown in Figure 5-6 & 7. Two different distance of the surface crack from the weld toe: 0.1 mm and 0.5 mm were investigated. It was found that the M_k factor decreases as the crack size increases and it converge to 1.0 when the crack size reach 10 mm in depth. It was noted that the weld magnification factor M_k is independent of loading conditions but it is various at different crack front locations. Comparing across different locations of weld toe cracks, the M_k factors are higher when the crack is closer to the weld toe due to the stress concentration effects of the weld toe region. Based on these results, the M_k factors calculated from FEM results could be fitted as:

$$M_k = p_k \left(\frac{a}{t}\right)^{n_k} \quad \text{when } 0.1 \text{ mm} \leq a \leq 10 \text{ mm} \tag{5-6}$$

Where the value of coefficients p_k and n_k can be obtained from the regression analysis of the finite element results. The results of these coefficients of cracks, either located at head-to-web region and web-to-base region, are presented in the depth direction and width direction as shown in Figure 5-7. The determination of the curve fitting, R^2 is more than 0.9 for all cases, which indicates good fitting between the calculated result and fitted regression line.

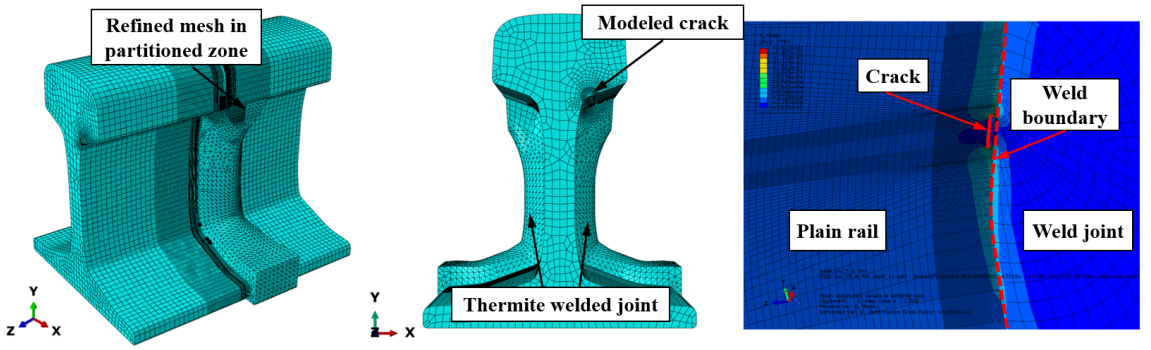

(a)

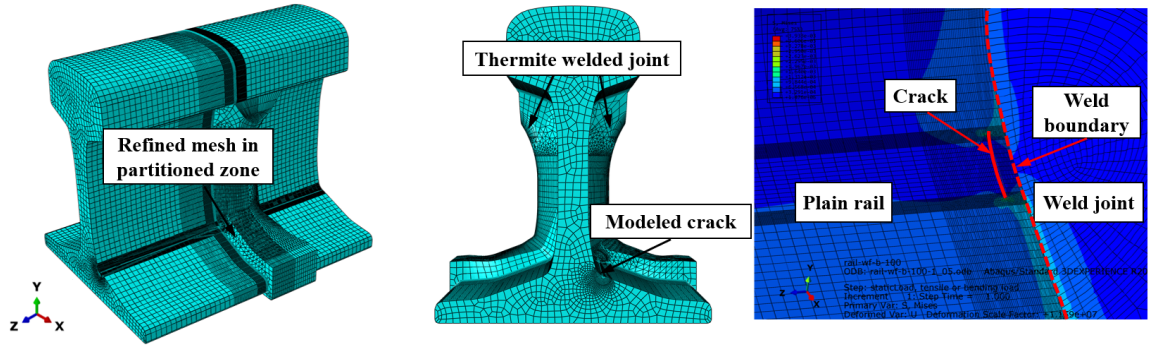

(b)

Figure 5-6: Global FE model and detailed mesh of surface crack at weld toe regions of (a) head-to-web location, and (b) web-to-base location

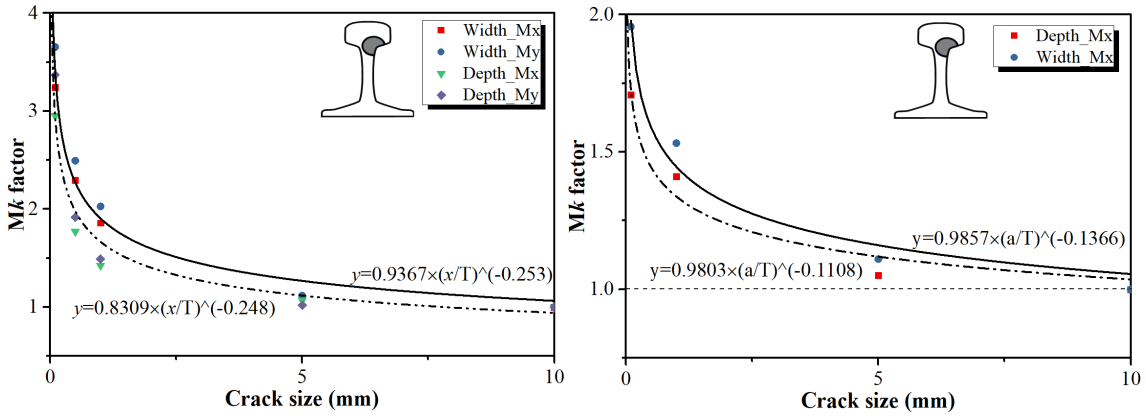

Crack located 0.1 mm from weld toe Crack located 0.5 mm from weld toe

(a) head-to-web weld toe cracks

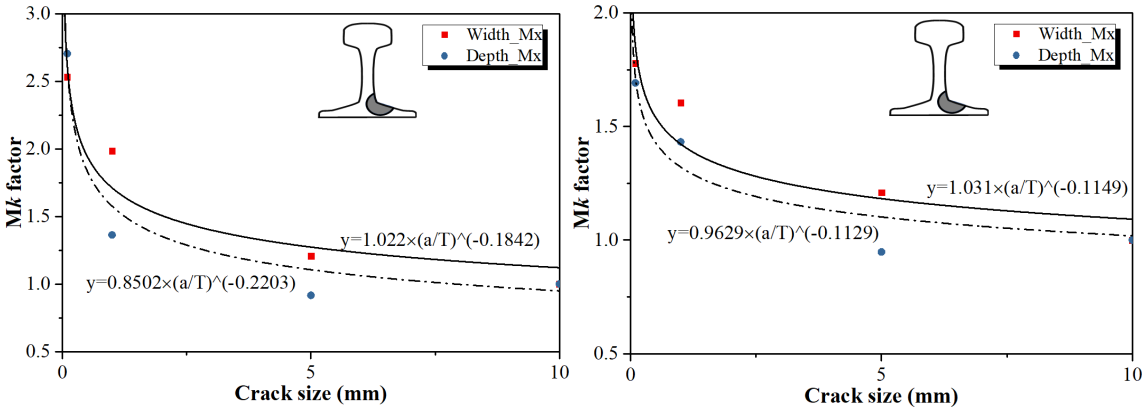

Crack located 0.1 mm from weld toe Crack located 0.5 mm from weld toe

(b) Web-to-base weld toe cracks

Figure 5-7: FEMs and results for M_k factor

Table 11: M_k factor parameters from FEM analysis results

Crack location		Head to web crack		Web to base crack	
					
Distance to weld toe		0.1 mm	0.5 mm	0.1 mm	0.5 mm
Depth direction	p_k	0.8309	0.9803	0.8502	0.9629
	n_k	-0.248	-0.1108	-0.2203	-0.1129
	R^2	0.9406	0.97	0.9401	0.9139
Width direction	p_k	0.9367	0.9857	1.022	1.031
	n_k	-0.253	-0.1366	-0.1842	-0.1149
	R^2	0.9799	0.9805	0.9517	0.9160

5.3 Fracture and fatigue properties

5.3.1 Testing set-ups

Specimens were machined from the thermite weld metal and parent rail metal for tension test, Charpy test, and fatigue crack growth rate (FCGR) test as shown in Figure 5-8a & b. The tension test specimen was extracted longitudinally from the parent rail metal (three pieces) and thermite weld metal (three pieces) respectively. The weld tension specimen consists entirely thermite weld metal in the reduced gauge length as shown in Figure 5-9a. Tensile test was performed in accordance to ASTM A370 [129]. Charpy V-notch test was performed for weld metal and the

dimensions of the specimen were $50 \times 10 \times 10$ mm with a V-notch of 2 mm at a 45 degrees angle and a 0.25mm radius along the base. The test was carried out in accordance to ISO 148-1 (2016) [130].Compact tension specimens were machined from the thermite weld metal longitudinally for determination of the fatigue crack growth rate. The notch was centered in the weld zone to investigate the crack growth in the transverse plane of the welded joints as shown in Figure 5-9c. The fatigue crack growth rate were determined according to ASTM E647[131].

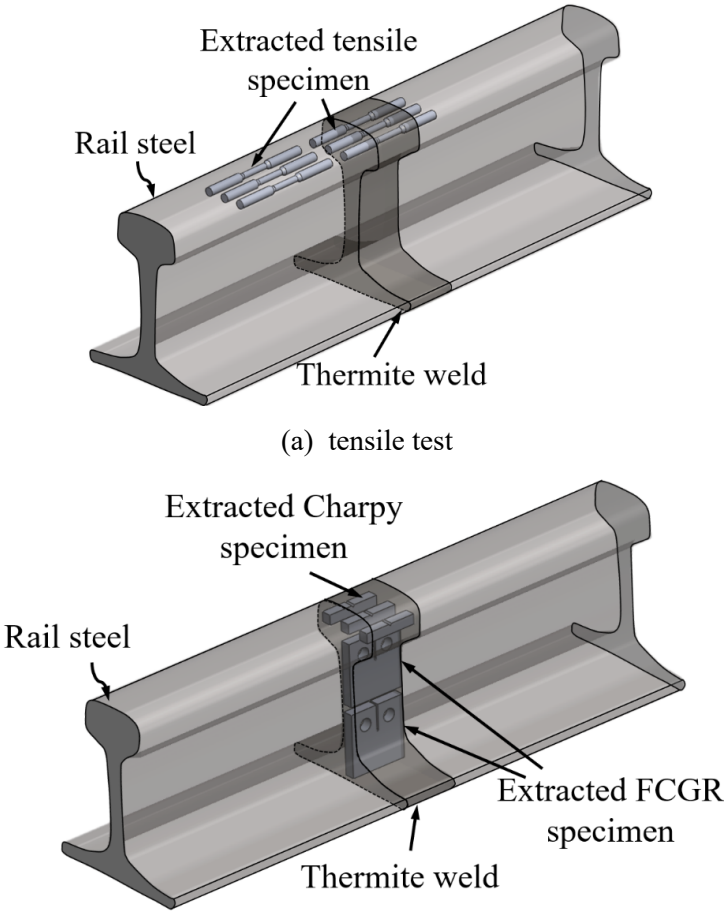

(a) tensile test

(b) Charpy and CT test

Figure 5-8: Schematic illustration of extraction plan

Vickers microhardness measurement was performed longitudinally across the thermite welded joint and the measured surface was 3-5 mm below the running head. The hardness was measured bilaterally along the weld and up to 20 mm into the uninfluenced rail parent material at intervals

of 2 mm. Nanoindentation tests were performed using a Berkovich diamond pyramid tip to obtain the mechanical properties of the thermite weld and HAZ such as hardness and Young's modulus in nanoscale. The measured points were selected on the different locations along the weld zone. For each location, 10 indentation points were measured, and the values were averaged.

In this chapter the fabrication steps and proposed designs for characterizing fatigue performance of rail and welded joints will be described. Crack Tip Opening Displacement (CTOD), fatigue crack growth rate (FCGR), tensile test, and Charpy test have been done to obtain the fracture toughness and fatigue growth rate of rail and welded joints. The fracture and fatigue test results will be discussed and compared with references.

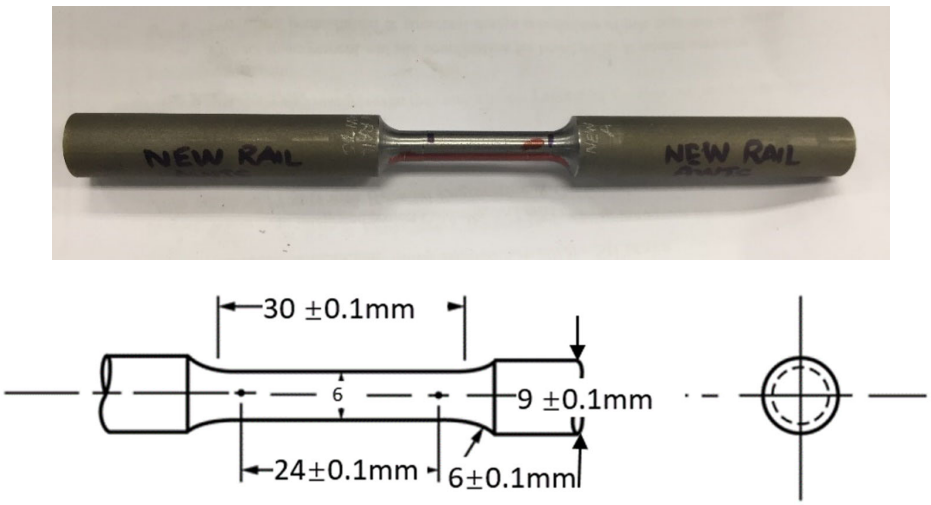

(a) Tension specimen

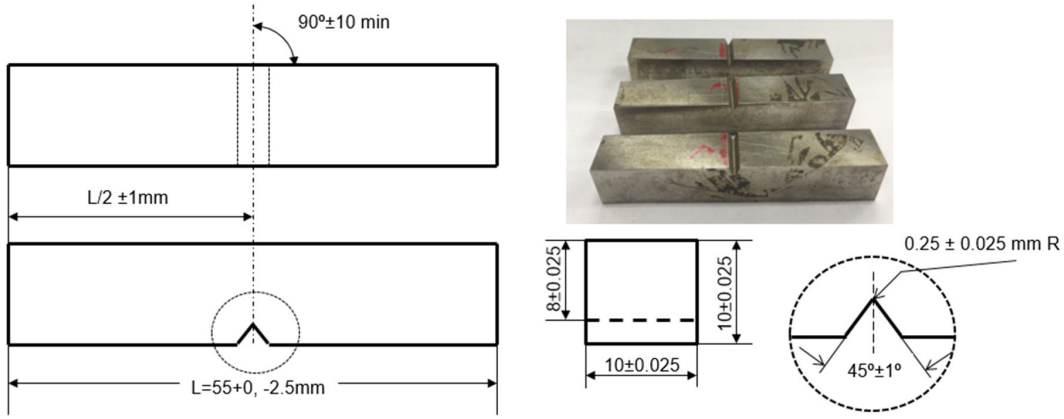

(b) Charpy Specimen

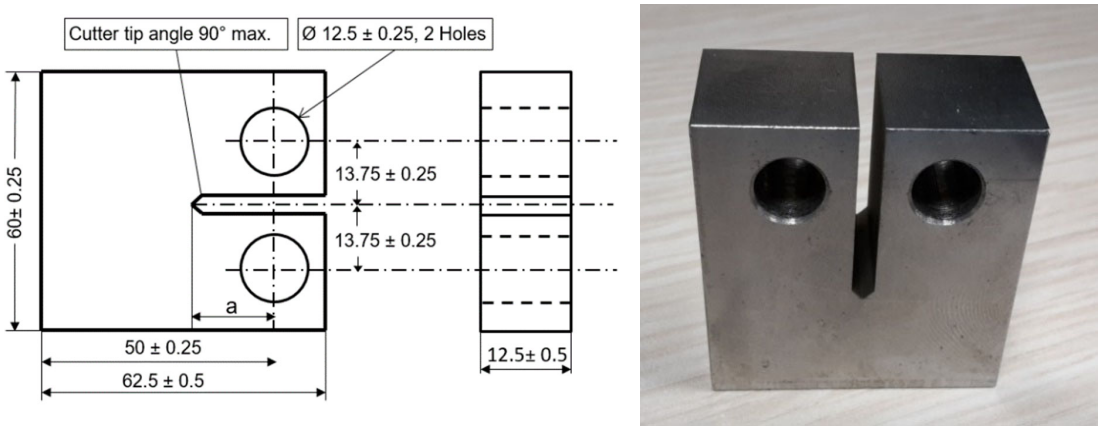

(c) Compact tension specimen

Figure 5-9: Detailed dimension of tested specimen

5.3.2 Experiments results

Tensile test

Tensile test was performed in accordance to ASTM A370 to determine the 0.2% offset yield strength and ultimate tensile stress of the thermite weldment as shown in Figure 5-10. Upon the addition of the parallel line, the 0.2% offset yield strength, σ_{ys}, of the weld was determined to be 720MPa. The presence of weld defects may cause the reduction of the strength and toughness of thermite weld metal. Firstly, the largely distributed defects decrease the cross-sectional area of the metal which is proportional to the strength and ductility of the weld. Furthermore, stresses are concentrated around the defects, particularly defects with abnormal geometries. The quantitative

investigation of the effect of the weld defects on the weld metal strength and ductility will be conducted in the next Chapter.

Table 12: Mechanical properties of parent rail R260 and thermite weld material

Specimen	Tensile test result						Charpy test result (Joule)
	Diameter (mm)	Gauge length (mm)	Elongation (%)	Reduction in area (%)	Yield strength (MPa)	Ultimate tensile strength (MPa)	
Thermite Weld	6.18	25	0.6	1	720 ($R_{p0.2}$)	758	2
Parent rail	4.02	16	10	15	534	986	10 [25]

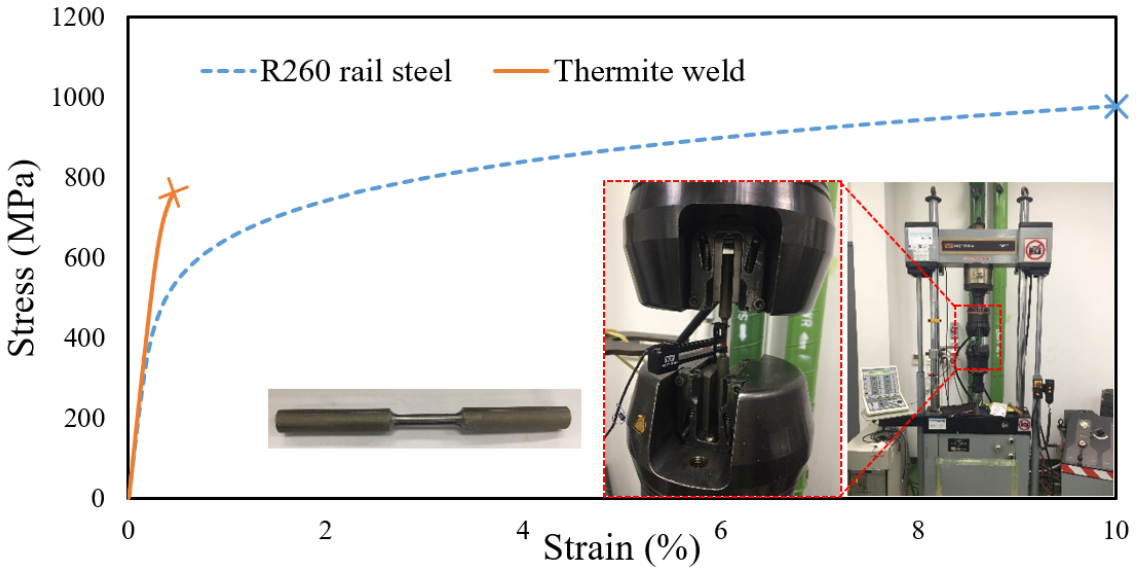

Figure 5-10: True stress-strain curve of thermite weldment and R260 rail steel

The mechanical variation across the welded joint is generally correlated with strength mismatch between the weldment and the parent metal. The mismatch of strength in terms of yield and ultimate tensile strength, as well as the hardness was found from the experimental investigations. In order to quantify the strength mismatch, the ratio of the yield strengths between the weld metal and parent metal is used as [132]:

$$M = \sigma_{YW}/\sigma_{YB} \tag{5-7}$$

where σ_{YW} and σ_{YB} is the yield strength of weld metal and parent metal respectively. The tensile test results and the typical stress-strain curve for each material are shown in Table 12 and Figure 5-10, respectively. For thermite weld metal, the 0.2% offset yield point is defined based on the ASTM standard E8/E8M - 16 [129]. A value of M = 1.35 was calculated showing a mismatch of approximately 35% between the weld metal and unaffected parent rail material. Besides the yield strength, the mismatch effect of the plasticity or work hardening properties was also observed from the plastic region of the stress-strain curves. It shows that the weld metal fractured shortly after elastic deformation while rail steel experienced a gradual elastic-plastic deformation until final fracture. Upon the completion of the Charpy impact test, the three test pieces of thermite weld had an average result of 2 Joules of absorbed energy under room temperature of 20 °C. In comparison, the energy for R260 rail is 10 Joules according to previous research [25]. The effects of these mismatches on the fracture and fatigue behaviour will be discussed in the next section.

Charpy Test

A Charpy test was performed in accordance to ISO 148-1 (2016) to determine the impact toughness of the thermite weld as shown in Figure 5-11 and Table 13. Upon the completion of the test, the energy absorbed by the test piece upon impact of the hammer was recorded and calculated. The three test pieces had an average result of 2 Joules of absorbed energy during fracture. In comparison, the energy for R260 rail is 10 Joules and 8 Joules for R350HT [25], which reflects that the weld material was with a lower fracture toughness. It can also be concluded that the impact toughness of R260 is a little bit higher than R350HT.

(a) (b)

Figure 5-11: Charpy test: (a) test machine and setup, (b) fractured specimen

Table 13: Test Results of Charpy Impact Test

Specimen Material	Specimen Dimension (mm)	Testing Temperature	Charpy Test Result (average, Joule)
R260	10×10, 2V	21℃	10
R350HT	10×10, 2V	21℃	8
Thermite Welding	10×10, 2V	20℃	2

Fracture toughness test

The pre-cracking was performed for fracture toughness compact tension specimen at a low enough stress intensity to minimize the plastic zone ahead of the crack. One of fracture toughness compact tension specimen manufactured broke during pre-cracking and the remaining one was used for testing. During the test, crack mouth opening displacement (CMOD) and force data is required to conduct analysis. This data can be taken by the help of a computer data acquisition system. To record the crack mouth opening displacement, a displacement gage is required. Thus, a displacement gage was mounted to the specimen via integral knife edges as shown in Figure 5-12.

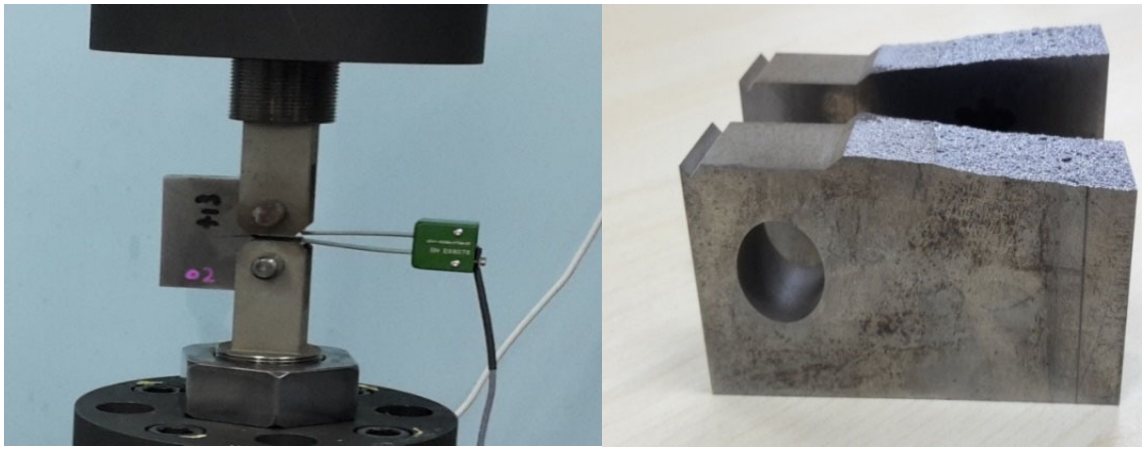

(a) Displacement Gage (b) Fractured Specimen after test

Figure 5-12: CT test set-up

The completion of the compact tension test has led to the plot of crack mouth opening displacement (CMOD) against tensile load shown as Figure 5-13 below. Base on the ASTM E399, P_Q is determined by plotting a line of gradient value 95% of the linear portion of the graph and calculate the load value of the intersection between the line derived and the obtained data. The ratio of P_{max} /P_Q does not exceed 1.10, where P_{max} is the maximum load the specimen sustained, it is able to calculate K_Q from below:

$$K_Q = \frac{P_Q}{B\sqrt{W}} f\left(\frac{a}{W}\right) \tag{5-8}$$

Where the equation for the function of $f\left(\frac{a}{W}\right)$ is as below:

$$f\left(\frac{a}{W}\right) = \frac{\left(2+\frac{a}{W}\right)\left[0.886 + 4.64\frac{a}{W} - 13.32\left(\frac{a}{W}\right)^2 + 14.72\left(\frac{a}{W}\right)^3 - 5.56\left(\frac{a}{W}\right)^4\right]}{\left(1-\frac{a}{W}\right)^{\frac{3}{2}}} \tag{5-9}$$

The calculation of results above would give the value of K_Q and equal to K_{IC}, which is governed by the validity equation in accordance to ASTM standard as below:

$$(W - a) > 2.5\left(\frac{K_Q}{\sigma_{YS}}\right)^2 \tag{5-10}$$

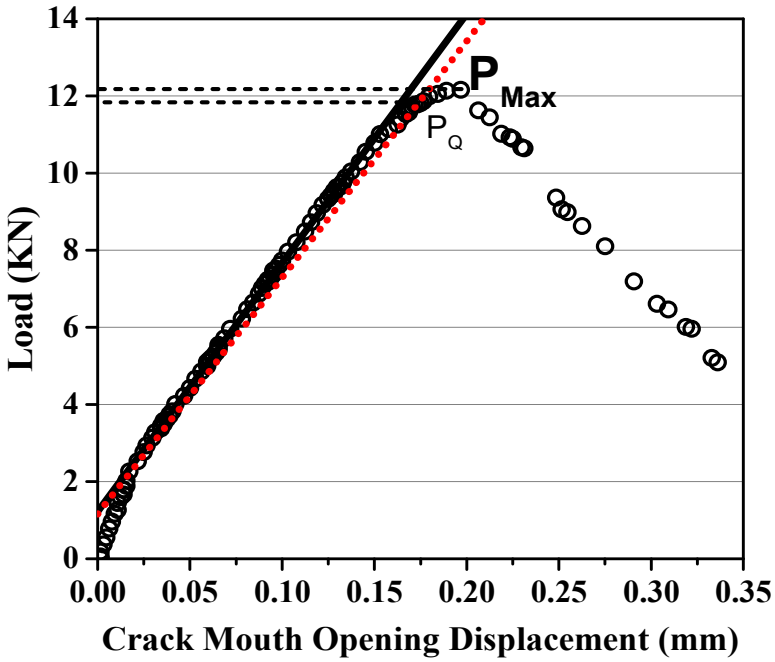

Figure 5-13: Fracture toughness compact tension test result

Table 14: Specimen Dimensions and Calculated Parameters

Sample Location	**Specimen Dimensions after Fractured (mm)**											***Yield Stress N/mm²**	**Max. Load (kN)**	**KIC $MPa\sqrt{m}$**
Web of Weldment	W	B	a1	a2	a3	a4	a5	a6	a7	a8	a9	724.00	12.15	36.05
	50.00	12.50	21.09	21.45	21.87	22.26	22.47	22.73	22.87	22.98	22.93			

* 1. 0.2% proof stress is calculated as yield stress and used for K_{IC} validity check,

2. E = 20700 N/mm2, υ=0.3 and the notch is in the middle of welding

It can be concluded that K_{1C} of the specimen extracted from the web of thermite welding joint is around 36.05 $MPa\sqrt{m}$.The detailed dimensions and calculation results are shown as Table 14**.**

Crack growth rate test

Fatigue crack growth tests [15] were conducted on a servo-hydraulic test machine by applying 10 kN and 1 kN as a maximum and minimum amplitude loads with a frequency of 1 Hz as shown in Figure 5-14. Fatigue crack growth rate curves, (da/dN - ΔK) from the tested specimen was

obtained as Figure 5-15 below. Stress-intensity range was calculated from the following expression below:

$$\Delta K = \frac{\Delta P}{B\sqrt{W}} \frac{2+\alpha}{(1-\alpha)3/2} (0.886+4.64\alpha-13.32\alpha^2+14.72\alpha^3-5.6\alpha^4) \quad (5\text{-}11)$$

where α=a/W= 0.24. Plots of fatigue crack growth rate in terms of applied stress intensity factor, (da/dN versus ΔK), was shown and compared with reported parent rail material (R260) [25]. The two specimens were labeled as FCGR 1 and FCGR 2 and the calculated C and m constants are 2.22E-16 and 7.84 for FCGR 1 and 1.49E-17 and 6.60 for FCGR 2 respectively. The unit of stress intensity factor is MPa$\sqrt{m}$ and the unit of crack growth rate, da/dN is m/cycle. Once the crack starts to propagate, the rate of crack advance is at similar rate for both the weld metal and parent rail steel. However, the propagation rate of weld metal increases more rapidly and it becomes higher than parent metal when the applied stress intensity factor exceeds 20 MPa$\sqrt{m}$. After this, the rates of crack advance in two different materials were observed to diverge and the crack propagation in the weld zone is significantly higher than that of the parent rail metal.

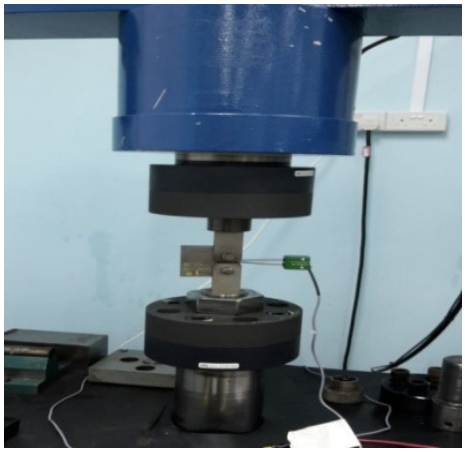

Figure 5-14: Fatigue Test Set-up

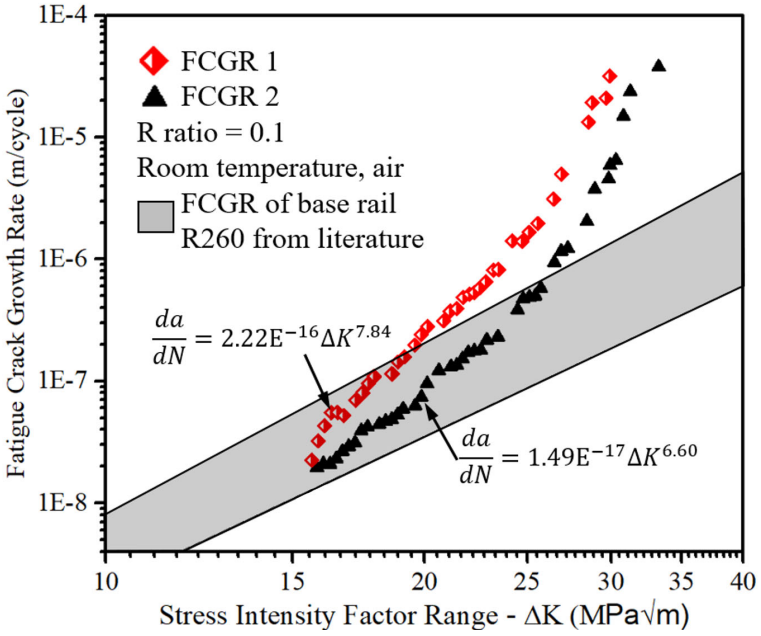

Figure 5-15: Fatigue crack growth rate result measured by compact tension test and comparison with literature data for parent rail [25]

Table 15: FCGR CT test results

Specimen	Final Crack Length a_f (mm)	Result	
		ΔK in MPa$\sqrt{m}$ **da/dN in m/cycle**	**ΔK in N/mm$^{3/2}$** **da/dN in mm/cycle**
Thermite weld A	26.87	$da/dN = 1.49\ E-17\ \Delta K^{7.84}$	$da/dN = 2.58\ E-26\ \Delta K^{7.84}$
Thermite weld B	26.09	$da/dN = 2.22\ E-16\ \Delta K^{6.60}$	$da/dN = 2.82\ E-23\ \Delta K^{6.60}$

5.4 Concluding remarks

This chapter provided a methodology for structural fatigue behaviours of rail steels and thermite welds subjected to in-plane and out-of-plane fatigue loading conditions. A FEM-derived SIF solution of the geometry factor Y and weld magnification factor M_k was presented for transverse surface cracks in rail steels and thermite weld. Two loading conditions including in-plane and out-of-plane loading were studied for cracks located at five different locations of the transverse cross-section. These results provided important closed-form SIF solutions for surface cracks in the cross-

section of rail steels and thermite weld. Experimental tests of fracture toughness and fatigue crack growth rates were conducted on weld metal material extracted from thermite welded joints samples. Thermite weld metal exhibited a lower fracture toughness with mild overmatched yield strength compared to the parent rail metal (R260). The fatigue crack propagation is a result of the competition between crack driving force and fracture toughness. The stress intensity factor, with the solution from the FE simulation and the Paris' Law constants determined from the fatigue crack growth rate test results, is selected as crack driving force for analysis based on the Linear Elastic Fracture Mechanics (LEFM). Further detailed discussion will be provided in the next Chapter.

Chapter 6 Fatigue Cracking Mechanism and Propagation Life Prediction

This chapter investigated the fatigue cracking behaviour of transverse surface cracks in the weld toe region of thermite welded rail joints subject to typical fatigue cyclic load conditions and residual stress resulting from the welding process. The transverse fatigue cracking mechanism at the fusion line is investigated based on the material characteristics across the welded joint. The effect of material imperfections on the fatigue performance of welded joints including the potential crack initiation sites and propagation path is also discussed. The fatigue crack propagation life of the surface cracks at the thermite welded rail joint were predicted using linear elastic fracture mechanics. The coupled root-mean-square integration approach and the weight function method are applied to consider the combined effect of the fatigue cyclic loads and residual stresses.

6.1 Problem specification

Structural fatigue research to assess the integrity of continuously welded railway steel structures is necessary to understand rail break failures. A lot of researches have investigated the fatigue failures related to rail tracks. Li et al. [133] analyzed transverse rail cracks in rails for heavy haul trains and summarized characteristics of transverse failures based on metallurgical and microstructural studies. The thermite welded joint and the adjacent HAZ represent a change in many material characteristics, including hardness, microstructure, and strength, which is easy for fatigue cracks to initiate and propagate [16]. The material characteristics across the thermite weldment joining rail steels and its effect on the fatigue cracking are generally recognized. Nevertheless, the comprehensive material characterizations of thermite welded rail joint and the interpretation of transverse fatigue cracking mechanism due to material inhomogeneity have not been clearly revealed. Besides, the residual stresses play an important role in the structural behaviour of welded joints, especially for their fatigue performance in the presence of cyclic loading. Various studies had been carried out to study the residual stress and its effect on the fatigue life of the thermite welded rail joints. However, a fully integrated fatigue life prediction

model considering the residual stresses resulting from the thermite welding process, as well as the residual stress relaxation behaviour under the cyclic fatigue load is not well developed yet. Furthermore, the current fatigue life calculation methods, without considering the residual stress and its relaxation under the cyclic load, will lead to an inaccurate prediction and therefore are not reliable to meet the service requirement.

In this chapter, the discussion about the transverse fatigue cracking mechanism at the fusion line based on the material characteristics is also performed. The affecting factors of the transverse fatigue cracking at the welded joint are identified and the results are validated with the service failures. The investigation will help to improve the understanding of material imperfections and their effects on the fatigue performance of the thermite welded joints. Furthermore, a structural fatigue life prediction model of thermite welded rail joints taking account of the weld-induced residual stress and stress relaxation by the external cyclic load is developed. This study provides a reliable stress-life based assessment approach for the thermite welded rail joint structures undergoing external cyclic load taking into account residual stresses.

6.2 Fatigue cracking mechanism based on material properties

6.2.1 The effect of material characteristics on mechanical properties

The interlamellar spacing has been shown to be another predominant factor for material mismatch and it is mainly related to the material's strength and hardness. The interlamellar spacing was determined using SEM images by an intercept method with the software Image J. Intercept lines have been etched perpendicular to the lamellae in each pearlite colony to obtain an intensity profile. A well contrasted image enables to differentiate cementite and ferrite lamellae and consequently to calculate the average interlamellar spacing. The average measured interlamellar spacing was shown in Table 16. According to the Hall-Petch equation [134], the yield strength, YS of pearlitic steel was correlated to the interlamellar spacing by:

$$\sigma_y = \sigma_0 + K_y \lambda^{-1} \quad (6\text{-}1)$$

where σ_0 is the friction stress for dislocation to move through the lattice, λ is the interlamellar spacing and K_y is the Hall-Petch slope and. σ_0 used in this study is 205.2 MPa [57] and K_y was expressed as:

$$K_y \approx 3.4 \cdot G \cdot b \quad (6\text{-}2)$$

where G is the ferrite shear modulus and b is the lattice dislocation Burgers vector. G = 8.1×10^4 N/mm2 and b = 2.48×10^{-7}mm. Based on this relation, the yield strength of unaffected parent rail with material of R260 and thermite weld metal was obtained and compared with the results from tensile tests as Table 16. Calculated results show that the yield strength of both R260 rail steel and thermite weld metal correlates well with their interlamellar spacing. A discrepancy of around 7~8% was observed for this calculation.

Table 16: The yield strength prediction using Hall-Petch relation

Material	Interlamellar Spacing λ (nm)	YS from Tensile test (MPa)	YS from Hall-Petch Relation (MPa)	Discrepancy (%)
Thermite weld	148.9 ± 0.2	720	662	8.1%
Rail material (R260)	183.2 ± 0.3	534	576	7.7%

6.2.2 The effect of weld defects on the fatigue limit and crack initiation

Thermite welded joints are susceptible to weld defects resulting from the welding process which can severely affect the fatigue performance. The ability to assess the effects of these defects on fatigue life of weld toe cracks in the thermite weld joint is therefore of practical significance. In order to assess the fatigue performance of each zones across thermite welded joint with respect of weld defects, an investigation into the degradation to the fatigue limit and the stress concentration were performed.

Fatigue limit degradation

The weld defects study of fatigue performance is usually based on the assumption that defects can be treated as effective cracks following Murakami's work [135]. Consequently, besides the applied stress, the range of mode I stress intensity factor was governed by geometrical parameters of weld defects as:

$$\Delta K_I = f \cdot \Delta\sigma_0 \sqrt{\pi\sqrt{area}} \tag{6-3}$$

where, ΔK_I is the mode I stress intensity factor range in MPa$\sqrt{m}$, $\Delta\sigma_0$ is the applied remote stress range resulting from bending loading condition, f = 0.65 for surface defects and 0.5 for internal defects, HV is the Vickers hardness in kgf/mm^2, $\sqrt{area}$ is the square root of the projected area of a defect onto the maximum principal stress plane in μm. Therefore, it is concluded that the size and distribution of the weld defects will significantly affect the toughness of the material.

Accordingly, the critical crack (as a substitute of defect) size was calculated based on formula:

$$\Delta K_{th} = g \cdot (HV + 120)\sqrt{area}_{critical}^{\,1/3} \tag{6-4}$$

where, $g = 3.3 \times 10^{-3}$ for surface defects and 2.77×10^{-3} for internal defects. ΔK_{th} is stress intensity factor threshold for stress ratio $R = -1$ in MPa$\sqrt{m}$, $\sqrt{area}_{critical}$ was considered as critical defect size in μm. Combining Eqn. 6-3 and 6-4, the fatigue limit σ_w for a structure with surface defects was expressed as:

$$\sigma_w = \eta \cdot \frac{(HV + 120)}{\left(\sqrt{area}\right)^{\frac{1}{6}}} \left[\frac{1 - R}{2}\right]^{\alpha} \tag{6-5}$$

where σ_w is the fatigue limit in MPa, η is the coefficient to describe the types of weld defect. The values equal to 1.43 and 1.56 for surface defects, and internal defects respectively. R is the stress ratio and $\alpha = 0.226 + HV \times 10^{-4}$. These equations are limited to physically small defects with size, $\sqrt{area}$, less than 1000 μm. From the value of f, g, η, it reveals that the surface defects are

more detrimental compared with internal defects and therefore only surface defects were discussed in this section.

Based on Eqn. 6-4 to 6-5, the bending fatigue limits of each zones across the thermite welded joint in terms of defect area were estimated as shown in Figure 12. It shows that all materials across the thermite welded joints follow the similar decreasing trend of fatigue limit with the increasing of defect area. However, the fatigue limit of the weld metal is found to be higher than other zones at all different defect sizes. The fusion line, with its narrow range and lower average value of fatigue limit, was observed to be more susceptible for fatigue cracking. Grossoni et al. [136] has obtained the fatigue stress limit for R260 rail steel from testing and the value is 352 MPa under reverse bending. A reliable prediction was achieved compared with the predicted results using Murakami's approach.

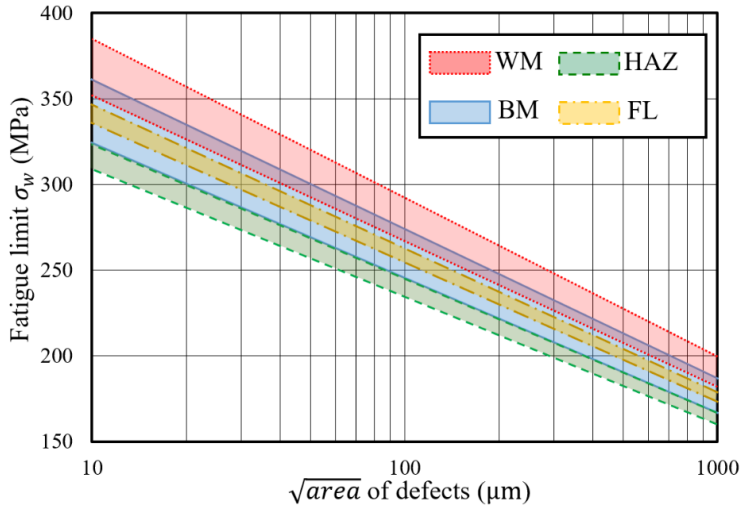

Figure 6-1: Fatigue bending limit of different area in terms of defect size

Local stress concentration arising from weld defects

From the perspective of localized effect of weld defects, these defects can significantly influence the stress field in the vicinity of weld when subjected to cyclic fatigue load. In most cases, weld defects act as potential crack initiation site resulting from the severe stress concentration and further degrade the fatigue life of the welded joints. The state of stress can be influenced by defects

in terms of their shape, position, size and orientation, as well as the pore-inclusion bonding. If physical properties of defects are identical, effects of the size and location of defects determining the stress distribution can be investigated by finite element simulation.

Past researches have investigated the effect of the defect size and location on the local surrounding stress conditions and fatigue initiation life of the structure [137]. In this study, the stress condition around defects with different morphology was investigated by means of FE simulation. The elastic-plastic behaviour of the material was also incorporated to account for the localized plasticity around the inclusions. As illustrated in Figure 6-2, 3D spherical defect with a layer of mesh refinement is modeled in a fatigue testing specimen using Abaqus/CAE 2019 [115]. Geometrical characteristics of the specimens were set up according to the required size from standard E466-15 [129]. The defect type was distinguished by the condition of bonding between the defect and the matrix and three types were considered: perfectly bonded Al_2O_3 inclusion, 90% bonded Al_2O_3 inclusion, and pore without any bonding. The defect, with diameter of D, is located at the cross-section plane cutting through the center of the specimen. The distance to the outer surface is defined as d. In this case, both the defect diameter D and the distance to the surface, d, were set as 50 μm. The inclusions were considered as elastic material with Young's modulus as 390 GPa, Poisson's ratio as 0.2 [138]. The model consists of 48513 elements with 10-node tetrahedron elements (C3D10) for defects and surround mesh refinement and 8-node triangular elements (C3D8R) for the remaining structure. The applied stress was set as 320 MPa, a load with magnitude lower than yield point but enough to cause fatigue initiation.

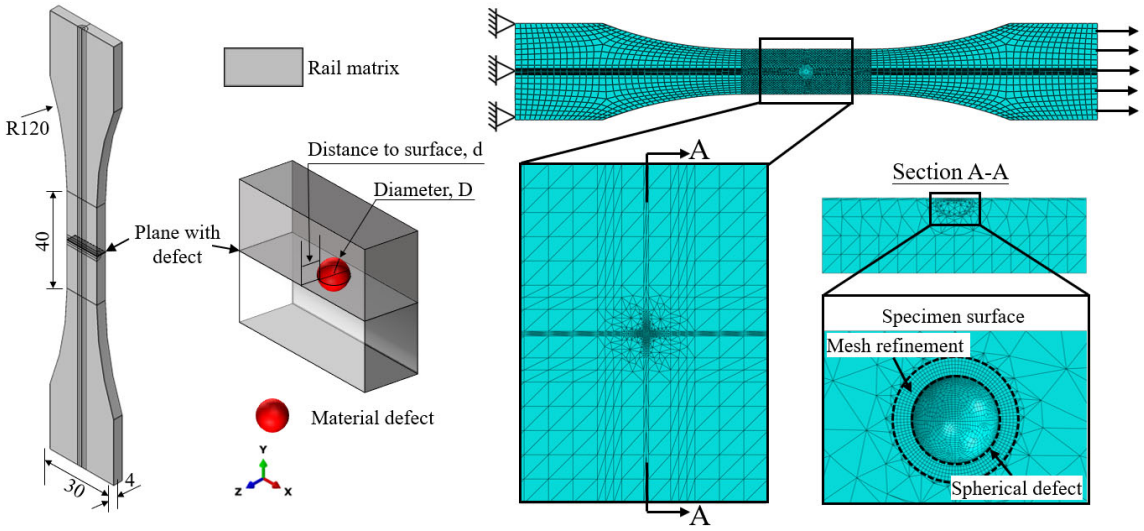

(a) (b)

Figure 6-2: Simulation details: (a) geometrical characteristics (b) global and local mesh

The arising stress concentration factor K_t was calculated as the ratio of the maximum local stress to the applied stress [139] and the results were presented in Figure 6-3. The von Mises stress near the inclusion was selected for calculation to account for the elastic-plastic effect. From the results, it shows that K_t is around 2.08 for the simulated pores and a similar result has been achieved by Sobotka et al. [140]. The fully bonded inclusion has a lowest stress concentration factor and the high stress is constrained in the direction parallel to the outer surface. The stress concentration factor decreased with the bonding between the defect and the matrix. The local stress concentration of partially bonded defect is found to located at the area where the debonding occurs. The pore is the extreme case of the completely debonding that the highest stress concentration was found near the outer surface The current studies in this paper simplified the shape of weld defects as perfectly spherical which is not always the actual case for most structures. The stress concentration arising from the material defect with irregular shape is much higher and thus may lead to more critical concern of fatigue cracking.

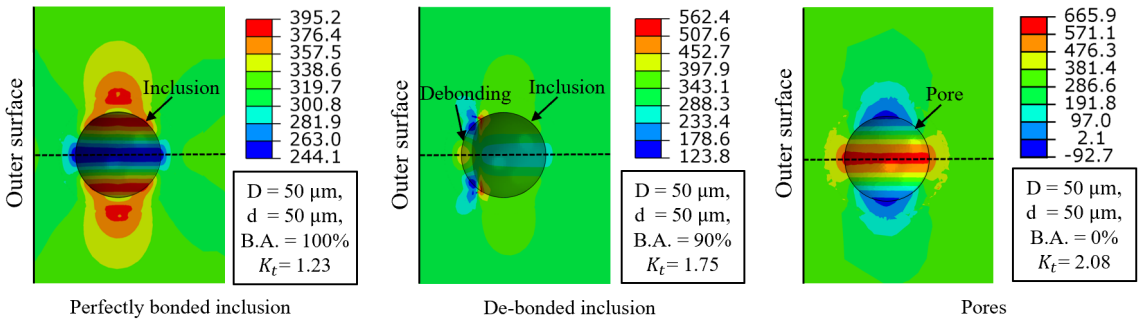

Figure 6-3: Stress distribution around weld defects

6.2.3 Fatigue crack propagation rate and growth path

It should be noted that the strength across the weld may influence the fatigue crack propagation path. Wang et al. [132] concluded that the initial crack locations in the various affected regions of the welded joint have significant effects on the local crack growth resistance and paths. This is mainly related to the strength mismatch or mechanical properties of each affected regions. Local strength mismatch was observed in the different material regions of thermite welded rail joints as shown in Chapter 5. When the sufficiently high load is applied to the inhomogeneous welded joints and weld defects is present, the plastic strain concentration between the defect tips and free surface will be resulted and the fracture resistance and crack growth paths will be affected inevitably. These can be analyzed for the initial cracks located at different positions in the thermite welded joints as shown in Figure 6-4.

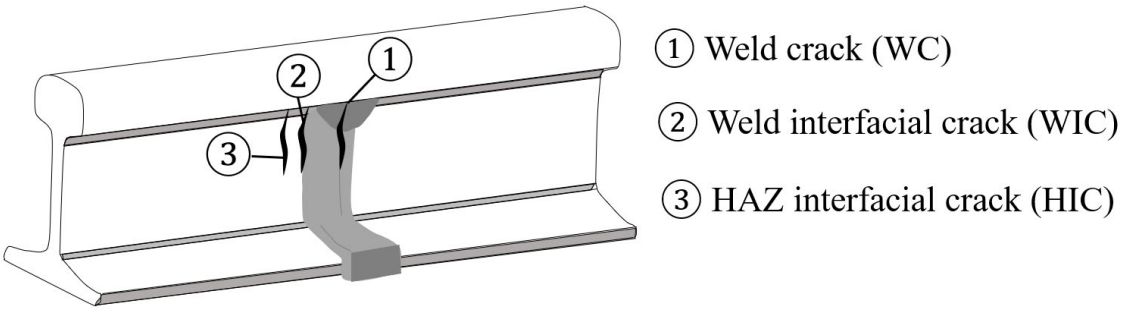

Figure 6-4: Different initial crack location of thermite welded rail joint

(1) Weld cracks (WC): for the cracks initiated from the weld center, since the weldment width is quite large (around 40 mm), the plastic zone is confined within the parent rail steel and crack tip is shield by the weld metal. The effect of strength mismatch has no effect on the fracture resistance and propagation path.

(2) Interfacial cracks (IC): when the cracks located near the interface, either from the weld side or HAZ side, the strength mismatch effects on the local fracture resistance and crack growth paths will be pronounced due to the dramatic variation in local strength. It can be concluded that strength of the HAZ near the interface region is observed to higher than the unaffected parent rail metal but lower than thermite weld metal. During the loading to the crack, the local plastic deformation and high stress triaxiality will predominately occur in the neighboring parent rail metal with lower strength, which promote the fracture process and make crack path deviate towards the parent metal side regardless of its higher toughness.

The analyses described above shows that a moderate strength overmatch is normally beneficial or desirable for thermite weld metal to prevent plastic deformation with its potential defects. However, caution should be taken when it is located near the fusion line of heat affected zone and, in this case, the beneficial effect will be lost, and the interfacial cracks seems to propagate towards parent metal with a shorter growth life.

6.2.4 Fatigue cracking mechanism discussion

The fatigue cracking mechanism of thermite welded joint was investigated and a schematic interpretation of the fatigue cracking process of the transverse weld toe cracks occurred in the rail/weld interface is illustrated in Figure 6-5. The material characteristics investigation of the thermite welded joints shows that the embrittlement of the HAZ near the fusion line and the presence of welding defects are the major factors leading to fatigue crack initiation. When the welded joint is subjected to fatigue loading, a fatigue crack easily initiates at the rail/weld interface

(fusion line) between overmatched thermite weld zone and parent metal due to the high stress concentration in the presence of weld defects, either pores or non-metallic inclusions as shown in Figure 6-5c. The coarse-grain microstructure in the embrittlement zone as shown in Figure 6-5b results in a reduction of crack resistance and further lead to an increase of fatigue crack growth. The variation of yield strength across the welded joints, or the mild strength overmatch, influences the fatigue crack propagation path with accordance to the plastic deformation constraint at the rail/weld interface. The growth path of a crack initiated near the fusion line or interface advances towards the parent rail and away from the rail/weld interface due to the lower strength and the presence of local plastic deformation. The crack then further propagates along the direction of maximum shear stress in the parent rail and turn into fast fracture once reached the critical fracture toughness as shown in Figure 6-5a. The predicted fatigue cracking path was validated by Figure 6-5d from service fatigue failures.

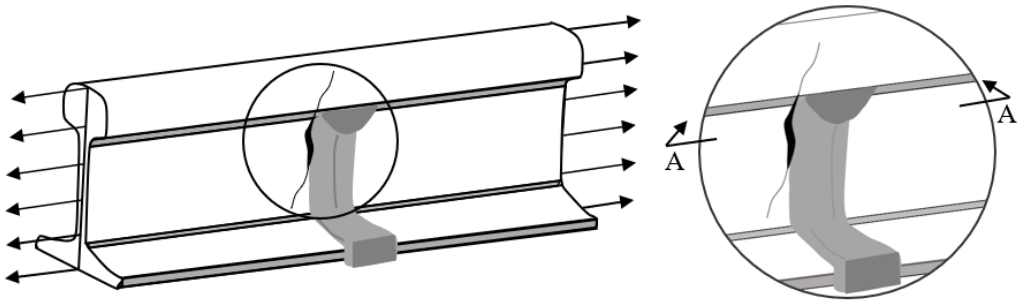

(a) Fatigue cracking of thermite welded joint

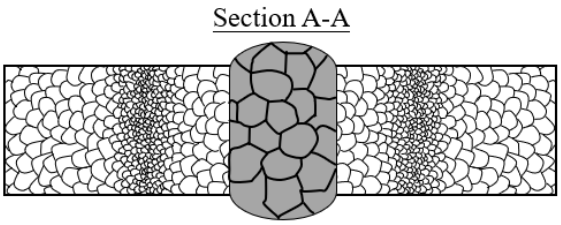

(b) Microstructure characteristics

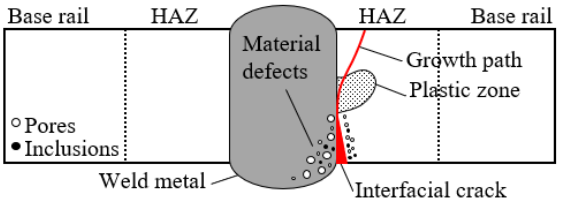

(c) Fatigue cracking mechanism

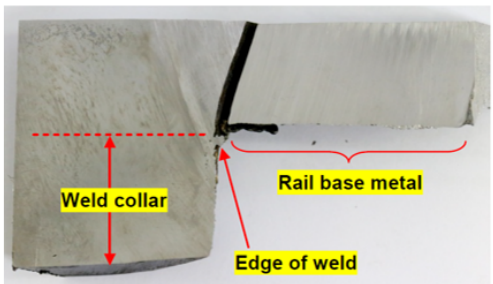

(d) The crack path of service failure

Figure 6-5: Fatigue cracking mechanism of thermite welded joint

The fracture face of the thermite welded joints failed via cracking thorough fusion zone was characterized with SEM to validate the failure mode as shown in Figure 6-6. Three typical zones can be distinguished by the macroscopic morphology: crack initiation region, fatigue propagation zone and overloaded zone. Figure 6-6a shows weld defects, both pores and Al_2O_3 inclusion found in the crack initiation area, indicating the negative effect of different weld defects to the structural fatigue behaviour. After initiation, the crack slowly propagates into the slow fracture or fatigue zone which is relatively smoother, brighter than the final fracture or fast fracture zone. The higher magnification of smooth fatigue zone indicated tearing features in microscale. Only weak striation or no regular striation observed between the progression marks. Along the crack front where the fatigue propagation ends, the fractured surface changes from inter-granular fracture feature to cleavage pattern, indicating the slow fatigue propagation altered to fast fracture. The growth rate of the crack in this region experienced a significant change until it reaches the final break. Cleavage features on the overloaded zone or fast fracture zone is a proof for the low energy brittle fracture after the fatigue crack reached the critical size.

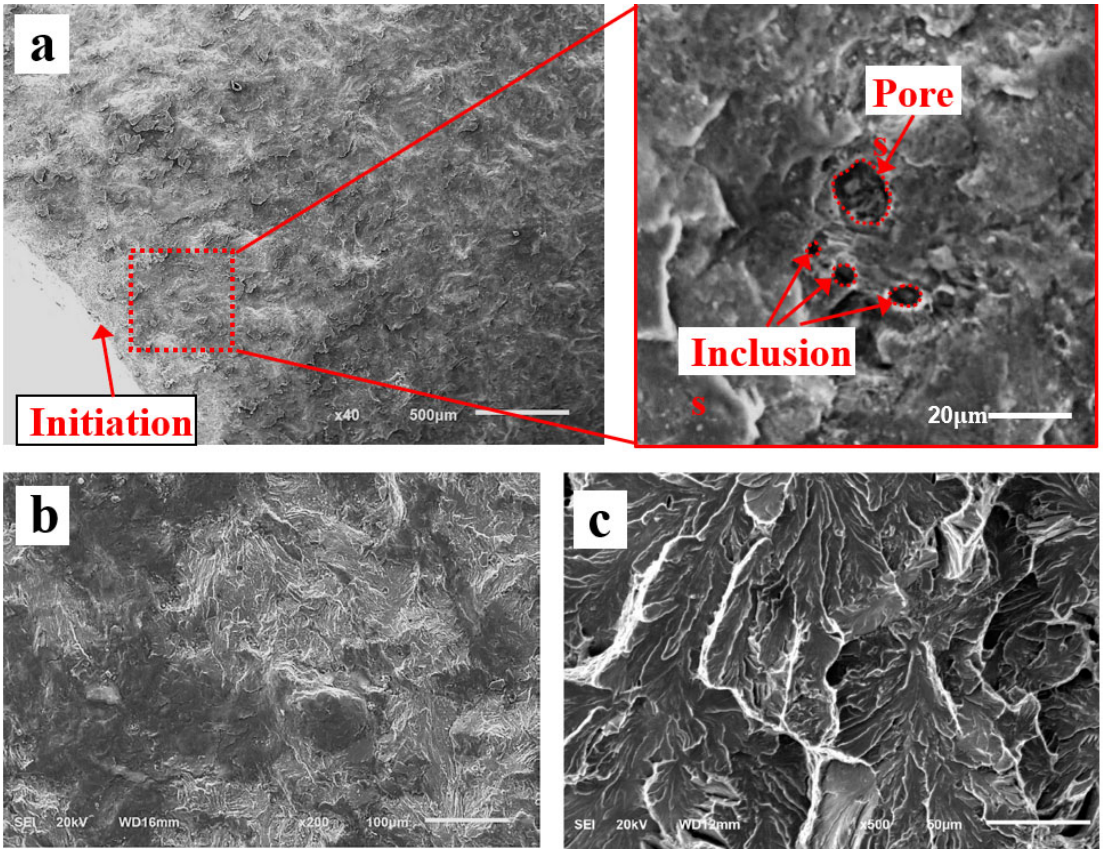

Figure 6-6: SEM fractographic observation of fractured rail surface: a) initiation site; b) fatigue propagation zone; c) overloaded zone

6.3 Fatigue crack propagation life subject to external cyclic loading

6.3.1 Fracture mechanics Methodology

In this study, LEFM concepts in fatigue crack propagation analysis were adopted. The SIFs determined through FEM analysis were used as the crack propagation driving force parameter [141-143]. The results of crack life prediction and crack shape evolution were also presented using the function of plotting in MATLAB. Based on the solutions of the SIF range (ΔK) and Paris' Law, crack propagation rate (da/dN) data can be numerically integrated in a fatigue crack growth life prediction algorithm developed in the MATLAB program, with Figure 6-7 showing the algorithm used.

LEFM is applicable to a wide range of materials following the assumption of small-scale yielding. A good approximation can also be achieved for elastoplastic material when the characterized stress level is much lower compared to the yield stress. Based on the fracture and fatigue testing results in Chapter 5 and reported properties from literature [144], both rail steel and thermite weld belong to pearlitic structure with relatively high strength, hardness and brittleness. Since the loading level under investigation is also low (100~300 MPa) as compared to the material's yield strength (750~1100MPa), the LEFM approach can be used to study the fracture and fatigue process of rail steel and thermite weld. The methodology presented in this study for fatigue crack growth analysis and life prediction is valid only when the cracks have initiated, and the fatigue propagation of short cracks is not considered. Due to the small scale yielding of the rail steels and thermite weld, the behaviour of short crack fatigue is also considered to be negligible.

According to Paris' Law, a quantitative prediction of crack propagation life of cracks in certain size could be accomplished by integration in terms of crack size based on the limit of initial crack size and final crack size causing fast fracture as:

$$\mathrm{N_p} = \int_{\mathrm{a_i}}^{\mathrm{a_f}} \frac{\mathrm{da}}{(\mathrm{C\Delta K})^{\mathrm{m}}} \tag{6-6}$$

where N_p is the estimated propagation life of cracks to fatigue failure, a_i is the initial crack size and a_f is the final crack size and ΔK is the SIF which is in terms of crack size and loading condition. C and m are two constants depending on material and loading condition, which are determined from experimental data.

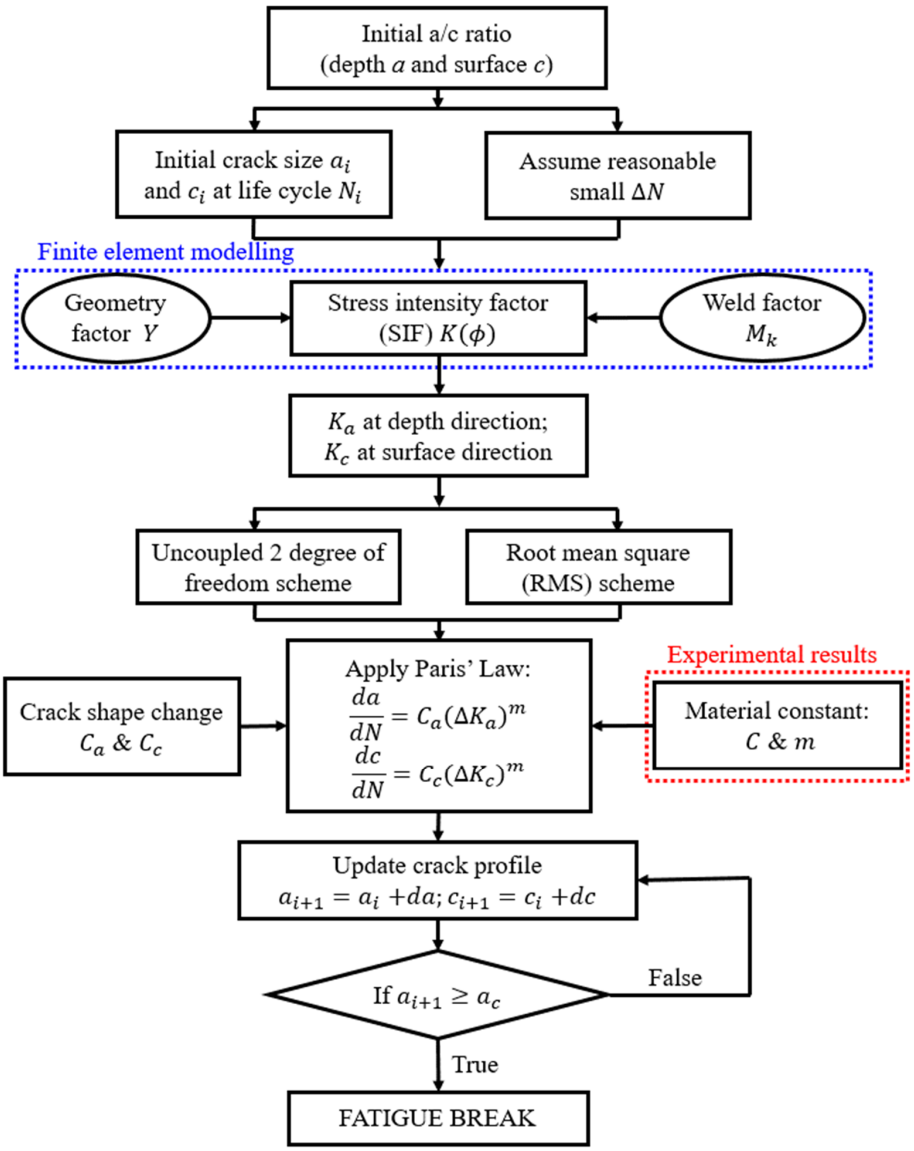

Figure 6-7: Schematic illustration of fatigue life prediction model

Uncoupled 2 Degree of Freedom and Coupled Root Mean Square Methods

A common approach to account for crack propagation based on SIF is the 2 degree of freedom (DOF) method which evaluates the local SIF at two points: the deepest point of crack front (crack depth) and the surface point along crack front (crack width at the outer surface). Two different schemes have been investigated for the consideration of SIF by using 2-DOF approach. The first scheme is the uncoupled 2-DOF scheme of which the two points were treated as separate point

and any other intermediate points along the crack front were not considered. The crack will propagate to a new shape with an increment of *da* and *dc* in separate direction after each loading cycle as shown in Figure 6-8. This method was used to predict fatigue crack growth ignoring the SIFs changes along the crack front.

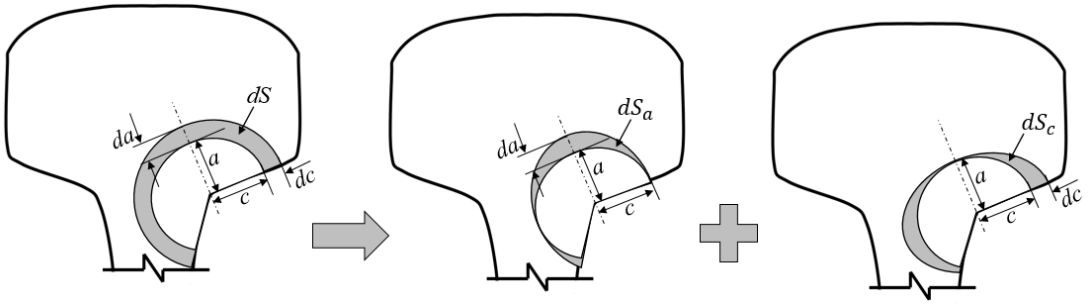

Figure 6-8: Superposition of crack growth dimension

Another more powerful scheme is the coupled root mean square (RMS) method proposed by Cruse and Besuner [145] which takes the effective increased average area in both deepest and surface direction into consideration. The RMS SIF expression in deepest direction is as:

$$K_{RMS,a}^2 = \frac{1}{\Delta S_a} \iint_{\Delta S_a} K^2(\phi)\, dS_a = \frac{2}{\pi} \int_0^{\pi} K^2(\phi) \sin^2\phi d\phi \tag{6-7}$$

while the RMS SIF expression in surface direction is as:

$$K_{RMS,c}^2 = \frac{1}{\Delta S_c} \iint_{\Delta S_c} K^2(\phi)\, dS_c = \frac{2}{\pi} \int_0^{\pi} K^2(\phi) \cos^2\phi d\phi \tag{6-8}$$

where *da* and *dc* represent the crack increment in deepest and surface direction respectively, ϕ is the angle from surface following anti-clockwise direction, ΔS_a and ΔS_c refer to the equivalent area increment after each load cycle using RMS scheme. Although only SIFs in two points were calculated, this coupled method combined the SIFs all along the crack front indirectly to crack growth along depth (*a*) and width (*c*) direction. The SIF solution at the crack front in terms of crack angle ϕ, $K(\phi)$ and RMS scheme was then incorporated into the fatigue crack growth algorithm to predict the crack shape evolution and fatigue crack propagation life will be developed.

Crack Shape Change and Increment

In order to account for cracks with different shapes, a correction factor considering different aspect ratio *a/c* was applied to the semi-circular solution. Previously, Merkle [146] has summarized that the SIF solution for semi-elliptic surface cracks with any aspect ratio *a/c* can be expressed as:

$$\mathrm{K}(\phi) = \frac{\mathrm{Y}\sqrt{\pi a}}{\Phi}\left[\sin^2\phi + \left(\frac{a}{c}\right)^2 \cos^2\phi\right]^{\frac{1}{4}} f_w \tag{6-9}$$

where a refers to the crack depth, c is the crack width. ϕ is the angle of the surface crack front following anti-clockwise direction. f_w refers to the finite-width correction factor as:

$$f_w = \sec\left(\frac{\pi c}{2b}\sqrt{\frac{a}{t}}\right) \tag{6-10}$$

and the value, Φ, is given as

$$\Phi = \int_0^{\pi/2}\left[1 - \left(1 - \frac{a^2}{c^2}\right)\sin^2\phi\right]^{\frac{1}{2}} d\phi \tag{6-11}$$

When using RMS scheme to calculate the equivalent area increment of each loading cycle, the assumption of angel dependent constant $\mathrm{C}(\phi)$ was made following Wu et al. [147] to make the crack shape remain consistent with the conventional two-point approach:

$$\mathrm{C}(\phi) = \frac{\mathrm{C}_a}{[1 + 0.1 \times (1 - \sin\phi)^2]} \tag{6-12}$$

where C_a corresponds to C constant of the crack front in the depth direction and ϕ denotes the parametric angle of crack front. The corrected Paris' Law for each point on the crack front was applied as:

$$\frac{da(\phi)}{dN} = C(\phi)[\Delta K(\phi)]^m \tag{6-13}$$

This correction model can be used to calculate the next growth increment at every angle of crack front in an iterative process from an initial crack size to a final crack size.

6.3.2 Fatigue propagation prediction results

Based on the solutions of geometry factor Y and weld magnification factor M_k at crack front, a fatigue crack growth life algorithm was developed. For C and m constants, the values of thermite weld material were obtained from fatigue test results in Chapter 5 while the values of rail steel material were from the reported results of Motameni and Eraslan [25].

Crack shape evolution under different loads

In the first case study, two types of loading conditions for in-plane load and out-of-plane loading were discussed separately to investigate the effect of loading type on the crack shape during the fatigue crack propagation. Both methods including uncoupled 2 DOF method and coupled RMS method were applied and compared for transverse cracks initiating from head-to-web transition region. The results of aspect ratio *a/c* in terms of crack size during crack propagation and the crack propagation path by using two different schemes were shown in Figure 6-9a. In Figure 6-9b, each blue circle represented the crack shape with a fixed increment of crack front growth in the depth direction. Therefore, the number of the blue crack shape contours like beach marks and the spacing between each contour or beach mark, described the fatigue life cycles and the crack growth and shape evolution process.

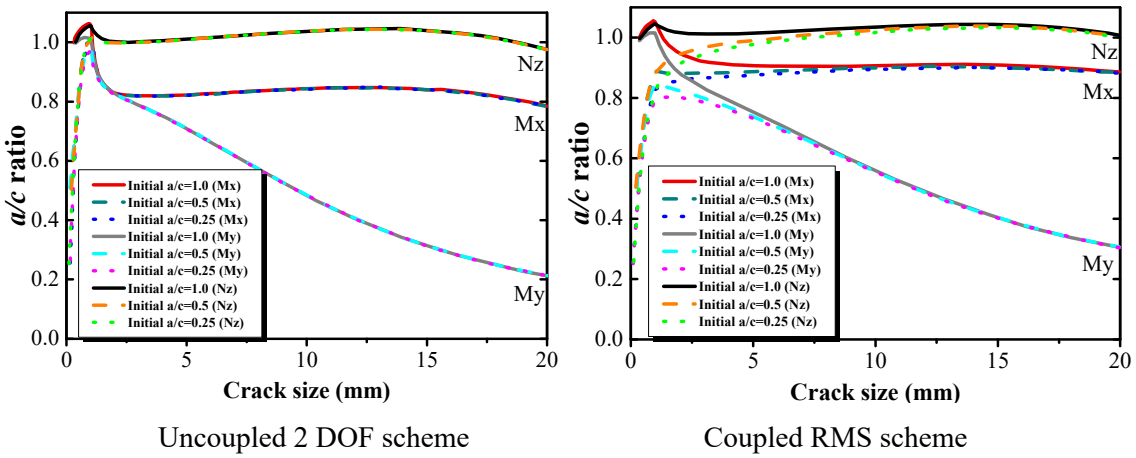

Uncoupled 2 DOF scheme Coupled RMS scheme

(a) crack shape evolution

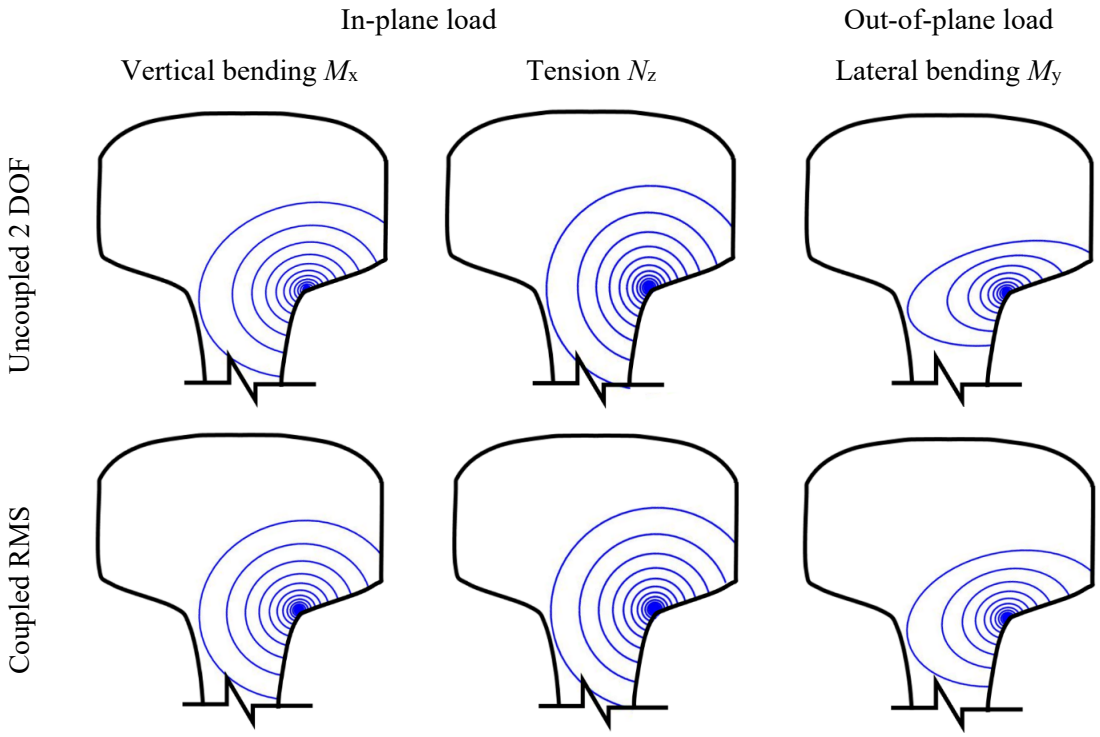

(b) crack propagation and shape change

Figure 6-9: Crack growth and shape evolution results

The results in Figure 6-9a showed that the crack shape for transverse surface cracks tend to keep to a constant crack aspect ratio for in-plane loading conditions. For in-plane vertical bending M_x and tension N_z, the crack aspect ratio is between 0.8~0.9 despite starting from different initial crack sizes and shapes. However, for out-of-plane bending loading, the crack aspect ratio varies

differently from the in-plane loading case. The crack aspect ratio decreases significantly until the final crack size is reached at rail break. The out-of-plane bending loading causes the fatigue crack to grow faster at the surface width directions than the depth direction, leading to a final crack shape that is semi-elliptical with a low crack aspect ratio *a/c* of 0.2~0.3. Furthermore, the faster crack growth behaviour led to a shorter fatigue life for surface cracks subjected to out-of-plane bending loading and is the more significant case compared to the in-plane loading cases. The out-of-plane bending load case is most significant in curves tracks or at curve-transition zone where sharp rail track curvature is found when thermite weld fatigue failures are commonly reported.

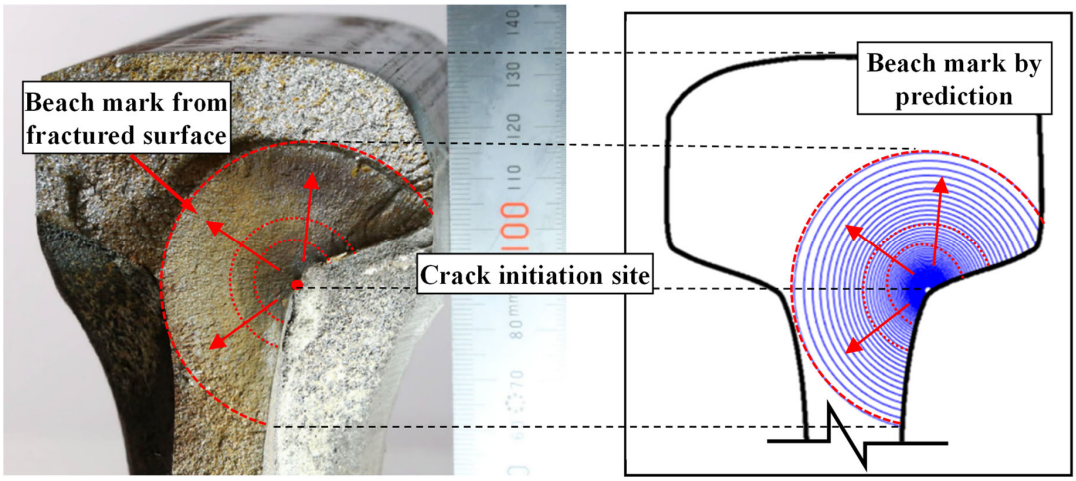

failure surface *a* RMS scheme prediction

(a) crack shape under pure in-plane load condition

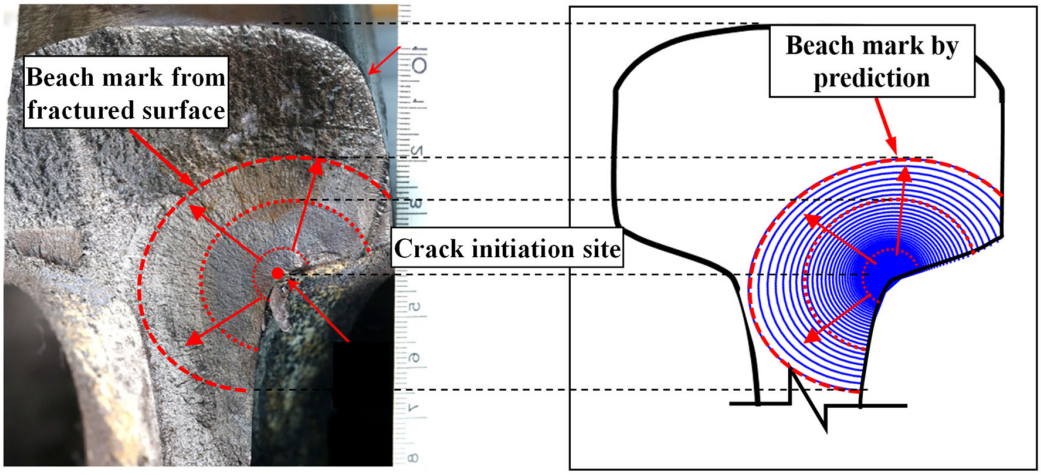

failure surface *b* RMS scheme prediction

(b) crack shape under mixed load condition

Figure 6-10: Different final crack shapes subjected to different loading condition

For the second case study, the fatigue crack shape evolution behaviour was further investigated for head-to-web cracks under two different loading scenarios: the pure in-plane loading condition includes vertical bending M_x and uniformly tension N_z, and the mixed load condition combined with the in-plane loads and out-of-plane load (lateral bending M_y). Figure 6-10 showed the two different final crack shapes after analysis using RMS approach and compared with an actual fatigue failure surface observed from service failure. It showed that under the complex loading condition, the fatigue crack growth algorithm developed was able to predict the actual crack shape observed from the fracture surface in Figure 6-10. The fracture surface for a transverse surface crack subjected to out-of-plane bending loading shows lower crack aspect ratio *a/c* trends towards a semi-elliptical shape.

Besides the investigation of the crack shape evolution, the fatigue crack propagation life prediction of these two cases in Figure 6-10 was also performed. The initial crack size was assumed as 0.1~0.2 mm and the loads were obtained from onsite measurement. The predicted fatigue crack propagation life of these two cases fell in the range of 9.3~18.1 million cycles and 2.8~5.7 million cycles respectively. Compared with the actual service life from the record, which are around 13.2 million cycles and 4.9 million cycles respectively, a relatively accurate prediction was achieved. In general, it was shown that this fatigue prediction algorithm by using RMS method has a good agreement with the actual service fatigue failures in both crack shape evolution and propagation life prediction.

Fatigue life prediction

The fatigue crack growth and life prediction analysis were conducted for a head-to-web crack subjected to complex loads with combination of both in-plane and out-of-plane loads. The vertical bending stress M_x was considered at three different stress levels of 100 MPa, 200 MPa and 300

MPa corresponding to low, medium and high stress levels to study the effect of stress magnitude on the fatigue growth and predicted life cycles to failure. The uniformly distributed tension N_z was considered as 30 MPa in the rail as reported [148]. The respective out-of-plane loading (lateral bending stress M_y) was selected as 30% of vertical bend in-plane loading for curve rail with a radius of 400 m and train speed of 80 km/h as reported by Powell and Gräbe [149].

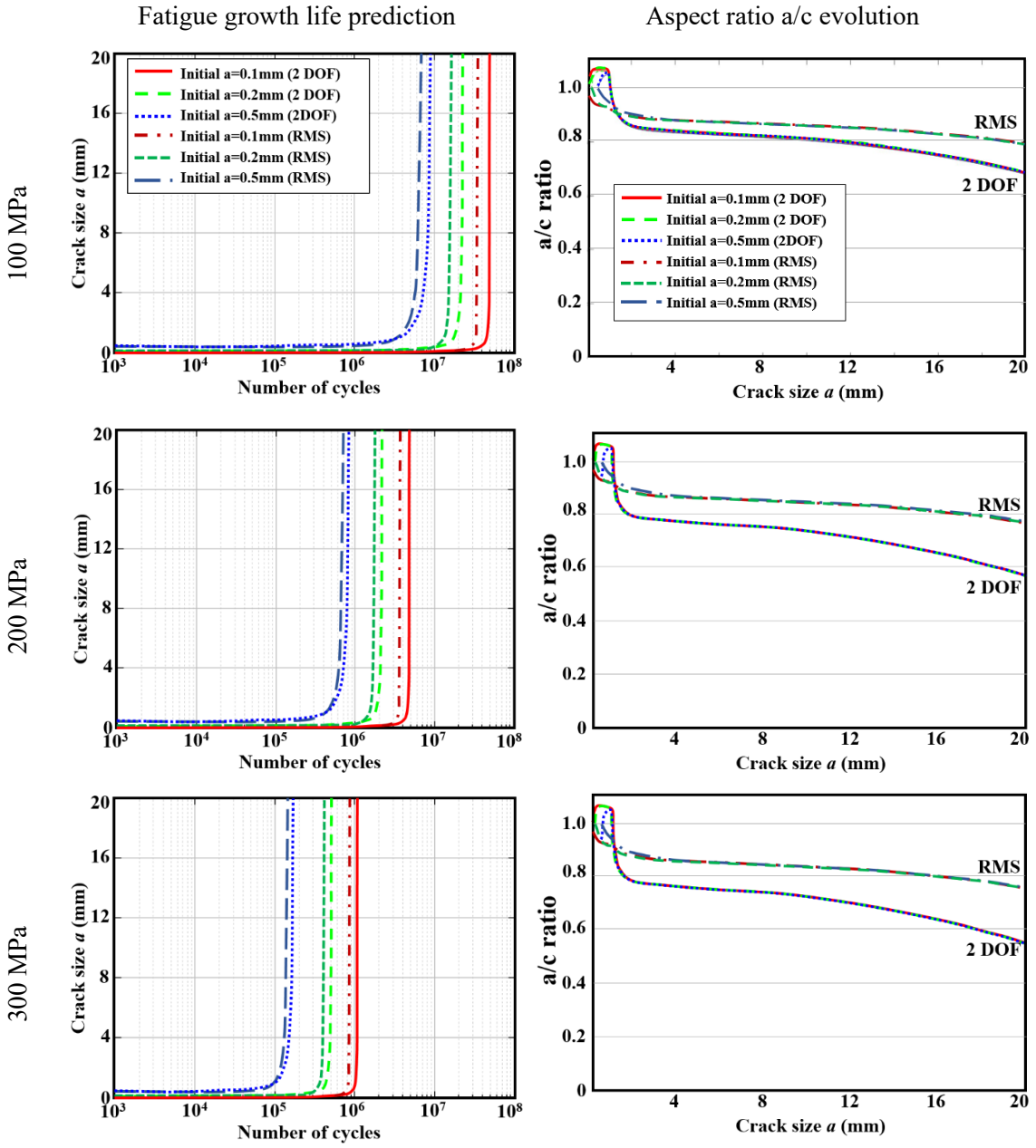

Figure 6-11: Fatigue growth prediction for R350HT rail steel at three stress levels

In order to obtain the most critical initial crack size, the fatigue propagation process for different initial crack size was investigated for cracks initiated from rail steel and thermite welded joints. A typical predicted plot of fatigue growth life during crack propagation for rail material of R350HT subjected to low (100 MPa), medium (200 MPa) and high (300 MPa) stress level was shown in Figure 6-11. The crack aspect ratio of crack depth (a) to crack width (c) have also been plotted with respect to the number of growth cycles.

The predicted results showed that the fatigue life of transverse surface cracks is highly sensitive to the initial crack size chosen (0.1, 0.2 and 0.5 mm) as shown in Figure 6-11. The fatigue crack propagation life decreases when the initial crack size chosen is larger. It also showed that there is no notable correlation between the magnitude of the stress and the aspect ratio a/c of the cracks. As for the scheme selected for investigation, Figure 14 indicated that the uncoupled 2 DOF scheme tend to overestimate the fatigue growth life compared to RMS scheme while the latter is less sensitive to the loading condition and magnitude. The predicted crack shape using uncoupled 2 DOF scheme showed lower crack aspect ratio *a/c* compared to the RMS scheme where the crack aspect ratio a/c ratio tend towards 0.7~0.8.

A summary of fatigue crack growth life prediction results for transverse surface cracks located at the head-to-web region with different material C and m constants was shown in Table 17. The fatigue crack growth algorithm predicted life for rail steel materials (R260 and R350HT) is in the range of 37~47 million cycles, for an initial crack size of 0.1 mm in depth. When the initial crack size increases to 0.2 and 0.5mm in depth, the fatigue crack propagation life reduces significantly.

Table 17: Predicted crack propagation life for rail transverse cracks (in million cycles)

Stress	**Low stress** (100 MPa)			**Medium stress** (200 MPa)			**High stress** (300 MPa)		
a_i	**0.1mm**	**0.2mm**	**0.5mm**	**0.1mm**	**0.2mm**	**0.5mm**	**0.1mm**	**0.2mm**	**0.5mm**
R260	47.6	21.5	7.4	4.2	1.9	0.6	0.92	0.41	0.14
R350HT	37.1	17.9	6.8	3.66	1.76	0.66	0.86	0.41	0.15
WMC	44.3	11.9	2.0	0.6	0.2	0.03	0.04	0.01	0.002
WTC	6.5	4.3	2.5	0.6	0.4	0.2	0.1	0.09	0.07

Further investigations for weld metal cracks (WMCs) propagating in the weld metal and weld toe cracks (WTCs) in the rail steel (R350HT) were presented in Figure 6-12. Both WTCs and WMCs refer to the cracks near the weld toe but WTCs are in the rail steel while the WMCs are in the welded metal as shown in Figure 6-12a. Hence the WTCs and WMCs shared the same weld magnification factor M_k when the material properties for fatigue prediction are different. The M_k for surface cracks 0.5 mm away from the weld toe region was applied.

The fatigue crack growth life of WTCs and WMCs decreases when the initial crack size increases from 0.1, 0.2 to 0.5mm in depth direction. It was observed that the fatigue life of WMCs is longer at the low-stress condition, but the life decrease more rapidly compared to WTCs once the stress level increase. This can be explained by the fatigue crack growth rate curves in Figure 11b from the test results. It shows that the growth rate (d*a*/d*N)* of weld metal in head-to-web region is smaller than rail steel (R350HT head) in lower SIF condition, but it increases faster as the ΔK increase.

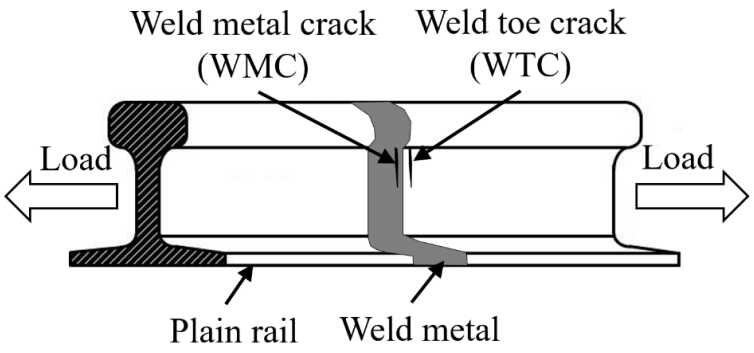

(a) definition of WTC and WMC

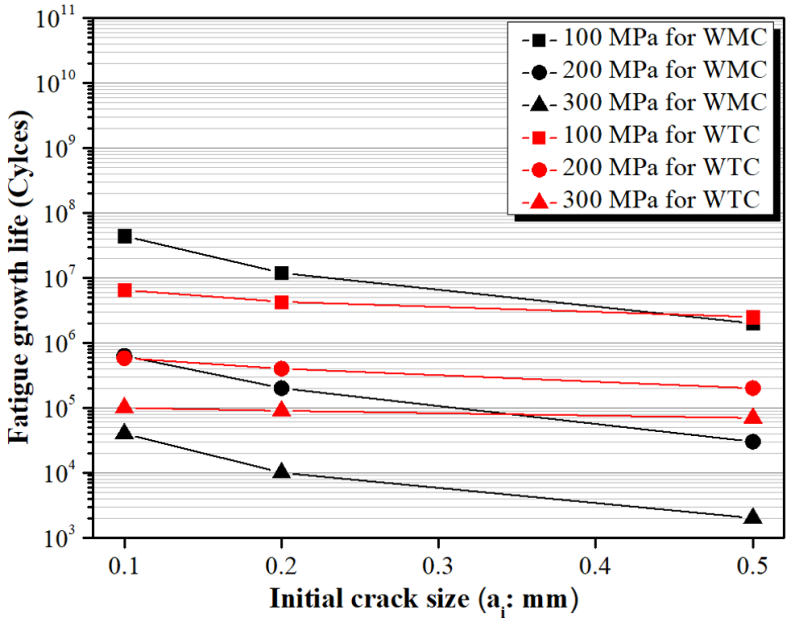

(b) fatigue life prediction result

Figure 6-12: Fatigue growth life predication of cracks initiated in different materials

Stress range-life curve prediction

With the fatigue crack growth and life prediction algorithm developed, further investigations to obtain the stress range-life curve of weld toe crack (WTC) case near the thermite weld toe region was investigated. By considering crack propagation from different initial crack sizes of initial crack depth of 0.1 mm, 0.2 mm and 0.5 mm and propagating to a final crack size in rail steel with material grade of R350HT. The predicted Stress Range versus Life curve is shown in Figure 6-13 where a_i refers to assumed initial crack size for life prediction. The load was selected as a pure in-

plane bending in accordance with BS EN 14730-1-2017 [19]. Using a load ratio of 0.1 (minimum load is 10% of maximum load), the final crack sizes were determined based on the critical SIF K_{Ic} with the consideration of shape factor Y and weld magnification factor M_k. M_k factor was calculated earlier for weld toe cracks located at 0.5 mm from the thermite weld toe region.

Table 18: Fatigue parameters of R350HT rail steel

K_{Ic}	C	m
43.4 MPa $\sqrt{m}$	5.034 E-14	4.62

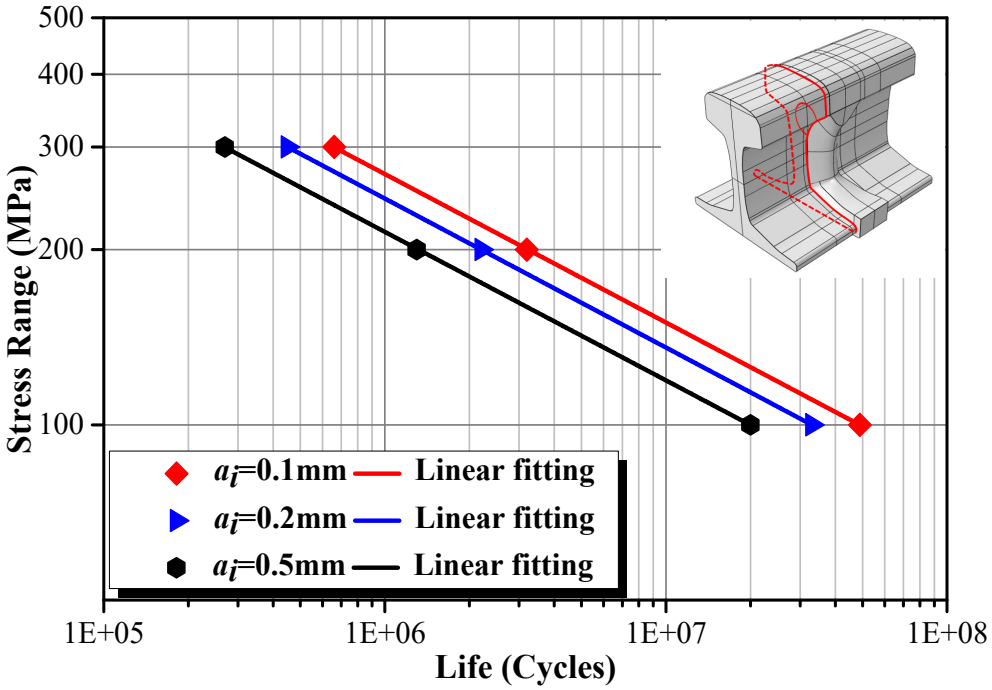

Figure 6-13: Stress Range-Life curve for thermite weld toe cracks by RMS scheme

6.4 Fatigue life prediction considering residual stress

6.4.1 Fatigue methodology considering residual stress and relaxation

To consider the effect of residual stress and stress relaxation on the fatigue life of the thermite welded joints, the fatigue life prediction model based on fracture mechanics was developed. The flow chart of the fatigue life model is illustrated in Figure 6-14.

Stress intensity factor under external load

Considering the combined effect of the residual stress and cyclic loading, the expression of effective stress intensity factor (K_{eff}) can be defined as:

$$K_{eff} = K_e + K_r \tag{6-14}$$

where K_e and K_r are the stress intensity factor (SIF) associated with the external cyclic loading and welding residual stress, respectively. K_e can be expressed as:

$$K_e = M_K \cdot K_p \tag{6-15}$$

where K_p is the stress intensity factor for rails without welded joints. M_K is the magnification factor dependent on the profile of the welding joint, and it has been calculated in Chapter 5 from FE simulation.

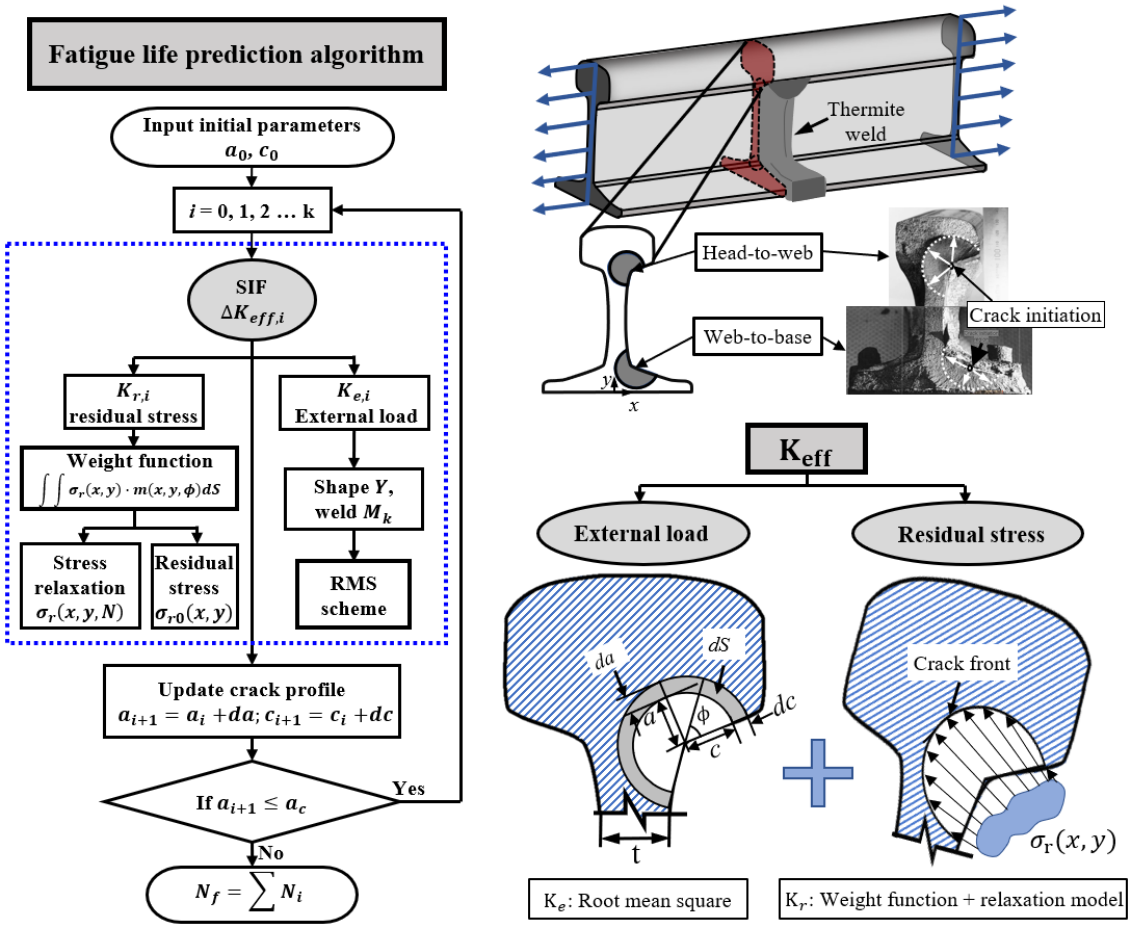

Figure 6-14: Schematic illustration of fatigue life prediction model (head-to-web: y=12.78 mm, web-to-base: y=24.7mm)

Stress intensity factor under residual stress

The effect of residual stress on the SIF was studied using weight function method [106] as:

$$\mathrm{K}_r = \int\int \sigma_r(x,y) \cdot m(x,y,\phi) dS \tag{6-16}$$

where σ_r is the residual stress distribution along the crack surface in the body without flaw and m is the point-load weight function at any point along the crack front and it is expressed as:

$$m(x,a) = \frac{2}{\sqrt{2\pi(a-x)}}\left[1 + \mathrm{M}_1 \cdot \left(1-\frac{x}{a}\right)^{0.5} + \mathrm{M}_2 \cdot \left(1-\frac{x}{a}\right) + \mathrm{M}_3 \cdot \left(1-\frac{x}{a}\right)^{1.5}\right] \tag{6-17}$$

where x refers to the distance of any point along the 1-D crack tips to the origin following the Figure 6-15. The analytical solution of weight function at deepest point and surface point can be obtained following Shen et al.'s study [150]. The residual stresses will be partially released under the cyclic loads and the mathematical description of this phenomenon using the Eqn. 4-8 and the corresponding fitting parameters in Table 9 was integrated to the fatigue model to investigate the effect of residual stress relaxation. For some loading cases, residual stress for cracks located at the transition locations is compressive and it tends to relax to a value close to 0 after the first fatigue loading cycle. Hence, the compressive residual stresses at those locations are treated as 0 and the crack closure is not considered in the current fatigue model,

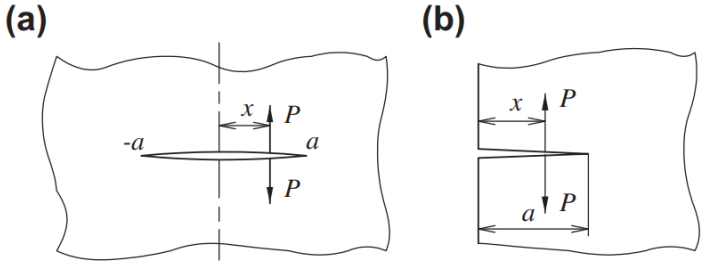

Figure 6-15: Configuration of infinite sheet with (a) center crack and (b) edge crack [150]

Fatigue life prediction model

Based on Walker equation, a quantitative prediction of crack propagation life can be accomplished by the integration as:

$$\frac{da}{dN} = C\left[\Delta K_{eff}(1 - R_{eff})^{\gamma-1}\right]^m \quad (6\text{-}18)$$

where γ is a constant of material property obtained from the testing result characterizing the effect of the stress ratio on the fatigue growth behaviour. The empirical value of 0.82 is taken from the testing results of Kim et al. [83] ΔK_{eff} and R_{eff} were calculated as below to account for the effects of both external loads and residual stresses:

$$\Delta K_{eff} = (K_{app.max} + K_r) - (K_{app.min} + K_r) = \Delta K_{app} \quad (6\text{-}19)$$

$$R_{eff} = (K_{app.min} + K_r)/(K_{app.max} + K_r) \quad (6\text{-}20)$$

Walk equation is simple and convenient to account for the stress ratio on the fatigue propagation behaviour of materials. However, certain limitations still exist which include 1) underestimating the final part of the fatigue propagation rate curve when the stress intensity factor approach the critical fracture toughness, and 2) neglecting the effect of material plasticity induced crack closure. Since the $\gamma = 0.82$ closing to 1 implies a relatively weak effect of stress ratio and the low fracture toughness of welded rail metal, it is reasonable to apply this approach for the fatigue life estimation.

6.4.2 Fatigue crack propagation life evaluation considering residual stresses and relaxation

The residual stress results of the thermite welding process both from experiments and simulations revealed a high longitudinal tensile stress at the web location and compressive at the head and base locations of the weld toe region. Following the study [118] of the wave-like deformation occurring at the rail and welded joints during the dynamic wheel-rail contact condition, both the upper rail web location (head-to-web) and the lower web location (web-to-base) are subjected to cyclic in-plane bending causing fatigue crack propagation as shown in Figure 6-16. It is worth mentioning that the past research showed that the majority of the transverse failures of thermite welded rail joints were founded to be at these typical locations: head-to-web (28%) and web-to-base (30%) [27, 32]. In this study, the uniaxial fatigue evaluation at the transverse plane of weld

toe region as shown in Figure 6-16 is considered, neglecting the effect of multiaxial stress state. As the stress component perpendicular to the transverse weld toe plane is the dominant stress to open the fatigue cracks, this simplification is acceptable for life prediction.

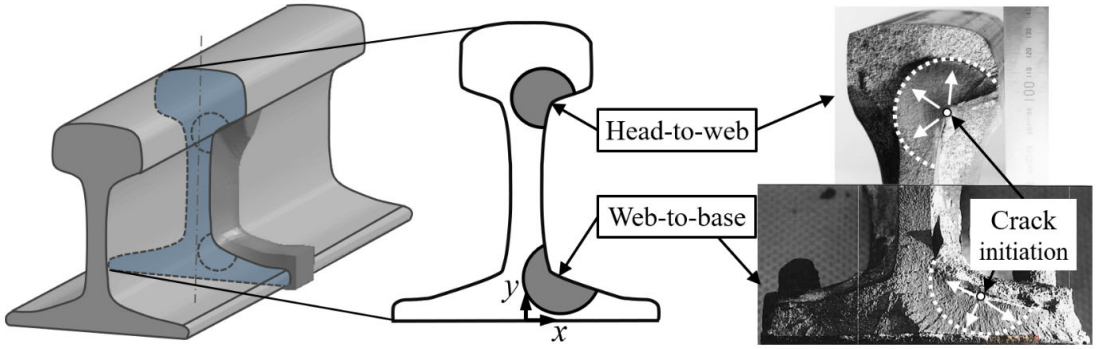

Figure 6-16: Analyzed crack position and configuration (head-to-web: y=12.78 mm, web-to-base: y=24.7mm)

As shown in Figure 6-16, the transverse fatigue cracks usually initiate from surface area of weld toe region and propagate inwards along the transverse plane. Two typical crack locations (head-to-web and web-to-base) were observed and benchmarks of the fractured surface were presented. For the locations of interests, the fatigue life prediction was conducted with different initial defect size (0.1 mm, 0.2 mm, and 0.5 mm) under the external cyclic load and residual stress. The present considered loads are quasi-static and therefore three different levels of axel loads were studied to include possible dynamic effects of contact load. The three levels correspond to 8 tons, 12 tons, and 16 tons with the load ratio of R = 0.1. The bending moment is applied to assure tensile stress at each calculated location and therefore the cracks at web-to-base location is under the inverse bending load. Crack growth data of Paris law constant is from the literature [25]. The critical stress-intensity factor range, ΔK_{IC} , is found to be 46 MPa$\sqrt{\text{m}}$. The results of shape factor, Y, and the weld magnification factor, M_k, are obtained the author's previous work [29]. Normally the crack propagation process will be completed once the stress intensity factor reaches ΔK_{IC} .

However, the maximum crack size is measured as 20-25 mm due to the limitation of the size of rail web and therefore the final crack size was set as 20 mm for investigation in this study.

A fatigue crack growth MATLAB code following the algorithm proposed was developed to perform the life evaluation and results are depicted as in Table 19. The discrepancy was calculated as:

$$Discrepancy\ (\%) = \frac{N_e - N_r}{N_e} \times 100\% \tag{6-21}$$

where $N_e$refers to the predicted fatigue life without consideration of residual stress and N_r refers to the predicted fatigue life with consideration of residual stress. In Table 19, crack location of HW refers to head-to-web and WB refers to web-to-base. D refer to the distance to the rail base and a_i refer to the initial crack size. $\sigma_{max}/\sigma_{min}$ is the resulted stress under external fatigue load. σ_r is the initial surface residual stress while σ_s is the stabilized surface residual stress after the stress relaxation.

Table 19: Fatigue life prediction of weld toe cracks at different locations (25 °C)

Crack location	d (mm)	a_i (mm)	$\sigma_{max}/\sigma_{min}$ (MPa)	σ_r (MPa)	σ_s (MPa)	N_e (10^6 cycles)	N_r (10^6 cycles)	Discre--pancy (%)
Axle load: 8 tons:(inverse bending moment for head-to-web location)								
HW	127.8	0.1	67.4/6.7	-72.0	-32.3	411.7	409.7	0.49
HW	127.8	0.2	67.4/6.7	-72.0	-32.3	271.7	269.1	0.96
HW	127.8	0.5	67.4/6.7	-72.0	-32.3	159.5	156.9	1.63
WB	24.7	0.1	80.1/8.0	372.0	312.4	185.3	138.8	25.09
WB	24.7	0.2	80.1/8.0	372.0	312.4	128.7	94.6	26.50
WB	24.7	0.5	80.1/8.0	372.0	312.4	79.1	56.7	28.32
Axle load: 12 tons: (inverse bending moment for head-to-web location)								
HW	127.8	0.1	101.1/10.1	-72.0	-12.9	78.1	77.2	1.15
HW	127.8	0.2	101.1/10.1	-72.0	-12.9	51.5	50.6	1.75

HW	127.8	0.5	101.1/10.1	-72.0	-12.9	30.2	29.3	2.98
WB	24.7	0.1	120.1/12.0	372.0	289.9	35.2	28.3	19.60
WB	24.7	0.2	120.1/12.0	372.0	289.9	24.5	19.3	21.22
WB	24.7	0.5	120.1/12.0	372.0	289.9	15.3	11.7	23.53
Axle load: 16 tons: (inverse bending moment for head-to-web location)								
HW	127.8	0.1	134.8/13.48	-72.0	2.1	24	22.1	7.92
HW	127.8	0.2	134.8/13.48	-72.0	2.1	15.8	14.5	8.23
HW	127.8	0.5	134.8/13.48	-72.0	2.1	9.3	8.5	8.60
WB	24.7	0.1	160.1/16.0	372.0	264.6	10.8	9.1	15.74
WB	24.7	0.2	160.1/16.0	372.0	264.6	7.5	6.2	17.33
WB	24.7	0.5	160.1/16.0	372.0	264.6	4.6	3.8	17.39

From Table 19, it can be concluded that the predicted fatigue life of weld toe cracks at web-to-base location is significantly degraded by the residual stress and the estimated reduction is around 15~30% in comparison with life without consideration of residual stress. The tensile residual stress at the web-to-base locations plays a detrimental effect on the fatigue strength and the amount of degradation is found to be more significant under lower axle load. This is can be explained by the fact that the residual stress relaxation level is more significant with higher applied stress amplitude. This degradation of fatigue life is found to be less significant (from 10% to close to 0%) at the head-to-web location. Although the compressive residual stress found in the surface of head-to-web location is beneficial to the fatigue life, the resulted tensile residual stress when the depth reach towards the interior also accelerate the crack propagation rate. The increment to the tensile stress is more significant at higher stress amplitude. At the lowest stress amplitude under axle load of 8 tons, nearly no influence of welding residual stress (around 1%) on the fatigue life is observed. This is because of the residual stress at this location tends to relax to a value close to 0 with the increase of cycle numbers. It is reported [43] that the conventional approach employing the weight function only considered the residual stress filed of a crack-free region. Hence, the partial crack surface closure, which is particularly typical for cracks in a compressive stress field, is not

considered in this study. Due to the low amplitude of residual stress and external load, no significant difference will occur without considering the additional crack closure mechanism [151].

It is expected that there will be significant variation of the fatigue life prediction with different material properties, weld geometry, crack locations, initial crack size and stress amplitude. This was partly investigated in the previous work by the author [29]. However, the residual stress and the effect to the fatigue strength were not taken into consideration previously. From Figure 6-17a & b, it is found that the reduction of estimated fatigue life is more significant for cracks at head-to-web location compared to the cracks at web-to-base with the increase of axel tons. On the other hand, the estimated fatigue life of cracks at web-to-base locations is found to be much shorter compared with head-to-web location with the same cyclic stress amplitude due to the presence of higher tensile residual stress. As for the effect of initial crack size as shown in Figure 6-17c & d, the fatigue crack propagation life decreases with the increase of assumed initial crack size, regardless the crack locations. A reduction of around 70~80% for fatigue life is found when the initial crack size increase from 0.1 mm to 0.5 mm. The assumption of the initial crack size for fatigue life prediction is associated with the microstructure characterization and material defect study. The formation of the material defects is correlated with the welding process and a recent study [76] shows that the shrinkage cavities with size from tens to hundreds μm were found in the web-to-base transition region due to the different cooling rate between the thinnest web to the thick base. These defects, especially with large size, will act as small cracks to nearly eliminate the crack initiation stage of the fatigue life and therefore lead to a poor fatigue performance.

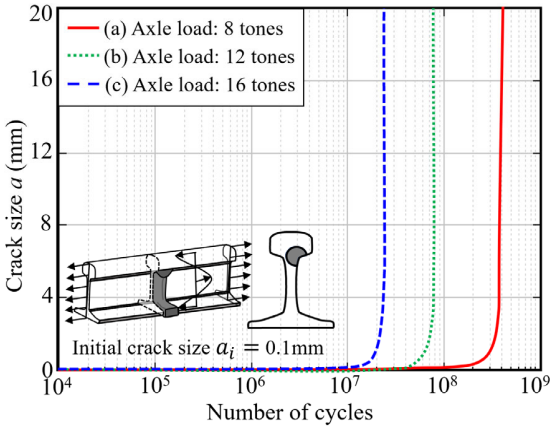

(a) head-to-web crack under different load

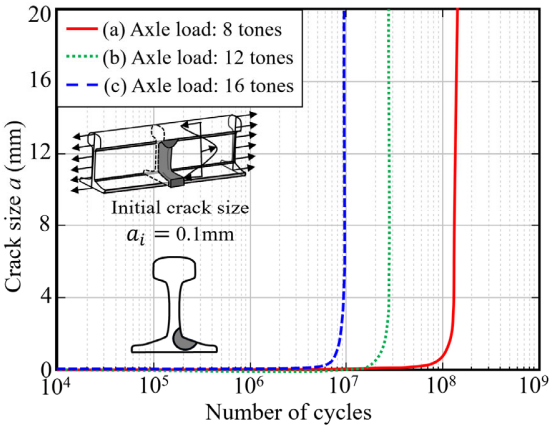

(b) web-to-base crack under different load

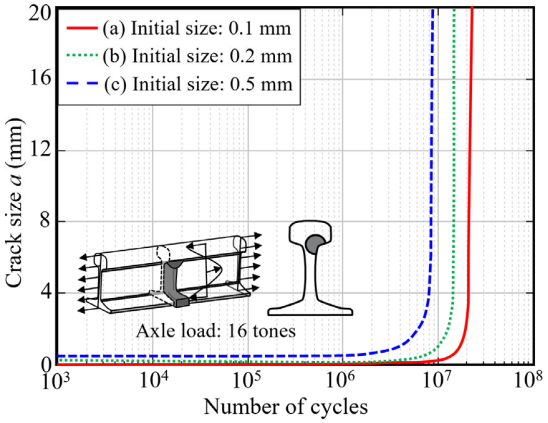

(c) head-to-web crack with different initial size

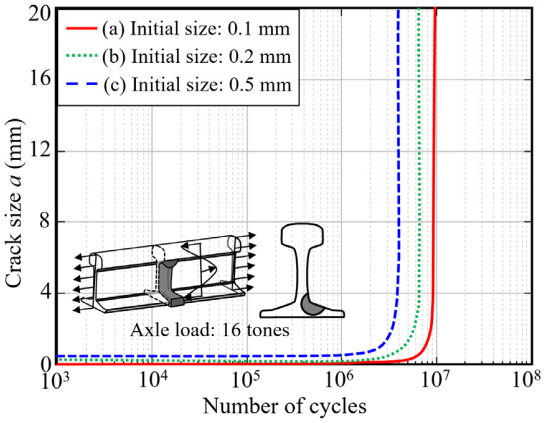

(d) web-to-base crack with different initial size

Figure 6-17: Comparison of fatigue life with different effecting factors

Evaluation of fatigue design curve under bending load:

The stress-life based method was used to describe relation between the nominal stress amplitude S, and the number of cycles to failure, N. Based on the fatigue life prediction algorithm proposed in this study, the stress range-life cycle curve of weld toe transverse cracks under bending load is calculated and plotted as shown in Figure 6-18. The curve which express the relationship between the stress level S and number of cycles to fail N_f can be given as below:

$$N_f S^n = C \tag{6-22}$$

where, C is the fatigue strength constant of the material and n is the slope of S-N curve. The bending moment is applied in different amplitude with stress ratio of R = 0.1. The endurance limit

is calculated based on the Murakami's [135] study with the assumption of defect size as 0.1 mm. The fatigue limit σ_w for the weld toe surface defects under cyclic bending load is expressed as:

$$\sigma_w = \eta \cdot \frac{(HV + 120)}{(\sqrt{area})^{\frac{1}{6}}} \left[\frac{1-R}{2}\right]^{\alpha} \tag{6-23}$$

where σ_w is the fatigue limit in MPa, η is the coefficient to describe the types of material defects and the values equal to 1.43 for surface defects. HV is the Vickers hardness in kgf/mm2. $\sqrt{area}$ is the square root of the projected "area" of a defect onto the maximum principal stress plane in μm and it is assumed as 100 μm. R is the stress ratio and $\alpha = 0.226 + HV \times 10^{-4}$. Based on this formula, the fatigue bending limit of the transverse weld toe defects is calculated as 357 ± 5 MPa and a good agreement is achieved compared with the tested results [136].

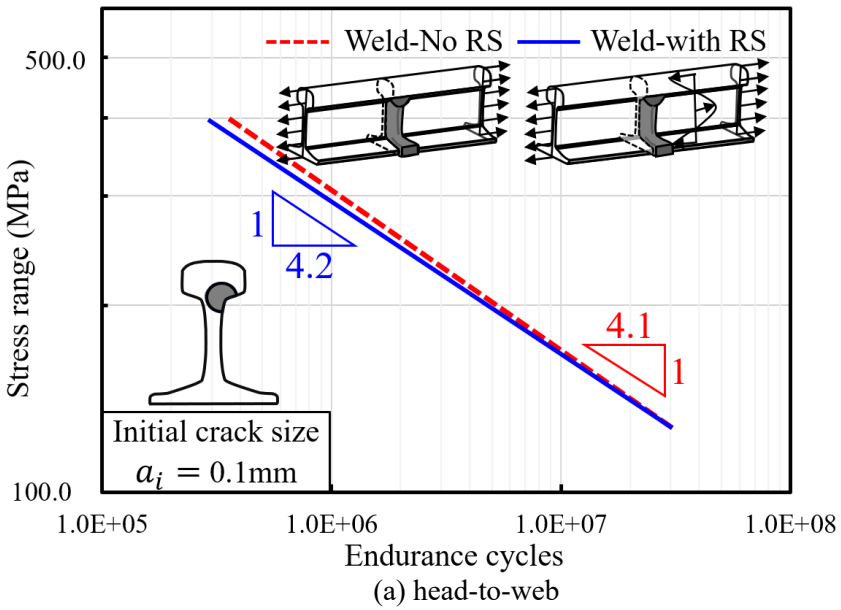

(a) head-to-web

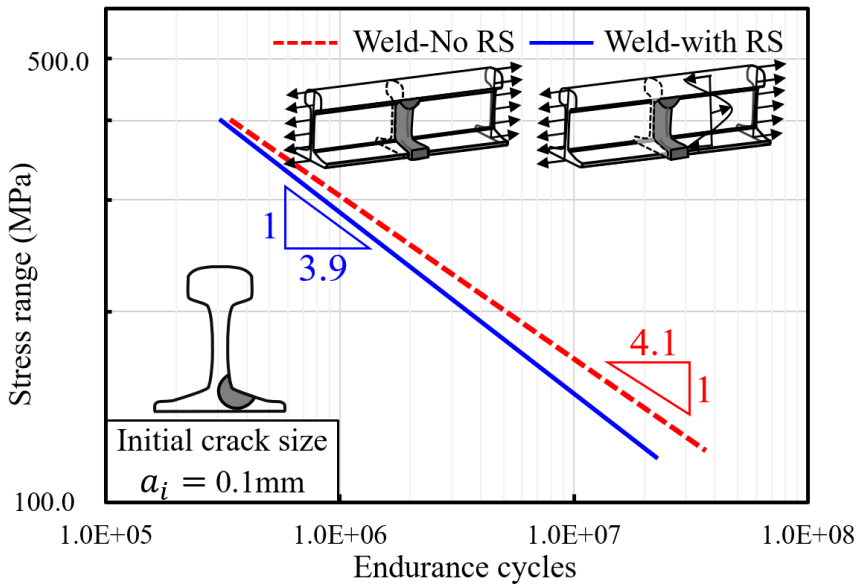

(b) web-to-base

Figure 6-18: Stress range-life cycle curve of cracks at different locations (RS: considering residual stress, the initial crack size = 0.1 mm and stress ratio = 0.1)

Figure 6-18 illustrated the difference of the predicted fatigue life between each case presented. It is found that the residual stress field resulting from the welding process, leads to fatigue strength degradation of thermite welded rail joints. Generally, the effect of residual stress on the fatigue life is therefore more significant with a higher stress amplitude after the superposition. Given by Figure 4-14, the residual stresses increase from compressive (-85 MPa) at the surface to tensile (175MPa) at deepest point for head-to-web location and decrease from tensile (380 MPa) to compressive(-130 MPa) for web-to-base location, respectively. The complex 3D distributions of the residual stresses, particularly after the relaxation, suppress and compensate to each other, giving rise to the fatigue life degradation of cracks located at both areas (head-to-web and web-to-base). However, some differences were observed for cracks at different locations. For head-to-web cracks, the tensile residual stress will be partially relaxed under the cyclic load and the extent of relaxation becomes higher with the increasing stress amplitude of the applied load. While the compressive residual stress at the head-to-web locations will be relaxed to be close to 0 or even become tensile in the interior away from the surface. Hence, the significance of the residual stress

is found to be higher for head-to-web cracks and lower for web-to-base cracks with the increasing of the applied stress amplitude.

Validation of the fatigue life prediction can be made by comparing the predicted fatigue life with the past failure records. From the records, the service life of the thermite welded joints varies from around 1 year to a few years, which corresponds to around 2.6 million to hundreds million life cycles based on the numbers of trains on service per day. Compared with the predicted results, it is worthy to mention that the fatigue life predict model proposed in this study, with quantification of influence of residual stress and relaxation, was found to provide a reasonable estimation for fatigue crack propagation life of thermite welded rail joints.

6.5 Concluding remarks

In this Chapter, the mechanism of the transverse fatigue cracking at the fusion line was discussed based on the material characteristics across the welded joint. Thermite weld metal exhibited a lower fracture toughness with mild overmatched yield strength and low impact toughness compared to the parent rail metal (R260). The fatigue crack propagation studies revealed that moderate strength overmatch is beneficial for weld cracks. However, for interfacial cracks, this beneficial effect is lost, and cracks tend to grow toward the parent metal, away from the fusion line with a shorter fatigue crack propagation life. It was also shown that the embrittlement of the HAZ near the fusion line and the presence of welding defects are the major factors leading to fatigue crack initiation. Furthermore, the mildly overmatched yield strength influences the cracking growth path while the material fatigue properties affect the propagation rate. Hence, transverse fatigue cracking of the thermite welded joints first initiates near the fusion line and advances towards the parent rail away from the rail/weld interface. The crack then further propagates following the direction of maximum shear stress in the parent rail until the final fracture once the critical fracture toughness is reached.

This Chapter also provides the methodology for conducting structural fatigue crack growth and life prediction for rail steels and thermite welds subjected to in-plane and out-of-plane fatigue loading conditions. Two different surface crack growth numerical integration schemes: namely the uncoupled 2 DOF and coupled RMS schemes are applied. A comparison was made between these two surface crack growth schemes and the coupled RMS scheme was able to better predict the fatigue crack growth and shape evolution. It was shown that irrespective of the initial crack shape and size, the transverse surface cracks in rail steel and thermite weld tended toward a near semi-circular shape when subject to in-plane loading condition and it will alter to semi-elliptical shape once under out-of-plane loads. This out-of-plane load, which is mainly found in the curved or transition track of the railway system, is more critical due to the relatively faster growth rate, particularly in the surface width direction. The investigation on the fatigue crack growth life for weld metal cracks (WMCs) and weld toe cracks (WTCs) showed that the fatigue life of WMCs is longer at a low-stress condition but the life decrease more rapidly compared to WTCs once the stress level increase. Hence thermite welded joints are more susceptible to structural fatigue crack growth failures arising from weld toe defects, especially under a high stress loading condition.

Regarding the residual stress resulting from the welding process, this chapter provides a comprehensive evaluation of fatigue crack propagation life considering the residual stress and its relaxation was conducted. The influence of residual stress and its relaxation on the fatigue life of thermite weld was investigated using the root mean square method and weight function to calculate the stress intensity factor under external cyclic load and residual stress field, respectively. The fatigue life prediction for weld toe transverse cracks at web-to-base location was found to be overestimated by around 10~30% which is associated with high tensile residual stress and further relaxation under external cyclic load. No significant difference was found for the fatigue life prediction of head-to-web cracks when considering the residual stress due to the presence of compressive stress and the relaxation.

Chapter 7 Conclusions and Recommendations

7.1 Conclusions

The structural integrity assessment of the thermite welded rail joints taking account of the material characterization and behaviour, the presence of flaws or defects and residual stress field with respect to the potential failure modes by fracture or fatigue was conducted. Based on the objectives and the research work carried out, the following conclusions can be made:

1-a). The material characteristics across the thermite welded joint and its correlation with mechanical and fatigue properties were investigated. The microstructure of thermite weld metal and parent rail material was observed to be pearlitic with a small amount of proeutectoid ferrite decorated in the grain boundary. No martensite was formed due to the slow continuous cooling. Weld defects including pores (gas pores) and inclusions (Al_2O_3 and MnS) were found both in the weld metal and fusion line while solidification shrinkage cavities were found in the weld center. The weld defects lead to a reduction of fatigue limit, as well as the severe localized stress concentration that acts as potential crack initiation sites. From the finite element simulation, the debonding inclusions located at the rail/weld interface matrix is concluded to be a critical initiation site with the highest local stress concentration.

1-b). Thermite weld metal exhibited a lower fracture toughness with mild overmatched yield strength and low impact toughness compared to the parent rail metal. The hardness of thermite weld metal and fusion line is significantly higher than the parent rail due to the material overmatch. Two obvious variations of hardness were observed in the heat affect zone. The highest hardness at the FGHAZ which is associated with the finer grain size resulting from the recrystallization under steeper thermal gradient and the soften zone in the intercritical zone is because of the spheroidization of cementite. The fatigue crack growth rate for weld metal was found to be lower in the low-stress regime and higher in the high-stress regime. The fatigue crack propagation studies

revealed that moderate strength overmatch is beneficial for weld cracks. However, for interfacial cracks, this beneficial effect is lost, and cracks tend to grow toward the parent metal, away from the fusion line with a shorter fatigue crack propagation life.

1-c). The transverse fatigue cracking at the fusion line was identified and the fatigue cracking mechanism was discussed. It was shown that the embrittlement of the HAZ near the fusion line and the presence of welding defects are the major factors leading to fatigue crack initiation. Furthermore, the mildly overmatched yield strength influences the cracking growth path while the material fatigue properties affect the propagation rate. Hence, transverse fatigue cracking of the thermite welded joints first initiates near the fusion line and advances towards the parent rail away from the rail/weld interface. The crack then further propagates following the direction of maximum shear stress in the parent rail until the final fracture once the critical fracture toughness is reached.

2-a). A FEM-derived SIF solution of the geometry factor Y and weld magnification factor M_k was presented for transverse surface cracks in rail steels and thermite weld. Two loading conditions including in-plane and out-of-plane loading were studied for cracks located at five different locations of the transverse cross-section. These results provided important closed-form SIF solutions for surface cracks in the cross-section of rail steels and thermite weld. Experimental tests of fracture toughness and fatigue crack growth rates were conducted on weld metal material extracted from thermite welded joints samples. The plane strain fracture toughness and Paris' Law constants for thermite weld metal material were determined from fracture toughness and fatigue crack growth rate test results.

2-b). A fatigue crack growth life prediction algorithm a developed using two different surface crack growth numerical integration schemes: namely the uncoupled 2 DOF and coupled RMS schemes. The comparison was made between these two surface crack growth schemes and the

coupled RMS scheme was able to better predict the fatigue crack growth and shape evolution. The fatigue crack shape evolution with predicted fatigue cycles was investigated under different loading conditions. It was shown that irrespective of the initial crack shape and size, the transverse surface cracks in rail steel and thermite weld tended toward a near semi-circular shape when subject to in-plane loading condition and it will alter to semi-elliptical shape once under out-of-plane loads. This out-of-plane load, which is mainly found in curved or transition track of the railway system, is more critical due to the relatively faster growth rate, particularly in the surface width direction. The investigation on the fatigue crack growth life for weld metal cracks (WMCs) and weld toe cracks (WTCs) showed that the fatigue life of WMCs is longer at low stress condition but the life decrease more rapidly compared to WTCs once the stress level increase. Hence thermite welded joints are more susceptible to structural fatigue crack growth failures arising from weld toe defects, especially under high stress loading conditions.

3-a). Thermal elastoplastic and thermomechanical analysis were performed using FE techniques to evaluate the temperature evolution and residual stress field arising from the rail thermite welding process. The FE results were compared with experimental measurement and an accurate prediction has been achieved. The effect of the welding process parameters such as preheating time on the residual stress field was also investigated. The 3D residual stress relaxation model was built considering the initial residual stress state and the cyclic hardening behaviour of the material. It shows that the stabilization of residual stress occurs after the first cycle. An analytical model was proposed to predict the stress relaxation and it revealed that the extent of residual stress relaxation is affected by the material properties, initial residual stress, applied stress amplitude, and the number of cycles.

3-b). A comprehensive evaluation of the residual stress arising from the thermite welding process and stress relaxation under cyclic fatigue bend load is conducted. A reliable fatigue life prediction model considering the residual stress and its relaxation was then proposed. The influence of

residual stress and its relaxation on the fatigue life of thermite weld was investigated using the root mean square method and weight function to calculate the stress intensity factor under external cyclic load and residual stress field, respectively. The adopted method was found to provide a reasonable prediction of fatigue crack propagation life for transverse cracks at the thermite weld toe region. The fatigue life prediction for weld toe transverse cracks at web-to-base location was found to be overestimated by at least 50% which is associated with high tensile residual stress and further relaxation under external cyclic load. No obvious difference was found for the fatigue life prediction of head-to-web cracks when considering the residual stress due to the presence of compressive stress and the relaxation.

7.2 Recommendations for future research

The current work has conducted the structural integrity assessment of the thermite welded rail joints. Based on this, mechanical properties, material characterization, and finite element modelling have been obtained to understand the fracture and fatigue performance. Some further works are recommended based on the current researches as below:

1. The reason why the stress ratio R=0.1 is selected in the proposed fatigue model is because of : a) the convenience of validation since the fatigue testing from the existing literatures is basically conducted with the stress ratio of 0.1, b) and the stress ratio of R=0.1 of two separate loading meets the requirement for fatigue response analysis of cracks under quasi-static loading conditions within the current the structural integrity framework. Past researches always treat the rail bottom as the most critical area and only limited studies mentioned the transition areas (head-to-web and web-to-base), which were found to be also susceptible to fatigue cracking. Based on the existing literature, the dynamic deformation of the rail, which bents upwards and downwards with different amplitude resulting from wheel/rail contact, may be the cause for the cracking in the transition area, especially the head-to-web area. Since the cracks are unlikely to be found in the head-to-web

area under the normal bending load condition and the stress ratio R=-1 over-simplify the external loading when accounting for the quasi-static fatigue response, the two static bending loads with R=0.1 to make the welded rail bent upwards and downwards separately were simulated to consider the dynamic effect of the loading. Although some limitations exist in this thesis, the selection of R=0.1 is found to be reasonable for cracks under the specific loading conditions, and some useful conclusions were made using the proposed fatigue model with the selected R ratio. These conclusions and recommendations provide the novel and in-depth knowledge of the fatigue response of transverse surface cracks located at thermite welded joints and shed a light for the future works. Future researches including the investigation of the fatigue response of cracks under loading conditions with variant R ratio, and the dynamic fatigue behaviour of these cracks under the measured loading spectrum, are worth of the elaborated efforts.

2. A lot of uncertainties exist when applying the current fatigue model to predict the fatigue life of the transverse surface cracks located at the welded joint. It is difficult to justify which factor, among all the factors discussed in this thesis (material properties, initial crack size, crack growth direction, residual stress distribution), has the most influence on the uncertainty of the fatigue prediction algorithm. However, the comprehensive estimation of the effect of each factor and the investigation of how those factors contribute to the overall prediction uncertainties can be one of the directions that the future researches might work towards.

Besides, there are certain factors that have been neglected for the ease of analysis that may also cause the uncertainties to the final fatigue prediction First of all, when applying the weight function method to investigate the effect of residual stress on the fatigue behaviour of welded rail joints, only the tensile mode-I fracture condition was considered. Besides, the crack closure phenomenon when the cracks remain closed or partially closed in the compressive residual stress field was neglected and it also influences the fatigue propagation of the welded joint. Further

studies of the fatigue propagation behaviour taking account of complicated loading condition and crack closure phenomenon are needed.

Secondly, with the presence of welding defects and residual stress, the investigation of the fatigue crack initiation and short cracks propagation in the welded rail joint is of great significance for the accuracy of the total fatigue cracking life prediction. The risk of fatigue crack initiation and the associated critical locations of the transverse weld-toe fatigue failures can be determined through the stress/strain condition using the multi-axial fatigue criterion in future works.

3. For the current standard thermite welding process, the material defects including pores and inclusions cannot be completely avoided. Some improvements of the thermite welding process including the optimization of the welding process and the design of the sand mould to increase the quality of thermite welded joints can be investigated.

The optimization of the thermite welding process to suppress the formation of the welding inclusions as well as to eliminate the porosities or shrinkage cavities is possible which needs in-depth researches. Possible affecting factors including the preheating time and method, liquid metal temperature and weld gap, and the interaction between each of them are interesting areas that worth further investigation. One solution is the post heat treatment. The effectiveness of the improvements can be studied regarding the microstructure development of welding during the solidification process, the reduction of the metallurgical discontinuities such as pores and inclusion, and furthermore, the improvement of the fatigue endurance. Other surface mechanical treatments are possible such as the weld toe treatments by hammer peening and grinding at the critical areas of concern, such as web-to-head and web-to-base regions. The study of the peeing-induced surface residual stress and the investigation for fatigue life enhancement are also of great interest.

As for the design of the sand mould, it is related to the geometric features of the completed weld joint, more specifically, the weld collar shape and the weld toe geometry. During the thermite welding process, the molten metal is firstly poured into the sand mould and the rail head surface of the solidified weld is dressed and grinded back to the connected rail profile after the mould removal. However, other regions of the welded joint (the under-gauge area, the web, and the base bottom) are kept as the original shape after welding completed. Since the transverse fatigue cracks are mainly found to be initiated from the web and bottom areas, the weld shape has a significant effect on the fatigue performance of the welded joints. The researches to understand the effect of the sand mould geometries and the results weld metal features, such as completed weld collar size and weld toe profile, on the fatigue risk of the joint are also needed.

Appendix A MATLAB Code for Prediction of Fatigue Crack Propagation Life

```
function [output1] = FatigueRail ()
clc
format long

global thickness width deltaK applied_stressx applied_stressy
applied_stressz yield_stress CA_const M_const Tha_const Thc_const
UA_const UC_const output final_crack bending cracks mpdc10 LT
crack_size = [0.1 0.2 0.5];%inital crack size mm [0.1 0.2 0.5]
% applied_stress=input;
applied_stressx = 100; %100,200,300
applied_stressy = 0;
applied_stressz = 0;
%location
thickness = 30; %unit mm
width = 200;
cracks_number=1;
cracks = zeros(length(crack_size),1);
cracks(:,1) = (linspace(width/2-5*3*(cracks_number-
1),width/2+5*3*(cracks_number-1),cracks_number))';
final_crack = 20.0;
cracks(:,2) = crack_size;
yield_stress = 1175; % (MPa)880 for R260, 1175 for R350HT, 758 for
weld
CA_const =1.14e-16 ;%da/dn=mm/cycle, deltaK=Mpa(mm)-0.5,1.14e-16 For
R260, 3.45e-16 for R350HT, 3.28e-24 for weld dadn mm/cycle delta K MPa
mm^0.5
M_const =4.1 ; %4.1 for R260, 3.91 for R350HT, 7.22 for weld

z = 1;
cracks(:,3) = crack_size; %crack width
cracks(:,4) = 0; %cycle count
cracks(:,:,1) = sortrows(cracks(:,:,1)); %sort

while max(cracks(1,2,z))<=final_crack
    %propagate crack
    notzero=find(cracks(:,1,z))';
    for x = notzero(1,:)
        [da,dc,dna] =
growcrack(cracks(x,2,z),cracks(x,3,z),cracks(x,4,z));
        cracks(x,:,z+1) = [cracks(x,1,z) cracks(x,2,z)+da
cracks(x,3,z)+dc cracks(x,4,z)+dna];
    end
    z=z+1;
end
output=cracks(:,:,numel(cracks(1,1,:)):-20:1);%output for graph
ploting
plotcrack(); %plot graphs
end

function plotcrack()
global output thickness width final_crack cracks applied_stress
```

```
figure('units','normalized','outerposition',[0 0 1 1],'Color',[1.0 1.0
1.0]);

%plot a vs fatigue life
%subplot(2,2,1);
    % 1 curve
   if numel(output(1,2,1))~=1
        plot
(reshape(max(output(1,4,:)),[],1),reshape(max(output(1,2,:)),[],1),'r'
);
   else
        plot
(reshape(output(1,4,:),[],1),reshape(output(1,2,:),[],1),'r','LineWidt
h',2);
   end
    hold on
    % 2 curve
   if numel(output(2,2,1))~=1
        plot
(reshape(max(output(2,4,:)),[],1),reshape(max(output(2,2,:)),[],1),'g'
);
   else
        plot
(reshape(output(2,4,:),[],1),reshape(output(2,2,:),[],1),'--
g','LineWidth',2);
   end
    hold on
    % 3 curve
   if numel(output(3,2,1))~=1
        plot
(reshape(max(output(3,4,:)),[],1),reshape(max(output(3,2,:)),[],1),':b
');
   else
        plot
(reshape(output(3,4,:),[],1),reshape(output(3,2,:),[],1),':b','LineWid
th',2);
   end
   xlabel('Number of cycles'); % x-axis label
   ylabel('a'); % y-axis label
   axis ([0,1.02*max(output(1,4,:)), 0, 20.0]);
   set(gca, 'XScale', 'log');
   grid on;
   legend(sprintf('Initial a=0.1 mm, Predicted life = %.f
cycles',max(cracks(1,4,end))),sprintf('Initial a=0.2 mm, Predicted
life = %.f cycles',max(cracks(2,4,end))),sprintf('Initial a=0.5 mm,
Predicted life = %.f
cycles',max(cracks(3,4,end))),'Location','NorthEastOutside');%
   print -dpng 'plot1.png';


%plot a/c vs a/t
%subplot(2,2,2)
figure('units','normalized','outerposition',[0 0 1 1],'Color',[1.0 1.0
1.0]);

% 1 curve
```

```
cd=reshape(output(1,2,:),numel(output(1,1,1)),[]);
cw=reshape(output(1,3,:),numel(output(1,1,1)),[]);
plot (cd(1,:),cd(1,:)./cw(1,:),'r','LineWidth',2);
hold on;
% 1 curve
cd=reshape(output(2,2,:),numel(output(1,1,1)),[]);
cw=reshape(output(2,3,:),numel(output(1,1,1)),[]);
plot (cd(1,:),cd(1,:)./cw(1,:),'--g','LineWidth',2);
hold on;
% 1 curve
cd=reshape(output(3,2,:),numel(output(1,1,1)),[]);
cw=reshape(output(3,3,:),numel(output(1,1,1)),[]);
plot (cd(1,:),cd(1,:)./cw(1,:),':b','LineWidth',2);
hold on;

xlabel('a'); % x-axis label
ylabel('a/c'); % y-axis label
axis([0.1,final_crack,0,1.1*max(cd(1,:)./cw(1,:)),]);
 legend(sprintf('Initial a=0.1
mm',max(cracks(1,4,end))),sprintf('Initial a=0.2
mm',max(cracks(2,4,end))),sprintf('Initial a=0.5
mm',max(cracks(3,4,end))),'Location','NorthEastOutside');%
print -dpng 'plot2.png';

figure(); %plot crack shape
for z = 1:3:numel(output(1,1,:))
    for x = 1:numel(output(:,1,1))
        if output(x,1,z)~=0
            plotshape(output(x,3,z),output(x,2,z),[output(x,1,z),0],
'blue');
            hold on;
        end
    end
end
axis([0,width,-thickness,thickness]);
xlabel('Width'); % x-axis label
ylabel('Thickness'); % y-axis label
title(sprintf('Stress range = %.1f MPa', applied_stress))

end

function [da,dc,dna] = growcrack(crack_depth,crack_width,cycle_number)
global thickness width applied_stress yield_stress angel CA_const
M_const Tha_const Thc_const UA_const UC_const bending LT
applied_stressx applied_stressy applied_stressz
    a = crack_depth;
    length = 0.01*a:0.1*a:0.99*a;
    c = crack_width;
    at = a/16.5;
    ac = a/c;
    theta = 0.4: 0.1: 3.5;
    z = ((sin
(theta)).^2+(ac).^0.5.*(cos(theta)).^2).^0.25./(sqrt(1+1.464.*(ac)^1.6
5))/0.6371;

    %%residusl stress
```

```
    %consider initial stress after relaxed
    %rs=0; %no residual stress effect
    %rs =(0.7328.*a^2-51.583.*a+264.6); %relaxed after 1st cycle 16t
    %rs =(-1.2344.*a^2+8.6111.*a+289.9); %relaxed after 1st cycle 12t
    rs = (-0.9893.*a^2+2.8544.*a+312.4); %relaxed after 1st cycle 8t
    rs = rs*(rs>0);%if rs is compressive, force to 0

%paramters for Y factor for web-to-base cracks
if crack_depth > 1 %for crack size large than 1
    px=0.607;
    nx=0.080;
    ax=-0.112;
    bx=0.111;
    cx=2.240;
    py=0.281;
    ny=-0.553;
    ay=1.196;
    by=-0.258;
    cy=-1.082;
    pz=0.686;
    nz=0.060;
    az=-0.332;
    bz=0.340;
    cz=-0.435;
else %for crack size smaller than 1
    px=0.643;
    nx=-0.002;
    ax=-40.028;
    bx=761.947;
    cx=0.075;
    py=0.693;
    ny=0.027;
    ay=52.387;
    by=-676.227;
    cy=-0.169;
    pz=0.697;
    nz=0.017;
    az=11.706;
    bz=-106.053;
    cz=-0.045;
end
    fx = 1.0 + (0.1+ax*at^2+bx*at^3).*((1-sin(theta+cx)).^2);
    qx = px*(at)^nx;
    fy = 1.0 + (0.1+ay*at^2+by*at^3).*((1-sin(theta+cy)).^2);
    qy = py*(at)^ny;
    fz = 1.0 + (0.1+az*at^2+bz*at^3).*((1-sin(theta+cz)).^2);
    qz = pz*(at)^nz;

    % Mk factor, only applicable for crack size smaller than 10 mm
if at < 0.6061
    hx = fx.*qx.*(0.9644*(at)^(-0.123)); %0.8757for 0.1mm 0.4379 for
0.5mm
    hy = fy.*qy.*(0.9644*(at)^(-0.123));
    hz = fz.*qz.*(0.9644*(at)^(-0.123));
else
```

```
    hx = fx.*qx;
    hy = fy.*qy;
    hz = fz.*qz;
end
%     hx = fx.*qx;
%     hy = fy.*qy;
%     hz = fz.*qz;

%weight function calculation

% ma
if a/25.0 < 0.8
    A0 = 1.0929+0.2581*(ac)-0.7703*(ac)^2+0.4394*(ac)^3;
    A1 = 0.456-3.045*(ac)-2.007*(ac)^2+(0.147+(ac)^0.688)^-1;
    A2 = 0.995-(0.027+(ac))^-1+22*(1-(ac))^9.953;
    A3 = -1.459+(0.014+(ac))^-1-24.211*(1-(ac))^8.071;
    Y0 = A0+A1*(a/25.0)^2+A2*(a/25.0)^4+A3*(a/25.0)^6;

    B0 = 0.4537+0.1231*(ac)-0.7412*(ac)^2+0.460*(ac)^3;
    B1 = -1.652+1.665*(ac)-0.534*(ac)^2+(0.198+(ac)^0.846)^-1;
    B2 = 3.148-3.126*(ac)-(0.041+(ac))^-1+17.259*(1-(ac))^9.286;
    B3 = -4.228+3.643*(ac)+(0.020+(ac))^-1-21.924*(1-(ac))^9.203;
    Y1 = B0+B1*(a/25.0)^2+B2*(a/25.0)^4+B3*(a/25.0)^6;

    Q = 1+1.464*(ac)^1.65;

    M1A = 2*pi*(2*Q)^-0.5*(2*Y0-3*Y1)-24/5;
    M2A = 3;
    M3A = 6*pi*(2*Q)^-0.5*(2*Y1-Y0)+8/5;
%mc
    C0 = 1.29782-0.1548*(ac)-0.0185*(ac)^2;
    C1 = 1.5083-1.3219*(ac)+0.5128*(ac)^2;
    C2 = -1.101-0.879*(0.157+(ac))^-1;
    F0 = (C0+C1*(a/25.0)^2+C2*(a/25.0)^4)*(ac)^0.5;

    D0 = 1.2687-1.0642*(ac)+1.4646*(ac)^2-0.7250*(ac)^3;
    D1 = 1.1207-1.2289*(ac)+0.5876*(ac)^2;
    D2 = 0.190-0.608*(ac)+0.199*(0.035+(ac))^-1;
    F1 = (D0+D1*(a/25.0)^2+D2*(a/25.0)^4)*(ac)^0.5;

    M1C = 3*pi*(Q)^-0.5*(5*F1-3*F0)-8;
    M2C = 15*pi*(Q)^-0.5*(2*F0-3*F1)+15;
    M3C = 3*pi*(Q)^-0.5*(10*F1-7*F0)-8;
%m(x,a) m(x,c)
    qxa = (1+M1A*(1-length/a).^0.5+M2A*(1-length/a)+M3A*(1-
length/a).^1.5);
    qxc = (1+M1C*(length/a).^0.5+M2C*(length/a)+M3C*(length/a).^1.5);
    mxa = rs*(1-length/a).^3.*(2*(2*pi*(a-length)).^-0.5).*qxa; %unit
    mxc = rs*(1-length/a).^3.*(2*(2*pi*(a-length)).^-0.5).*qxc; %unit

    Qmxa = trapz(mxa*0.1*a); %unit conversion from m to mm
    Qmxc = trapz(mxc*0.1*a); %unit
else
    Qmxa = 0; %unit conversion from m to mm 100MPa residual stress
    Qmxc = 0;
end
```

```
%     Qmxa = 0; %unit conversion from m to mm 100MPa residual stress
%     Qmxc = 0;
%correction for different shape

    %stress ratio
    R=0.1;

    SIFxmax  = applied_stressx*(sqrt(pi*crack_depth)).*hx.*z;
    SIFxmin  = R*applied_stressx*(sqrt(pi*crack_depth)).*hx.*z;  %K_a
    SIFymax  = applied_stressy*(sqrt(pi*crack_depth)).*hy.*z;   %K_a
    SIFymin  = R*applied_stressy*(sqrt(pi*crack_depth)).*hy.*z;
    SIFzmax  = applied_stressz*(sqrt(pi*crack_depth)).*hz.*z;   %K_a
    SIFzmin  = R*applied_stressz*(sqrt(pi*crack_depth)).*hz.*z;   %K_a


    RMSax = (SIFx).^2.*(sin(theta-0.4)).^2; %value before integral
    RMScx = (SIFx).^2.*(cos(theta-0.4)).^2;
    %value before integral
    RMSax = (SIFxmax-SIFxmin).^2.*(sin(theta-0.4)).^2;
    RMScx = (SIFxmax-SIFxmin).^2.*(cos(theta-0.4)).^2;
    RMSaxmax = (SIFxmax).^2.*(sin(theta-0.4)).^2;
    RMScxmax = (SIFxmax).^2.*(cos(theta-0.4)).^2;


    RMSay = (SIFy).^2.*(sin(theta-0.4)).^2; %value before integral
    RMScy = (SIFy).^2.*(cos(theta-0.4)).^2;
    RMSaz = (SIFz).^2.*(sin(theta-0.4)).^2; %value before integral
    RMScz = (SIFz).^2.*(cos(theta-0.4)).^2;


    QRMSax = trapz(RMSax*0.1);
    QRMScx = trapz(RMScx*0.1);
    QRMSaxmax = trapz(RMSaxmax*0.1);
    QRMScxmax = trapz(RMScxmax*0.1);

    QRMSay = trapz(RMSay*0.1);
    QRMScy = trapz(RMScy*0.1);
    QRMSaz = trapz(RMSaz*0.1);
    QRMScz = trapz(RMScz*0.1);

if (rs)
    ESIFAWx =
sqrt(QRMSax/pi*2)*(sqrt(QRMSax/pi*2)/(sqrt(QRMSaxmax/pi*2)+Qmxa))^(0.8
2-1);
    ESIFCWx =
sqrt(QRMScx/pi*2)*(sqrt(QRMScx/pi*2)/(sqrt(QRMScxmax/pi*2)+Qmxc))^(0.8
2-1);%delta_K_a
else
    ESIFAWx = sqrt(QRMSax/pi*2); %delta_K_a
    ESIFCWx = sqrt(QRMScx/pi*2);
end

    ESIFAWy = sqrt(QRMSay/pi*2); %delta_K_a
    ESIFCWy = sqrt(QRMScy/pi*2);
    ESIFAWz = sqrt(QRMSaz/pi*2); %delta_K_a
    ESIFCWz = sqrt(QRMScz/pi*2);
```

```
%stress intensity factor a & c
ESIFAW = ESIFAWx+ESIFAWy+ESIFAWz; %delta_K_a
ESIFCW = ESIFCWx+ESIFCWy+ESIFCWz; %delta_K_c

% Crack Propagation calculation
da = 0.001*crack_depth;
dna = da/(CA_const.*((ESIFAW)^M_const));
dc = dna*(CA_const).*(ESIFCW.^M_const);  %dc =
dna*24.0*(CA_const*0.9^M_const).*(ESIFCW.^M_const);
end

function [output2] = colour(input)
    global mpdc10
    output2 = mpdc10(input,:);
end

function plotshape(a,b,C,colour) %function to plot crack shape

    % range to plot over
    %-------------------------------------
    N = 10;
    theta = 0:1/N:2*pi+1/N;

    % Parametric equation of the ellipse
    %-----------------------------------------
    state(1,:) = a*cos(theta);
    state(2,:) = b*sin(theta);

    % Coordinate transform (since your ellipse is axis aligned)
    %-----------------------------------------
    X = state;
    X(1,:) = X(1,:) + C(1);
    X(2,:) = X(2,:) + C(2);

    % Plot
    %-----------------------------------------
    plot(X(1,:),X(2,:),'Color', colour,'LineWidth',2.0);
    hold on;
%     plot(C(1),C(2),'r*');
    axis equal;
    grid;
end
```

Appendix B Articles Published During This PhD Research

Published Journal Papers:

1. Y. Liu, K. S. Tsang, N. A. Subramaniam, J. H. L. Pang, “Structural fatigue investigation of thermite welded rail joints considering weld-induced residual stress and stress relaxation by cyclic load”, Engineering Structures, Volume 235, 2021, 112033, ISSN 0141-0296, (Q1, IF: 3.548)

2. Y. Liu, K. S. Tsang, E. Z. Tan, N. A. Subramaniam, J. H. L. Pang, “Investigation on material characteristics and fatigue crack behavior of thermite welded rail joint”, Construction and Building Materials, Volume 276, 2021, 122249, ISSN 0950-0618, (Q1, IF: 4.419)

3. Y. Liu, K. S. Tsang, H. J. Hoh, X. Shi, and J. H. L. Pang, "Structural fatigue investigation of transverse surface crack growth in rail steels and thermite welds subjected to in-plane and out-of-plane loading," *Engineering Structures,* vol. 204, p. 110076, 2020. (Q1, IF: 3.548)

4. X. Shi, Y. Liu, Z. Liu, H. J. Hoh, K. S. Tsang, and J. H. L. Pang, "An integrated fatigue assessment approach of rail welds using dynamic 3D FE simulation and strain monitoring technique," *Engineering Failure Analysis,* p. 105080, 2020. (Q1, IF: 2.897)

5.. Liu, Z, Tsang, KS, Liu, Y, Pang, JHL. “Finite element and experimental study on multiaxial fatigue analysis of rail clip failures”, *Fatigue Fract. Eng. Mater Struct*., 2020, 43: 2390– 2401. (Q1, IF: 3.031)

Conference Papers:

6. Y. Liu et al., "Mechanical Properties and Microstructural Analysis of Rail Thermite Welding Joints," in *the 2018 International Conference on Intelligent Rail Transportation (ICIRT),* 12-14 Dec. 2018, 2018, pp. 1-4.

7. Y. Liu, X. Sun, and J. H. L. Pang, "A YOLOv3-based Deep Learning Application Research for Condition Monitoring of Rail Thermite Welded Joints," presented at the Proceedings of *the 2020 2nd International Conference on Image, Video and Signal Processing, Singapore*, 2020

8. X. P. Shi *et al.*, "Wireless Strain Sensors for Dynamic Stress Analysis of Rail Steel Structural Integrity," in *Advances in Condition Monitoring and Structural Health Monitoring*, Singapore, 2021, pp. 471-480: Springer Singapore.

References

[1] R. Lewis and U. Olofsson, *Wheel/Rail Interface*. Cambridge: Woodhead Pub., 2009.

[2] U. Zerbst, M. Schödel, and R. Heyder, "Damage Tolerance Investigations on Rails," *Engineering Fracture Mechanics,* vol. 76, no. 2637-2653, 2009.

[3] B. L. Josefson and J. W. Ringsberg, "Assessment of uncertainties in life prediction of fatigue crack initiation and propagation in welded rails," *International Journal of Fatigue,* vol. 31, no. 8, pp. 1413-1421, 2009/08/01/ 2009.

[4] A. Skyttebol, B. L. Josefson, and J. W. Ringsberg, "Fatigue crack growth in a welded rail under the influence of residual stresses," *Engineering Fracture Mechanics,* vol. 72, no. 2, pp. 271-285, 2005/01/01/ 2005.

[5] T. Bonniot, V. Doquet, and S. H. Mai, "Mixed mode II and III fatigue crack growth in a rail steel," *International Journal of Fatigue,* vol. 115, pp. 42-52, 2018/10/01/ 2018.

[6] W. J. Jiang, C. Liu, C. G. He, J. Guo, W. J. Wang, and Q. Y. Liu, "Investigation on impact wear and damage mechanism of railway rail weld joint and rail materials," *Wear,* vol. 376-377, pp. 1938-1946, 2017/04/15/ 2017.

[7] A. Caprioli, A. Cigada, and D. Raveglia, "Rail inspection in track maintenance: A benchmark between the wavelet approach and the more conventional Fourier analysis," *Mechanical Systems and Signal Processing,* vol. 21, no. 2, pp. 631-652, 2007/02/01/ 2007.

[8] Kenji SAITA and K. KARIMINE, "Trends in Rail Welding Technologies and Our Future Approach," in "Nippon Steel & Sumitomo Metal Technical Report " 2013, vol. No. 105.

[9] I. Salehi, A. Kapoor, and P. Mutton, "Multi-axial fatigue analysis of aluminothermic rail welds under high axle load conditions," *International Journal of Fatigue,* vol. 33, no. 9, pp. 1324-1336, 2011/09/01/ 2011.

[10] R. K. Steele, "Field Welding of Rails," in "Association of American Railroads Report," Chicago, IL1985, vol. No. R-618.

[11] L. Schroeder and D. Poirier, "The Mechanical Properties Of Thermite Welds In Premium Alloy Rails," *Materials Science and Engineering,* vol. 63(1) pp. 1-21, 1984.

[12] K. Zhou *et al.*, "A review of recent works on inclusions," *Mechanics of Materials,* vol. 60, pp. 144-158, 2013/07/01/ 2013.

[13] M. Jezzini-Aouad, P. Flahaut, S. Hariri, D. Zakrzewski, and L. Winiar, "Improving Fatigue Performance of Alumino-Thermic Rail Welds," *Applied Mechanics and Materials,* vol. 24-25, pp. 305-310, 2010.

[14] N. Ilić, M. T. Jovanović, M. Todorović, M. Trtanj, and P. Šaponjić, "Microstructural and Mechanical Characterization of Postweld Heat-Treated Thermite Weld in Rails," *Materials Characterization,* vol. 43, no. 4, pp. 243-250, 1999/10/01/ 1999.

[15] K. V. Redkin, C. I. Garcia, and A. J. DeArdo, "Microstructural Analysis of Thermite Welds," in *ASME 2010 Rail Transportation Division Fall Technical Conference*, 2010, vol. ASME 2010 Rail Transportation Division Fall Technical Conference, pp. 1-8.

[16] J. A. Oderio, "A Metallurgical Study of the Detail Fractures in Thermite-welded Railroad Rails," Master of Science, Department of Materials Science and Engineering, University of Illinois, Urbana, Illinois, 1991.

[17] *BS EN 13674-1:2011+A1:2017 Railway applications -Track - Rail*, 2017.

[18] Y.-q. Wang, H. Zhou, Y.-j. Shi, and B.-r. Feng, "Mechanical properties and fracture toughness of rail steels and thermite welds at low temperature," *International Journal of Minerals, Metallurgy, and Materials,* vol. 19, no. 5, pp. 409-420, 2012/05/01 2012.

[19] *BS EN 14730-1-2017 Railway application - Track - Aluminothermic welding of rails*, 2017.

[20] A. S. J. A. Z. Jilabi, "Welding of Rail Steels," PhD, Faculty of Engineering and Physical Sciences, University of Manchester, 2015.

[21] D. A. Brandt and J. C. Warner, *Metallurgy fundamentals : ferrous and nonferrous*, Sixth edition ed. Tinley Park, IL: The Goodheart-Willcox Company, Inc., 2021.

[22] J. Myers, G. H. Geiger, and D. R. Poirier, "Structure and Properties of Thermite Welds in Rails," *Welding Research Supplement,* pp. 258-268, 1982.

[23] *E399-17.Standard Test Method for Linear-Elastic Plane-Strain Fracture Toughness Kic of Metallic Materials*, 2017.

[24] *ASTM E647 - 15e1 Standard Test Method for Measurement of Fatigue Crack Growth Rates*, 2015.

[25] A. Motameni and A. N. Eraslan, "Fracture and Fatigue Crack Growth Characterization of Conventional and Head Hardened Railway Rail Steels," *Journal of Scientific and Engineering Research,* vol. 3(3), pp. 367-376, 2016.

[26] J. I. Vercleja, J. O. García, D. Plaza, and J. A. Pero-Sanz, "Fatigue test of aluminothermic welded rails," presented at the RDM Revista de Minas, 2000.

[27] Frederick V. Lawrence, Eric T. Ross, and C. P. L. Barkan, "Reliability of Improved Thermite Welds," University of Illinois at Urbana Champaign Illinois, US2004.

[28] Y. Chen, F. V. Lawrence, C. P. L. Barkan, and J. A. Dantzig, "Weld defect formation in rail thermite welds," *Proceedings of the Institution of Mechanical Engineers, Part F: Journal of Rail and Rapid Transit,* vol. 220, no. 4, pp. 373-384, 2006.

[29] Y. Liu, K. S. Tsang, H. J. Hoh, X. Shi, and J. H. L. Pang, "Structural fatigue investigation of transverse surface crack growth in rail steels and thermite welds subjected to in-plane and out-of-plane loading," *Engineering Structures,* vol. 204, p. 110076, 2020.

[30] C. Shao, H. Cui, F. Lu, and Z. Li, "Quantitative relationship between weld defect characteristic and fatigue crack initiation life for high-cycle fatigue property," *International Journal of Fatigue,* vol. 123, pp. 238-247, 2019.

[31] Z. Mikulski and T. Lassen, "Fatigue crack initiation and subsequent crack growth in fillet welded steel joints," *International Journal of Fatigue,* vol. 120, pp. 303-318, 2019/03/01/ 2019.

[32] P. J. Mutton and E. F. Alvarez, "Failure modes in aluminothermic rail welds under high axle load conditions," *Engineering Failure Analysis,* vol. 11, no. 2, pp. 151-166, 2004/04/01/ 2004.

[33] M. T. Yoshihiro Terashita, "Analysis of Damaged Rail Weld," *QR of RTRI,* vol. 44, no. 2, 2003.

[34] W. W. Hay, *Railroad engineering*. New York: John Wiley & Sons, 1982.

[35] I. Salehi, P. Mutton, and A. Kapoor, "The effect of geometric features on multi-axial fatigue behaviour of aluminothermic rail welds," *Proceedings of the Institution of Mechanical Engineers, Part F: Journal of Rail and Rapid Transit,* vol. 226, no. 4, pp. 360-370, 2012.

[36] H. Shitara, Y. Terashita, M. Tatsumi, and Y. Fukada, "Nondestructive Testing and Evaluation Methods for Rail Welds in Japan," *Quarterly Report of Rtri,* vol. 44, pp. 53-58, 05/01 2003.

[37] O. M. Akselsen, Ø. Grong, and J. K. Solberg, "Structure-property relationships in intercritical heat affected zone of low-carbon microalloyed steels," (in English), *Materials Science and Technology (United Kingdom),* Article vol. 3, no. 8, pp. 649-655, 01 / 01 / 1987.

[38] S. Kittima, M. Yoshiharu, M. Yukio, and S. Nobushiro, "Fatigue Strength Estimation Based on Local Mechanical Properties for Aluminum Alloy FSW Joints," *Materials (1996-1944),* Article vol. 10, no. 2, p. 186, 2017.

[39] Y. Wang, R. Kannan, and L. Li, "Identification and Characterization of Intercritical Heat-Affected Zone in As-Welded Grade 91 Weldment," *Metallurgical and Materials Transactions A,* journal article vol. 47, no. 12, pp. 5680-5684, December 01 2016.

[40] T. Nykänen, G. Marquis, and T. Björk, "Fatigue analysis of non-load-carrying fillet welded cruciform joints," *Engineering Fracture Mechanics,* vol. 74, no. 3, pp. 399-415, 2007/02/01/ 2007.

[41] P. K. Singh, K. K. VAZE, A. K. Ghosh, H. S. Kushwaha, D. M. Pukazhendi, and D. S. R. Murthy, "Crack resistance of austenitic stainless steel pipe and pipe welds with a circumferential crack under monotonic loading," *Fatigue & Fracture of Engineering Materials & Structures,* vol. 29, no. 11, pp. 901-915, 2006.

[42] C. M. Sonsino, "Fatigue testing under variable amplitude loading," *International Journal of Fatigue,* vol. 29, no. 6, pp. 1080-1089, 2007/06/01/ 2007.

[43] R. Sunder, A. Biakov, A. Eremin, and S. Panin, "Synergy of crack closure, near-tip residual stress and crack-tip blunting in crack growth under periodic overloads – A fractographic study," *International Journal of Fatigue,* vol. 93, pp. 18-29, 2016/12/01/ 2016.

[44] G. T. Fry, F. V. Lawrence, and A. R. Robinson, "A Model for Fatigue Defect Nucleation in Thermite Rail Welds," *Fatigue & Fracture of Engineering Materials & Structures,* vol. 19, no. 6, pp. 655-668, 1996.

[45] S. Luo, B. Wang, Z. Wang, D. Jiang, W. Wang, and M. Zhu, "Morphology of Solidification Structure and MnS Inclusion in High Carbon Steel Continuously Cast Bloom," *ISIJ International,* vol. 57, no. 11, pp. 2000-2009, 2017.

[46] J. M. Zhang, S. X. Li, Z. G. Yang, G. Y. Li, W. J. Hui, and Y. Q. Weng, "Influence of inclusion size on fatigue behavior of high strength steels in the gigacycle fatigue regime," *International Journal of Fatigue,* vol. 29, no. 4, pp. 765-771, 2007/04/01/ 2007.

[47] H. L. J. Pang and T. G. F. Gray, "FATIGUE ANALYSIS OF SURFACE CRACKS AT FILLET WELDED TOES," *Fatigue & Fracture of Engineering Materials & Structures,* vol. 16, no. 2, pp. 151-164, 1993.

[48] K. Dang Van, M. H. Maitournam, Z. Moumni, and F. Roger, "A comprehensive approach for modeling fatigue and fracture of rails," *Engineering Fracture Mechanics,* vol. 76, no. 17, pp. 2626-2636, 2009/11/01/ 2009.

[49] H. Desimone and S. Beretta, "Mechanisms of mixed mode fatigue crack propagation at rail butt-welds," *International Journal of Fatigue,* vol. 28, no. 5, pp. 635-642, 2006/05/01/ 2006.

[50] C. m. lee, J. L. Rose, and Y. Cho, "A guided wave approach to defect detection under shelling in rail," *NDT & E International,* vol. 42, no. 3, pp. 174-180, 2009/04/01/ 2009.

[51] Y. Liu, L. Liu, and S. Mahadevan, "Analysis of subsurface crack propagation under rolling contact loading in railroad wheels using FEM," *Engineering Fracture Mechanics,* Article vol. 74, no. 17, pp. 2659-2674, 2007.

[52] E. Magel, P. Mutton, A. Ekberg, and A. Kapoor, "Rolling contact fatigue, wear and broken rail derailments," *Wear,* vol. 366-367, pp. 249-257, 2016/11/15/ 2016.

[53] D. Nikas, "Influence of combined thermal and mechanical loadings on pearlitic steel microstructure in railway wheels and rails," DOCTOR OF PHILOSOPHY, Department of Industrial and Materials Science, CHALMERS UNIVERSITY OF TECHNOLOGY, Gothenburg, Sweden, ISBN 978-91-7597-801-7, 2018.

[54] D. Peng, R. Jones, and T. Constable, "An investigation of the influence of rail chill on crack growth in a railway wheel due to braking loads," *Engineering Fracture Mechanics,* vol. 98, pp. 1-14, 2013/01/01/ 2013.

[55] J. H. Bulloch, "Fatigue crack growth studies in rail steels and associated weld metal," *Theoretical and Applied Fracture Mechanics,* vol. 6, no. 2, pp. 75-84, 1986/10/01/ 1986.

[56] M. Cevdet and E. Turgut, "THE METALLURGICAL SPECIFICATIONS AND HARDNESS PROFILE OF A RAIL THERMITE WELD," *Pamukkale University Journal of Engineering Sciences, Vol 4, Iss 2, Pp 649-654 (1998),* article no. 2, p. 649, 1998.

[57] M. Dollar, I. Bernstein, and A. Thompson, "Influence of deformation substructure on flow and fracture of fully pearlitic steel," *Acta Metallurgica,* vol. 36, no. 2, pp. 311-320, 1988.

[58] K. E. Easterling, *Introduction to the physical metallurgy of welding*. Burlington: Butterworth Heinemann/Elsevier Science, 2013.

[59] H. O. Fuchs and R. I. Stephens, *Metal fatigue in engineering*. New York ; Toronto: J. Wiley., 2001.

[60] H. Granjon, *Fundamentals of welding metallurgy*. Cambridge: Abington Pub., 2002.

[61] C. Esveld, *Modern Railway Track*. MRT-Productions, 1989.

[62] U. Zerbst and S. Beretta, "Failure and damage tolerance aspects of railway components," *Engineering Failure Analysis,* vol. 18, no. 2, pp. 534-542, 2011/03/01/ 2011.

[63] D. I. Fletcher and A. Kapoor, "Rapid method of stress intensity factor calculation for semi-elliptical surface breaking cracks under three-dimensional contact loading," *Proceedings of the Institution of Mechanical Engineers, Part F: Journal of Rail and Rapid Transit,* vol. 220, no. 3, pp. 219-234, 2006.

[64] P. J. Webster, X. Wang, G. Mills, and G. A. Webster, "Residual stress changes in railway rails," *Physica B: Condensed Matter,* vol. 180-181, pp. 1029-1031, 1992/06/02/ 1992.

[65] T. Tankova *et al.*, "Residual stresses in welded I section steel members," *Engineering Structures,* vol. 197, p. 109398, 2019/10/15/ 2019.

[66] X. Liu and K.-F. Chung, "Experimental and numerical investigation into temperature histories and residual stress distributions of high strength steel S690 welded H-sections," *Engineering Structures,* vol. 165, pp. 396-411, 2018/06/15/ 2018.

[67] A. Volkwein, K. Osterminski, F. Meyer, and C. Gehlen, "Distribution of residual stresses in reinforcing steel bars," *Engineering Structures,* vol. 223, p. 111140, 2020/11/15/ 2020.

[68] Y.-F. Hu, K.-F. Chung, H. Ban, and D. A. Nethercot, "Investigations into residual stresses in S690 cold-formed circular hollow sections due to transverse bending and longitudinal welding," *Engineering Structures,* vol. 219, p. 110911, 2020/09/15/ 2020.

[69] P. J. Webster, G. Mills, X. D. Wang, W. P. Kang, and T. M. Holden, "Residual stresses in alumino-thermic welded rails," *The Journal of Strain Analysis for Engineering Design,* vol. 32, no. 6, pp. 389-400, 1997.

[70] D. Yin, D. Wang, W. Li, X. Li, H. Zhang, and S. Naher, "Development of a new 3D model for the prediction of residual stress and fracture behaviour in Ti-6Al-4V after ultrasonic peening treatment," *Journal of Materials Processing Technology,* vol. 247, pp. 29-39, 2017/09/01/ 2017.

[71] Y. Chen, F. V. Lawrence, C. P. L. Barkan, and J. A. Dantzig, "Heat transfer modelling of rail thermite welding," *Proceedings of the Institution of Mechanical Engineers, Part F: Journal of Rail and Rapid Transit,* vol. 220, no. 3, pp. 207-217, 2006.

[72] A. Moarrefzadeh, "Study of Heat Affected Zone (HAZ) in Thermit Welding Process," *International Journal Of Multidisciplinary Sciences And Engineering,* vol. 2, no. 7, 2011.

[73] S. Manzke, I. Riehl, T. Fieback, and U. Gross, "A Reduced Numerical Model for the Thermit Rail Welding Process," *Heat Transfer Engineering,* vol. 39, no. 13-14, pp. 1296-1307, 2018/08/27 2018.

[74] Z. Zeng, L. Wang, P. Du, and X. Li, "Determination of welding stress and distortion in discontinuous welding by means of numerical simulation and comparison with experimental measurements," *Computational Materials Science,* vol. 49, no. 3, pp. 535-543, 2010/09/01/ 2010.

[75] D. Tawfik, P. J. Mutton, and W. K. Chiu, "Experimental and numerical investigations: Alleviating tensile residual stresses in flash-butt welds by localised rapid post-weld heat treatment," *Journal of Materials Processing Technology,* vol. 196, no. 1, pp. 279-291, 2008/01/21/ 2008.

[76] N. Tuchkova, "Prozessanalyse und Simulationstechnische Optimierung Des Aluminothermischen Schweißens von Schienen," Ph.D., Otto-von-Guericke-University Magdeburg, Germany, 2011.

[77] J.-C. Kim, S.-K. Cheong, and H. Noguchi, "Residual stress relaxation and low- and high-cycle fatigue behavior of shot-peened medium-carbon steel," *International Journal of Fatigue,* vol. 56, pp. 114-122, 2013/11/01/ 2013.

[78] R. Pan, T. Pirling, J. Zheng, J. Lin, and C. M. Davies, "Quantification of thermal residual stresses relaxation in AA7xxx aluminium alloy through cold rolling," *Journal of Materials Processing Technology,* vol. 264, pp. 454-468, 2019/02/01/ 2019.

[79] H. Desimone, A. Bernasconi, and S. Beretta, "On the application of Dang Van criterion to rolling contact fatigue," *Wear,* vol. 260, no. 4, pp. 567-572, 2006/02/24/ 2006.

[80] L. B. Godefroid, L. P. Moreira, T. C. G. Vilela, G. L. Faria, L. C. Candido, and E. S. Pinto, "Effect of chemical composition and microstructure on the fatigue crack growth resistance of pearlitic steels for railroad application," *International Journal of Fatigue,* vol. 120, pp. 241-253, 2019/03/01/ 2019.

[81] J. Debehets *et al.*, "Analysis of the variation in nanohardness of pearlitic steel: Influence of the interplay between ferrite crystal orientation and cementite morphology," *Materials Science and Engineering: A,* vol. 616, pp. 99-106, 2014/10/20/ 2014.

[82] A. Kumar, G. Agarwal, R. Petrov, S. Goto, J. Sietsma, and M. Herbig, "Microstructural evolution of white and brown etching layers in pearlitic rail steels," *Acta Materialia,* vol. 171, pp. 48-64, 2019/06/01/ 2019.

[83] J.-K. Kim and C.-S. Kim, "Fatigue crack growth behavior of rail steel under mode I and mixed mode loadings," *Materials Science and Engineering: A,* vol. 338, no. 1, pp. 191-201, 2002/12/15/ 2002.

[84] S. M. Hasan, M. Ghosh, D. Chakrabarti, and S. B. Singh, "Development of continuously cooled low-carbon, low-alloy, high strength carbide-free bainitic rail steels," *Materials Science and Engineering: A,* vol. 771, p. 138590, 2020/01/13/ 2020.

[85] W. Hui, Z. Xu, Y. Zhang, X. Zhao, C. Shao, and Y. Weng, "Hydrogen embrittlement behavior of high strength rail steels: A comparison between pearlitic and bainitic microstructures," *Materials Science and Engineering: A,* vol. 704, pp. 199-206, 2017/09/17/ 2017.

[86] Y. Sarikavak, O. S. Turkbas, and C. Cogun, "Influence of welding on microstructure and strength of rail steel," *Construction and Building Materials,* vol. 243, p. 118220, 2020/05/20/ 2020.

[87] F. C. O. Robles Hernandez, Anderson O, "Laser Cladding of Welds to Improve Railroad Track Safety," University of Houston, Texas, Houston, Texas2015.

[88] C. Meriç, E. Atık, and S. Şahın, "Mechanical and metallurgical properties of welding zone in rail welded via thermite process," *Science and Technology of Welding and Joining,* vol. 7, no. 3, pp. 172-176, 2002/06/01 2002.

[89] B. Younise *et al.*, "Micromechanical analysis of mechanical heterogeneity effect on the ductile tearing of weldments," *Materials & Design,* vol. 37, pp. 193-201, 2012/05/01/ 2012.

[90] M. S. Sichani and B. Yann, "Differential wear modelling – Effect of weld-induced material inhomogeneity on rail surface quality," *Wear,* vol. 406-407, pp. 43-52, 2018/07/15/ 2018.

[91] J. Schijve, *Fatigue of structures and materials*. Dordrecht: Springer, 2014.

[92] A. K. Motarjemi, A. H. Kokabi, A. A. Ziaie, S. Manteghi, and F. M. Burdekin, "Comparison of the stress intensity factor of T and cruciform welded joints with different main and attachment plate thickness," *Engineering Fracture Mechanics,* vol. 65, no. 1, pp. 55-66, 2000/01/01/ 2000.

[93] F. V. Antunes, J. M. Ferreira, and J. Byrne, "Stress intensity factor calculation based on the work of external forces," *International Journal of Fracture,* vol. 98, no. 1, pp. 1-14, 1999/05/01 1999.

[94] M. Farjoo, S. Pal, W. Daniel, and P. A. Meehan, "Stress intensity factors around a 3D squat form crack and prediction of crack growth direction considering water entrapment and elastic foundation," *Engineering Fracture Mechanics,* Article vol. 94, pp. 37-55, 2012.

[95] K. Guo, R. Bell, and X. Wang, "The stress intensity factor solutions for edge cracks in a padded plate geometry under general loading conditions," *International Journal of Fatigue,* vol. 29, no. 3, pp. 481-488, 2007/03/01/ 2007.

[96] C. Cui, Q. Zhang, Y. Bao, Y. Bu, and Y. Luo, "Fatigue life evaluation of welded joints in steel bridge considering residual stress," *Journal of Constructional Steel Research,* vol. 153, pp. 509-518, 2019/02/01/ 2019.

[97] P. P. Benham and R. J. Crawford, *Mechanics of engineering materials*. Harlow, Essex, England: Longman Group, 1996.

[98] J. C. Newman and I. S. Raju, "An empirical stress-intensity factor equation for the surface crack," *Engineering Fracture Mechanics,* vol. 15, no. 1, pp. 185-192, 1981/01/01/ 1981.

[99] M. Aleyaasin, *Mechanics of finite deformation and fracture*. 2016.

[100] P. C. Miedlar, A. P. Berens, A. Gunderson, and J. P. Gallagher, "Handbook for Damage Tolerant Design," University of Dayton Research Institute2003.

[101] D. n. V. A.S.Computas, "On the Principle of Superposition for Stress Intensity Factors," *Engineering Fracture Mechanics,* vol. Vol.8, pp. 437-440, 1976.

[102] G. Glinka, "Effect of Residual Stresses on Fatigue Crack Growth in Steel Weldments Under Constant and Variable Amplitude Loads," C. W. Smith, Ed. West Conshohocken, PA: ASTM International, 1979, pp. 198-214.

[103] A. P. Parker, "Stress Intensity Factors, Crack Profiles, and Fatigue Crack Growth Rates in Residual Stress Fields," J. F. Throop and H. S. Reemsnyder, Eds. West Conshohocken, PA: ASTM International, 1982, pp. 13-31.

[104] D. V. Nelson, "Effects of Residual Stress on Fatigue Crack Propagation," J. F. Throop and H. S. Reemsnyder, Eds. West Conshohocken, PA: ASTM International, 1982, pp. 172-194.

[105] K. Walker, "The Effect of Stress Ratio During Crack Propagation and Fatigue for 2024-T3 and 7075-T6 Aluminum," M. S. Rosenfeld, Ed. West Conshohocken, PA: ASTM International, 1970, pp. 1-14.

[106] R. Ghajar and H. Saeidi Googarchin, "General point load weight function for semi-elliptical crack in finite thickness plates," *Engineering Fracture Mechanics,* vol. 109, pp. 33-44, 2013/09/01/ 2013.

[107] X. J. Zheng, A. Kiciak, and G. Glinka, "Weight functions and stress intensity factors for internal surface semi-elliptical crack in thick-walled cylinder," *Engineering Fracture Mechanics,* vol. 58, no. 3, pp. 207-221, 1997/10/01/ 1997.

[108] Z. Barsoum and I. Barsoum, "Residual stress effects on fatigue life of welded structures using LEFM," *Engineering Failure Analysis,* vol. 16, no. 1, pp. 449-467, 2009/01/01/ 2009.

[109] Y. Z. Itoh, S. Suruga, and H. Kashiwaya, "Prediction of fatigue crack growth rate in welding residual stress field," *Engineering Fracture Mechanics,* vol. 33, no. 3, pp. 397-407, 1989/01/01/ 1989.

[110] D. F. Cannon, K.-O. Edel, S. L. Grassie, and K. Sawley, "Rail defects: an overview," *Fatigue & Fracture of Engineering Materials & Structures,* vol. 26, no. 10, pp. 865-886, 2003.

[111] P. J. Mutton, "Horizontal split web fatigue failure of rail welds," presented at the Conf. Failure Analysis in Materials Engineering, Melbourne, 1994.

[112] C. B. Smith, *Railway engineering*. Toronto; Montreal: Biggar, Samuel, 2018.

[113] B. B. Vinokur, O. G. Kasatkin, and S. E. Kondratyuk, "Calculation models for determining the mechanical properties of structural steels," *Metal Science and Heat Treatment,* journal article vol. 31, no. 7, pp. 479-483, July 01 1989.

[114] J. TRZASKA, "Calculation of Critical Temperatures by Empirical Formulae," *Archives of Metallurgy and Materials,* vol. 61, no. No 2B, pp. 981–986, 2016.

[115] D. S. S. Corp. ABAQUS/Standard User's Manual, Version 6.14 [Online].

[116] B. L. Josefson, "Residual Stresses and Their Redistribution During Annealing of a Girth-Butt Welded Thin-Walled Pipe," *J. Pressure Vessel Technol.; (United States),* vol. 104:3, 08/01 1982.

[117] G. Schleinzer and F. D. Fischer, "Residual stress formation during the roller straightening of railway rails," *International Journal of Mechanical Sciences,* vol. 43, no. 10, pp. 2281-2295, 2001/10/01/ 2001.

[118] O. Orringer, Y. H. Tang, J. E. Gordon, D. Y. Jeong, J. M. Morris, and A. B. Perlman, *Crack propagation life of detail fractures in rails*. Washington, DC: U.S. Department of Transportation, Federal Railroad Administration, 1988.

[119] H. Hamdi, H. Zahouani, and J.-M. Bergheau, "Residual stresses computation in a grinding process," *Journal of Materials Processing Technology,* vol. 147, no. 3, pp. 277-285, 2004/04/20/ 2004.

[120] C.-H. Lee, K.-H. Chang, and V. N. V. Do, "Finite element modeling of residual stress relaxation in steel butt welds under cyclic loading," *Engineering Structures,* vol. 103, pp. 63-71, 2015/11/15/ 2015.

[121] X.-f. Xie, W. Jiang, Y. Luo, S. Xu, J.-M. Gong, and S.-T. Tu, "A model to predict the relaxation of weld residual stress by cyclic load: Experimental and finite element modeling," *International Journal of Fatigue,* vol. 95, pp. 293-301, 2017/02/01/ 2017.

[122] *BS 7910 Guide to Methods for Assessing the Acceptability of Flaws in Metallic Structures*, 2013.

[123] *API 579-1 Fitness-For-Service*, 2016.

[124] G. Glinka, Z. Gmur, and Z. Świderski, "An examination of mixed fatigue-tensile surface crack growth in rails," *Engineering Fracture Mechanics,* Article vol. 20, no. 1, pp. 103-112, 1984.

[125] J. J. Han and M. Dhanasekar, "A method for tracking internal crack propagation in railhead," *International Journal of Fracture,* Article vol. 130, no. 3, pp. 705-719, 2004.

[126] J. W. Ringsberg, B. L. Josefson, and A. Skyttebol, "Fatigue crack growth in welded rails," in *11th International Conference on Fracture 2005, ICF11*, 2005, vol. 8, pp. 5627-5632.

[127] D. Bowness and M. M. K. Lee, "Prediction of weld toe magnification factors for semi-elliptical cracks in T–butt joints," *International Journal of Fatigue,* vol. 22, no. 5, pp. 369-387, 2000/05/01/ 2000.

[128] J. H. L. Pang, K. S. Tsang, and H. J. Hoh, "3D stress intensity factors for weld toe semi-elliptical surface cracks using XFEM," *Marine Structures,* vol. 48, pp. 1-14, 2016/07/01/ 2016.

[129] *ASTM E8/E8M -16 Standard Test Methods for Tension Testing of Metallic Materials*, 2016.

[130] *BS EN ISO 148-1:2016 Metallic materials — Charpy pendulum impact test* 2016.

[131] *ASTM E647-05 - Standard test method for measurement of fatigue crack growth rates*, 2005.

[132] H. T. Wang, G. Z. Wang, F. Z. Xuan, and S. T. Tu, "An experimental investigation of local fracture resistance and crack growth paths in a dissimilar metal welded joint," *Materials & Design,* vol. 44, pp. 179-189, 2013/02/01/ 2013.

[133] Y. D. Li, C. B. Liu, N. Xu, X. F. Wu, W. M. Guo, and J. B. Shi, "A failure study of the railway rail serviced for heavy cargo trains," *Case Studies in Engineering Failure Analysis,* vol. 1, no. 4, pp. 243-248, 2013/10/01/ 2013.

[134] A. J. Perez-Unzueta and J. H. Beynon, "Microstructure and wear resistance of pearlitic rail steels," *Wear,* vol. 162-164, pp. 173-182, 1993/04/13/ 1993.

[135] Y. Murakami, *Metal fatigue : effects of small defects and nonmetallic inclusions*. 2019.

[136] I. Grossoni, P. Shackleton, Y. Bezin, and J. Jaiswal, "Longitudinal rail weld geometry control and assessment criteria," *Engineering Failure Analysis,* vol. 80, pp. 352-367, 2017/10/01/ 2017.

[137] X. Zhao, W. Dongpo, C. Deng, Y. Liu, and S. Zongxian, "The fatigue behaviors of butt welds ground flush in the super-long life regime," *International Journal of Fatigue,* vol. 36, no. 1, pp. 1-8, 2012.

[138] M. T. Tilbrook, R. J. Moon, and M. Hoffman, "On the mechanical properties of alumina–epoxy composites with an interpenetrating network structure," *Materials Science and Engineering: A,* vol. 393, no. 1, pp. 170-178, 2005/02/25/ 2005.

[139] R. E. Peterson, *Stress Concentration Design Factors*. 1974.

[140] J. C. Sobotka, M. P. Enright, and R. C. McClung, "Application of critical distances to fatigue at pores," *Fatigue & Fracture of Engineering Materials & Structures,* vol. 42, no. 8, pp. 1646-1661, 2019.

[141] S. Tanaka, T. Kawahara, and H. Okada, "Study on crack propagation simulation of surface crack in welded joint structure," *Marine Structures,* vol. 39, pp. 315-334, 2014/12/01/ 2014.

[142] M. Skorupa and A. Skorupa, "Experimental results and predictions on fatigue crack growth in structural steel," *International Journal of Fatigue,* vol. 27, no. 8, pp. 1016-1028, 2005/08/01/ 2005.

[143] K. Sadananda and A. K. Vasudevan, "Fatigue crack growth mechanisms in steels," *International Journal of Fatigue,* vol. 25, no. 9, pp. 899-914, 2003/09/01/ 2003.

[144] S. Maya-Johnson, A. J. Ramirez, and A. Toro, "Fatigue crack growth rate of two pearlitic rail steels," *Engineering Fracture Mechanics,* vol. 138, pp. 63-72, 2015/04/01/ 2015.

[145] T. A. Cruse and P. M. Besuner, "Residual life prediction for surface cracks in complex structural details," *Journal of Aircraft,* vol. 12, no. 4, pp. 369-375, 1975.

[146] J. G. Merkle, "A review of some of the existing stress-intensity factor solutions for part-through surface cracks," in "ORNL-TM-3983," Atomic Energy Commission, U.S.1973.

[147] S. X. Wu, "Shape change of surface crack during fatigue growth," *Engineering Fracture Mechanics,* vol. 22, no. No.5, pp. 897-913, 1985.

[148] Reza Masoudi Nejad, Khalil Farhangdoost, Mahmoud Shariati, and Majid Moavenian, "Stress Intensity Factors Evaluation for Rolling Contact Fatigue Cracks in Rails," *Tribology Transactions,* vol. 60, no. 4, pp. 645-652, 2017.

[149] A. F. Powell and P. J. Gräbe, "Exploring the relationship between vertical and lateral forces, speed and superelevation in railway curves," *Journal of the South African Institution of Civil Engineering,* vol. 59, pp. 25-35, 2017.

[150] G. Shen and G. Glinka, "Weight functions for a surface semi-elliptical crack in a finite thickness plate," *Theoretical and Applied Fracture Mechanics,* vol. 15, no. 3, pp. 247-255, 1991/08/01/ 1991.

[151] H. Y. Li, H. L. Sun, P. Bowen, and J. F. Knott, "Effects of compressive residual stress on short fatigue crack growth in a nickel-based superalloy," *International Journal of Fatigue,* vol. 108, pp. 53-61, 2018/03/01/ 2018.